

ABSTRACT

Title of Dissertation: THE EFFECTS OF FINITE-RATE
REACTIONS AT THE GAS/SURFACE
INTERFACE IN SUPPORT OF THERMAL
PROTECTION SYSTEM DESIGN

Adam Farrell Beerman, Ph.D., 2011

Directed By: Professor and Department Chair Mark J. Lewis,
Department of Aerospace Engineering

Gas-surface modeling is dependent on material type and atmospheric reentry conditions. Lower molecular collisions at the low pressure trajectories make it more likely for occurrences of nonequilibrium, or finite-rate, reactions. Equilibrium is often assumed at the surface of a material as it is a subset of nonequilibrium and is easier to compute, though it can lead to overly conservative predictions. A case where a low density material experiences a low pressure trajectory and designed for equilibrium is the Stardust Return Capsule (SRC) with the Phenolic Impregnated Carbon Ablator (PICA) as its heatshield. Post-flight analysis of the recession on the SRC found that the prediction from the equilibrium model can be more than 50% larger than the measured recession. The Modified Park Model was chosen as the finite-rate model as it contains simple four reactions (oxidation, sublimation, and nitridation) and has been previously used to study individual points of the SRC trajectory. The Modified

Park Model cannot model equilibrium so a model BFIAT was developed that allows finite-rate reactions to be applied to the surface for a certain length of time. Finite-rate sublimation was determined to be reaction of importance in the Park Model for SRC-like conditions. The predicted recession on the SRC heatshield experienced a reduction in its overprediction; the finite-rate predictions fall with the measurement error of the recession at three points on the heatshield. The recession reduction was driven by a significant reduction in char formation. There was little change in the pyrolysis gas rate. The finite-rate model was also applied to simulations of various arc-jet tests that covered a range of heating conditions on the surface of the PICA material. Comparison to this experimental data further showed the role of finite-rate reactions and sublimation in the Park Model and conditions that favor the nonequilibrium assumption (heating over 1000 W/cm^2). For the emerging PICA material, used for the Mars Science Laboratory and one of two material choices for the Crew Exploration Vehicle, and SRC-like trajectories, a finite-rate model was developed such that the more robust nonequilibrium assumption can be applied to design processes to reduce heatshield mass.

THE EFFECTS OF FINITE-RATE REACTIONS AT THE GAS/SURFACE
INTERFACE IN SUPPORT OF THERMAL PROTECTION SYSTEM DESIGN

By

Adam Farrell Beerman

Dissertation submitted to the Faculty of the Graduate School of the
University of Maryland, College Park, in partial fulfillment
of the requirements for the degree of
Doctor of Philosophy
2011

Advisory Committee:

Professor and Department Chair Mark J. Lewis, Chair
Associate Professor Christopher Cadou
Associate Professor James Baeder
Associate Professor David Akin
Associate Professor Tien-Mo Shih

© Copyright by
Adam Farrell Berman
2011

DEDICATION

To my mother, Robin

Motivator, Cheerleader, Mom

ACKNOWLEDGEMENTS

I would like to first thank my advisor, Dr. Mark J. Lewis who guided me through this long process and expanded my knowledge, not only in the area of material response, but in other subjects. I am a smarter man for being his student. I would also like to send my thanks to my committee members Dr. James Baeder, Dr. Christopher Cadou, Dr. David Akin, and Dr. Tien-Mo Shih. Their advice and constructive criticism help make this dissertation stronger. Additional thanks to Dr. Ryan Starkey who helped guide me through my early years at the University of Maryland.

Much gratitude is extended to Dr. Bohdan Cybyk and others at the Johns Hopkins Applied Physics Laboratory in Laurel, Maryland. The experience working alongside these people in a non-academic setting helped attack problems in a different direction. They proved an invaluable source of help and information. I was able to be both a student and a professional simultaneously when I had to bend their ears for problem solving.

The Constellation University Institutes Program funded the research contained within and for that, thanks is given. At NASA, Dr. Michael Wright, Dr. David Hash, Dr. Ioana Cozmuta, and Dr. Frank Milos provided invaluable advice and insight. They helped guide this research and gave me the opportunity to expand my knowledge during two internships at the NASA Ames Research Center.

For creating an atmosphere where it was actually enjoyable to go into an office everyday, I must thank those who worked beside me in the Hypersonics group at the University of Maryland. When lines of code started to blur, a yell over a cubicle wall to discuss either our latest research or the latest movie provided a welcomed break. Rather than single out a handful of people, everyone I have worked with or beside since arriving at the University of Maryland, I laud. Each of you helped contribute to this dissertation in small ways.

Finally, I would be remiss if I did not thank my family. It hasn't always been smooth sailing, but with the support system provided by blood, I could take comfort within my family even if the seas were rough. The man I am today is because of how that boy from yesterday was raised. I could not have asked for better people to be there for a late-night call when I was stressing out or for a quick-fire joke when a situation needed defusing. They didn't need to motivate me I motivated myself to honor them.

Table of Contents

Dedication	ii
Acknowledgements	iii
Table of Contents	v
List of Tables.....	vi
List of Figures	ix
List of Symbols	xxvi
Chapter 1 Introduction	1
1.1 Motivation	1
1.2 Previous Ablation Work.....	12
1.3 Background on Chemistry and Stardust Return Capsule.....	24
Chapter 2 The Surface/Gas Interface.....	30
2.1 Material Choice	30
2.2 The Fully Implicit Ablation and Thermal Material Response Program	35
2.3 Nonequilibrium Gas Properties	46
2.4 Surface Interactions	52
2.5 The Multicomponent Ablation Thermochemistry (MAT) Program.....	64
Chapter 3 Stardust Return Capsule Trajectory Analysis	72
3.1 Preliminary Design Trajectory	72
3.1.1 Equilibrium	72
3.1.2 Nonequilibrium	79
3.2 Final Design Trajectory.....	108
3.2.1 Stagnation Point – Entire Trajectory	112
3.2.2 Stagnation Point – Heating Tail.....	138
3.2.3 Stagnation Point – Post Peak Heating	146
3.2.4 Stagnation Point – Post Sublimation.....	156
3.2.5 Near Stagnation Point – Equilibrium	164
3.2.6 Near Stagnation Point – Nonequilibrium	174
3.2.7 Core 2 – Point 47 – Equilibrium	181
3.2.8 Core 2 – Point 47 – Nonequilibrium	188
Chapter 4 Comparison with Experimental, Numerical, and Flight Test Data Sets...	194
4.1 Park Model and the SRC Preliminary Design Trajectory.....	194
4.2 Stardust Return Capsule Measured Data.....	200
4.3 Arc-Jet Test Data	214
4.4 State of the Art Park-Based Material Response Model	234
Chapter 5 Summary and Conclusions	243
Chapter 6 Future Work	248
6.1 Improving the Finite-Rate Model	248
6.2 Inclusion of Pyrolysis Gas Effects.....	250
6.3 Expansion to Two Dimensions.....	251
6.3 Additional Comparisons Against Varied Atmospheric Entry Data.....	252
6.4 Increase Knowledge of the Reactions Physics and Model Building	253
Bibliography.....	257

LIST OF TABLES

1.1	The freestream conditions encountered by the SRC during the heat pulse ...	28
3.1	The effects of varying the volume assumption on the charring rate in MAT in the use of the Park Model	80
3.2	The general pressure, B'_g , and B'_c values used to construct the B' table	81
3.3	A comparison of peak temperatures for different equilibrium and nonequilibrium cases for the preliminary SRC trajectory	99
3.4	The peak values of the surface heating terms for the final SRC trajectory	120
3.5	The peak values of the surface chemistry heating terms in equilibrium and finite-rate models for the final SRC trajectory	131
3.6	The peak values of the surface heating terms for two points of the heatshield for the final SRC trajectory	170
3.7	The total heat loads of the surface heating terms at the stagnation and near stagnation point for the final SRC trajectory	173
3.8	The peak values of the surface heating terms at the near stagnation point during two chemical assumptions for the final SRC trajectory	178
3.9	The total heat loads of the surface heating terms at the near stagnation point in equilibrium and nonequilibrium for the final SRC trajectory	180

3.10	The peak values of the surface heating terms for two points of the heatshield for the final SRC trajectory	187
3.11	The total heat loads of the surface heating terms at the stagnation and Core 2 – Point 47 location for the final SRC trajectory	187
3.12	The absolute value of the peak in-depth heat flux terms at the stagnation and Core 2 – Point 47 location for the final SRC trajectory	187
3.13	The peak values of the surface heating terms for equilibrium and nonequilibrium at Core 2 – Point 47 for the final SRC trajectory	193
3.14	The total heat loads of the surface heating terms for equilibrium and nonequilibrium at the Core 2 – Point 47 for the final SRC trajectory	193
3.15	The absolute value of the peak in-depth heat flux terms for equilibrium and nonequilibrium at the Core 2 – Point 47 for the final SRC trajectory	193
4.1	The total mass blowing (ablation) rate and convective heat flux at 54 seconds for a direct iterative scheme using Stardust peak heating conditions and for a process using MAT and FIAT	197
4.2	The measured recession and the predicted recession for the SRC	201
4.3	The measured recession and the predicted recession for the SRC when nonequilibrium is applied only partially to the trajectory	203
4.4	The average measured recession rate and the average predicted recession rate for the two highest Covington heating environments	218
4.5	The average measured surface temperature and the average predicted surface temperature for the two highest Covington heating environments	221

4.6	The average measured recession rate and the average predicted recession rate for the two lowest Covington heating environments	223
4.7	The average measured surface temperature and the average predicted surface temperature for the two lowest Covington heating environments	223
4.8	The results from the four arc-jet cases where a nitrogen-oxygen flow is used and FIAT's predictions using the measured enthalpy	226
4.9	The results from the four arc-jet cases where a nitrogen-oxygen flow is used and FIAT's predictions using the DPLR enthalpy to account for shape change	227
4.10	The results from the argon arc-jet cases where there is a significant amount of argon in the flow but only a mass fraction 0.086 in MAT	231
4.11	The results from the argon arc-jet cases where there is a significant amount of argon in the flow but only a mass fraction 0.086 in MAT for comparison between finite-rate and simple kinetics predictions	242

LIST OF FIGURES

1.1	A TPS material undergoing high heating and experiencing pyrolysis and char formation	2
1.2	Measured heating rates for Apollo 4 compared to those predicted by using nonequilibrium surface conditions [from Ref. 4]	5
1.3	Measured heating rates for Apollo 6 compared to those predicted by using nonequilibrium surface conditions [from Ref. 4]	6
1.4	The locations of the three points of analysis for the Stardust Return Capsule, with only the two Core points being physically measured upon recovery....	10
1.5	Possible streamlines for each of the points under consideration in the analysis	10
1.6	The notional trajectory for the Stardust Return Capsule reentry	29
2.1	The stagnation recession rate of various ablators, including carbon-phenolic ablators (c-LCA) at a heat flux of 460 W/cm^2 and a pressure of 0.081 atm [from Ref. 47]	32
2.2	Physical representation of what is occurring on the PICA material during high heating and what needs to be calculated in a material response model	37
2.3	Representation of the heating on the PICA material during high heating and what needs to be calculated in a material response model	37

2.4	A typical grid layout in FIAT	39
2.5	The three reaction regimes for a CEV-like aerothermal environment [from Ref. 58]	51
2.6	A sample <i>B'</i> table with the char ablation rate on the y-axis and different values of the pyrolysis gas rate [from Ref. 52]	54
2.7	The mass fluxes at the surface of a thermal protection system in a hypersonic boundary layer	66
3.1	The surface heating profile for the preliminary Stardust Return Capsule trajectory	73
3.2	The heatshield material layout for the preliminary design SRC trajectory analysis	75
3.3	The equilibrium temperature profile for the preliminary SRC equilibrium trajectory	77
3.4	The mass loss profile for the preliminary SRC equilibrium trajectory	77
3.5	The heat load profile for the preliminary SRC equilibrium trajectory	79
3.6	Temperature profile for the preliminary SRC trajectory using Park's Model with nitridation	83
3.7	Temperature profile for the preliminary SRC trajectory using Park's Model without nitridation	84
3.8	The char ablation rate for the preliminary SRC trajectory using Park's Model with nitridation	85
3.9	The char ablation rate for the preliminary SRC trajectory using Park's Model without nitridation	86

3.10	A side-by-side comparison of the char ablation rate for the preliminary SRC trajectory for both subcases of Park’s model	86
3.11	The pyrolysis gas rate for the equilibrium and Park models for the preliminary SRC trajectory	87
3.12	The total surface blowing rate for the equilibrium and Park models for the preliminary SRC trajectory	88
3.13	The convective heat flux for the equilibrium and Park models for the preliminary SRC trajectory	89
3.14	The heat loads for the equilibrium case and Park Model for the preliminary SRC trajectory	90
3.15	The recession for the equilibrium case and the Park Model, with and without the nitridation reaction, for the preliminary SRC trajectory	91
3.16	The temperature profile for a reaction set without diffusion-limited oxidation and nitridation for the preliminary SRC trajectory	93
3.17	The char ablation rate for the reaction sets without diffusion-limited oxidation and nitridation and without nitridation only and for an equilibrium analysis for the preliminary SRC trajectory	93
3.18	The pyrolysis gas rate for the reaction sets without diffusion-limited oxidation and nitridation and without nitridation only and for an equilibrium analysis for the preliminary SRC trajectory	94
3.19	The total ablation rate for the reaction sets without diffusion-limited oxidation and nitridation and without nitridation only and for an equilibrium analysis for the preliminary SRC trajectory	94

3.20	The temperature profile for the preliminary SRC trajectory without sublimation	97
3.21	The surface temperature profile for the preliminary SRC trajectory for three surface conditions	97
3.22	The char ablation rate for equilibrium, nonequilibrium without nitridation and nonequilibrium without nitridation and sublimation for the preliminary SRC trajectory	99
3.23	The general trends of the surface temperature and char ablation rate for nonequilibrium without sublimation for the preliminary SRC trajectory	99
3.24	The pyrolysis gas rate for equilibrium and nonequilibrium without nitridation and nonequilibrium without nitridation and sublimation for the preliminary SRC trajectory	100
3.25	The total ablation rate for equilibrium and nonequilibrium without nitridation and nonequilibrium without nitridation and sublimation for the preliminary SRC trajectory	101
3.26	The recession profile for three finite-rate assumptions for the preliminary SRC trajectory	102
3.27	The convective heat fluxes for equilibrium, nonequilibrium without nitridation and nonequilibrium without nitridation and sublimation for the preliminary SRC trajectory	103
3.28	The wall enthalpy for the three cases under examination for the preliminary SRC trajectory	104

3.29	The blown transfer coefficient for equilibrium, nonequilibrium without nitridation, and nonequilibrium without nitridation and sublimation for the preliminary SRC trajectory	105
3.30	The heat fluxes when sublimation is not considered at each preliminary SRC trajectory point	106
3.31	The heat loads for equilibrium and nonequilibrium without nitridation and sublimation for the preliminary SRC trajectory	107
3.32	The heat flux terms acting upon the surface of a material	109
3.33	The heatshield material layout for the final design SRC trajectory analysis	111
3.34	The environmental heat fluxes, not including radiation, at the stagnation point for the preliminary and final SRC trajectories and with the convective and total heat flux being the same for the final trajectory	113
3.35	The heat transfer coefficient at the stagnation point for the preliminary and final SRC design trajectories	113
3.36	The temperature profile for the final design SRC trajectory	114
3.37	The predicted char blowing rate profile for the preliminary and final design SRC trajectory	116
3.38	The predicted pyrolysis gas blowing rate profile for the preliminary and final design SRC trajectory	116
3.39	The predicted total ablation rate profile for the preliminary and final design SRC trajectory, with and without failure	117

3.40	The predicted heating profile, including chemistry terms, for the final design SRC trajectory	118
3.41	The predicted heating profile only considering chemistry terms and conduction for the final design SRC trajectory	119
3.42	The predicted heat loads, including chemistry terms, for the final design SRC trajectory	120
3.43	The predicted chemistry and conduction heat loads for the final design SRC trajectory	121
3.44	The in-depth heating as a function of depth at the stagnation point at peaking heating for the final design SRC trajectory	122
3.45	Summation of the heat fluxes in-depth during the final design SRC trajectory at the stagnation point	123
3.46	A comparison of the conduction leaving the surface and the conduction present in-depth	123
3.47	The recession for the two SRC trajectories, both in equilibrium and nonequilibrium	124
3.48	The pyrolysis gas rate for the final design SRC trajectory in equilibrium and nonequilibrium	126
3.49	The char rate for the final design trajectory in equilibrium and nonequilibrium	126
3.50	The total ablation rate for the final design trajectory in equilibrium and nonequilibrium	127

3.51	The surface and TC 1 temperature predictions for equilibrium and finite-rate chemistry models for the final design SRC trajectory	128
3.52	The net convective heat flux predictions for equilibrium and finite-rate chemistry models, with and without wall enthalpy, for the final design SRC trajectory	129
3.53	The char and pyrolysis gas heat flux predictions for equilibrium and finite-rate chemistry models for the final design SRC trajectory	130
3.54	The injected heat flux predictions for equilibrium and finite-rate chemistry models for the final design SRC trajectory	131
3.55	The conduction predictions for equilibrium and finite-rate chemistry models for the final design SRC trajectory	132
3.56	The heat load predictions for the finite-rate chemistry model for the final design SRC trajectory	132
3.57	The wall enthalpy predictions for equilibrium and finite-rate chemistry models for the final design SRC trajectory	134
3.58	The wall enthalpy predictions for equilibrium and finite-rate chemistry models, with and without nonchar indexes, for the final design SRC trajectory	134
3.59	The conduction predictions for the finite-rate chemistry model, with and without nonchar indexes, for the final design SRC trajectory	135
3.60	The in-depth heat flux predictions for the finite-rate chemistry model for the final design SRC trajectory	136

3.61	Recession predictions for the equilibrium assumption, finite-rate over the entire final design SRC trajectory assumption, and finite-rate only at the heating tail assumption	139
3.62	Recession rate predictions for equilibrium assumption, finite-rate over the entire final design SRC trajectory assumption, and finite-rate only at the heating tail assumption	140
3.63	The char rate for the final design trajectory in equilibrium during the entire trajectory assumption, finite-rate during the entire trajectory assumption, and finite-rate during the heating tail assumption	141
3.64	The pyrolysis gas rate for the final design trajectory in equilibrium during the entire trajectory assumption, finite-rate during the entire trajectory assumption, and finite-rate during the heating tail assumption	141
3.65	The total ablation rate for the final design trajectory in equilibrium during the entire trajectory assumption, finite-rate during the entire trajectory assumption, and finite-rate during the heating tail assumption	142
3.66	The surface temperature and the temperature at the depth of the first thermocouple couple for the final design trajectory in equilibrium during the entire trajectory assumption, finite-rate during the entire trajectory assumption, and finite-rate during the heating tail assumption	143
3.67	The char and pyrolysis gas heat fluxes on the surface for the final design trajectory in equilibrium during the entire trajectory assumption, finite-rate during the entire trajectory assumption, and finite-rate during the heating tail assumption	143

3.68	The injected heat flux for the final design trajectory in equilibrium during the entire trajectory assumption, finite-rate during the entire trajectory assumption, and finite-rate during the heating tail assumption	144
3.69	The surface conduction heat flux for the final design trajectory in equilibrium during the entire trajectory assumption, finite-rate during the entire trajectory assumption, and finite-rate during the heating tail assumption	145
3.70	The in-depth heat fluxes for the final design trajectory in a finite-rate during the heating tail assumption	145
3.71	Recession predictions for the equilibrium assumption, finite-rate over the entire final design SRC trajectory assumption, and finite-rate beginning at the peak heating assumption	148
3.72	Recession rate predictions for the equilibrium assumption, finite-rate over the entire final design SRC trajectory assumption, and finite-rate beginning at the peak heating assumption	148
3.73	The char rate for the final design trajectory in equilibrium during the entire trajectory assumption, finite-rate during the entire trajectory assumption, and finite-rate after peaking heating assumption	149
3.74	The pyrolysis gas rate for the final design trajectory in equilibrium during the entire trajectory assumption, finite-rate during the entire trajectory assumption, and finite-rate after peaking heating assumption	150
3.75	The total ablation rate for the final design trajectory in equilibrium during the entire trajectory assumption, finite-rate during the entire trajectory assumption, and finite-rate after peaking heating assumption	150

3.76	The surface temperature and the temperature at the depth of the first thermocouple couple for the final design trajectory in equilibrium during the entire trajectory assumption, finite-rate during the entire trajectory assumption, and finite-rate after peak heating assumption	151
3.77	The net convection and radiation out heat flux predictions when equilibrium is assumed over the entire final design SRC trajectory and when finite-rate reactions are applied after peak heating	152
3.78	The net convection and radiation out heat flux predictions when nonequilibrium is assumed over the entire final design SRC trajectory and when finite-rate reactions are applied after peak heating	153
3.79	The char and pyrolysis gas heat fluxes on the surface for the final design trajectory in equilibrium during the entire trajectory assumption, finite-rate during the entire trajectory assumption, and finite-rate after the peak heating assumption	154
3.80	The injected heat flux for the final design trajectory in equilibrium during the entire trajectory assumption, finite-rate during the entire trajectory assumption, and finite-rate after the peak heating assumption	154
3.81	The surface conduction heat flux for the final design trajectory in equilibrium during the entire trajectory assumption, finite-rate during the entire trajectory assumption, and finite-rate after the peak heating assumption	155
3.82	The in-depth heat fluxes for the final design trajectory in a finite-rate after the peak heating assumption	156

3.83	The surface temperature and the temperature at the depth of the first thermocouple couple for the final design trajectory in equilibrium during the entire trajectory assumption, finite-rate during the entire trajectory assumption, and finite-rate after 3000 K assumption	158
3.84	Recession rate predictions for the equilibrium assumption, finite-rate over the entire final design SRC trajectory assumption, and finite-rate after 3000 K assumption	159
3.85	Recession predictions for the equilibrium assumption, finite-rate over the entire final design SRC trajectory assumption, and finite-rate after 3000 K assumption	159
3.86	The char rate for the final design trajectory in equilibrium during the entire trajectory assumption, finite-rate during the entire trajectory assumption, and finite-rate after 3000 K assumption	160
3.87	The pyrolysis gas rate for the final design trajectory in equilibrium during the entire trajectory assumption, finite-rate during the entire trajectory assumption, and finite-rate after 3000 K assumption	160
3.88	The total ablation rate for the final design trajectory in equilibrium during the entire trajectory assumption, finite-rate during the entire trajectory assumption, and finite-rate after 3000 K assumption	161
3.89	The net convection and radiation out heat flux predictions when equilibrium is assumed over the entire final design SRC trajectory and when finite-rate reactions are applied after 3000 K	162

3.90	The net convection and radiation out heat flux predictions when nonequilibrium is assumed over the entire final design SRC trajectory and when finite-rate reactions are applied after 3000 K	163
3.91	The char and pyrolysis gas heat fluxes on the surface for the final design trajectory in equilibrium during the entire trajectory assumption, finite-rate during the entire trajectory assumption, and finite-rate after the 3000 K assumption	163
3.92	The injected heat flux for the final design trajectory in equilibrium during the entire trajectory assumption, finite-rate during the entire trajectory assumption, and finite-rate after 3000 K assumption	164
3.93	The near stagnation and flank core points, along with a shoulder point, indicated in red on the Stardust Return Capsule [from Ref. 84]	165
3.94	The cold wall heat flux for the stagnation point and the near stagnation point location for the final design SRC trajectory	166
3.95	The pressure profile for the stagnation point and the near stagnation point location for the final design SRC trajectory	166
3.96	The predicted char ablation rate for the stagnation point and near stagnation point locations for the final design SRC trajectory	167
3.97	The predicted pyrolysis gas rate for the stagnation point and near stagnation point locations for the final design SRC trajectory	168
3.98	The total ablation rate for the stagnation point and near stagnation point locations for the final design SRC trajectory	168

3.99	The recession profile for the stagnation and near stagnation points for the final design SRC trajectory	169
3.100	The recession rate profile for the stagnation and near stagnation points for the final design SRC trajectory	169
3.101	The percent difference of the surface heat fluxes that are entering the surface when considering the stagnation point and near stagnation point locations for the final design SRC trajectory	172
3.102	The percent difference of the surface heat fluxes that are leaving the surface when considering the stagnation point and near stagnation point locations for the final design SRC trajectory	172
3.103	The percent difference of the in-depth heat fluxes when considering the stagnation point and near stagnation point locations for the final design SRC trajectory	173
3.104	The recession profiles for the stagnation point and near stagnation point in equilibrium and with finite-rate reactions for the final design SRC trajectory	175
3.105	The char ablation rates for the stagnation point and near stagnation point in equilibrium and with finite-rate reactions for the final design SRC trajectory	175
3.106	The pyrolysis gas rates for the stagnation point and near stagnation point in equilibrium and with finite-rate reactions for the final design SRC trajectory	176

3.107	The total ablation rates for the stagnation point and near stagnation point in equilibrium and with finite-rate reactions for the final design SRC trajectory	176
3.108	The temperature profiles at the surface and at the TC 1 depth location at the near stagnation point in both equilibrium and nonequilibrium for the final design SRC trajectory	177
3.109	The injected heat flux at the near stagnation point when undergoing equilibrium and nonequilibrium reactions for the final design SRC trajectory	179
3.110	The injected heat flux at the near stagnation point when undergoing equilibrium and nonequilibrium reactions for the final design SRC trajectory	179
3.111	The in-depth heat fluxes at the near stagnation point when undergoing nonequilibrium reactions for the final design SRC trajectory	180
3.112	The heat transfer coefficient for the three locations on the SRC heatshield for the final design trajectory	182
3.113	The surface pressure for the three locations on the SRC heatshield for the final design trajectory	182
3.114	The cold wall heat flux for the three locations on the SRC heatshield for the final design trajectory	183
3.115	The recession rate at the three locations on the SRC heatshield for the final design trajectory	184

3.116	The recession profile at the three locations on the SRC heatshield for the final design trajectory	184
3.117	The pyrolysis gas rate at the Point 47 and stagnation point locations for the final design SRC trajectory	185
3.118	The predicted surface temperature and in-depth temperatures at the Core 2 – Point 47 location for the final design SRC trajectory	186
3.119	The recession profile comparing the Core 2 - Point 47 location to the stagnation point for the final design SRC trajectory	189
3.120	The recession rate profile comparing the equilibrium to nonequilibrium implementation at the Core 2 – Point 47 location for the final design SRC trajectory	189
3.121	The surface and TC 1 temperature profile comparing the equilibrium to nonequilibrium implementation at the Core 2 – Point 47 location for the final design SRC trajectory	190
3.122	The char ablation rate comparing the equilibrium to nonequilibrium implementation at the Core 2 – Point 47 location for the final design SRC trajectory	191
3.123	The pyrolysis gas rate comparing the equilibrium to nonequilibrium implementation at the Core 2 – Point 47 location for the final design SRC trajectory	192
3.124	The total ablation rate comparing the equilibrium to nonequilibrium implementation at the Core 2 – Point 47 location for the final design SRC trajectory	192

4.1	The pyrolysis gas and total blowing rate for Park and Olynick’s assumptions, with a comparison to the nonequilibrium assumption applied to the preliminary SRC trajectory	198
4.2	The total heat flux for various models for the preliminary SRC trajectory	199
4.3	The density profile at the near stagnation (Core 1) point	205
4.4	The density profile at the Core 2 – Point 47 location	205
4.5	The equilibrium and finite-rate mole fractions for the three products of the Park Model during SRC reentry as experienced in the final design trajectory	208
4.6	The FIAT surface temperature predictions for the three chemical assumptions versus the SLIT data processed with the two methods to get upper and lower bounds	212
4.7	The recession rate measurements and FIAT predictions for a heating environment of 1630 W/cm ²	217
4.8	The recession rate measurements and FIAT predictions for a heating environment of 1150 W/cm ²	217
4.9	The surface temperature measurements and FIAT predictions for a heating environment of 1150 W/cm ²	220
4.10	The surface temperature measurements and FIAT predictions for a heating environment of 1150 W/cm ²	220
4.11	The recession rate measurements and FIAT predictions for a heating environment of 580 W/cm ²	221

4.12	The recession rate measurements and FIAT predictions for a heating environment of 400 W/cm^2	222
4.13	A typical B' table where the effects of the pyrolysis gas are not separated from the flow [from Ref. 80]	235
4.14	A B' table that considers the pyrolysis gas as a separate entity than from the flow, which results in more plateaus [from Ref. 80]	236
4.15	The percent error between the various finite-rate implementations and the actual measured values	240
4.16	The recession predicted for various finite-rate implementations and the actual measured values	240

LIST OF SYMBOLS

B'	= Dimensionless mass blowing rate, $\dot{m} / \rho_e u_e C_M$
B	= Pre-exponential factor, s^{-1}
(C - i)	= Adatom i, O or N
C_i	= Mass fraction for species i
C_H	= Stanton number for heat transfer
C_M	= Stanton number for mass transfer
c	= Specific heat, J/kg-K
D_i	= Diffusion coefficient for species i , m^2/s
E	= Activation temperature, K
F	= View factor
h	= Enthalpy, J/kg
h_p	= Planck's Constant, J-s
\bar{h}	= Partial heat of charring, J/kg
H_r	= Recovery enthalpy, J/kg
k	= Boltzmann constant, J/K
K	= Kelvin
K_i	= Equilibrium constant
k_t	= Thermal conductivity, W/m-K

M	=	Molecular weight, kg/mole
\dot{m}	=	Mass flux, $\text{kg/m}^2 - \text{s}$
p	=	Pressure, N/m^2
q_{cond}	=	Conductive heat flux, W/m^2
q_{rad}	=	Radiative heat flux, W/m^2
R	=	Gas constant, J/kmol-K
\dot{s}	=	Surface recession rate, m/s
T	=	Temperature, K
t	=	Time, s
u	=	Velocity, m/s
v	=	Mass injection velocity, m/s
x	=	Moving coordinate system, m
y	=	Stationary coordinate, m
Y	=	Element mass fraction
X	=	Mole fraction
α	=	Surface absorption
β	=	Efficiency of gas-surface interaction
∇	=	Gradient
Γ	=	Volume fraction of resin
ε	=	Surface emissivity
θ	=	Surface concentration
λ	=	Blowing reduction parameter
ρ	=	Density, kg/m^3

σ = Stefan-Boltzmann constant, $\text{W/m}^2\text{-K}^4$

ψ = Decomposition reaction order

Subscripts

c = Char

d = Density component

e = Boundary layer edge

g = Pyrolysis gas

i = Surface species

k = Element or gaseous base species

v = Virgin

w = Wall

Chapter 1

Introduction

1.1 Motivation

During periods of intense temperatures or high heating, thermochemical ablation may occur. Thermochemical ablation refers to the phenomenon of surface erosion of an ablative due to severe thermal attack by an external heat flux. To protect against ablation that could be harmful to the base structure undergoing the high heating a Thermal Protection System (TPS) can be added to shield the structure. The TPS can become high in mass if the required thickness to prevent base structure erosion is high or if the material used in the TPS is high in density. For heatshields, TPS determination, the necessary thickness and mass, takes place during the design process as the environment around the spacecraft is simulated and the amount of heating and ablation is determined. The improvement of the accuracy of physics-based modeling of the TPS will help lower the mass cost by minimizing the uncertainties in designing the system.

The TPS undergoes chemical processes internally and on its surface. The associated reactions of the ablative process result in the production of decomposition gases and solid char residue.¹ The decomposition gas is called pyrolysis and is the internal endothermic decomposition of the solid that does not use any of the gas species from the boundary layer flow. The char layer is a phase change of the virgin

material. Char has a lower density than the virgin material but higher thermal conductivity which means the heating on the surface may travel faster through the material if there is a large section of char. Pyrolysis gas flows through the material towards its surface. Some of the char and pyrolysis gas are then injected into the surrounding flow. The formation of char and pyrolysis and their injection into the flow is used by a TPS material to protect the spacecraft structure from the high heating. At the surface of the material there needs to be a boundary layer heat transfer consideration to describe how the heating reaches the material, a complex energy balance equation to model how the heating from the flow will affect the material internally, and a thermochemical ablation model for char and pyrolysis gas consideration. The TPS material itself is a changing variable due to the formation of char and pyrolysis gas which changes its properties and will affect the ablation and surface energy balance models. Figure 1.1 is a TPS material during conditions that cause ablation, from the beginning of heating to some time after

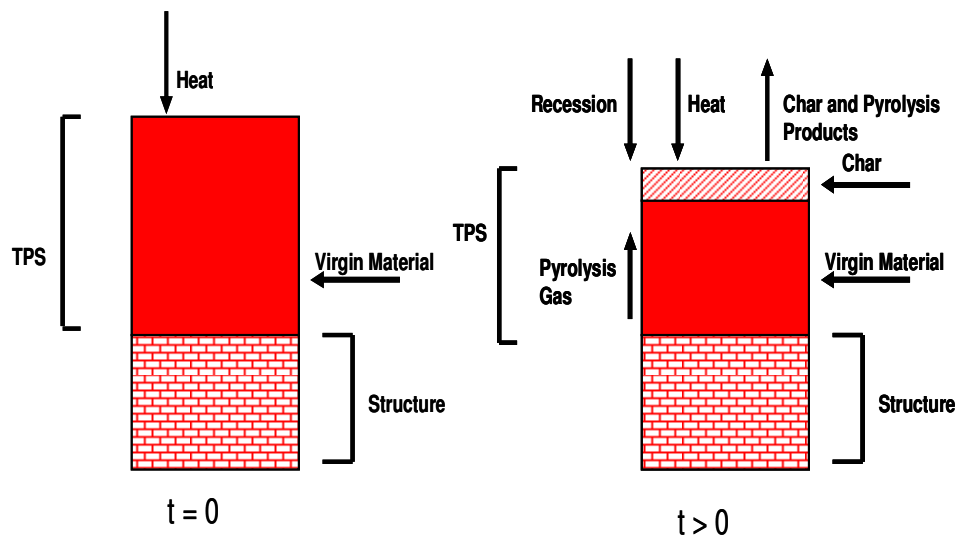


Figure 1.1. A TPS material undergoing high heating and experiencing pyrolysis gas and char formation.

Vehicles entering Earth's atmosphere experience both hypersonic speeds and high temperatures which may lead to thermochemical nonequilibrium conditions. Nonequilibrium reactions can occur in the flow around the craft. At the surface of the ablating material, the flow gas and the surface interact with each other, with that interaction possibly being in nonequilibrium. A nonequilibrium, or finite-rate, assumption means that reactions are occurring in an unsteady state and are dependent on time. A conservative approach is to assume equilibrium for the reactions instead, ignoring any time constraints and allowing the reactions to occur fully and in a steady state. If nonequilibrium is modeled at the surface, it will affect the charring and pyrolysis gas rates, which in turn will affect how the material is changing and the energy found at the surface. How a material changes in equilibrium will differ from how it is changing in nonequilibrium, based on the reactions under consideration. Including nonequilibrium and equilibrium assumption in the modeling of TPS will help improve the fidelity of the model.

The models must be judiciously applied based on experience and relevant experimental data.² If the model is assuming that the surface reactions are occurring in equilibrium, the accuracy may decrease if the gas/surface interface conditions lead to the reactions being unsteady in time, causing nonequilibrium. It is very difficult to simulate these gas/surface interactions at orbital or entry velocities in the lab to determine if they are unsteady in time³; the database available for various heatshield materials experiencing reentry conditions in the lab is not as large as it would be for other cases where velocities are lower and recreated more easily and chemical reactions are a key area of analysis. This places an increased importance on the

computational models that have been developed while leaving these models very little experimental data to use to compare the numerical simulations to physical phenomenon.

Park and Tauber⁴ reviewed analysis of the heatshield surface during the reentry of Apollo missions and determined that the surface may not have reached chemical equilibrium. At the conditions encountered by a reentry vehicle, the reactions between the surface of the heatshield and gas may not have enough time to fully react causing an equilibrium assumption to not be a robust approximation of what is occurring on the surface. In the updated model devised by Park and Tauber it is shown that the result of the assumption of equilibrium leads to an overprediction of the heat fluxes on the surface of the Apollo capsule. The assumption of nonequilibrium gas-surface interaction put forth by Park and Tauber for the Apollo 4 and 6 stagnation point data set can be seen in Figs. 1.2 and 1.3. The nonequilibrium assumption, which used the kinetic boundary condition with reactions such as nitridation, lessens the overprediction of the theory derived in 1972. Further research into applying nonequilibrium surface interactions to the Pioneer-Venus probes and Galileo probe produce similar results to that of the Apollo case: the new assumption decreases the discrepancies between the predicted value and the actual flight test data at the stagnation point.⁴ This reduction of heating means that the craft is not experiencing as harsh of an environment as predicted during the equilibrium analysis. The Park and Tauber nonequilibrium model still remains conservative, but is closer to the actual physical conditions. In Ref. 5, for the Pioneer-Venus probes, the heatshield mass made up about 15% of the final weight and was the third highest mass, only

slightly less than the mass of the structures for the two modules found on each probe. That final heatshield mass was designed with an equilibrium surface prediction. Park and Tauber's results indicate that the presence of nonequilibrium surface reactions causes a lower heating environment that is closer to the actual experienced environment such that it remains a robust prediction. If the finite-rate assumption was used pre-flight to design the Pioneer-Venus heatshield, the heatshield layout may have changed as it did not need to be as massive to insulate the craft from the environment. This reduction in the heatshield can reduce overall weight or allow more payload.

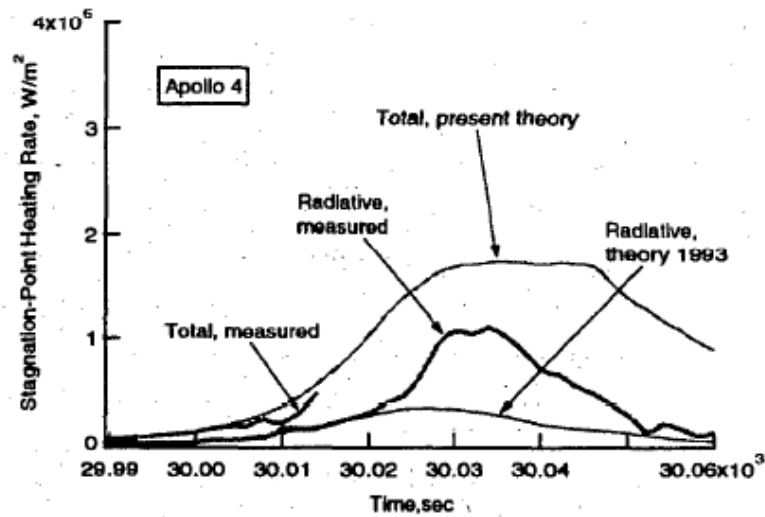


Figure 1.2. Measured heating rates for Apollo 4 compared to those predicted by using nonequilibrium surface conditions.⁴

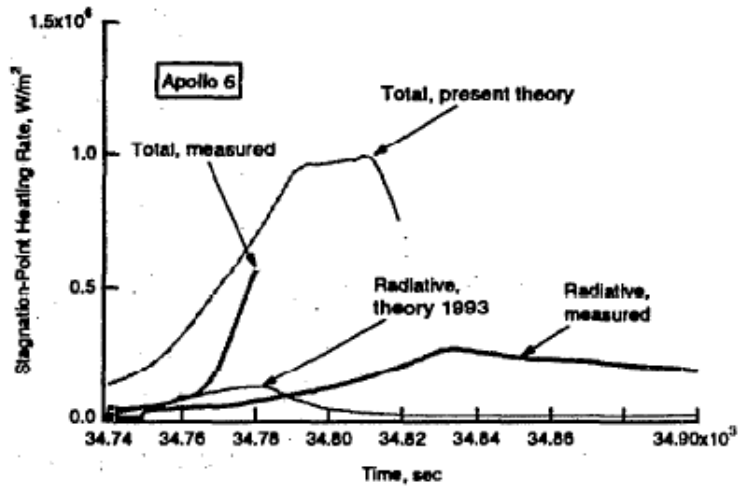


Figure 1.3. Measured heating rates for Apollo 6 compared to those predicted by using nonequilibrium surface conditions.⁴

The effects of nonequilibrium reactions are also dependent on the material choice of the heatshield. The Apollo missions used a carbon-silicon carbide heatshield; the Pioneer-Venus probes and Galileo entry probe used carbon-phenolic for their heatshield.⁴ If the material is carbon-based that limits the reactions that can be considered to be occurring on the surface of the material as reactions with carbon as a reactant will make up a large portion of the surface reaction set. Often times the set is simplified to only consider reactions that use a solid carbon species as a reactant. As innovative reentry materials that are not purely graphite or made with a common infiltrate are being tested and used, the assumption of equilibrium may not hold due to introduction of new species causing previously unseen reactions to take place which may be in nonequilibrium. For a full model, it is important to know what species are present in the interactions between the surface and the flow gas. The implementation of the finite-rate reactions in the chemistry model would allow for nonequilibrium analysis if the reentry conditions limit the reaction time. The

conservative equilibrium assumption treats all the surface reactions the same. A robust finite-rate model can allow for equilibrium to be reached along with the ability to model nonequilibrium, allowing for less conservative design practices, as such parameters as recession will be modeled more closely to their physical results and allow for optimal heatshield designs. New lightweight materials for the heatshield that lower the mass of the heatshield alongside a low pressure trajectory will create a different reentry environment and species present than analyses done on higher pressure trajectories and higher density TPS materials, such as the conditions seen in the Apollo case. There is a need to model low density and low pressure on a heatshield interacting with these new materials.

Various studies by Park and Yoon,⁶ Park and Ahn,⁷ Park,⁸ and Milos and Chen⁹ have examined nonequilibrium surface interactions on heatshields reentering Earth's or other planets' atmospheres. These efforts have concentrated on how nonequilibrium affects the heating that reaches the surface but they are not extended in those studies to compute ablation. Park derived a numerical model⁸ for the Stardust Return Capsule (SRC), which is a low pressure, low TPS density mission, that used finite-rate ablation to calculate the species concentrations on the surface, with a reaction set that includes sublimation, nitridation and one oxidation reaction. The total ablation rates from Olynick et al.'s¹⁰ equilibrium analysis of the SRC were used to account for total ablation. Park held the total ablation rate constant and used the equilibrium condition to predict charring and from there computed the pyrolysis gas rate using the difference between the two rates. The model ignores the effect of finite-rate reactions on the pyrolysis gas rate by assuming the total ablation rate is constant

between equilibrium and nonequilibrium. The work of Refs. 6-9 show how incomplete the current state of the art is when considering nonequilibrium. It has only been applied sparingly with many assumptions made to make it easier to calculate.

To construct a more robust material response model, one that uses finite-rate calculations to better approximate surface interactions, the Fully Implicit Ablation and Thermal (FIAT) response model,¹¹ is employed to model the material. FIAT can predict the recession, char and pyrolysis gas rates, and surface temperature of a heatshield based on the environmental inputs. It has been previously used for SRC analysis.^{10,11} Though FIAT only does analysis in one-dimension, the geometry of the blunt body of the SRC (base diameter is only four times larger than the nose radius and the thickness of the heatshield is much smaller than the other dimensions) allows for a robust one-dimensional analysis, though this may not hold as one nears the shoulder. The surface chemistry is usually assumed chemical equilibrium at the surface. The Multicomponent Ablative Thermochemistry (MAT)¹² program generates the needed surface chemistry tables for a material response program like FIAT. The previous work done on the SRC trajectory using finite-rate reactions found in Refs. 8 and 9 is incomplete due to either limiting the analysis to one point in the trajectory or making an equilibrium assumption for charring. The SRC heatshield¹³ (the Phenolic Impregnated Carbon Ablator (PICA), an emerging TPS material) is low in density and its trajectory being low in pressure. Those factors make the SRC trajectory an ideal choice to study how a finite-rate model may be implemented and used to improve TPS design. Additionally, it was determined that the final recession predicted for the SRC at the near stagnation (Core 1) point was 50% larger than what

was actually measured.¹³ Three points, the stagnation point, Core 1 and Core 2 points are analyzed in this dissertation (Fig. 1.4). The possible streamlines for each point are found in Fig. 1.5. The Core 1 and stagnation point should be similar in terms of heating and surface effects due to their relative proximity to each other and similar geometry while the Core 2 point is further along the heatshield, has a slightly different geometry, and differences in the heating when compared to the stagnation and Core 1 locations.

The SRC heatshield was designed around the large predicted recession, leading it to be more massive than it ended up needing to be because the analysis was done as a fully equilibrium trajectory. With the Modified Park Model, described in Ref. 8 where it was only applied at peak heating, applied to the entire trajectory and at the three locations, recession is underpredicted. If the SRC TPS is designed around this underprediction, then the mission would be a failure. Since neither the equilibrium or nonequilibrium assumption over the entire trajectory seems to robustly capture what was actually going on during the SRC entry, it is determined that there must be some mixture of equilibrium and nonequilibrium occurring on the surface of the material.

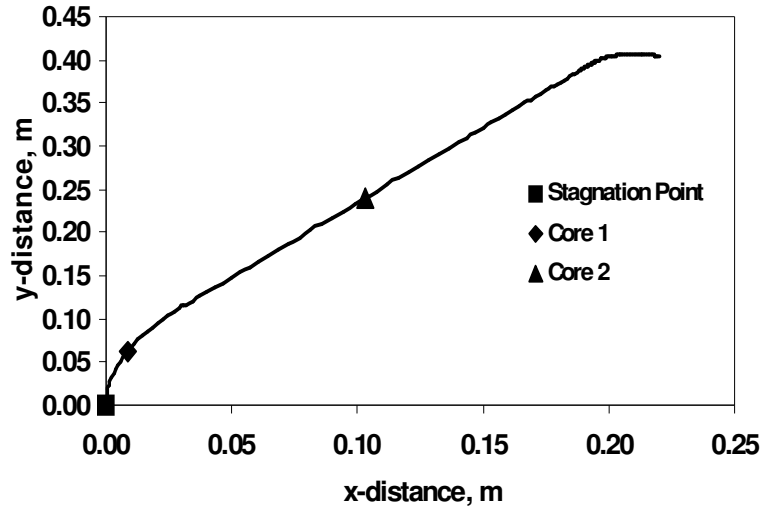


Figure 1.4. The locations of the three points of analysis for the Stardust Return Capsule, with only the two Core points being physically measured upon recovery.

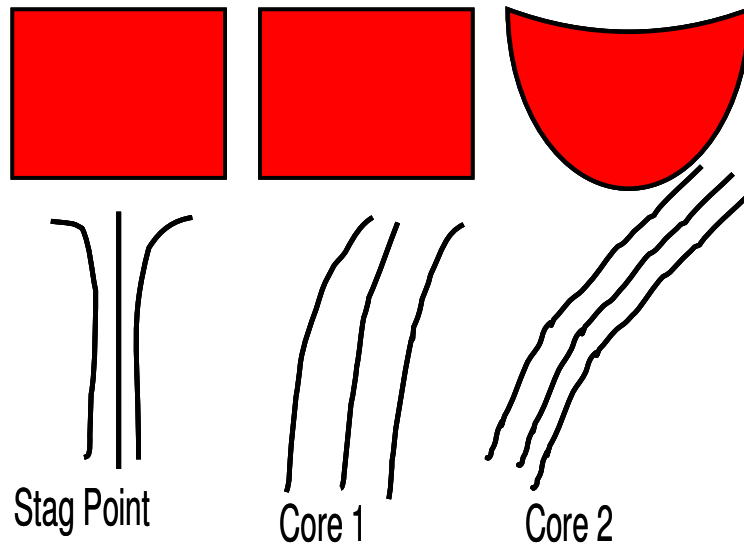


Figure 1.5. Possible streamlines for each of the points under consideration in the analysis.

A new program, BFIAT (an augmented FIAT/MAT-like coupling with unique surface thermochemistry, or B' , tables), is developed so that the user can define when

nonequilibrium should be applied on the surface. When nonequilibrium is reached only once sublimation (a reaction in the Modified Park Model) is activated, the final recession prediction at the stagnation point and Core 1 matches the measured recession, indicating that sublimation is occurring in a finite-rate manner during the low pressure trajectory over the surface of low density carbon-phenolic material. When examining arc-jet test data for the PICA material and recreating the test conditions in equilibrium and nonequilibrium, at certain high heating regimes ($\sim 1000 \text{ W/cm}^2$) the finite-rate reactions as presented in the Modified Park Model better approximate the actual conditions on the surface of the material than the equilibrium assumption, with sublimation being shown as a key driver of the model. This dissertation develops, applies, and studies the affects of a finite-rate model over a carbon-phenolic and makes recommendations on how the model can be used to improve the design process of a Thermal Protection System. It is the first work to apply finite-rate reactions to a large portion of the SRC trajectory and extensively study the effects of finite-rate reactions on the PICA material. The dissertation will cover:

- Previous studies of ablation and finite-rate application to an ablative material
- The unique properties of the TPS used on the SRC and how it affects the surface reactions
- The methodology needed when modeling surface interactions
- Analysis of two SRC trajectories, including the final design trajectory

- The reasoning why equilibrium-based predictions for the SRC ended up overpredicting what was actually measured and how finite-rate calculations can help
- PICA arc-jet tests and whether equilibrium or nonequilibrium should be applied during those heating regimes
- What is learned from the application of the finite-rate Park Model, what it shows about the physics of finite-rate reactions, and how better to improve the model

1.2 Previous Ablation Work

Ablation first became a focal point of research in the 1960s and 1970s as NASA concentrated on projects that would entail a spacecraft to travel through the Earth's or other planet's atmosphere. Most of the research involved either coupling or decoupling the set of equations used for ablation calculations to improve the reliability of the results. Kendall et al.¹⁴ investigated the techniques that were being used at the time to couple and analyze the transient thermal response of ablative materials. These previous methods used correlations which may not accurately predict ablation. Kendall developed a simplified set of equations associated with a multicomponent reacting boundary layer with unequal diffusion coefficients so that a better accuracy can be reached. Bartlett et al.¹⁵ sought to decouple the complex calculations such as the shock-layer species equations, the radiation model, and the mass and energy balances at the surface since coupling these equations was out of the capability of the level of technology in that era. At the time, the scientific community

concentrated on material response and the surface thermochemical boundary condition and not these other areas. By focusing on a chemically-reacting stagnation-point boundary layer fully coupled to a steady-state ablation boundary condition, Bartlett was able eliminate the need for a finite-difference charring ablation solution coupling, which would be difficult to calculate using the technology available. Bartlett also came to the conclusion that a space vehicle's size should be based on the ablation rate of the material present and not the total heating. Much of the research in the 1960s and 1970s concentrated on how to calculate complex ablation parameters within the capabilities of the technology and methodology of the time.

Further simplification of the methodology was attempted by Putz and Bartlett¹⁶ through the study of the transient response of a surface. A simplification of said response would reduce the analysis time, especially when the process is being applied to a heat-shield or nosetip setup. Putz and Bartlett found that any mathematical reduction of the transient response can lead to a reduction to the nonreacting boundary-layer flows. In addition, a reduction can help determine correlations for the chemical-reacting boundary-layer calculations. Further correlations were found that could be applied to the graphite or carbonaceous characteristics that were commonly being used in the early years of research; at the time, graphite and other carbon materials were in use as reentry vehicle heatshields. Researching an extension of the Earth based reentry methods to other heavenly bodies, Peterson and Nicolet¹⁷ found that such an extension could be made due to the introduction of materials that could reflect incident radiation from the gas cap of the entry vehicle. A comparative analysis was conducted for two concepts: carbon

phenolic and Teflon, which is one of the first ablative materials ever tested. The most important conclusion from testing the two materials in different environments was that the methods being applied to Earth can be applied to any other type of atmospheric entry no matter the material choice. Research began to move away from the initial assumption of a pure carbon heatshield and only Earth reentry conditions to include a wider array of materials and possible application outside of Earth.

In the following decades there were periods of decreased research into ablation due to other concerns arising and the lack of technological innovations. When the ability to run complex calculations in shorter period of times due to computers arose, ablation research saw an increased focus. At the beginning of the 1990s, two important discoveries were made that dealt with ablation. Yang and Cheung¹⁸ sought to find a correlation between mechanical erosion and thermochemical ablation. Yang and Cheung broke the ablative process down into four parts. The first stage began with the onset of thermal attack until decomposition gases started to form. The second stage began with decomposition gas formation and ended when a carbonaceous char layer started to accumulate on the surface of the material. The third stage was from the onset of char formation until the moment just before the melting of the charred material. The fourth and final stage was when the mechanical erosion and thermochemical ablation occurred simultaneously. Yang and Cheung developed a two-dimensional material erosion model that could predict the performance of high-temperature ablative materials under condition similar to a solid rocket exhaust. This model illustrated that due to the ever evolving state of computer technology, where computers become faster and easier to use, and a more

fundamental understanding of what is going on during ablation, a more robust ablation analysis tool can be developed to take advantage of these improvements.

Keenan and Chandler¹⁹ introduced a new method designed to investigate the flowfield around a reentry vehicle in a thermochemical nonequilibrium state for all species. To make their calculation simpler, Keenan and Chandler limited the nonequilibrium state to two internal models: vibrational and translational-rotational. To further simplify the research, they chose the material graphite to model since that would not produce a char layer. From their results Keenan and Chandler were able to find that shock location over a surface is not affected by ablation; moreover, only surface concentrations of the flow species only are affected in a steady-state condition. Conclusions from their results include that in transient flow certain aspects approach steady-state after a length of time.

Keenan and Chandler's research identified key components of ablation. Heat flux and surface temperature are important factors in calculating ablation, as Keenan and Chandler's showed that as one can see that as one moves away from the wall surface, there is a precipice where the heat flux and temperature drop in both cases. However, the ablating case has a catalytic wall, hence why the initial heat flux and temperature are higher than the non-ablating case.

Continuing with their research, Keenan and Chandler²⁰ expanded the scope of their focus to include an application to the large heating rates that occur during reentry of a space vehicle, between the altitudes of 40 to 80 km. They kept the same assumptions from the previous report, that is, that thermochemical nonequilibrium flow is allowed with heat conduction in all spatial directions, along with an increased

emphasis on the material properties of graphite. The team was led to a new discovery: the results from the report showed that that oxidation is the primary ablation mechanism on the conical shape of the heatshield at all altitudes and this mechanism is the primary mode over the entire body at higher altitudes. In addition, sublimation importance increases as altitude decreases. Hence, oxidation and sublimation are two key reactions to consider when examining the surface reactions between the flowfield and the heatshield material and are dependent on the altitudes in the trajectory.

One of the applications of modern ablation modeling is dealing with conditions encountered on the Space Shuttle. Bouslog et al.²¹ looked into completing the characteristics of Thermal Protection System (TPS) of the Space Shuttle, more specifically the High-temperature Reusable Surface Insulation (HRSI) and Reinforced Carbon/Carbon that had yet to be completely defined. The researchers investigated the catalytic properties and recombination of the material behind the shock formed during hypersonic maneuvers. This event would induce heat transfer. It was not possible for Bouslog to run these tests on the Space Shuttle during flight, so to approximate these conditions they used arc-jet test experimentation. The results documented the recombination coefficients for wall temperatures ranging from 1470 to 1810 K. There was some discrepancy with previous findings, but that was rationalized as being the result of using lower HRSI values. So a laboratory process mirrored flight data well and showed that the current methodology could approximate real life results.

Multiple constituents make it more difficult to accurately model ablation. Milos and Marshall²² found that the standard ablation modeling code, dubbed

Aerotherm Chemical Equilibrium (ACE), encountered difficulty in providing accurate results with materials that had substantial fractions of two or more dissimilar ablative reaction elements. In practice, an ablative material may in fact have more than one surface constituent so a more general code was needed. The researchers introduce a new theory involving multispecies ablation. In this new theory, undersaturation of the gas phase was allowed, slightly modifying all the previous assumptions and research which had ignored this effect. This new assumption changed one of the key equations used in the ACE code. Milos and Marshall, using ACE as a foundation, developed a new code named MAT which stands for Multicomponent Ablation Thermochemistry. The new code predicted higher temperatures than then ACE code but with comparable enthalpy between the two. These were favorable results; however, Milos and Marshall did not view their research as complete and recommended further refinement of the MAT code.

Continuing their work on the MAT code, Milos and Chen¹² strove to develop a more accurate code. As they expanded the MAT code, the previous iteration of MAT had already been used as a comparable model for the Reinforced Carbon/Carbon (RCC) material found on the Space Shuttle. It was now desired to further refine the code so that it may be able to accurately predict conditions during an abortive reentry into Earth's atmosphere, one that would have a massive loss of sealant. The tables produced by the next generation of the MAT code compared favorably to arc-jet test results simulating a nominal, heavy-weight, or transoceanic abort scheme. Milos and Chen's work further developed correlations for the RCC, SiC (silicone carbon) and sealant materials. Milos and Chen developed the MAT

program to provide surface chemistry data for a defined material and today it is often used while being coupled to another code, usually a material reaction program.

Milos and Chen²³ then further refined their code to work in three-dimensions, where previous attempts only used two dimensions. Three separate test cases were run, with reentry at 0, 10, and 90 degrees, with the results compared previous accepted findings. They dubbed the new model adequate and called for further study into its possible applications. Also, the researchers desired that the current reference tables should include the special case of chemical equilibrium during general chemical nonequilibrium.²⁴ To attain this, a full Navier-Stokes computation for finite surface ablation would be needed. Problems encountered in finite rate simulation included the lack of complete knowledge on how the heatshield material and the surface and how the gas would interact. Hence, carbon and carbon-phenolic were chosen is the study for better information since these materials and their properties were better known. Once again, Milos derived a new ablation code, a finite rate surface boundary conditions formulation for the Navier-Stokes equation solver dubbed GIANTS for the carbonaceous materials. There were different sub-models used and there was some discrepancy between the models, though Milos and Chen believed their new code was accurate. The FIAT code¹⁰ was developed by Milos and Chen to remove potential numerical instabilities found in other material reaction codes and to contain an equation for internal radiative flux, optimized TPS thickness and a flow code interface. By using solving four equations (internal decomposition, internal mass balance equation, internal energy equation, and the surface energy equation) the program could predict how a material will react under ablative

conditions. FIAT is often coupled with GIANTS and MAT. FIAT assumes surface thermochemistry equilibrium in its calculations, where the assumption is derived from the input parameters from MAT. Changing how MAT calculates the surface chemistry and then coupling the refined program to FIAT as it has been developed to do so will allow FIAT to analyze the material response of a heatshield undergoing surface nonequilibrium.

Katte et al.²⁵ attempted to further extend ablation models accurately into two dimensions. The goal of the research was to make multidimensional analysis less complex than models that had been developed decades before. The main problem encountered whenever a dimensional extension was made is that ablation modeling concerns spatial variation of heat flux and there are different transformations that occur at different locations over a surface. More dimensions meant more equations and inputs, both of which were usually very intricate. It was due to this involvedness that previous simplification in the one-dimension case led to either a time dependent or time independent analysis, but never both in the same model. However, Katte overcame this problem by using coordinate transformation to lessen the difficulty of extending into two dimensions; moreover, Katte used an adjustable time step numerical scheme to also ease the extension. The new model, in comparison with quasi-one dimensional modeling, showed better accuracy in using a two-dimensional approach.

An extension to ablative research to include what would happen upon entry to other heavenly bodies like what was earlier attempted was attempted again once its associated computations became less time consuming. Congdon and Curry²⁶

presented new heatshield designs for Mars based on ablative properties. Their emphasis was on lightweight and flexible heatshields, filled with silicones and phenolics. The phenolic filled material could stand up to 3400 to 14000 kJ/m² and was deemed suitable for Earth return vehicles. In addition, the carbon-silicone ablators could be used for Earth aerocapture and the silica-silicone ablators were deemed suitable for Mars aerocapture.

Congdon et al.²⁷ applied ablative testing to the conditions a spacecraft might encounter during an entry into Titan's, a moon of Saturn, atmosphere. Previous reports showed that a mission and entry to Titan would have lower convective heating than one to Mars, but significant levels of thermal radiation would be present. Various tests to approximate the conditions on Titan showed that the ablator responses to radiation heating produced higher temperatures than those that occur during convective heating. Congdon came to the conclusion that the final results had a dependence on the final entry-heating environments, which is applicable not only to Titan entry, but any entry into an unknown atmosphere. Fujita et al.²⁸ used a Venus trial balloon mission as a benchmark to research the effects of interplanetary hypersonic reentry conditions in order to find a more accurate model. Preliminary findings indicated a net heat transfer rate on the surface of a vehicle depended on the chemical composition of the ablation products and its interactions with the shock layer near the surface. Convective heat flux was found to be highly dependent on the species present around an ablating material. Under this situation, chemical nonequilibrium was to be expected. Fujita chose to focus on the chemical aspect of

ablation and highlighted the need to take into account the reactions that occur on the surface of a reentry vehicle.

The larger focus of ablative research continued to be the improvement of modeling. Cybyk et al.²⁹ investigated the unified analysis capabilities of the ablating gas/solid interfaces and the general approach and coupling procedures behind it. The research used a generic missile nosecone to demonstrate the state of numerical prediction of thermochemical ablation and thermomechanical ablation. Much like Keenan and Chandler's research, the goal was to find a comprehensive capability by concentrating on thermochemical nonequilibrium; moreover, the analysis was extended to surface thermal responses and injection-induced turbulence. The complete model used to predict ablation consisted of a Computational Fluid Dynamics model and an in-house material thermal response model that used boundary condition treatments. Through their research it was found that this coupling could potentially reduce time factors and it was determined the code can help with future nosecone applications. Cybyk et al.³⁰ then chose to focus on the integration of time-dependent solutions of compressible flows with variable surface boundary conditions. Previously, these two conditions were solved separately. In addition, they looked at the possibility of extending ablative analysis into the second or third dimensions. The addition of a feedback loop of fluid dynamics and the thermal response models in their previous code allowed Cybyk and his peers to develop a model that now accounted for recession. With their results in hand, the researchers came to the conclusion that further development of the current level of coding was

needed so that a comprehensive, integrated, multi-dimensional methodology may be found.

Improvements in models in terms of ease of use and quickness to run calculations permitted investigations into what materials would be optimal for taking the brunt of reentry conditions. Palaninathan and Bindu³¹ looked into carbon based and plastic matrix Thermal Protection Systems and its response to reentry-level conditions. Since the early days of ablation research the amount of information had been vast but often the work was classified and unable to be referenced, putting an increased importance on the current generation of research. The testing conducted in the report pertained to the stress and thermal conditions of reentry, something not particularly investigated in previous attempts. The reradiation effect was ignored in the model as well as the heat blockage due to chemical and thermal ablations. The model that was developed used the finite element method and the mechanical ablation aspect of the new model was called upon to be validated at that time.

Suzuki et al.³² attempted to integrate a thermochemical nonequilibrium flow code with a two-dimensional ablation code in corresponding with results found in arc-jet testing. They also studied the effect of a flowfield by coupling and examined the effect of thermal conductivity which depends on the direction of travel. Once again, refinement of a previously derived code, in this case the Super Charring Material Ablation (SCMA) code, was used by the researchers to get their desired results. They found that the new method could be validated against the old standard with a shape change at stagnation point, which was deemed appropriate. Also discovered was that the temperature along a centerline of an ablative test piece could be affected by the

thermal conduction along a radial direction. Research into the development of an approximate, less complex model for TPS sizing with a high fidelity model was attempted by Dec and Braun.³³ High fidelity models are often complex and an effort to make them simpler was desired. The methodology employed in the research was one of using a trajectory input among other more common inputs so that the necessary boundary conditions can be found. Then by iterating the heatshield thickness, other user-defined conditions can be met. These calculations were carried out only in one-dimension. Comparison to previous trajectory condition research showed that this new TPS sizing tool did comparably well to previous tools. They compared their results with those that Milos and Chen found earlier to validate their model. The new tool combined an industry-stand high fidelity program with an approximate method. One problem area was that for low-density materials the approximate solution did not perform as well as for other cases.

Ablation is an important aspect of space flight, as reentry has the potential to be a dangerous endeavor if not properly handled. Previous work demonstrates the need for better computational models and physical data. As computing time decreases, more and more analyses can be run and data collected, which would lead to a better understanding of ablation. Refinements have been made to previous models while new methods have also been introduced. Ablation computational research is dependent on the level of technology currently available, as computational limitations may dictate what assumptions need to be made to decrease the time of analysis. Ablation research is also limited by the amount of available experimental data. As more flight test data is on hand due to instrumentation and new materials are

developed and tested, there is a better understanding of the physics behind the ablation process, which helps with how the material is modeled.

1.3 Background on Chemistry and Stardust Return Capsule

Chemical reactions can be thought of as being divided into two general conditions: equilibrium and nonequilibrium with each condition having its own advantages and disadvantages. One of the reasons why nonequilibrium reactions are harder to calculate than those in equilibrium is the timeframe in which to take the reactions under consideration. For example, let's look at the application of thermochemical nonequilibrium to a fluid flow. If the characteristic time for a fluid element to travel the flow field is not much larger than or much smaller than the characteristic time for the chemical reaction and/or vibrational energy to approach equilibrium, then the flow can be considered at a nonequilibrium state.³⁴ If the characteristic time for travel is much larger, the species has enough time to chemically react and reach equilibrium state. If the chemical reaction time is much larger, then the species travels through the flow fast enough that no chemical reactions can take place and the flow is considered "frozen." The area immediately downstream of a shock is the region where changes in the flow properties may happen at a high enough speed that a reaction that cannot keep up with the high flow speed and the changes and can be considered in a nonequilibrium state. While both nonequilibrium and equilibrium flow conditions dictate that there are species present in the flow, nonequilibrium flow conditions place an increased importance on identifying the significant reaction mechanisms and how quickly they may react. An equilibrium calculation will often rely upon simplified mechanisms, leaving only a

few species to consider and no time dependency. A nonequilibrium calculation, however, will have to consider all of the species present, how they react over a given timescale, and the equations associated with these species often cannot be reduced or eliminated. For example, the net reaction rate of oxygen in the reaction $O_2 + M \rightarrow 2O + M$ can be calculated from the following equation:

$$\frac{d[O]}{dt} = 2k_f [O_2][M] - 2k_b [O]^2[M] \quad (1.1)$$

The bracketed species is the species concentration and k_f and k_b are the forward and reverse reaction rates, respectively. The species M is the catalytic molecule and is a collisional partner for the other molecule in a chemical reaction. For an equilibrium reaction, this net rate is assumed to be zero; there is no change in time. In a nonequilibrium reaction, the rate is finite and nonzero and cannot be ignored.

The interactions of the species under the present conditions are of key importance. The consideration of individual species means that all calculations must take into account the reactions at the molecular and atomic level; special attention is paid to what elements occur in the flow and on the ablating surface. The enthalpy for each individual species is calculated in part from the energy contribution of vibrations and translation, which may be in nonequilibrium. The total enthalpy is the sum of each species enthalpy weighted with the mass concentration of each species. The assumption of nonequilibrium dictates a need for a species continuity consideration, along with an examination of the enthalpy of each species.

A possible avenue to derive a general equation set for each species is to write the time rate of population change of atoms and molecules, with a specific energy state, as the difference between the sum of rates of all collisional radiative transitions

that populate a given state and the sum of rates that depopulate this state. This particular system that is derived is commonly referred to as "master equations."³⁵ Further concerns include vibrational excitation and intermolecular potential. Vibrational excitation can be considered the main process of energy transmission to the upper levels of the atom at low temperatures and appropriate correlations can be made. In addition, intermolecular potential energy depends on the radial distance between molecules and internuclear separations. These conditions add to the complexity of nonequilibrium calculations, as nonequilibrium can be extended past the chemical reactions.

There has been previous research into hypersonic nonequilibrium that focused on the individual affects on finite-reactions on particle interaction.^{36,37} There exists sample equations for materials responses to the flow.³⁸ As technology improved more robust Computational Fluid Dynamics (CFD) models were developed. Such advances have lead to the derivation of an analytical theory of hypersonic, blunt nose shock standoff based on the compressibility coordination transformation method for inviscid shock-layer flow³⁹ and further testing and validation of surface heat transfer methods in a CFD setting.⁴⁰ As the time to run as simulation has decreased, identifying the nonequilibrium conditions has been under increased focus, as discussed in Section 1.2.

There has been some research into the affects of nonequilibrium flow but it is often not extended to include nonequilibrium surface conditions on a low-density material reentering the Earth's and other planetary atmospheres.^{4,6-8} The next generation of space vehicle, which included NASA's Orion Crew Exploration

Vehicle (CEV), will encounter a variety of atmospheres with newer heatshield materials. In particular, the CEV was to be designed for both Terran and Martian atmospheric entries. Of particular interest is the reentry of the Stardust capsule. The Stardust Return Capsule, whose mission included an interception with a comet to collect data, had the highest entry velocity of any Earth entry vehicle, at a speed of 12.8 km/s. As a comparison, the Apollo capsule returned at a speed of 11.0 km/s. As mentioned, for flows, the speed at which the particle physically travels and encounters the surface is a determinate in whether or not equilibrium is reached. The high SRC velocity will affect surface interactions. In designing a craft for the type of mission Stardust undertook, in addition to the desire to keep total mass low to reduce launch costs, there is a tradeoff between the mass of the spacecraft and the amount of mass Stardust could collect from the comet.¹⁰ The final design mass of the SRC is 46 kg, including the heatshield, with the total mass of the Stardust mission being 385 kg. The nominal trajectory and expected conditions encountered by Stardust during its reentry can be seen in Table 1.1 and Fig. 1.6.¹³ The trajectory is within the altitudes studied by Keenan and Candler^{19,20} where they found oxidation and sublimation to be important reactions. The Stardust forebody aeroshell is a 60-degree half angle sphere-cone with a base radius of 0.41 m.¹³ For the preliminary design trajectory, it was predicted that the heatshield would experience a heat flux of approximately 1200 W/cm² upon its reentry. The Stardust capsule was launched in 1999.

The Stardust Return Capsule was recovered on January 16, 2006. Kontinos et al.¹³ determined that the actual trajectory closely followed the final design nominal trajectory. For the nominal trajectory, the majority of the reentry flight is in the

continuum regime⁴² where molecular collisions will occur indefinitely, an important factor in determining nonequilibrium conditions. A DC-8 was flown as an airborne observatory to optically determine average surface temperature.⁴³ Because the capsule was not instrumented to measure reentry conditions, Jenniskens⁴⁴ used an Echelle spectroscope to observe the flow around the capsule as it returned to Earth. Post-flight analysis determined surface temperature and recession. The observed data suggested that the previous Stardust models were inaccurate; recession was overpredicted by 50% at some locations on the capsule.⁴⁵ The SRC used PICA⁴⁶ for its heatshield, a low density material that is also used in the Mars Science Laboratory and was selected as one of two heatshield materials for NASA's Crew Exploration Vehicle. PICA was developed in the mid-1990s with a recent increase in arc-jet testing and experimental data due to its selection as the heatshield material for the CEV. The Stardust heatshield also has a sandwich-like structure of aluminum honeycomb.

Table 1.1. The freestream conditions encountered by the SRC during the heat pulse

Time, s	Altitude, km	Velocity, m/s	Density, kg/m³	Temperature, K
34.00	81.64	12,590.4	9.63×10^{-6}	216.93
42.00	71.92	12,413.4	1.29×10^{-5}	221.42
48.00	65.44	12,004.0	1.06×10^{-4}	229.00
54.00	59.77	11,136.7	2.34×10^{-4}	238.47
60.00	55.02	9,718.7	4.39×10^{-4}	248.48
66.00	51.19	7,956.9	7.21×10^{-4}	253.55
76.00	46.51	5,178.9	1.35×10^{-3}	256.90

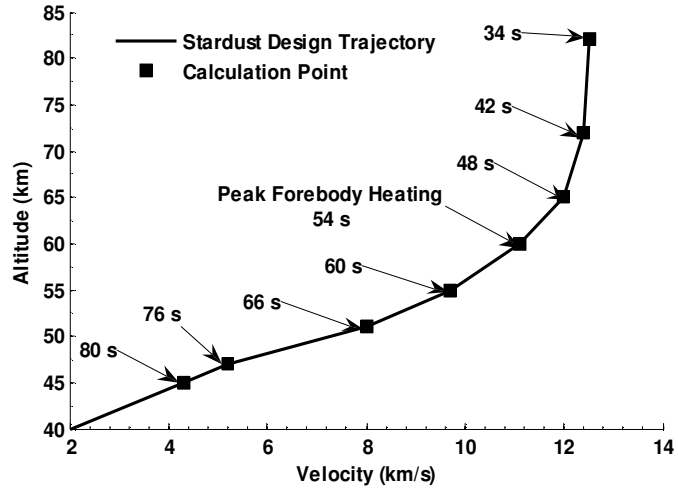


Figure 1.6. The notional trajectory for the Stardust Return Capsule reentry.

There has been substantial research into equilibrium and nonequilibrium flow for ablation materials that are both high in density and experience high atmospheric pressure and those materials that are low in density and experience low pressure assuming an equilibrium condition at the surface. However, very little consideration has been made in coupling the assumption of nonequilibrium surface conditions to the material response of a heatshield, leaving ablation out of the analysis. The extension into nonequilibrium surface conditions, particularly those experienced by low density heatshield materials during a low pressure trajectory, would provide more robust results; a reentry vehicle's return to Earth and the associated conditions may lead the interactions on its surface to be at a nonequilibrium state. This addition would help in the development of new missions and spacecraft, as the models being used to help design the heatshield would not be as over-conservative as equilibrium models currently are and hence more accurately mirror real reentry conditions.

Chapter 2

The Surface/Gas Interface

2.1 Material Choice

The discussion of how the gas and the surface interacts should include how the material choice for a TPS affects how the flow gas interacts with the material, how FIAT predicts the material response, the effects of nonequilibrium on the flow and the surface, and how MAT models the surface thermochemistry. The choice of material is important due to its associated thermodynamic properties. The material must protect the reentry craft from the high thermal effects it will experience. A typical material used in reentry vehicle heatshields is carbon, which may contain a secondary material such as a phenolic composite. A pure carbon heatshield typically has a density which ranges between 0.96 and 1.60 g/cm³.⁴⁶ However, if one adds an infiltrate, this density may decrease and become more mass efficient.

The infiltration of a secondary material into a material such as carbon required a special technique to control the amount of resin present. This allows for the final product to maintain a high porosity and low thermal conductivity, making it a better performing insulator. However, once the material begins to char, the thermal conductivity may increase, depending on the pressure and temperature. The choice of what infiltrate to use is based on what percentage of the original material will be converted into char, with this value being called the char yield of the material.

Common infiltrates include phenolic, epoxy, and polymethyl methacrylate (pmma).⁴⁶ Adding infiltrates means additional time to properly manufacture materials with these materials present due to the different curing processes and drying procedures needed.

Testing of materials during high heating regimes can be done by simulating a high enthalpy gas flow caused by an electrical discharge in an arc-jet facility. Testing conducted by Tran⁴⁶ indicated that a carbon-phenolic ablator would have a char yield of 61%, which is higher than the yield of a carbon-pmma and carbon-epoxy. As a result of the high yield, the carbon-phenolic mass loss flux is half of that of other carbon ablators. Most of the material is being converted into char and not being ablated away. The high charring rate of a carbon-phenolic is due to two factors: the high melting temperature of carbon, so melting does not contribute to the mechanical fail unless those high temperatures are reached, and the high emittance rate of carbon, which rejects most of the heating on the surface back into the flow. The lower mass loss flux rate leads to carbon-phenolic having a lower recession rate than most other common ablators as seen in Fig. 2.1. The property of having lower recession means that a carbon phenolic does not need to be as thick and massive as other materials. In Fig. 2.1, the *c* prefix indicates a carbon material while the *s* prefix indicates silica, another commonly used ablator. The common combination of carbon and phenolic is an improvement over other combinations of materials in terms of getting a lower recession rate.

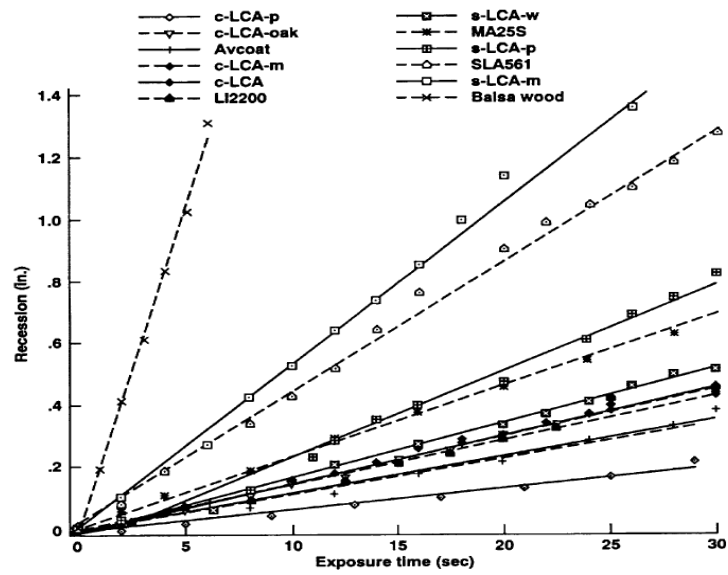


Figure 2.1. The stagnation recession rate of various ablators, including carbon-phenolic ablators (c-LCA) at a heat flux of 460 W/cm^2 and a pressure of 0.081 atm .⁴⁷

The PICA⁴⁶ material is an example of a newer ablation material that is made up of carbon and phenolic. PICA utilizes a low density, preformed carbon fiber substrate and a unique infiltration technique to place the phenolic resin inside the carbon. The uniqueness of the infiltration technique is the key driver in how PICA differs from other carbon-phenolic materials. The carbon fiber insulation has a starting density of 0.152 to 0.176 g/cm^3 with the overall density falling in the range of 0.224 to 0.248 g/cm^3 . Comparing these densities to those of the more common carbon-phenolic class, PICA can be between four to eight times less dense than a simple carbon-phenolic ablator.

The ablation performance of PICA can be divided into three dissimilar regimes based upon the heat flux a sample experiences.⁴⁶ The first regime has the ablation being oxidation-controlled. The recession in this regime is caused primarily by oxidation. High stagnation pressures cause an increase in the concentration of

oxygen atoms, which increases the oxidation rate and related surface recession. In the second regime, PICA's ablation is diffusion-controlled, with the rejection of heat occurring through reradiation.

The third and final regime is sublimation-controlled. In this regime, the surface recession is due to the sublimation of the carbon found in the material. The carbon fibers begin to sublime due to the high surface temperatures experienced; in addition, this contributes to the high recession. In general, these reactions that occur on the surface of PICA are similar to those that occur on other carbon materials.⁴⁸ Arc-jet testing by Covington et al.⁴⁹ at heating rates of 1150 and 1630 W/cm² found that diffusion-controlled recession may occur in PICA under those conditions.

Through arc-jet testing⁴⁶ it was demonstrated that PICA has notable insulative properties. Temperatures encountered further in-depth and away from the surface reached peak temperatures significantly lower than those encountered on the surface. Also, these temperatures were encountered later in time than the peak temperatures on the surface. This result reaffirms that most of the heat is rejected by reradiation. Other arc-jet testing results show that PICA has a low heat capacity due to its porosity. The material class rejects the heat at the surface and it is not stored via heat conduction. Due this characteristic, PICA could be directly bonded to the structure of a vehicle without any additional insulation. Also, PICA thickness could be less than other carbon-phenolic ablators due to its thermal response characteristics. It has also been shown that that as the pressure increases over a PICA material, the charring rate decreases if the temperature is held constant; at some constant temperature the PICA

material may experience different char and pyrolysis gas rates depending on the pressures encountered on its surface.

With the PICA material chosen, it is important to consider what reactions are taking place when the material is interacting with the flowfield. A common model of a flowfield considering a carbon-phenolic material such as PICA is an 18-species reaction model with the following species: CO_2 , CO , N_2 , O_2 , NO , C_2 , C_3 , CN , H_2 , HCN , C , N , O , H , C^+ , N^+ , O^+ , e^- . A typical chemistry model with these species can contain of 9 dissociation reactions, 8 exchange reactions, and 3 electron impact ionization reactions.¹⁰ Forward and backward reaction rates need to be considered when dealing with each species and their reactions. The associated coefficients needed in determining the forward reaction rate can be found in Ref. 10. Based on their small mass fraction in a flow, the ions N_2^+ , O_2^+ and NO_2^+ are dropped from the reaction set for computational reasons. Due to the lack of actual reentry data concerning PICA, the chemistry models used of this type are only preliminary attempts to approximate the reaction set. The flowfield reaction set can be thought of a collection of species that are made up of species present in the atmosphere, species formed from reactions in the flowfield (like HCN), and species formed from reactions between the gas and the surface (like CO , C_3 or CN). The first and third parts can be used to set up a reaction set for the gas/surface interface.

In terms of the use of a flowfield reaction set in relation to ablation, Olynick et al.¹⁰ compared an ablating 18-species set with a non-ablating 11-species set. The 11-species set could be considered non-ablating due to it dropping the species that contained carbon and hydrogen, with carbon being the biggest contribution from an

ablating PICA. The researchers found that the non-ablating conditions lead to higher heat fluxes at the PICA/SLV interface on the Stardust Return Capsule. At the stagnation point, the condition which had the higher heat flux, either ablating or non-ablating, depended on time and could not easily be determined.

The focus of this dissertation is to examine how the flowfield and the material interact and the results of that interaction on the material. The assumption of equilibrium surface interactions makes it easier to determine the flowfield at the cost of having to approximate the reactions that are occurring at the surface. To accurately determine nonequilibrium surface reactions, the material cannot be considered trivial; its responses to certain conditions must be known. PICA is an emerging material choice and there is not a wide experimental or numerical database available which describes the phases and chemical reactions the material may undergo under different reentry conditions. However, there is enough information to form a baseline case and perform a comparison.

2.2 The Fully Implicit Ablation and Thermal Material Response Program

The Fully Implicit Ablation Thermal material response code is a material response program that for a set of environmental inputs, usually from a predetermined flowfield and trajectory, can simulate the conditions that a predefined heatshield material stackup will encounter during some time period. An initial temperature is defined on the surface of the material and the backface of the heatshield, where it attaches to the spacecraft structure. The environmental boundary conditions, the flow enthalpy and heat transfer coefficient, help determine the convective heat flux on the

surface. Radiation leaving the surface is based on the material property of emissivity and current surface temperature. The difference from that heating rate and the amount of radiation determines in part the amount of conduction within the material. The decomposition of the heatshield into char and pyrolysis gas is based on the amount of heat that is conducted into the material. To get the heating from the char and pyrolysis gas being injected into the flow, the mass flux of those parameters as they travel through and out of the material is computed along with the enthalpies of the char, pyrolysis gas, and wall to find the injected heat flux. From the charring rate and any significant mechanical fail, the recession rate and final recession can be determined. Pyrolysis gas does not contribute to recession even though it causes mass loss. If the material under analysis is a good insulator like PICA then the backface temperature should not drastically change throughout the heating conditions while the surface temperature should rise based on the conditions. The heatshield layout of PICA and the trajectory of the SRC keep the backface temperature constant as there is no heat flux across the backface. Figure 2.2 is the physical snapshot of the material, while Fig. 2.3 is a snapshot of the typical heating occurring on and in the material.

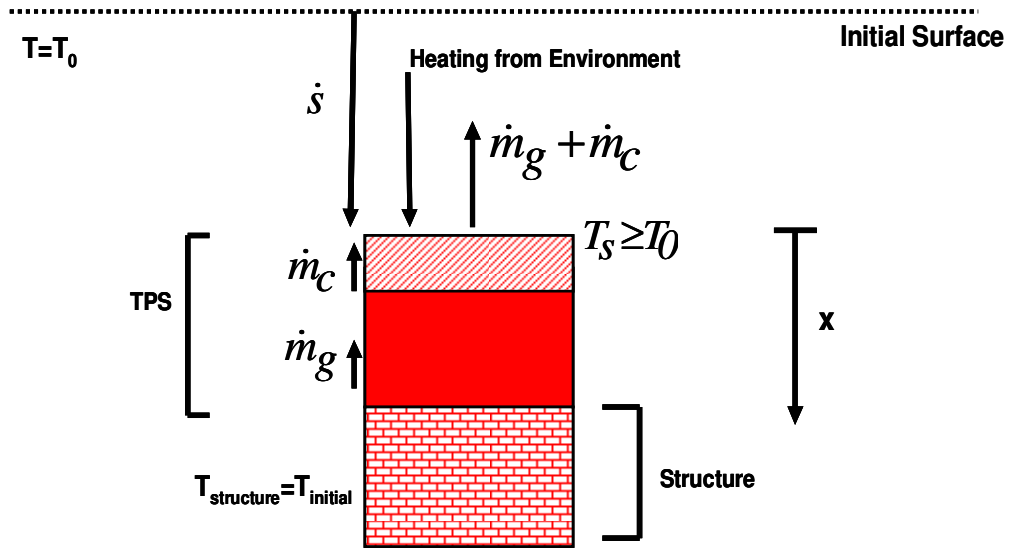


Figure 2.2. Physical representation of what is occurring on the PICA material during high heating and what needs to be calculated in a material response model.

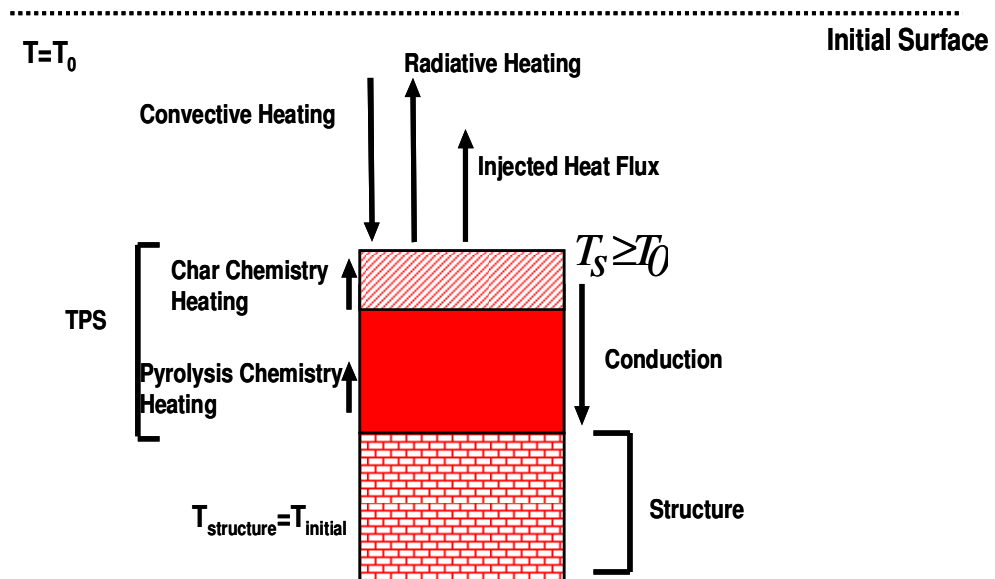


Figure 2.3. Representation of the heating on the PICA material during high heating and what needs to be calculated in a material response model.

In previous material response codes, the use of an explicit method in linking its internal equations the CMA code caused a high sensitivity to time-steps and in-depth grid size.⁵⁰ To eliminate this sensitivity, Milos and Chen¹¹ developed FIAT, a

material/thermal response code which can be loosely coupled to a flow environment code. An additional program to calculate radiative effects can also be coupled to FIAT. FIAT computes the transient one-dimensional thermal response of TPS materials arranged in a multilayer stackup, subject to aerothermal heating on one surface.¹¹ Thermochemistry properties at surface of the material, such as wall enthalpy, are calculated from species formation/reactions between the gas and the surface, are developed and determined outside of FIAT, in such programs as Aerotherm Charring Material Thermal Response and Ablation (ACE) program and MAT and arranged into B' tables.^{12,22,50} A B' table is constructed for a certain pressure and a range of char and pyrolysis rates which FIAT then interpolates between to get the current char and pyrolysis rates and wall enthalpy at the exact environmental conditions. These surface thermochemistry codes often assume equilibrium surface interactions.

Analysis is done at the surface and at nodes in-depth, based on a grid system, as seen in Fig. 2.4. The grid moves with the surface and keeps the same number of points as the material ablates. The internal nodes are used as points in the internal energy balance equation. The internal energy balance is a transient thermal conduction equation and also includes pyrolysis terms:

$$\frac{\partial}{\partial x} \left(k_t \frac{\partial T}{\partial x} \right) + (h_g - \bar{h}) \frac{\partial \rho}{\partial \theta} + \dot{s} \rho c_p \frac{\partial T}{\partial x} + \dot{m}_g \frac{\partial h_g}{\partial x} = \rho c \frac{\partial T}{\partial t} \quad (2.1)$$

The x-coordinate system moves with the receding surface while the y-coordinate system is stationary. If the x-coordinate system is considered stationary then the energy caused by recession (the third term from the left) is assumed zero. Conceptually, the internal energy balance equations states that at an internal node the

rate of storage of sensible energy is equal to the sum of the thermal conduction, the energy consumed in the formation of pyrolysis, convection of sensible energy due to coordinate system movement (energy that causes recession), and the energy convected by pyrolysis as it moves towards the surface. The internal energy is interconnected to the energy at the surface, as conduction from the surface flow in-depth of the material, which then generates pyrolysis gas and char, which then affects heating arriving on the surface from within the material. The in-depth energy terms have never been analyzed for the PICA material. An examination is carried out in this dissertation of the energy effects in-depth which will illustrate the insulative properties of the PICA material.

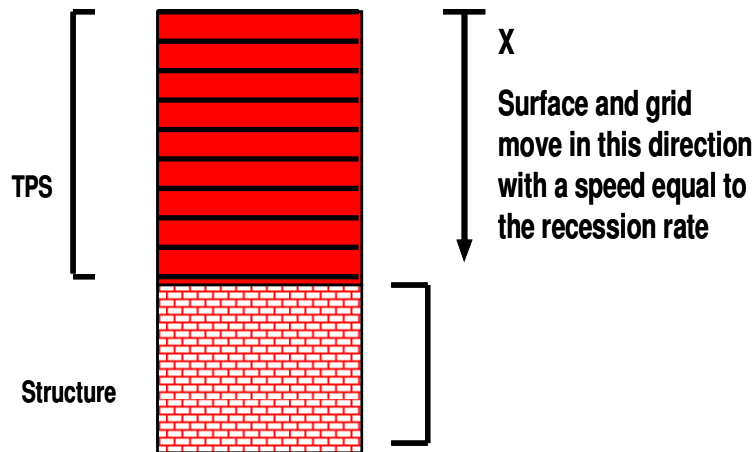


Figure 2.4. A typical grid layout in FIAT.

If the heatshield material contains an infiltrate of some kind, like the phenolic in a carbon-phenolic, then the heatshield can be said to be made of two materials that have their own densities: the reinforced material, such as carbon, and the infiltrate, which can be modeled as containing up two unique resins. For the internal decomposition, a three component model is used with an instantaneous density¹¹

$$\rho = \Gamma(\rho_A + \rho_B) + (1 - \Gamma)\rho_C \quad (2.2)$$

And the decompose relationship is as follows

$$\frac{\partial \rho_i}{\partial t} \Big|_y = -B_i e^{-E_i/T} \rho_{vi} \left(\frac{\rho_i - \rho_{ci}}{\rho_{vi}} \right)^{\Psi_i} \quad (2.3)$$

In Eq. 2.2, the subscripts *A* and *B* are the components of the filler (phenolic) material, *C* represents the reinforcing (carbon) material and Γ , an input value, is the volume fraction of the filler. For the change in density with respect to time, ρ_{vi} is the original (virgin) density and ρ_{ci} is the residual density of component *i* in Eq. 2.3, which illustrates the how each component decomposes. Both the carbon and the phenolic ablate and char, changing their individual densities and the composite density. It is from the density of the material that the char layer depth is determined. From the material database, the density of the fully charred material is known, alongside the virgin density. If the density at the current node in-depth is less than the char density plus some defined percentage, for example 5%, of the difference between the char and virgin densities, then the current node is in the char zone. If the density is greater than the char density plus 95% of the difference between the two densities, the node is considered in the virgin zone. If the density does not fall within the two zones, then it is considered to be in the transition zone, where pyrolysis gas is forming and traveling.

With an assumption of quasi-steady one-dimensional flow and an impermeable backface, the internal mass balance equation relates the pyrolysis gas mass flux to decomposition¹¹

$$\frac{\partial \dot{m}_g}{\partial x} = \frac{\partial \rho}{\partial t} \quad (2.4)$$

The change in density of the material over time is equal to the change in the pyrolysis gas as it moves through the material. The PICA material begins as a porous material, so as pyrolysis gas forms and leaves the material in time, the material becomes more porous, lessening its density. A general surface energy balance equation for an ablating surface is¹¹

$$\rho_e u_e C_H (H_R - h_w) + \dot{m}_c h_c + \dot{m}_g h_g + \rho_e u_e C_M \left[\sum (Z_{ie}^* - Z_{iw}^*) h_i^{T_w} - B' h_w \right] + \alpha_w q_{rad} - F \sigma \epsilon_w T_w^4 - q_{cond} = 0 \quad (2.5)$$

with the first term as the sensible (net) convective heat flux. The convective heat flux is dependent on both the environment (H_R is the enthalpy from the flow) and wall enthalpy. The second, third, and fourth terms encompass the total chemical energy at the surface. The mass flux of char and pyrolysis, along side the enthalpy of each component, dictate the amount of heat is brought to the surface. Transport of the chemical energy associated with the reactions at the wall and boundary are represented by the Z terms and represent the diffusion of heat across the gas/surface interface. The B' term, where B' represent the total mass loss due to nonmechanical ablation, so charring and pyrolysis gas, represents the heat that is injected into the flow by char and pyrolysis gas entering the flow. The fifth and sixth terms are the radiative heat fluxes absorbed and reradiated by the wall. The final term is the rate of conduction into the thermal protection system.¹¹ For heating equilibrium, the Equations 2.1 through 2.5 are the general principles upon which the FIAT code operates.

For simplification purposes the program allows for three options concerning the surface energy equation ⁵¹ allowing for the representation of different physical boundary conditions and the determination the heat flux q_{cond} for the those conditions. The conduction flux is the heating that will enter the material and affect the in-depth parameters. One potential boundary condition is employed if the material is undergoing a cool-down period. A cool-down boundary condition is indicative that there is no high heating acting upon the surface, such as when a test material coupon that experienced high heat flow is rest in the room or a craft that has gone through an atmosphere and landed. The only heat fluxes acting upon its surface are those found by emittance and absorption, not by the recession of the material or the flow around the material.

A secondary option allows for assigning temperature to the surface other than the initial temperature. This is called the C_T or the T-type heat transfer. The following equation may be used to determine heat transfer in this case⁵¹

$$C_T(T_R - T_W) + q_{rad} - \sigma \epsilon_w T_W^4 - q_{cond} = 0 \quad (2.6)$$

Here, C_T (T-type heat transfer coefficient), T_R , and q_{rad} are the inputs used to calculate q_{cond} . T_R , the recovery temperature, which is the temperature at the stagnation point far away from the surface, and q_{rad} and C_T are calculated from the flowsolver. This option is not as simple as a cool-down condition as it involves a temperature gradient. This is used in cases where ablation may not be occurring but there may be a formation of pyrolysis gas. Surface chemistry tables are not needed for this boundary condition.

The most complete boundary condition involves the calculation of the convective heat flux. It involves the H-type heat transfer coefficient C_{HI} which is used in the equation¹¹

$$C_{HI}(H_R - (1 + B'_1)h_w) + \dot{m}_g h_g + \dot{m}_c h_c + q_{rad} - \sigma \epsilon_w T_w^4 - q_{cond} = 0 \quad (2.7)$$

C_{HI} , H_R , and q_{rad} are the inputs from the environment. H_R is the recovery enthalpy, which is defined as the enthalpy of the stagnation point far away from the surface. Also, λ , the blowing reduction parameter, is an input used to relate C_{HI} , the unblown value, with C_H , the blown transfer coefficient.

$$\frac{C_H}{C_{HI}} = \frac{2\lambda B'_1}{e^{(2\lambda B'_1)} - 1} = \frac{\ln(1 + 2\lambda B'_1)}{2\lambda B'_1} \quad (2.8)$$

where $B'_1 = \frac{\dot{m}}{C_{HI}}$ and $B'_1 = \frac{\dot{m}}{C_H}$.

Equation 2.7 and the correction of Eq. 2.8 are used when the material is ablating. The blowing reduction parameter takes into account the reduction in the heat transfer coefficient due to the injection of gases from pyrolysis and surface ablation into the boundary layer. If λ is approaching zero then the particles are being swept away quickly, leaving less time for heat transfer to occur and reducing the correction. The use of the unblown transfer coefficient during an ablating case is modeling the gas and char products as never leaving the surface, increasing heat transfer due to no particles interacting with the flow or shock layer, as shown in Ref. 28.

Generally, laminar flow, such as the one around the Stardust Return Capsule, allows for an assumption of 1/2 for the blowing reduction parameter. Transitional or turbulent flow will have a smaller parameter due to the flow carrying away the

injected particles in such a way that they do not remain near the surface and absorb the heat. Equation 2.7 is similar to Eq. 2.5, with C_H being used to denote the quantity $\rho_e u_e C_H$, where C_H is the dimensionless heat transfer coefficient. This term is akin to $\rho_e u_e C_M$, which contains the dimensionless mass transfer coefficient, C_M . Both terms describe how mass and heat travel to the surface. The similarity between Eq. 2.5 and Eq. 2.7 is not surprising, as Equation 2.5 is used to calculate values for the surface energy, and Equations 2.6 and 2.7 involve a special condition of the surface energy concerning wall boundary condition. An additional simplifying assumption is made to Equation 2.7 in FIAT:

$$C_H H_r + q_{chem} + q_{rad} - \sigma \epsilon_w T_w^4 - q_{cond} = 0 \quad (2.9)$$

Equation 2.9 groups the heat fluxes due to chemistry, that is, those due to charring, pyrolysis and the injection of material species from charring and pyrolysis gas, as one term. This term is found from the calculated wall enthalpy from the predictions made by a surface thermochemistry program such as MAT. Equation 2.9 also eliminates any convective heat flux loss due to wall enthalpy and instead contains only the convective heat flux that arrives due to the flow enthalpy. For a more complete surface energy balance, one that includes the individual contributions from the char and pyrolysis gas rates, in FIAT Eq. 2.9 is restructured for this work to include the individual contributions from the chemistry-driven heat fluxes. This allows for better understanding of the char and pyrolysis gas effects on heating on the surface.

Milos and Chen have extended the FIAT code into the two- and three-dimensions.^{23,52,53} The same governing equations employed by the one-dimension work are used in all the different dimensional versions. To work in two-dimensions, a

transformation from Cartesian coordinates to a general body-fitted coordinate system is employed. In Ref. 53, the two-dimensional code, renamed TITAN, is coupled with a flow solver code to perform thermal response and shape change simulation. TITAN was validated against arc-jet tests by Chen et al.⁵⁴ It was found that above 3000 K, the surface chemistry is a strong function of temperature with sublimation being a key driver. Lower than 3000 K diffusion-controlled oxidation determines the ablation rate. These two reactions are important to consider when calculating nonequilibrium conditions.

The one-dimensional approach of FIAT is used for analysis of the Stardust Return Capsule, a blunt body, because of the nose radius and the base diameter dimensions. As seen in the development of TITAN^{53,54}, the relationship between the radius of curvature (nose radius) and the base diameter is important in determining the heating upon the surface of a material. If the radius of curvature is close to or larger than the diameter, the heatshield surface, especially around the nose region, can be thought of as flat and heating should not change that much across the surface. The larger nose radius means the bow shock in this region is flatter over the nose, meaning more streamlines will experience the same “normal” shock. This means that there would be a large temperature gradient in the direction along the heatshield, leaving only the in-depth temperature gradient to be examined, a one-dimensional analysis. For Stardust, the nose radius is 0.22 m and the base diameter is 0.83 m, meaning that the base diameter is only about 4 times as long as the radius of curvature. The heatshield can be considered relatively flat and the heating relatively constant. Another parameter to look at to determine if a one-dimensional approach is

sound for the SRC is comparing the thickness of the heatshield to the other body dimensions. The thickness of the heatshield, around 0.05 m, is much less than the body dimensions. A similar analysis dealing with heatshield thickness was done for the Pioneer-Venus probes. In that case, the thickness was determined to be so small when compared to the other dimensions only heat transfer in one dimension was considered.⁵⁵ The findings of Ref. 54 where certain geometries produce similar predictions in both the two-dimensional analysis of TITAN and the one-dimensional analysis of FIAT are applicable to analysis of the Stardust.

Careful consideration of a one-dimensional approach must be taken at a corner region, where the high radius of curvature will dictate high heating on a surface. For example, the corner radius of the SRC is 0.02 m, which means the base diameter is nearly 41 times longer, leading to a highly curved region. Though the Core 2 point used for analysis is not in the shoulder region, it is about halfway in between the suitable for 1-D analysis stagnation point and the suspect shoulder region. The 1-D approximation may start to break down at that location.

2.3 Nonequilibrium Gas Properties

Nonequilibrium can occur in four forms: thermochemical, vibrational, translational and rotational. An understanding of what these different types of nonequilibrium mean and how they may affect the derivation of computational models is necessary to carry out any finite-rate prediction. The complex equations associated with each nonequilibrium state often leads to computational simplifications that concentrate on only one nonequilibrium state while assuming the other states are in equilibrium. The translational state is often coupled with the other

states and is not usually considered on its own. Due to the temperature associated with its nonequilibrium state quickly reaching equilibrium with the translational (gas) temperature, the rotational state is often ignored in nonequilibrium calculations.⁵⁶ Both forms of nonequilibrium are considered minor and in most studies, the focus is on the vibrational or thermochemical nonequilibrium phase that takes place on a material's surface or in a gas.

Molecular collisions cause vibrational and chemical processes to take place. The number of collisions required to begin these processes depends on the molecule and the relative kinetic energy between the interacting particles. Generally, as the temperature of a particle becomes higher, the number of required collisions to excite the vibrational state decreases. However, these collisions are slow to occur no matter the conditions; the nonequilibrium state is dependent on the relationship between the internal chemistry time and the fluid-dynamic time, so the gas may not have enough time to completely react due to the slow rate of collisions. The collision frequency (Z) can be related to the pressure and temperature of the gas by the equation:³⁴

$$Z \propto \frac{P}{\sqrt{T}} \quad (2.10)$$

So for a low pressure condition the collisional frequency will be low. From the standpoint of collision time versus the time frame for analysis, this low frequency indicates that the vibrational or thermochemical process will likely be in some state of nonequilibrium. The trajectory of the Stardust Return Capsule can experience between a peak of 0.37 to 0.44 atm (35 kPa to 45 atm), which is considered a low pressure trajectory and can slow down the molecular collisions.

Vibrational nonequilibrium is important when considering species concentration. The concentration for an equilibrium assumption is significantly different than a calculation of species concentration from a nonequilibrium analysis. In addition, the radiative heat transfer in nonequilibrium largely depends on the vibrational temperature. In reentry analysis, the vibrational temperature was found to depend upon the reentry craft's altitude.³ Altitude dictates the continuum regime the craft is encountering and the associated density of the freestream flow. As altitude increases, so does the mean free path between two molecules, which decreases the amount of collisions in the flow, which in turn affects the vibrational temperature. At high altitudes the rotational and vibrational temperatures remain essentially constant at the freestream temperature indicating few significant collisions

According to the research done by Olynick et al.,¹⁰ the effects of vibrational nonequilibrium flow on the Stardust heatshield during its reentry is negligible. By increasing the vibrational relaxation time, Olynick and his group were able to model vibrational nonequilibrium. The researchers studied the two areas of the Stardust capsule that Olynick modeled: the forebody, which is made up of PICA, and the aftbody, which is made up of another impregnated material, SLA-561V. The forebody showed only a minimal change with the inclusion of vibrational nonequilibrium. The afterbody showed a 35% increase in heating and 25% increase in pressure.

Olynick and his group came to the conclusion that the increase in the relaxation time of the vibrations affected the wake flow structure, which affected the heating and pressure, and the increase was not due to the vibrations themselves;

moreover, previous research showed that because the larger relaxation times increase the forebody shock distance that the pressure and heating on the afterbody change.³ This finding, coupled with those of Olynick, show that the local effects of vibrational nonequilibrium appear to be minimal on trajectories similar to that of Stardust and it can be ruled out as a significant method of nonequilibrium for the PICA material. Ref. 10 also finds that changing the forebody cone angle of the SRC resulted in different heating profiles on the surface, in particular, the heating experienced by the aftbody. While ablation should not affect the cone angle as greatly as the cases Olynick tests (50, 60, and 70 degree cone angles), Ref. 10's results when predicting heating as the shape of the forebody heatshield changes shows that altering the contour of the heatshield, such as changing the angle or through mass loss due to ablation, can affect the rest of the craft and is more a driver of the aftbody effects than the vibrational contributions.

Chemical nonequilibrium, or a finite-rate reaction, occurs as an adjustment period when molecules collide, such as when there is a sudden temperature change. In this period, chemical reactions are taking place at a definitive net rate. When analyzing reaction rates, two questions can be asked: what conditions must be satisfied by the molecules if they are to fully react and how frequently are these conditions satisfied.⁵⁷ An assumption for what type of reaction is occurring is usually made for the first question. The condition can be a bimolecular reaction where two molecules collide, of which a common example is dissociation ($AB + M \rightarrow A + B + M$). It may also be a reaction where three molecules collide; the recombination reaction ($A + B + M \rightarrow AB + M$) is a common example.

Recombination reactions from catalytic walls may increase the overall heat flux up to two times the amount experienced by non-catalytic walls. Finally, if the reaction is assumed to occur spontaneously by the decomposition of a single molecule that is currently in a high energy level it is a unimolecular reaction. An example is the special case of dissociation ($AB^* \rightarrow A + B$) where the molecule is already reacting. Dissociation is of primary importance in the chemistry at high temperatures. Due to the unimolecular assumption being the most difficult to deal with theoretically and also having little importance for gas-dynamic purposes, it is not often used in computational models. The primary focus in high-temperature gas dynamics is the bimolecular assumption and its associated dissociation reaction.

The relationship between the characteristic flow time and the characteristic relaxation time of a reaction, which determines whether or not a reaction is in equilibrium, nonequilibrium or frozen can be defined by the Damkohler (Da) number.⁵⁸ The Damkohler number is the ratio of the flow time to the relaxation time. Generally, if this number is above 10^0 , the reactions are considered to be occurring in equilibrium while below this threshold, the reactions are considered to be frozen. If the ratio is around 10^0 , then nonequilibrium is occurring on the surface of the material or in the flow. For chemical nonequilibrium the characteristic flow time can be determined from the velocity of the flow and the standoff distance of the shock while the characteristic relaxation time is unique for each reaction and is dependent on the mass fraction of the product and temperature. The dependence on speed and standoff distance comes from the rapid change the flow undergoes after a shock, for example, and how quickly a particle travels in that region. If the particle travels fast enough

through this region, the changes appear to occur quickly. If the particle is slow, the changes can seem to never occur as the particle travels away from the shock. Figure 2.5 shows a sample Mach versus Da number for a CEV-like trajectory. The reactions under consideration are nitrogen and oxygen dissociation. It is seen that for the aerothermal environment under consideration, nonequilibrium may occur at the lower end of the Mach speeds.

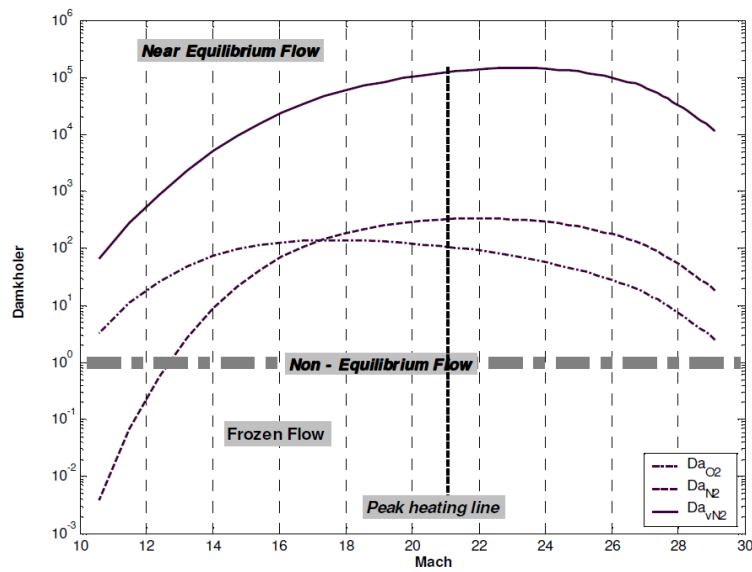


Figure 2.5. The three reaction regimes for a CEV-like aerothermal environment⁵⁸

The effectiveness of an ablative heatshield is sensitive to the chemical state of the ablation-product gas; this is due to how the pyrolysis gas decomposes into the flowfield. In addition, emissivity and wall chemical activity affect the heatshield from a chemical and flowfield standpoint. For example, a poor catalytic thermal protection system may be used to accommodate lower heat fluxes.⁵⁹ The nonequilibrium chemical condition is often applied to the flowfield, with the surface interactions being simplified or assumed. The trends seen in finite-rate application in flowfields are the same when analyzing the interaction between the gas and the surface.

2.4 Surface Interactions

To understand the affects of nonequilibrium surface interactions, one must first understand what is going on at the surface. All carbon materials consist of a matrix of carbon atoms in which each atom occupies an apex of an equilateral triangle. This arrangement lends itself to having a high attractive potential between a foreign molecule and the molecules found on the surface; that means that a gas atom can be easily absorbed by the surface.⁶⁰ On a microscopic level, the bonds between the atoms found in a heatshield dictate how the shield will react during reentry conditions.

During reentry, a vehicle experience may experience one or more spikes in heating with the magnitude of these spikes depending on the trajectory. It is during this time that the heatshield material decomposes most rapidly; at the end of the spike, a char layer may exist at the top of the heatshield. In a carbonaceous heatshield, the char can vaporize through sublimation, oxidation or combining with atomic nitrogen to form CN, called nitridation. The ablation product that is injected into the flow is the pyrolysis gas and the vapor from the char layer.

Analysis of the Apollo data showed that for steady-state ablation, the mass ratio between the pyrolysis gas and the gaseous carbon is not the same as the mass ratio of the components of the virgin material.⁶¹ That is, the ratio of species found in the unaffected material is not the same as the ratio of those species in the flowfield during ablation. Due to this discrepancy, more complex behavior is seen in charring cases due to the char and pyrolysis having dissimilar compositions. The porous residual char that remains after ablation has a lower density than the original solid and

different thermal and structural properties. Chars have a lower mechanical strength and can spall at high heating conditions.

The pyrolysis gas injection rate is not directly related to the surface vaporization rate because it is dictated by the heat transfer through the heatshield. At lower pressures, the pyrolysis gas spends a substantial amount of time traveling through the char and transition zones. Because the gas remains in the material for some nontrivial amount of time, it acts as a coolant and absorbs heat. Equilibrium vapor pressure and density of a pyrolysis can be calculated from the following equations, respectively:^{62,63}

$$P_{equil} = AT^{1.5} \cdot e^{(-B/T)} \quad (2.11)$$

$$\rho_{equil} = C\sqrt{T} \cdot e^{(-B/T)} \quad (2.12)$$

where A and C are some prescribed coefficient, T is the gas temperature, and B is activation temperature. The pressure can be used to calculate the equilibrium wall mass fraction which is used in reaction equations.

The properties that would help determine how the freestream gas and the ablation products interact are calculated in the surface thermochemistry B' tables which are commonly established by solving the chemical equilibrium relations and the elemental species balance equation using the thin film transfer theory. However, it is desired to assume a more general state of chemical nonequilibrium in a B' table derivation. This may be computationally expensive due to the complicated interactions between the solid surface and the ambient gas. A B' table includes one pressure, a dimensionless pyrolysis gas rate (B'_g), and a dimensionless char ablation rate (B'_c). A correction cannot be added to these tables to account for nonequilibrium

because a correction still assumes a steady-state of the reactions; the tables need to be regenerated assuming a finite rate model.⁹ These tables are provided to FIAT through ACE or MAT. For the equilibrium B' table in Fig. 2.6, it is apparent that as the gas rate increases, the range of surface temperatures that can be experienced becomes smaller, tending to cluster around 3000 K. The increase in pyrolysis gas is acting like a coolant and keeping the temperature from significantly increasing past 3000 K.

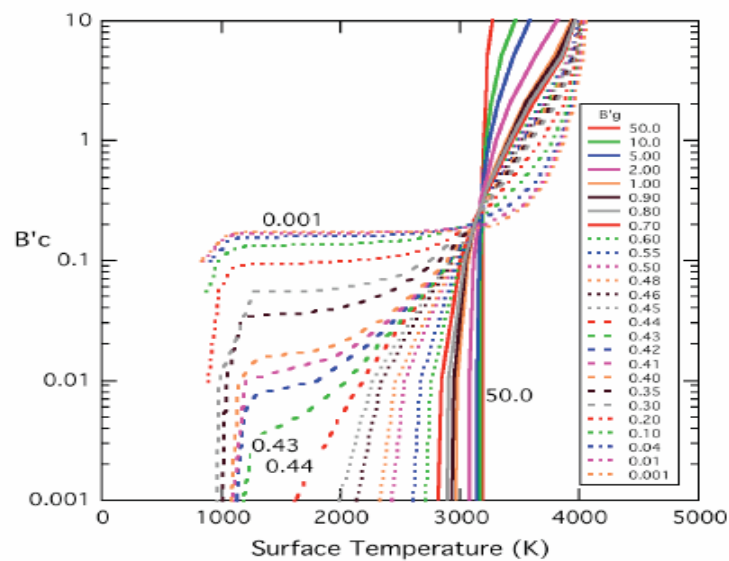


Figure 2.6. A sample B' table with the char ablation rate on the y-axis and different values of the pyrolysis gas rate.⁵²

Since there are many possible reactions taking place at the surface of an ablating material, it is important to identify the correct method to illustrate the reactions. Park conducted extensive research into deriving a finite-rate gas/surface interaction model.^{7-9,61,63} Oxidation (Eqs. 2.13 and 2.14), nitridation (Eq. 2.15), and sublimation of the carbon (Eq. 2.16) on the heatshield surface, are considered in Park's model.

$$\dot{m}_1 = \rho C_O \bar{v}_O \beta_O \frac{M_C}{M_O} \quad (2.13a)$$



$$\dot{m}_2 = 2\rho C_{O_2} \bar{v}_{O_2} \beta_{O_2} \frac{M_C}{M_{O_2}} \quad (2.14a)$$



$$\dot{m}_3 = \rho C_N \bar{v}_N \beta_N \frac{M_C}{M_N} \quad (2.15a)$$



$$\dot{m}_4 = \rho(C_{C_3,E} - C_{C_3}) \bar{v}_{C_3} \beta_{C_3} \quad (2.16a)$$



$$\dot{m}_c = \dot{m}_1 + \dot{m}_2 + \dot{m}_3 + \dot{m}_4 = \rho_{(s)} \dot{s} \quad (2.17)$$

The quantity \bar{v}_i is defined as

$$\sqrt{kT_w / 2\pi m_i} \quad (2.18)$$

Oxidation is chosen as a reaction due experiments that saw when a beam of neutral atoms bombarded the surface of a material only carbon monoxide formed around the surface.⁷ Further experiments at different conditions showed that in the vapor around the material C_3 was present in large quantities, indicating sublimation. Previous research has shown that ions have little effect on convective heating. Park's model assumes that the reaction rates are negligibly small for both the oxygen atom and nitrogen atom recombination.

In an autonomous Park's model, species mass conservation at the surface is written as:

$$-\rho D_i \nabla X_i + \rho v_w C_i = \hat{N}_i + \dot{m}_g C_{i,g} \quad (2.19)$$

The mass transfer through diffusion (D_i) is the first term on the left, with mass transfer due to convection being the second term. \hat{N}_i is the source term and it is calculated for CO, CN, C₃, N, O, and O₂ species based on their inclusion in Eqs. 2.13-2.16.

$$\begin{aligned} \hat{N}_{CO} &= \dot{m}_1 \frac{M_{CO}}{M_C} + \dot{m}_2 \frac{M_{CO}}{M_C}, \quad \hat{N}_{CN} = \dot{m}_3 \frac{M_{CN}}{M_C}, \quad \hat{N}_{C_3} = \dot{m}_4 \\ \hat{N}_N &= -\dot{m}_3 \frac{M_N}{M_C}, \quad \hat{N}_O = -\dot{m}_1 \frac{M_O}{M_C}, \quad \hat{N}_{O_2} = -\dot{m}_2 \frac{M_{O_2}}{2M_C} \end{aligned} \quad (2.20)$$

For all the other species, the source term is equal to zero. Equation 2.19 is modeling how the particles diffused and blown around the surface is equal to the particles created by the finite-rate reactions and the particles arriving at the surface from pyrolysis gas.

The total ablation based on the global mass balance is:

$$\rho v_w = \dot{m}_c + \dot{m}_g \quad (2.21)$$

In Park's model, the equilibrium vapor pressure based off Eq. 2.11 is:

$$P_{equil} = 6.27 \times 10^{15} \cdot e^{(-90908/T)} \quad (2.22)$$

Previous use of the Park Model⁹ did not indicate how to derive the mass fraction from the equilibrium pressure vapor or what reference frame it should be calculated from, the equilibrium or nonequilibrium. The mass fraction for the

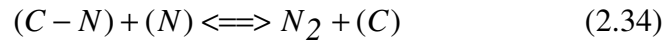
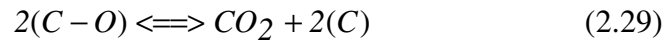
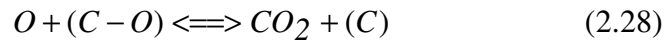
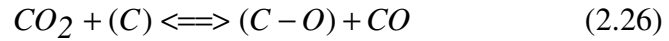
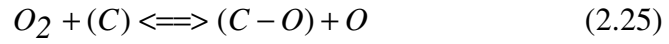
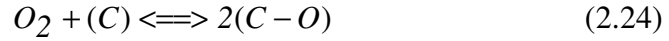
equilibrium C_3 is assumed to be the same as the ratio of the equilibrium C_3 pressure to the total pressure experienced in the analysis. This is akin to assuming that the mole fraction is equal to the mass fraction for this concentration calculation. This postulation is made because it is assumed that the hypothetical total molecular weight in this specific calculation will be the molecular weight of C_3 only.

The Modified Park Model will not predict the special case of equilibrium due to assumptions made in its development. In the model, for oxidation, nitridation, and sublimation, the reverse reaction rates were assumed to be negligible.⁶¹ Park made this assumption based on the equilibrium constants for each reaction being small, making the reverse reactions rate appear negligible when compared to the forward rate. In equilibrium, the net reaction rate, the difference between the forward and reverse rates, should be zero, with no change in time. The elimination of any consideration for the reverse reaction means that the model cannot calculate the net rate of each reaction as zero unless the forward reaction alone goes to zero. From an environmental conditions standpoint, the forward reactions of the Modified Park Model will only approach this limiting case if the temperature approaches zero, which is highly unlikely to occur in the high heating of reentry.

The presence of a significant reverse reaction rate does not preclude nonequilibrium but it does help drive the net rate towards the limiting case of zero change. Ignoring the reverse reaction rate is a mathematical simplification made based off unique experimental conditions using the comparison of the magnitude of the forward and reverse rates, via the equilibrium constant, and incorporated into the model such that the reverse reaction rate is deemed negligible for the reactions under

all possible conditions. Because of this assumption, in the Modified Park Model nonequilibrium is built into the model.

Zhluktov's model is a surface kinetic method based on reaction rates that includes both forward and reverse reactions.^{9,64} It was seen in Ref. 64 that the model may approach equilibrium under certain conditions. The model does not take into account nitridation which may cause under prediction of the ablation rate. The surface interaction model is as follows:



The reaction rates for each of the equations are as follows:

$$r_{23} = k_{f23}(pX_O^{\Theta_0} - \Theta_O / K_{23}) \quad (2.35)$$

$$r_{24} = k_{r24}(K_{24}pX_{O_2}(\Theta^0)^2 - (\Theta_O)^2) \quad (2.36)$$

$$r_{25} = k_{f25}(pX_{O_2}\Theta^0 - pX_O\Theta_O / K_{25}) \quad (2.37)$$

$$r_{26} = k_{f26}(pX_{CO_2}\Theta^0 - pX_{CO}\Theta_O / K_{26}) \quad (2.38)$$

$$r_{27} = k_{f27}(\Theta^0 - pX_{CO}\Theta^0 / K_{27}) \quad (2.39)$$

$$r_{28} = k_{f28}(pX_O\Theta_O - pX_{CO_2}\Theta^0 / K_{28}) \quad (2.40)$$

$$r_{29} = k_{f29}((\Theta_O)^2 - pX_{CO_2}(\Theta^0)^2 / K_{29}) \quad (2.41)$$

$$r_{30} = k_{r30}\Theta^0(K_{30} - pX_C) \quad (2.42)$$

$$r_{31} = k_{r31}(\Theta^0)^2(K_{31} - pX_{C_2}) \quad (2.43)$$

$$r_{32} = k_{r32}(\Theta^0)^3(K_{32} - pX_{C_3}) \quad (2.44)$$

$$r_{33} = k_{f33}(pX_N\Theta^0 - \Theta_N / K_{33}) \quad (2.45)$$

$$r_{34} = k_{r34}(K_{34}pX_N\Theta_N - pX_{N_2}\Theta^0) \quad (2.46)$$

There are two possibilities for the equilibrium constants for K_{23} and K_{34} . For an assumption of mobile absorption:

$$\frac{1}{K_i} = B \frac{kT}{P_0} \left(\frac{2\pi m_i kT}{h^2} \right)^{1/2} e^{-T d_i / T} \quad (2.47)$$

For immobile adsorption:

$$\frac{1}{K_i} = B \frac{kT}{P_0} \left(\frac{2\pi m_i kT}{h^2} \right)^{3/2} e^{-T d_i / T} \quad (2.48)$$

P_0 is 1.01325×10^5 Pa, $m_{23} = m_{O_2}$, $m_{34} = m_{N_2}$, and $B = 3.5 \times 10^{19} \text{ m}^{-2}$. The other equilibrium constants are not independent and are related to K_{23} and K_{34} through the following equations:

$$K_{24} = (K_{23})^2 K_{O_2} \quad (2.49)$$

$$K_{25} = K_{23} K_{O_2} \quad (2.50)$$

$$K_{26} = K_{23} K_{CO_2} \quad (2.51)$$

$$K_{27} = K_{30} / (K_{23} K_{CO_2}) \quad (2.52)$$

$$K_{28} = K_{30} / (K_{23} K_{CO_2}) \quad (2.53)$$

$$K_{29} = K_{30} / ((K_{23})^2 K_{CO_2}) \quad (2.54)$$

$$K_{31} = (K_{30})^2 / K_{C_2} \quad (2.55)$$

$$K_{32} = (K_{30})^3 / (K_{C_2} K_{C_3}) \quad (2.56)$$

$$K_{33} = 1 / (K_{34} K_{N_2}) \quad (2.57)$$

K_{30} can be determined numerous ways. Zhlukov and Abe highlighted methods derived by Blottner's⁶⁵ and Scala and Gilbert.⁶⁶ They chose Blottner's approach, which results in K_{30} 2.5 times larger than other methods. The equilibrium constants for the species N_2 , O_2 , CO , CO_2 , C_2 and C_3 are found by applying a best fit curve to the data found in the JANAF tables.⁶⁷

The backward and forward reactions rates for the reactions taking place are taken from Havstad and Ferencz⁶⁸ and use the following expressions:

$$k_{f23} = \varepsilon_{23} F_O \quad (2.58)$$

$$k_{f24} = \varepsilon_{24} B \left(\frac{kT}{h_p} \right) e^{-T_{a2}/T} \quad (2.59)$$

$$k_{f25} = \varepsilon_{25} F_{O_2} e^{-T_{a3}/T} \quad (2.60)$$

$$k_{f26} = \varepsilon_{26} F_{CO_2} \quad (2.61)$$

$$k_{f27} = \varepsilon_{27} B \left(\frac{kT}{h_p} \right) e^{-T_{a5}/T} \quad (2.62)$$

$$k_{f28} = \varepsilon_{28} F_O e^{-T_{a6}/T} \quad (2.63)$$

$$k_{f29} = \varepsilon_{29} B \left(\frac{kT}{h_p} \right) e^{-T_{a7}/T} \quad (2.64)$$

$$k_{f30} = \varepsilon_{30} F_C \quad (2.65)$$

$$k_{f31} = \varepsilon_{31} F_{C_2} \quad (2.66)$$

$$k_{f32} = \varepsilon_{32} F_{C_3} \quad (2.67)$$

$$k_{f33} = \varepsilon_{33} F_N \quad (2.68)$$

$$k_{f34} = \varepsilon_{34} F_{N_2} e^{-T_{a12}/T} \quad (2.69)$$

where

$$F_i = P_0 / \sqrt{2\pi m_i kT}$$

$$\begin{aligned} \varepsilon_{23} = 1, \varepsilon_{24} = 0.0008, \varepsilon_{25} = 1, \varepsilon_{26} = 0.9, \\ \varepsilon_{27} = 0.1, \varepsilon_{28} = 0.8, \varepsilon_{29} = 1, \varepsilon_{30} = 0.24, \\ \varepsilon_{31} = 0.5, \varepsilon_{32} = 0.023, \varepsilon_{33} = 1, \varepsilon_{34} = 1, \end{aligned}$$

$$T_{d1} = 45,000$$

$$T_{d11} = 36,600$$

$$T_{a2} = 2T_{d1} - T_{DO_2}$$

$$T_{a3} = T_{DO_2} - T_{d1}$$

$$T_{a12} = T_{DN_2} - T_{d11}$$

$$T_{a5} = 40000$$

$$T_{a6} = 2000$$

$$T_{a7} = 40000$$

From the work of Havstad and Ferencz, it can be determined that the T_D for O_2 and N_2 are 56200 and 113200 K, respectively.

The rates of species production on the surface are:

$$\dot{m}_O = (-r_{23} + r_{24} - r_{28})M_O \quad (2.70)$$

$$\dot{m}_{CO} = (r_{26} + r_{27})M_{CO} \quad (2.71)$$

$$\dot{m}_{CO_2} = (-r_{26} + r_{28} + r_{29})M_{CO_2} \quad (2.72)$$

$$\dot{m}_C = r_{30}M_C \quad (2.73)$$

$$\dot{m}_{C_2} = r_{31}M_{C_2} \quad (2.74)$$

$$\dot{m}_{C_3} = r_{32}M_{C_3} \quad (2.75)$$

$$\dot{m}_{NO} = 0 \quad (2.76)$$

$$\dot{m}_{CN} = 0 \quad (2.77)$$

$$\dot{m}_N = (-r_{33} - r_{34})M_N \quad (2.78)$$

$$\dot{m}_{O_2} = (-r_{24} - r_{25})M_{O_2} \quad (2.79)$$

$$\dot{m}_{N_2} = r_{34}M_{N_2} \quad (2.80)$$

For a stationary regime, the species production equations are as follows:

$$\dot{m}_{(C-O)} = (r_{23} + 2r_{24} + r_{25} + r_{26} - r_{27} - r_{28} - 2r_{29})M_O = 0 \quad (2.81)$$

$$\dot{m}_{(C-N)} = (r_{33} - r_{34})M_N = 0 \quad (2.82)$$

Using Eqs. 2.70-2.80, the total surface mass blowing rate is:

$$\dot{m} = M_C(r_{27} + r_{28} + r_{29} + r_{30} + 2r_{31} + 3r_{32}) \quad (2.83)$$

The sum of surface coverage concentrations is equal to 1:

$$\Theta_O + \Theta_N + \Theta^0 = 1 \quad (2.84)$$

The free surface concentration and surface coverage concentrations for O and N are unknowns; however, if you couple Eqs. 2.81, 2.82, and 2.84, these unknowns can be solved for and used in Eqs. 2.23-2.34 to determine all the reaction rates. The species conservation at the surface is:

$$-\rho D_i \nabla X_i + \rho v_w C_i = \dot{m}_i + \dot{m}_g C_{i,g} \quad (2.85)$$

In Zhlukov's model, the porosity of graphites is ignored. The model is considered a rough fit to experimental data due as any discrepancies are caused in part by the lack of intermediate reactions in the Zhlukov Model.

Both Eqs. 2.19 and 2.85 are nonlinear and can be solved through iterations. The surface temperature, pyrolysis gas injection rate and species concentrations of pyrolysis gas must be specified so that the species concentration at the wall and the velocity can be updated. Equations 2.19 and 2.85 are not needed in the MAT code, as

it has its own iterative process to find species concentrations and gas rates at the gas/surface interface.

The high level complexity, with its use of Arrhenius equations and equilibrium constants and increased number of reactions, of the Zhlukto Model makes it more robust than the Modified Park Model, but more difficult to implement in MAT. When incorporated into MAT, the Zhlukto Model does not converge without any predictions found for the char rates and wall enthalpy. The need to solve for the unknown surface concentrations as (Eq. 2.84) creates a situation within MAT where a solution cannot be found for the concentrations. MAT tries to find a set of concentrations that satisfy the conditions and if found, the solution is such that the resultant reactions rates are too large to find a viable char rate, creating nonconvergence. The Zhlukto Model is not used for any calculations in this dissertation as only the Modified Park Model is successfully integrated within MAT. The Zhlukto Model is presented to show a more complex finite-rate model that has been used in a limited manner for the SRC as seen in Ref. 9 but cannot currently be used in a more encompassing manner to create a B' table that can be used at more than one point in a trajectory or analysis.

2.5 The Multicomponent Ablation Thermochemistry (MAT) Program

By examining the B' tables and how they are generated, one can understand how thermochemistry results are calculated and modify them such that one can simulate the affect of nonequilibrium surface conditions. MAT originally calculated

nonequilibrium surface conductions based only on finite-rate oxidation.¹² The reactions that could produce oxidation that MAT takes into account were as follows:



Carbon dioxide and nitrogen species surface reactions were neglected because they were deemed slower than Eqs. 2.86–2.88. This caused reactions involving sublimation and nitridation to be ignored. The chemical reactions are modeled as a conversion of one pseudo-element in a condensed reactant species into another element of the same atomic weight in one of the product species. This allows for the reactions to take place in an “unsteady” manner if nonequilibrium is occurring by assuming the reactants are not fully formed with the conversion pushing it towards the proper product. The program takes into account all species that may be present between the flow and the heatshield with the boundary layer based on elements defined by the user. For the Stardust Return Capsule trajectory and PICA material the elements present in the interaction between the flow and the surface are typically hydrogen, carbon, nitrogen, and oxygen. The interaction of the air and PICA material produces a total of 74 molecular combinations. JANAF tables are used to compute heat of formations, enthalpy, and curve fits to specific heat at constant pressures for each species formed at the gas/surface interface. MAT originally used two early kinetic models (Park⁶⁹ and Scala⁷⁰) in its calculation of nonequilibrium oxidation rates. The early Park Model is an attempt to update a semiempirical formula that described ablation rates of commercial grade graphites. The approach however is not

applicable to low-density materials, like PICA. The model uses reaction probability to improve upon the semiempirical model which leads to a higher predicted ablation rate and greater mass loss value.

Physically, MAT is modeling the surface as a thin layer where there are char and pyrolysis elemental fluxes entering the layer from one direction and diffusional and convective elemental fluxes leaving the surface. While a material response program will consider the total mass loss associated with charring and pyrolysis gas, a thermochemistry program is considering the elemental breakdown of those processes. Figure 2.7 shows how the mass fluxes for each element are entering and leaving the surface.

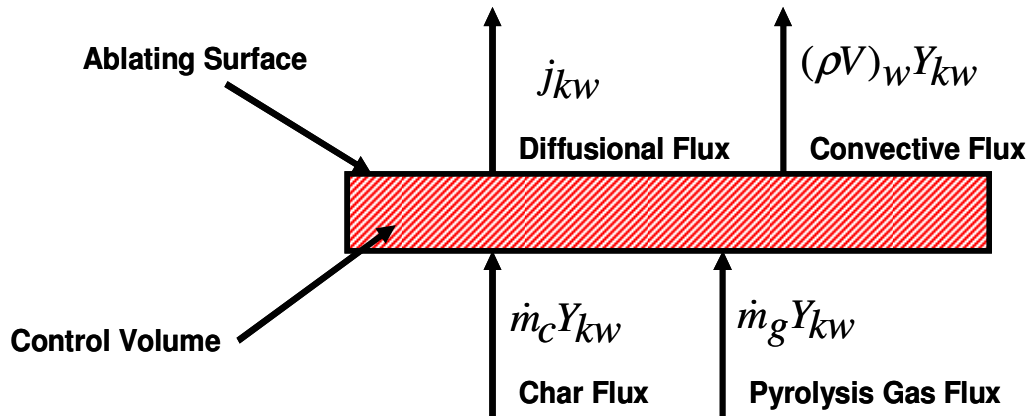


Figure 2.7. The mass fluxes at the surface of a thermal protection system in a hypersonic boundary layer.

The use of the early Park and Scala models, applied to a reinforced carbon-carbon protection system, predict a more rapid increase of B'_c with temperature increase than arc-jet test data results. MAT predicts that there is constant charring ($B'_c = 0.18$) for a range of temperatures, corresponding to a diffusion-limited production of CO which is not apparent in arc-jet testing. The difference in what

MAT predicts in the use of the Scala and the early Park Model and the arc-jet tests is acceptable because the uncertainties in free stream properties make it difficult to predict carbon oxidation in arc-jet tests and the MAT solutions are within an allowable 50% uncertainty range.

The equilibrium element conversation equation used in MAT is:²²

$$\dot{m}_g Y_{kg} + \dot{m}_c Y_{kc} = j_{kw} + (\rho v)_w Y_{kw} \quad (2.89)$$

when summed over k , the number of elements, becomes

$$\dot{m}_g + \dot{m}_c = \sum_k j_{kw} + (\rho v)_w \quad (2.90)$$

Traditional usage has the diffusional fluxes j_{kw} obtained by the transfer potential method, such that:

$$j_{kw} \approx \rho_e u_e C_M (Z_{kw}^* - Z_{ke}^*) \quad (2.91)$$

The diffusion-coefficient weighted average of mass and mole fractions is represented in the variable Z^* .⁷¹ As an assumption, the diffusion coefficients are equal; moreover, this makes Z and Y equivalent. The diffusional flux is equal to the mass transfer at the surface. The summation of the diffusional fluxes is zero, eliminating it from Eq. 2.90. Without the diffusional flux in Eq. 2.90 the convective flux is equal to the pyrolysis and char flux. Mathematically, this is MAT's consideration for the physical trait of injected products that stem from pyrolysis and char formation. Substituting Eq. 2.91 into Equation 2.89 and using the summation of Eq. 2.90 yields the equilibrium element flux balance as:

$$Y_{kw} = \frac{Y_{ke} + B'_g Y_{kg} + B'_c Y_{kc}}{1 + B'_g + B'_c} \quad (2.92)$$

B'_c and B'_g are often specified as independent parameters. Since Y_{kw} cannot be negative, the numerator provides an upper bound, while the value of Y_{kw} being less than or equal to 1 allows the denominator to serve as another upper bound. Y_{kw} is also calculated from Eq. 2.93, which derives the quantity from the sum of the partial pressures and mass concentrations.

$$Y_{kw} = \frac{M_k}{PM} \sum_i c_{ki} P_i \quad (2.93)$$

Equation 2.93 is the gaseous mass fraction at the wall/surface. MAT iterates on this equation, changing parameters such as temperature which in turn affects the mass concentration and partial pressure until Eqs. 2.92 and 2.93 are equal. Equilibrium constants are calculated as a function of partial pressures and mole fractions. MAT first tries to find a converged solution using the smallest B'_c or T and going through all combinations of pressure and B'_g . It then sweeps through the ranges of B'_c that the user defined to calculate wall enthalpy and char at those quantities.

For the nonequilibrium dimensionless reaction mass flux (B'_{kr}), based on the conversion of the pseudo-element, the reaction mass flux is calculated from

$$B'_{kr} = \frac{M_k}{\rho_e u_e C_M} \sum_n \sum_m (\mu_{mn}^R - \mu_{mn}^P) c_{kn} \bar{R}_m \quad (2.94)$$

where \bar{R}_m is the net reaction rate, μ the reaction coefficient, n is the species, m is the reaction number, c_{kn} is the atoms of element k in species n , R is the reactant and P is the product. It must be applied to the elements found at the surface of the ablating material. C_M , the mass transfer coefficient, is related to C_H by the equation⁷²

$$C_M = C_H Le^{2/3} \quad (2.95)$$

where Le is the Lewis number. Often, this relationship is further simplified so that the diffusion coefficient and heat transfer coefficient are equal. FIAT uses C_H in its input calculations and so this assumption will be made such that the available data for C_H will be applied for C_M .

The new elemental flux balance equation using the reaction mass flux would be:¹²

$$Y_{kw} = \frac{Y_{ke} + B'_g Y_{kg} + B'_c Y_{kc} - B'_{kr}}{1 + B'_g + B'_c} \quad (2.96)$$

Because a finite-rate reaction is not steady in time and may not produce the element under consideration as much as if it is occurring in equilibrium, the dimensionless finite-rate reaction term acts as a physical penalty. Without it, some larger mass concentration of element k is reached due to the equilibrium assumption. With it, the element will not reach that value, as the element is not being fully produced. It is possible that if a reaction rate becomes large, then B'_{kr} may become a dominant term in Eq. 2.96 and be describing a physically impossible situation, one where a finite-rate reaction no longer described a reaction that produces element k . If this occurs, the mass fractions for the two elements involved in the reaction may be modified so that B'_{kr} appears in the equation for one element.¹² This is what happens for the Zhlukto Model if there is a convergence of the surface concentrations and due to the complexity of its reactions, no modification can take place to correct the error. In place of computing B' tables, MAT can use equilibrium gas mixtures at assigned temperatures and pressure to get gas phase conditions.⁷³ This mode is not relevant to the material response computations found in FIAT.

MAT uses the numerical procedure known as the Newton-Raphson method to solve the nonlinearity of its equation set. This method uses logs of positive quantities as variables. The primary unknowns (which can be found in Ref. 12 and includes the element flux, temperature, and surface mole fraction) are contained in vector X . The iteration for the Newton-Raphson is:

$$\Delta X = -J^{-1}E \quad (2.98a)$$

$$X = X + \Delta X \quad (2.98b)$$

E is the error vector and the Jacobian matrix is formed from:

$$J = \frac{\partial E}{\partial X} \quad (2.98c)$$

Typically, without reduction, the system may contain 30 to 60 equations and unknowns. Mathematically, this stems from MAT using between 4 and 6 base elements and considering 20 to 40 gas species. This set can be reduced until there only remain 12 to 18 equations and unknowns. The convergence criterion is that the change in error with respect to changes in pressure and temperature is zero. The mass fraction can be calculated from the ratio of the species density (using the partial pressure) and total density.

$$C_i = \frac{p_i/R_iT}{p_{total}/R_{total}T} \quad (2.99)$$

where

$$R_{total} = \frac{8314}{MW_{total}}, \quad R_i = \frac{8314}{MW_i}$$

The mass fraction depends on the molecular weight of the species being taken under consideration since R , the specific gas constant, is not constant. R is not

constant due to the reacting nature of the gas. It is assumed that the molecular weight is given in grams and needs to be converted to kilograms. Although a correction term Z is sometimes added to the state equation to account for effects of hypersonic speeds,⁷⁴ it is not needed for mass fraction because it will cancel out with itself. Incorporating these changes into the MAT code should update its ability to calculate nonequilibrium surface conditions using newer models.

The models of Park and Scala only concentrate on a specific subset of reactions, oxidation. Replacing the earlier models by the more modern models proposed by Park^{7-9,61,63} and Zhlukov⁶⁴ allows for an expansion of reactions under consideration to include sublimation and nitridation while still considering some oxidation reactions. Nitridation has the ability to cause a greater rate of ablation, though it is often ignored due to the slowness of reaction, as seen in its omission for the Scala and early Park models.⁷⁵ Additionally, sublimation was seen to affect graphite materials by Keenan and Candler in Ref 20. The oxidation, sublimation, and nitridation reactions must be accounted for when their elemental components are called upon in Eqs. 2.93 and 2.96. Carbon will have the most reactions associated with it, as it is present in both the material and the flow. Being that it is found the ablating material, carbon is involved in all reactions presented by Park and Zhlukov.

Chapter 3

Stardust Return Capsule Trajectory Analysis

3.1 Preliminary Design Trajectory

3.1.1 Equilibrium

Two design trajectories for the Stardust Return Capsule are examined: a preliminary design and the final design trajectory. Each trajectory has a similar total heating on the PICA heatshield. The equilibrium and nonequilibrium assumptions are made at the surface and drive the material response predictions. Each reaction in the Modified Park Model is studied for importance during SRC heating conditions. For the final design trajectory, analysis is done at three different locations on the SRC.

The preliminary design trajectory includes radiation to the surface and lasts 750 seconds. Only one point is considered in the preliminary trajectory: the stagnation point. The peak pressure at the stagnation point is 0.44 atm (45 kPa), with the average pressure being 0.14 atm (14 kPa). The analysis will only concentrate on the surface energy balance, with consideration for convective heat flux and radiation in, and not analyze any in-depth energy terms. The cold wall heat flux, net convection and radiative heat fluxes upon the SRC heatshield are shown in Fig. 3.1. The cold wall heat flux, along with the radiative heat flux, is determined from the environmental inputs. The heat pulse, the time during the reentry where the majority

of heating occurs, lasts 100 seconds. During this time, the maximum cold wall flux onto the surface is 950 W/cm^2 , with the max radiation being 140 W/cm^2 . Something that is described as being a “cold wall” is that parameter as it would occur if the wall stayed at some low initial ambient temperature. At this low temperature, there would be no ablative or pyrolytic products. This is the parameter used in calculating the environment a reentry vehicle will experience from a general standpoint.

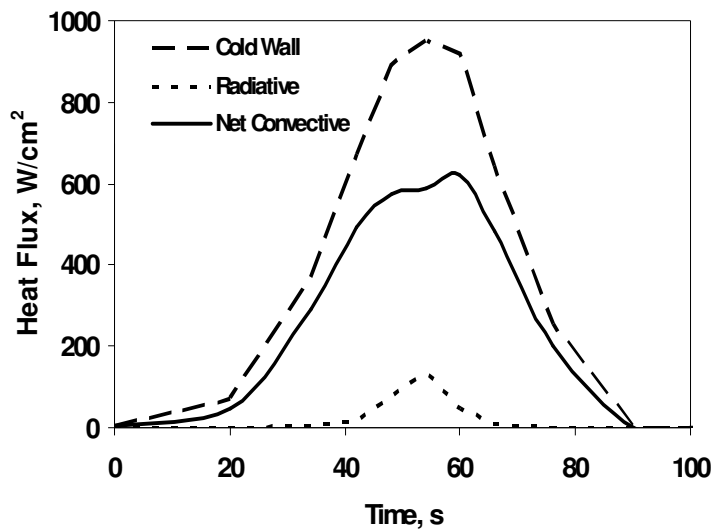


Figure 3.1. The surface heating profile for the preliminary Stardust Return Capsule trajectory.

The cold wall heat flux will remain the same in all cases as long as the trajectory remains the same since it is the product of the environment and not any surface chemistry such as wall enthalpy. Typically, data sets only focuses on the cold wall heat flux or the corrected convective heat flux that is derived from the blown transfer correction and ignore any contribution due to the wall enthalpy. However, for the preliminary trajectory, wall enthalpy was considered in calculations for the net convective heat flux. The peak total heat flux, cold wall heat flux plus radiative heat

flux, is 1100 W/cm^2 and is found at 54 seconds in the trajectory. The peak heat flux predicted by Olynick et al.¹⁰ (which uses a preliminary trajectory) and Kontinos et al.¹³ (which uses the final design trajectory) for the SRC was approximately 1200 W/cm^2 , so the peak found in the preliminary trajectory is within 10% of the peak found by Kontinos and Olynick. The allowable heating envelope used for predictions is 25% for Stardust, so the environment in the preliminary environment can be said to match the environment used in Olynick's analysis. Olynick's results will serve as the baseline case for comparison when the preliminary trajectory is used. As a comparison¹⁰ to other peak heating at stagnation points, for the Shuttle, it is between $40\text{-}50 \text{ W/cm}^2$ and for the Viking probe it is 25 W/cm^2 . There is significantly higher heating at the stagnation point for the SRC due in part to the high speed of reentry of the capsule.

Olynick et al.¹⁰ predicted the total heat flux on the SRC heatshield when ablation takes place as approximately 800 W/cm^2 . Olynick breaks down his net convective heat flux into diffusional and transient terms and includes the contribution due to wall enthalpy. Wall enthalpy is then included in the preliminary design trajectory analysis when computing net convective heat fluxes. The maximum net convective heat flux found in equilibrium for the preliminary trajectory is 590 W/cm^2 , which leads to a total heat flux that replaces the cold wall heat flux with the net convective heat flux of 730 W/cm^2 at 54 seconds. Both the total heat flux with cold wall heat flux and net convective heat flux are within 10% of previously predictions by Olynick meaning the preliminary trajectory used for analysis in this dissertation is essentially the same as the Olynick trajectory.

Although equilibrium calculations are not expected to be affected by the implementation of nonequilibrium in FIAT and MAT, a comparison case is run to both confirm that the partitioning works and to illustrate some of the problems with the equilibrium assumption for the Stardust reentry. The heatshield for the preliminary trajectory is made up of PICA, graphite polycynate, and aluminum honeycomb (Fig. 3.2). PICA is the thickest material, at 5.08 cm. In addition to predicting the surface temperature, FIAT predicts in-depth temperatures at 3 locations: 1.27, 2.54, and 5.08 cm from the original surface. Note that since the deepest FIAT thermocouple is also the thickness of the PICA material, it is measuring the bondline temperature between PICA and the graphite polycynate.

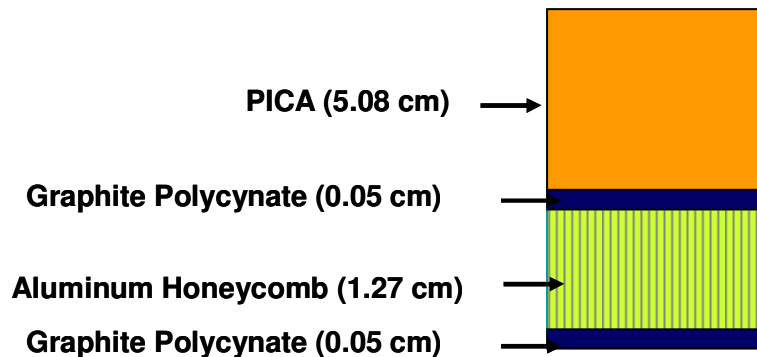


Figure 3.2. The heatshield material layout for the preliminary design SRC trajectory analysis

Pyrolysis with surface recession is also assumed to occur on the SRC. An H-type heat transfer is employed in the calculations as described in Section 2.2. In addition, a blowing rate of 0.5 is used for Eq. 2.8. The initial temperature on the surface of the heatshield (and set as the initial temperature through the heatshield) is 294 K.

Figures 3.3 and 3.4 are the temperature and mass loss rates as predicted by FIAT. The peak temperature is about 3370 K (at a time of 54 s); at a depth of 1.27 cm the peak is about 1970 K (at a time of 77 s). At the 2.54 cm depth it is 716 K (at a time of 122 s) and at the depth of 5.08 cm the peak temperature is at about 516 K (at a time of 606 s). As expected, the peak temperatures at the more in-depth thermocouples are both lower and occur later than the results found at the less deep thermocouples above it. This is due to the insulative properties of PICA and shows that reradiation rejects most of the heat. Also, after about 400 seconds, the temperature found throughout the PICA ply reaches a steady-state of about 500 K, \pm 28 K.

The mass loss rates are important in determining the physical effects of ablation and pyrolysis gas formation on the heatshield. Through ablation, the Galileo forebody heatshield lost approximately 79 kg from its 337 kg entry mass, a 23% reduction in mass.⁷⁶ Pyrolysis gas losses added approximately 1.5 kg of mass loss for the Galileo probe. For the SRC preliminary trajectory reentry, in equilibrium, the max char ablation rate is about 0.080 kg/m²s and occurs around 55 seconds into the trajectory. The max char ablation rate occurs around the period of the most intense heating as the heating drives the charring. The max pyrolysis gas rate is roughly 0.0078 kg/m²s and is on the order of 10 times less than the char ablation rate. A side-by-side comparison of the various blowing rates can be found in Fig. 3.4.

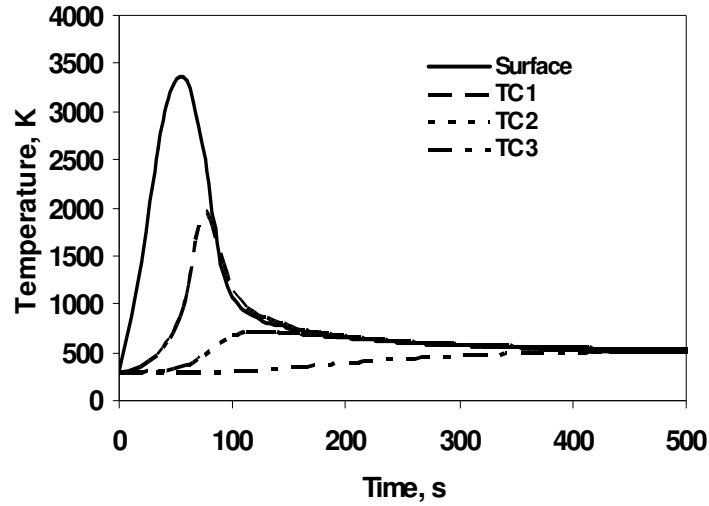


Figure 3.3. The equilibrium temperature profile for the preliminary SRC equilibrium trajectory.

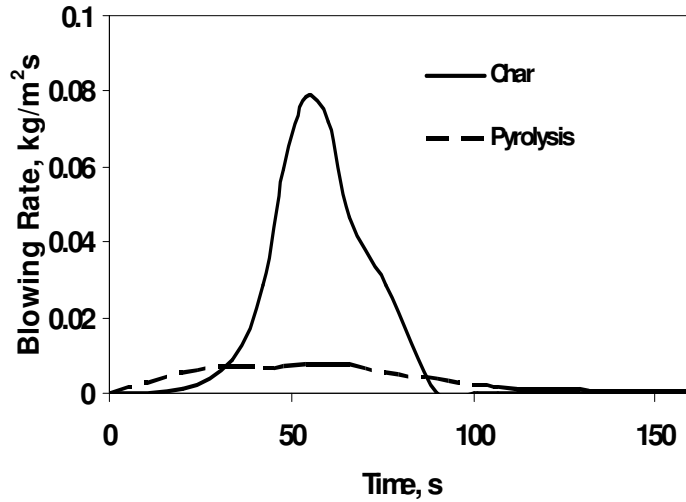


Figure 3.4. The mass loss profile for the preliminary SRC equilibrium trajectory

Olynick et al.¹⁰ found very similar ablation rates with the pyrolysis gas only making up a small portion of the total rate. The total surface recession is 1.12 cm or about one-fifth of the original thickness (6.1 cm). The majority of virgin material mass loss occurs due to char ablation and not pyrolysis gas conversion for a PICA

material. This is similar to how the majority of the mass loss was due to ablation in the Galileo probe.⁷⁶ Since there is no mechanical failure assumed for the preliminary trajectory, the recession is driven by char loss alone.

A total heat load is the time-independent effects of heating. It measures how much heating was on the surface due to each heating source. The maximum total heat load experienced by a PICA Stardust aeroshell is 30000 J/cm^2 . The material reaches this value at roughly 200 seconds and remains there for the duration of the analysis, as shown in Fig. 3.5. Once again, the convective heat effects are the main contribution to the total heat loads, as the effects from the radiative process only contribute a minor percentage beginning after 50 seconds. The convective heat load plateaus at about 28000 J/cm^2 while the radiative heat load remains at or around 2000 J/cm^2 . The radiative heat load only contributes 6.4% of the total heat load. This low contribution from the radiative properties (for both heat load and heat flux) for Stardust application was discussed by Chen and Milos in their works concerning FIAT.¹¹ The heat loads reach their peak values near the end of the heat pulse, after which the heat loads remain constant, due to no more heating occurring on the surface. The integrated heat load experienced by the Space Shuttle¹⁰ during its heat pulse is similar in magnitude; the Shuttle heat pulse lasts 20 times longer than the heat pulse in the preliminary design trajectory. Despite the preliminary design trajectory lasting 750 seconds, the most intense heating occurs quickly and earlier in the trajectory. Though it has higher heating at the stagnation point, the SRC's heat pulse length is less than both the Shuttle and Viking pulses so it will experience higher heating but have similar long term heating effects to the Shuttle.

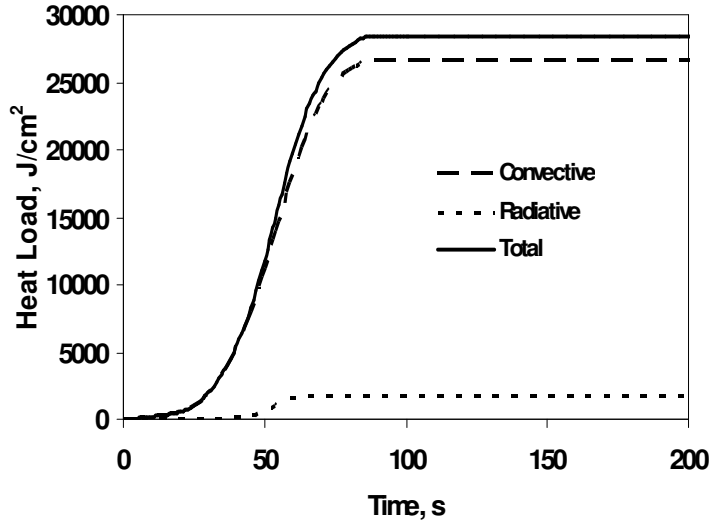


Figure 3.5. The heat load profile for the preliminary SRC equilibrium trajectory

3.1.2 Nonequilibrium

For the preliminary trajectory analysis, element mass is needed to calculate the mean molecular speed, \bar{v} . The density of the species is readily available from the species partial pressure using the equation of state, hence, the mass can be found with an assumption concerning the volume. This assumption should be such that the char and pyrolysis rate calculations are comparable in the magnitude of previous blowing rates. Using Milos and Chen's work⁹ applying Park's model to the peak heating condition as a benchmark, the nonequilibrium blowing rate calculated by MAT should be on the order of 10^{-2} . Table 3.1 shows how different volumes affect the blowing rate. As the volume decreases, the species are grouped more tightly together, causing them to interact more and increase the char and pyrolysis rates on the surface. Although outliers much smaller than the lower bound of each range appear, they

either occur in nonablating conditions not considered by FIAT or in high pressure conditions that the Stardust reentry does not experience.

Table 3.1. The effects of varying the volume assumption on the charring rate in MAT in the use of the Park Model.

Volume (kg/m³)	Charring Rate Range (kg/m²s)
1.00E-03	1.00E-14 – 1.00E-12
1.00E-06	1.00E-13 – 1.00E-11
1.00E-09	1.00E-12 – 1.00E-10
1.00E-12	1.00E-11 – 1.00E-09
1.00E-15	1.00E-08 – 1.00E-06
1.00E-18	1.00E-07 – 1.00E-05
1.00E-21	1.00E-06 – 1.00E-04
1.00E-24	1.00E-03 – 1.00E-01

A volume assumption around a magnitude of 10^{-24} kg/m³ will allow the char blowing rate to be similar in magnitude to the total blowing rate found by Ref. 9, where it is assumed that the char blowing rate will make up the majority of the total rate. A volume of 10^{-23} kg/m³ is chosen to avoid blowing rates larger in magnitude than the published results. The element carbon is used in all four reactions that Park takes under consideration and hence will have the largest mass flux associated with it. From MAT, as the reaction rate of carbon increased, so did the temperature and enthalpies associated with that particular pressure and pyrolysis gas rate. Hydrogen is not used at all in either surface-kinetics reaction model and will have its mass flux set to zero.

Along with the calculation of a new char ablation rate which will directly impact the recession rate, the addition of the finite-rate equations in the MAT affects the construction of the B' table by varying two key parameters. Table 3.2 is an example of the general pressures and char and pyrolysis rates used in the preliminary trajectory analysis. For the same general pressure, user-defined B'_g and B'_c , the table

will have new values of temperature and enthalpy due to the nonequilibrium assumption. The nonequilibrium dimensionless mass flux of carbon is added as an additional input to FIAT. For the preliminary trajectory, the char blowing rate due to finite-rate reactions (Eq. 2.17) is nondimensionlized by the heat transfer coefficient at the peak heating point for equilibrium. When nonequilibrium conditions want to be examined in FIAT, this new input will be used as the B'_c value, replacing the assumed general char blowing rates that are user-defined in MAT.

Table 3.2. The general pressure, B'_g , and B'_c values used to construct the B' table.

Pressure (atm)	B'_g	B'_c
0.43	10	100
0.1	2.5	20
0.05	1	5
0.01	0.25	0.5
0.005	0.01	0.4
0.001	0.001	0.3
	0.0001	0.2
		0.1
		0.01
		0.001
		0.0001

It is lower than the equilibrium rate because there will not be enough “time” in a finite-rate approximation for char to fully occur. In modeling the material response, the wall enthalpy is the difference between the enthalpy that is delivered to the wall from the traveling of pyrolysis and char mass and the enthalpy that comes from the chemical reactions on the surface:

$$h_{w_{new}} = B'_g(h_{gas} - h_{w_{old}}) + B'_c(h_{char} - h_{w_{old}}) - h_{w_{old}} \quad (3.1)$$

where B'_g is same general value used in both equilibrium and nonequilibrium cases but B'_c differs between the two cases along with h_{wold} (which is the enthalpy from the surface chemistry).

Milos and Chen studied the effect of finite-rate nitridation in their use of the Park Finite-Rate Model.⁹ In the present work, the same approach is taken and incorporated into MAT such that the full Park Finite-Rate model is examined along with sets that do not include one or more reactions. The removal of any of the reactions in the model is essentially assuming that the particular reaction under consideration fully reacts in the timespace and does not need to be specifically calculated when finite-rate reactions are applied. The removal of a reaction allows MAT to calculate that reaction as it would do in equilibrium. The first reaction studied is that of nitridation and will be removed for the reaction set.

Nonequilibrium surface interactions are applied to the entire trajectory; however, though nonequilibrium may only occur during certain sections of the trajectory based on the conditions. Temperature, as found in Figs. 3.6 and 3.7, remains relative close to equilibrium conditions. In the model that includes nitridation, the surface temperature decreases from a peak of 3370 K at 54 seconds to a peak of 3150 K at the same time, a change of 6.5%. Without nitridation, the peak is 3140 K, also at 54 seconds. When peak values are occurring at 54 seconds in the trajectory, which is concurrent with the prediction of peak heating at that time. During the heat pulse, the backface temperature remains around 300 K; the craft experiences temperatures near its initial temperature. The greatest change is at a depth of 1.27 cm, where the temperature decreases to a peak of 1380 K from the

equilibrium peak of 1970 K which occurs three seconds earlier. This is a 30% change. Due to this large decrease, there is a 10% decrease in peak temperature at the thermocouple prediction that is more in-depth, at 2.54 cm, from 716 K to 644 K. The backface temperature sees a decrease of only 0.58%, from 516 K to 513 K for both the reaction set that includes nitridation and the set that does not. Despite changes in surface and in-depth temperatures, the backface temperature reaches a similar steady-state temperature in both equilibrium and nonequilibrium, showing the insulative properties of PICA.

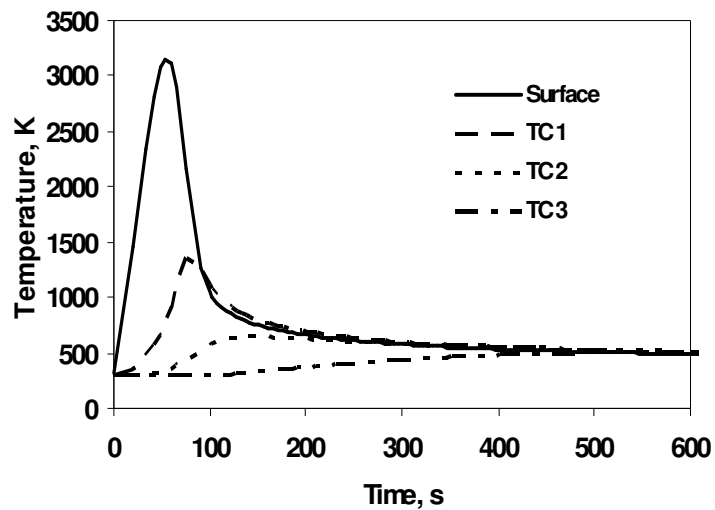


Figure 3.6. Temperature profile for the preliminary SRC trajectory using Park's Model with nitridation.

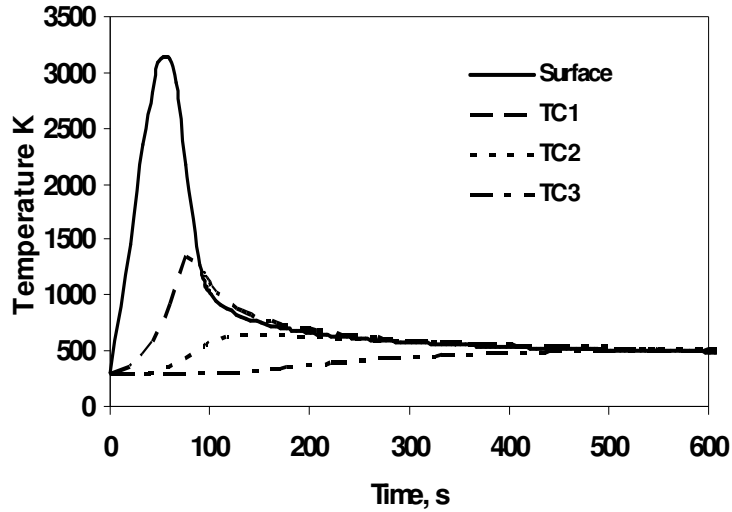


Figure 3.7. Temperature profile for the preliminary SRC trajectory using Park's Model without nitridation.

The total ablation rate, which may also be referred to as the total surface blowing rate, directly affects the recession rate as it contains the charring rate, which is calculated from the Park Model. Figures 3.8 and 3.9 show the char rate for nitridation and without nitridation, respectively, for Park's model compared to the equilibrium case. The rate at which char ablation occurs is much less for the nonequilibrium case. Figure 3.10 compares the nitridation charring to the charring found in the non-nitridation case. They are about the same, and a deeper look at the B' tables constructed for nitridation and without nitridation shows that nitridation does not greatly affect the carbon mass flux. At its peak char rate nitridation causes a loss of char at $0.053 \text{ kg/m}^2\text{s}$, while without nitridation, the loss is also roughly $0.053 \text{ kg/m}^2\text{s}$. This is a decrease of 34% from the peak char rate in equilibrium. Since the cases for nitridation and without nitridation do not differ from each other by more than a few percentage points, nitridation is not a key contributor to the Park model

under Stardust-like conditions and when the Modified Park Model is referred to in the following sections, it will be in reference to the results of the full reaction set unless otherwise noted. The negligible difference between the predictions when nitridation is accounted for and when it is not may be explained by Ref. 77; Goldstein showed that CN did not form around ablating graphite concluding that nitridation can be considered as not occurring. Instead of nitridation happening by itself, it is likely that the CN molecules undergo an exchange reaction with nitrogen atoms and produce nitrogen and carbon. Carbon may then be condensed back into the wall. This set of secondary reactions is equivalent to a nitrogen surface catalytic process which eliminates the assumption of nitridation.

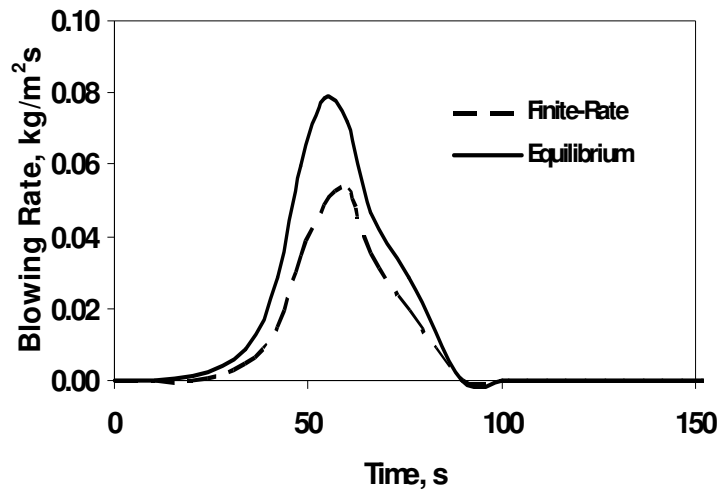


Figure 3.8. The char ablation rate for the preliminary SRC trajectory using Park's Model with nitridation

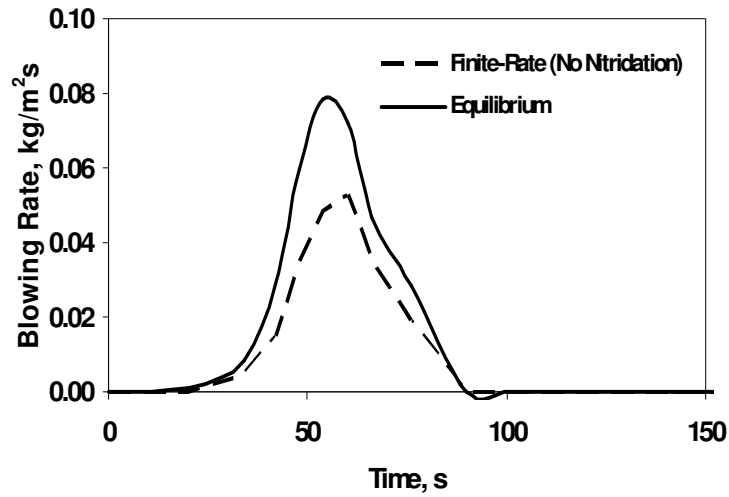


Figure 3.9. The char ablation rate for the preliminary SRC trajectory using Park's Model without nitridation.

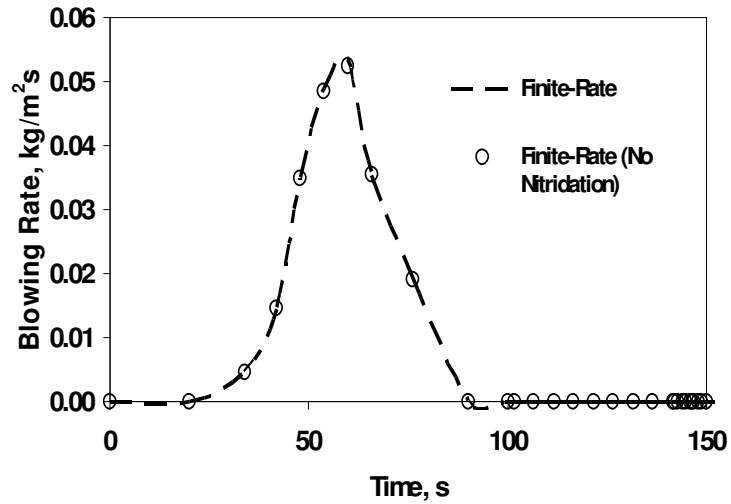


Figure 3.10. A side-by-side comparison of the char ablation rate for the preliminary SRC trajectory for both subcases of Park's model.

Like the char ablation rate, the pyrolysis gas rate also decreases between the equilibrium and nonequilibrium assumption (Fig. 3.11). Where in the equilibrium a peak gas rate of $0.0078 \text{ kg/m}^2\text{s}$ is reached at 60 s, the use of the Park model has the

peak occurring earlier, at roughly 29 seconds. The peak is reduced to $0.0064 \text{ kg/m}^2\text{s}$. Because there is less heating on the surface, less of it enters the material and drives down the rate at which pyrolysis forms, driving its peak value downwards and when it occurs earlier in the trajectory. Since the change in the char ablation rate is greater than the change in the pyrolysis gas rate in terms of relative magnitude and absolute magnitude, it can be concluded that a finite-rate approximation of reactions on the surface affect the formation of char more than the formation of pyrolysis. Charring can occur closer to the surface than pyrolysis formation and is directly affected by surface interactions.

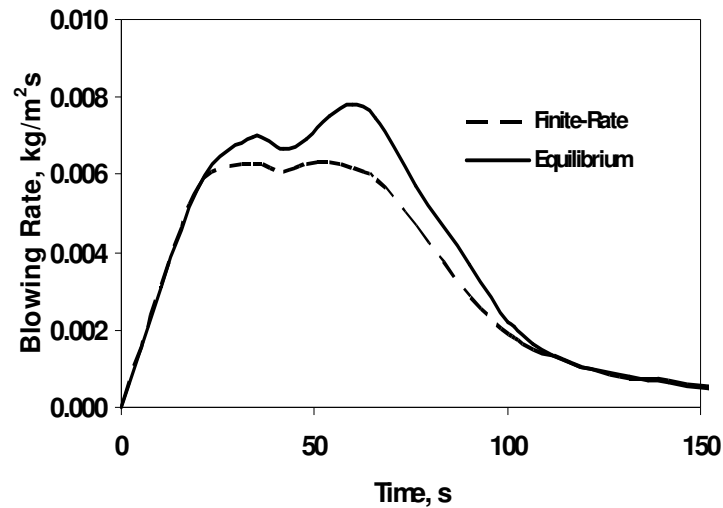


Figure 3.11. The pyrolysis gas rate for the equilibrium and Park models for the preliminary SRC trajectory.

The total ablation rate for both chemical cases is shown in Fig. 3.12. The peak blowing rate for equilibrium has a value of $0.088 \text{ kg/m}^2\text{s}$ at peak heating while for the Park Model, the peak occurs slightly after peak heating with a decrease of 33% to a value of $0.059 \text{ kg/m}^2\text{s}$. The peak total surface blowing rate happens when the char

ablation rate is the highest and the char rate is the largest contributor in both cases. This emphasizes the importance of the char in the material response modeling.

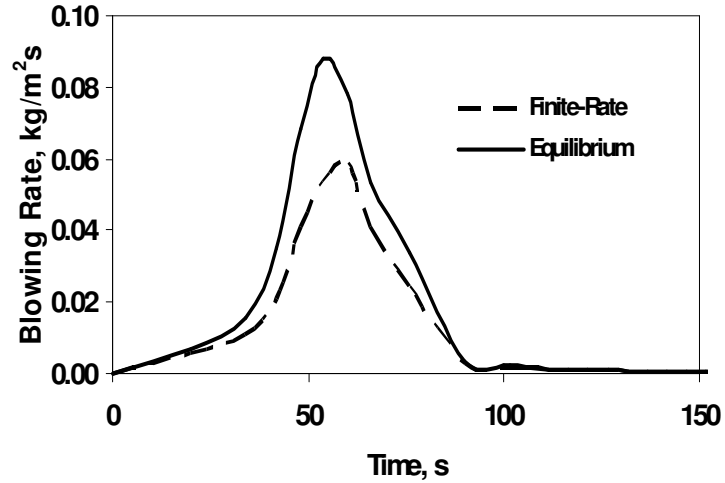


Figure 3.12. The total surface blowing rate for the equilibrium and Park models for the preliminary SRC trajectory.

Recall Eq. 2.8:

$$\frac{C_H}{C_{H1}} = \frac{2\lambda B'}{e^{(2\lambda B')} - 1} = \frac{\ln(1 + 2\lambda B')}{2\lambda B'} \quad (2.8)$$

Since Eq. 2.8 depends on the total ablation rate, B' , then the net convective heat flux also depends on the total surface blowing rate since it is calculated from the corrected heat transfer coefficient. If B' decreases, the ratio C_H/C_{H1} increases and there will be an increase in the blown transfer coefficient. If the other parameters remain constant, then the net convective heat flux will increase, causing an increase in heating on the surface. The craft will encounter higher heating due to the nonequilibrium decrease of the mass blowing rate and leaving less mass around the surface to absorb the heat. However, the enthalpy at the wall is not constant between

the equilibrium and nonequilibrium cases and is greater due to the increase in mole fractions of contributors of enthalpy at the wall, counteracting the increase in the corrected blown coefficient. There is actually a decrease in the net convective heat flux between the equilibrium and nonequilibrium cases, which is seen in Fig. 3.13.

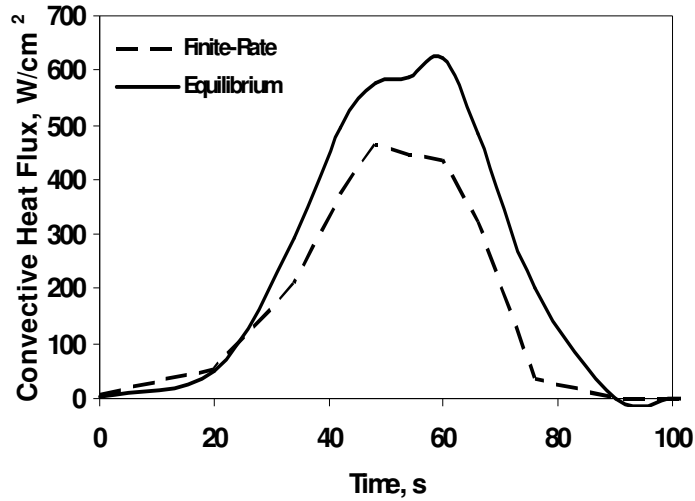


Figure 3.13. The convective heat flux for the equilibrium and Park models for the preliminary SRC trajectory.

The radiative heat flux remains the same between the equilibrium and nonequilibrium cases, as the only change involves the chemical reactions. The maximum net convective heat flux using finite-rate reactions occurs at an earlier time of 48 s and decreases to 460 W/cm². The maximum total heat flux encountered in the Park Model encountered at 48 s as well and is 580 W/cm². This is a decrease of approximately 20% from the equilibrium set of reactions. Although the blowing rate decreased nearly 40% between the two general cases, the maximum net heat flux did not match the magnitude of change, as it only decreased by half that rate. The presence of wall enthalpy makes the relationship between total ablation rate and

convective heat flux more complex than a simple direct correlation. The decrease in the heat fluxes leads to a decrease in the convective heat load and the total heat load encountered by the PICA material (Fig. 3.14).

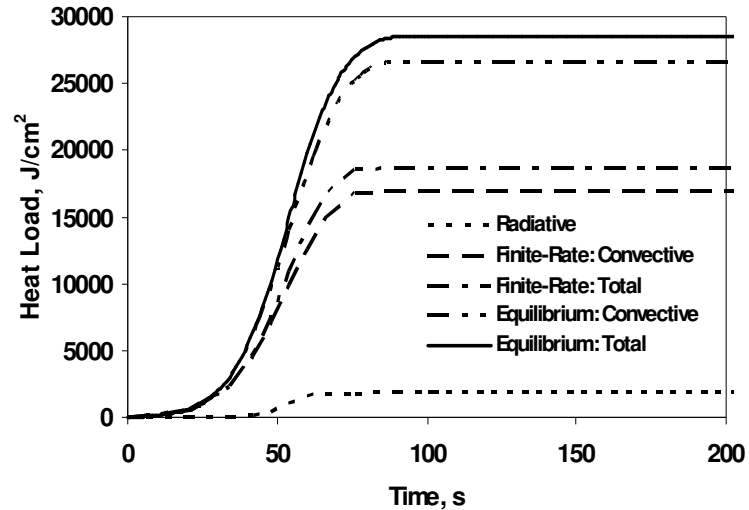


Figure 3.14. The heat loads for the equilibrium case and Park Model for the preliminary SRC trajectory.

The maximum total heat load experienced is 19 kJ/cm^2 , a decrease of 32% from the equilibrium case, and is once again reached after the end of the heat pulse. The radiative heat load now contributes roughly 9.7% of the total heat load, up from 6.4% in the equilibrium case. The result of chemical reactions not achieving equilibrium cause the radiative effects to become more important as convection is decreased and the radiation stays the same.

The lower total ablation rate leads to a decrease the surface recession. Because there is less mass being loss due to charring, not as much of the PICA material will ablate (Fig. 3.15). The surface recession is reduced from 1.1 cm to 0.72 cm for both the nitridation and non-nitridation case. The nonequilibrium recession is a reduction

of 36% of the equilibrium case. Because of the calculated rate of the char is decreased when Park's Model is implemented at the surface in the construction of B' tables for FIAT, other key parameters change, which in turn reduces the recession. The char mass flux has been identified as an important parameter.

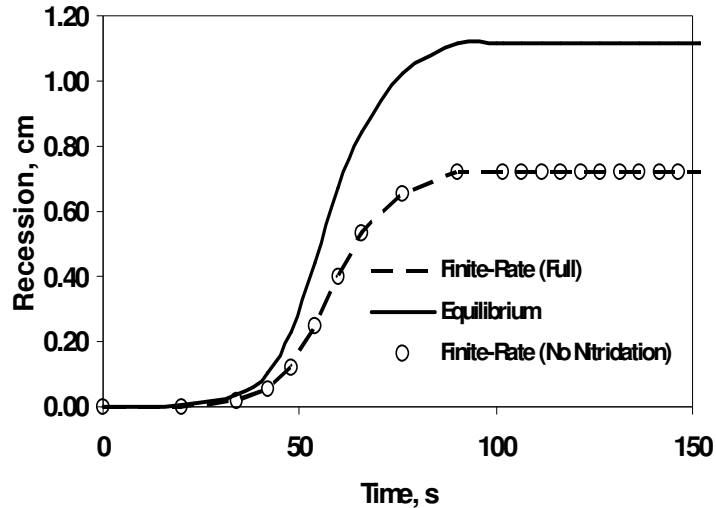


Figure 3.15. The recession for the equilibrium case and the Park Model, with and without the nitridation reaction, for the preliminary SRC trajectory.

Since the Park Model only involves four reactions, it is easy to isolate one or more reactions to study the effects of chemical process. Nitridation has already been studied. At low heat fluxes, the primary reaction that causes char recession is the diffusion-limited oxidation reaction involving O_2 (Equation 2.14).⁷⁸ To examine whether or not the importance of this reaction holds during the conditions predicted to be encountered by the SRC, it is removed from the Park Model, along with the nitridation reaction, to simulate these reactions as occurring in equilibrium during a finite-rate process. Nitridation is removed because it was previously seen not to cause a significant difference in the nonequilibrium results and its elimination would help further emphasize the remaining reactions' roles in the analysis.

Figure 3.16 shows the temperature profile of a nonequilibrium assumption without the inclusion of nitridation or diffusion-limited oxidation. The peak temperature on the surface is 3150 K, reached at 54 seconds, which is 10 K more than what is experienced in the absence of only nitridation. Concerning the temperatures, the change from equilibrium to nonequilibrium had the biggest impact on the conditions felt at the depth of 1.27 cm. In the case where diffusion-limited oxidation and nitridation is absent, the peak at that depth is 1380 K. This is the same temperature reached with and without nitridation, which is still a 30% decrease from the equilibrium temperature. The temperature experienced on the backface during the heat pulse still reaches 300 K. Overall, the temperature profile for the diffusion-limited oxidation and nitridation absent chemical reaction set does not differ greatly from the profile seen when nitridation and diffusion-limited oxidation are included. This trend continues when comparing the char ablation, pyrolysis gas, and total ablation rates, as seen in Figs. 3.17-3.19. These rates are similar to those found when nitridation is considered and when only nitridation is eliminated. Similarly, there is only a 2% difference in the convective heat flux between a diffusion-controlled oxidation absent case and one where the Park Model is applied in full.

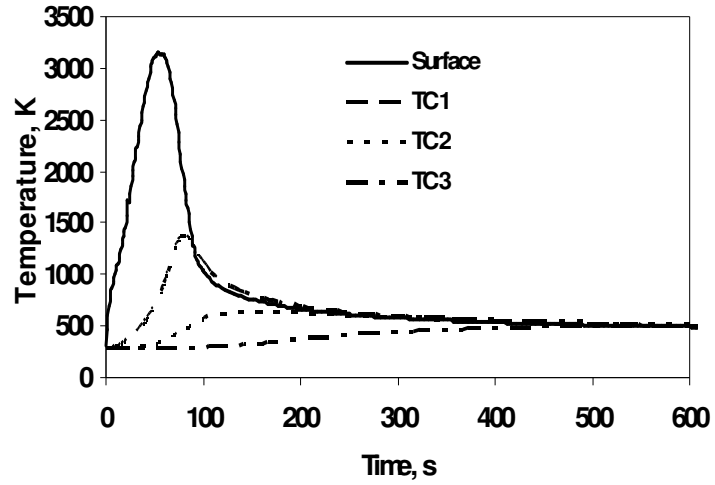


Figure 3.16. The temperature profile for a reaction set without diffusion-limited oxidation and nitridation for the preliminary SRC trajectory.

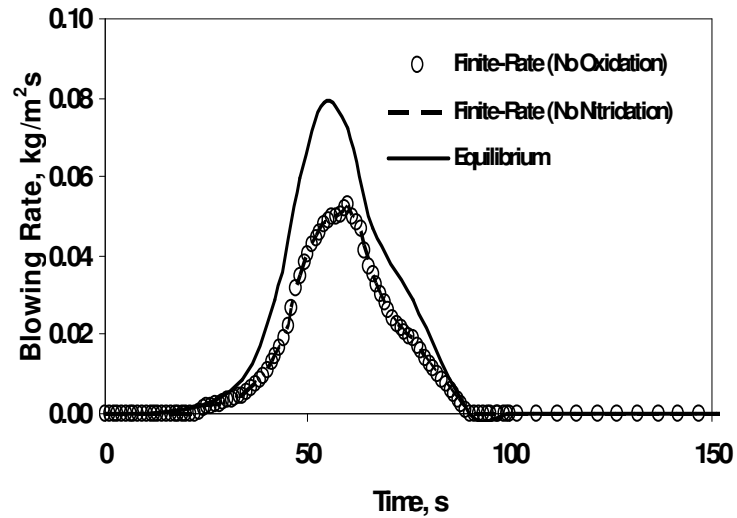


Figure 3.17. The char ablation rate for the reaction sets without diffusion-limited oxidation and nitridation and without nitridation only and for an equilibrium analysis for the preliminary SRC trajectory.

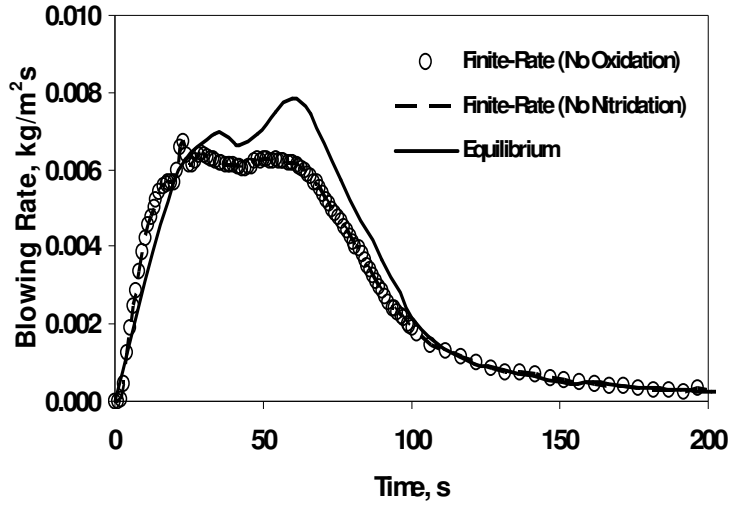


Figure 3.18. The pyrolysis gas rate for the reaction sets without diffusion-limited oxidation and nitridation and without nitridation only and for an equilibrium analysis for the preliminary SRC trajectory.

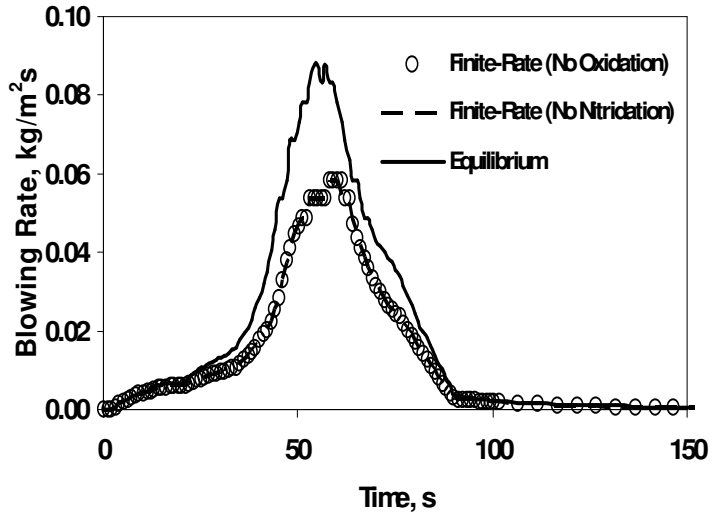


Figure 3.19. The total ablation rate for the reaction sets without diffusion-limited oxidation and nitridation and without nitridation only and for an equilibrium analysis for the preliminary SRC trajectory.

Due to the lack of any significant changes when diffusion-limited oxidation is eliminated from the reaction set, it cannot be said to be the most important reaction for nonequilibrium analysis of the Stardust Return Capsule although Covington⁴⁹

identified that at conditions similar to those found at SRC peak heating in an arc-jet test there is a present of diffusion-limited oxidation. However, those tests are run at constant heating and do not experience a heat pulse with different heating rates which changes how the material chars and what the material properties are at peak heating. Rate-limited oxidation is generally a significant driver of nonequilibrium flow if the temperature is less than 2000 K.⁷⁸ However, it is seen that for the SRC, the temperature quickly surpasses that boundary. A Park Model without rate-limited oxidation produces very similar results as for the Park Model without diffusion-limited oxidation, which is almost exactly the same as the Park Model without nitridation. Three out of the four reactions found in the Park Model do not greatly affect the nonequilibrium predictions. Over the entirety of the SRC trajectory, oxidation and nitridation do not play a large role in finite-rate calculations and can be considered as occurring in equilibrium. However, for completeness, they will remain in the Park Model.

Sublimation can be an important reaction if the temperatures encountered are high in magnitude, usually higher than 3000 K.⁷⁸ A very high resistance to boundary-layer diffusion when there is a low mass transfer coefficient will cause the sublimation rate to be controlled by that boundary-layer diffusion.⁷⁹ As the resistance to diffusion decreases, sublimation kinetics will begin to dominate and control the mass loss rate. A high surface temperature would be required to maintain a sublimation mass loss rate equivalent to the boundary-layer diffusion rate.

Sublimation, along with nitridation, will be removed from the Park Model reaction set, leaving only the two oxidation reactions to be considered finite-rate

reactions. Since, in equilibrium, the surface of the SRC experiences temperatures in excess of 3000 K for roughly 25 seconds, or $\frac{1}{4}$ of the heat pulse, the sublimation should be occurring in the SRC trajectory, though it is unknown if it will be an equilibrium reaction. There is a noticeable impact on the material response when sublimation is not included in the nonequilibrium reaction set. The high temperature activation of sublimation is represented in the Park Model by the use of current mass concentration and equilibrium mass concentration. To prevent negative mass loss such that the sublimation reaction would be occurring in reverse where C_3 is forming solid carbon, the sublimation reaction cannot occur below some set temperature where the equilibrium concentration is smaller than the actual concentration. Since sublimation cannot occur under certain conditions, it is expected that its absence will be felt once its threshold value is reached and it does not appear in the Park Model. Before that threshold value is reached, however, the removal of sublimation from finite-rate calculations should not have a significant impact.

Looking at the temperature profile (Fig. 3.20) the absence of sublimation is felt at the higher temperatures where sublimation is expected to occur. There is a sharp drop-off in the surface temperature around 54 seconds. A comparison to the previous chemical cases as seen in Fig. 3.21 shows that this drop happens more quickly and reaches a lower temperature than the prior analyses. However, the comparison also shows that the predictions made in the absence of sublimation do not greatly differ from the absence of nitridation before peak heating. At 54 seconds, the surface temperature is about 3000 K, the temperature threshold for sublimation. The final steady-state temperature that the surface eventually reaches for nonequilibrium

without sublimation is only between 20 K and 30 K less than for a full reaction set. These trends support the idea that finite-rate sublimation plays a large part in the reaction set during the time period where it would be activated, but below that activation temperature, there is little impact.

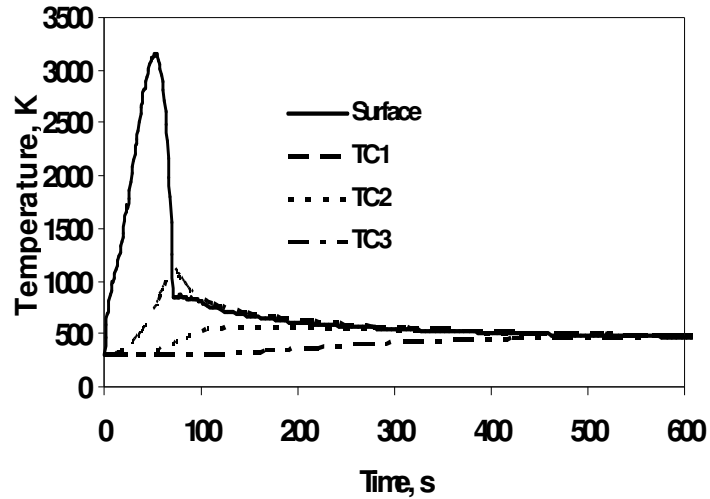


Figure 3.20. The temperature profile for the preliminary SRC trajectory without sublimation

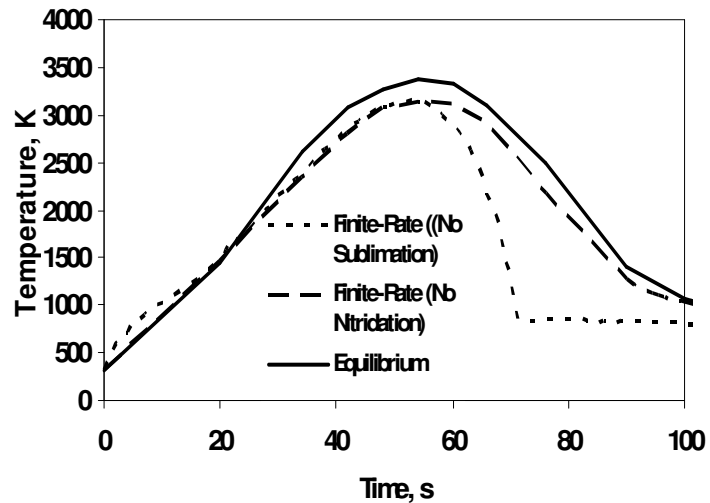


Figure 3.21. The surface temperature profile for the preliminary SRC trajectory for three surface conditions.

The predicted temperatures at the different thermocouples are intrinsically linked to the temperature on the surface due to the thermal conduction through the PICA material. It would be expected that a lower surface temperature would mean lower in-depth temperatures. Because of the drop in surface temperature when sublimation is eliminated, for nonequilibrium the peak temperature at a depth of 1.27 cm it is now 1120 K, a decrease of 19% from the nonequilibrium case and 43% from the equilibrium case. Table 3.3 lists the different temperatures encountered in equilibrium, nonequilibrium without nitridation and nonequilibrium without sublimation, for the various thermocouples depths. During the heat pulse, the backface peak temperature is still roughly 300 K, keeping the spacecraft near room temperature.

Table 3.3. A comparison of peak temperatures for different equilibrium and nonequilibrium cases for the preliminary SRC trajectory

Depth (cm)	Peak Temperature (K)		
	Equilibrium	No Nitridation	No Sublimation
Surface	3370	3140	3160
1.27	1970	1380	1110
2.54	720	640	570
5.08	530	510	480

The trends seen by the temperature profile show that the time after approximately 54 seconds, in the second half of the heat pulse, will be affected by the removal of sublimation. This is reflected by other predictions as well. The char ablation rate, as shown in Fig. 3.22, diverges from the previously found nonequilibrium results at 54 seconds. The char ablation rate at that time is 0.047 kg/m²s. It then decreases to 0.012 kg/m²s at roughly 70 seconds into the trajectory before rapidly decreasing to rates 10⁻⁴ to 10⁻³⁰ in magnitude. For both equilibrium and

non-nitridation nonequilibrium the char ablation rate does not reach that magnitude until after 90 seconds. The steep drop at 70 seconds corresponds to the surface temperature reaching a temporarily plateau after its decrease (Fig. 3.23).

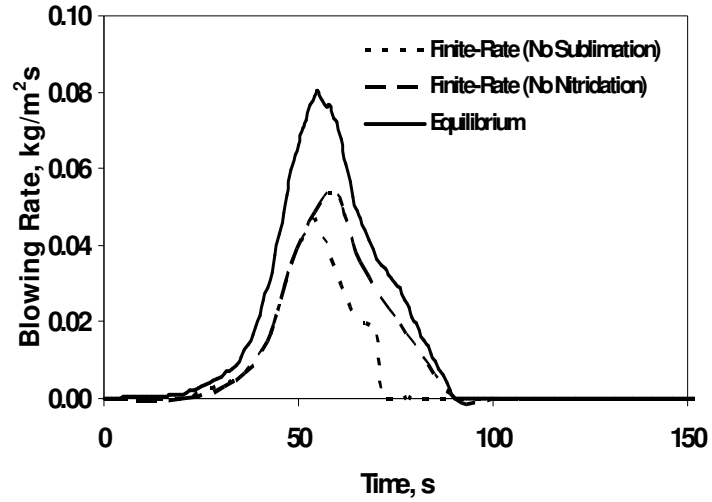


Figure 3.22. The char ablation rate for equilibrium, nonequilibrium without nitridation and nonequilibrium without nitridation and sublimation for the preliminary SRC trajectory.

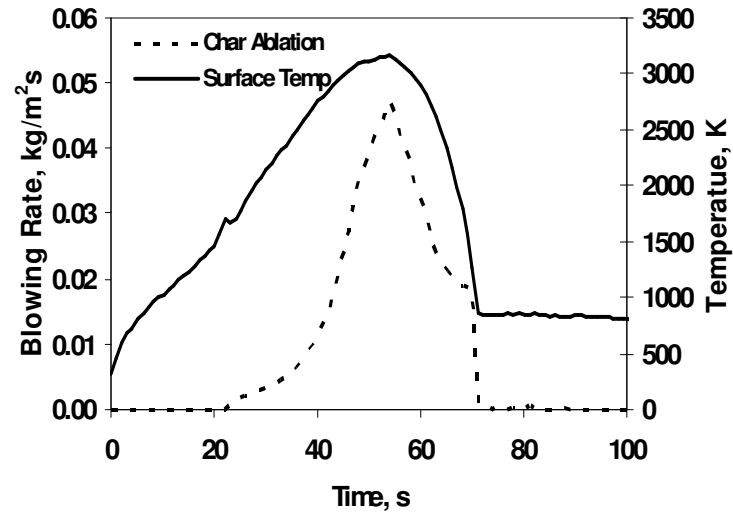


Figure 3.23. The general trends of the surface temperature and char ablation rate for nonequilibrium without sublimation for the preliminary SRC trajectory.

For the pyrolysis gas rate, the divergence between the nonequilibrium cases once again occurs at 54 seconds. There is, however, no abrupt drop like in the char ablation. The peak pyrolysis gas rate remains at $0.0063 \text{ kg/m}^2\text{s}$ at 29 s. Figure 3.24 illustrates that the pyrolysis gas rate follows the general development seen in the other cases, just at a lower rate after the divergence. In addition to not experiencing a sharp drop like the char ablation rate, the pyrolysis gas rate also remains within one magnitude less than the rate encountered in the non-nitridation case in the later time period.

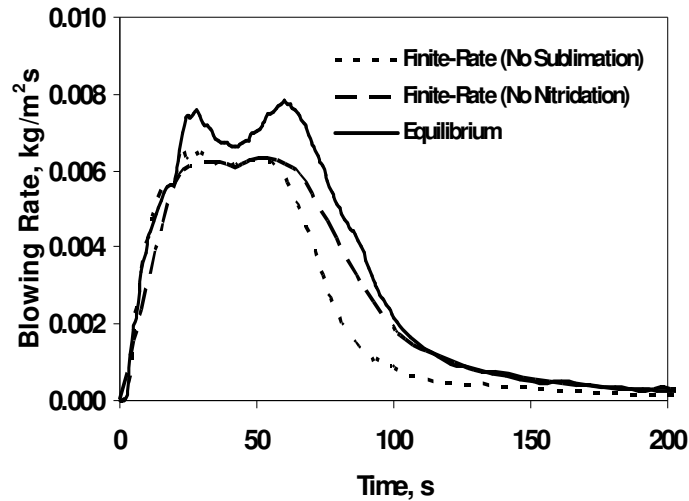


Figure 3.24. The pyrolysis gas rate for equilibrium and nonequilibrium without nitridation and nonequilibrium without nitridation and sublimation for the preliminary SRC trajectory.

When the char ablation rate and pyrolysis gas rate are combined in this case to calculate the total ablation rate (Fig. 3.25), the significance of the char ablation rate is once again seen. The char ablation rate, specifically the decline at 70 seconds, drives the total ablation rate to be dissimilar from the total rates earlier calculated. The peak total ablation is $0.054 \text{ kg/m}^2\text{s}$ compared to a rate $0.059 \text{ kg/m}^2\text{s}$ in the full Park Model

set. The total ablation rate before the decline at 70 seconds is $0.023 \text{ kg/m}^2\text{s}$. There is a minor effect of the pyrolysis gas on the total ablation: since it remains close to the non-nitridation nonequilibrium and equilibrium values in the later time period the gas formation drives the total ablation rate to be similar to the smaller ablation rates found in the equilibrium and other nonequilibrium cases.

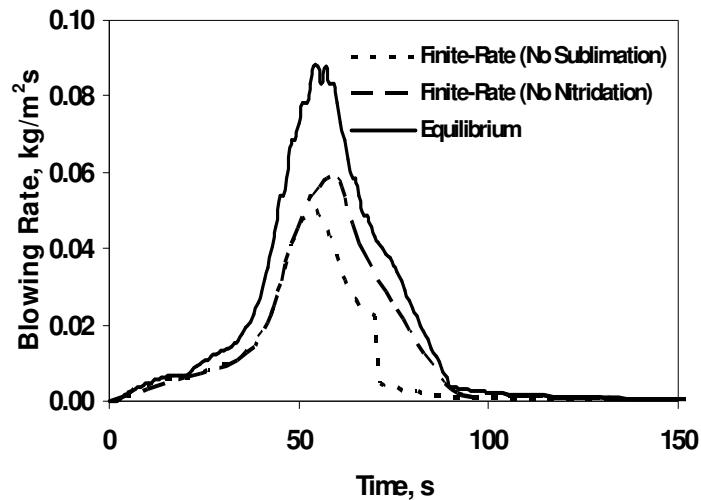


Figure 3.25. The total ablation rate for equilibrium and nonequilibrium without nitridation and nonequilibrium without nitridation and sublimation for the preliminary SRC trajectory.

The ablation rate results for the absence of sublimation shows that sublimation mainly causes the char layer formation at temperatures above 3000 K. This conclusion is drawn from the observation that the percent difference at the majority of points after 54 seconds is greater for the char ablation rate than the pyrolysis gas rate when compared previously nonequilibrium results. The greater impact on the char ablation predictions is due to sublimation being concerned with solid carbon, which is found in the material and tends to char. Sublimation does not have as a big an impact on pyrolysis because pyrolysis is a gas. Physically, since the PICA material is made

mainly of carbon, the lack of sublimation leaves carbon on the surface and there isn't as much char formation. This is reaffirmed when the recession is examined. Figure 3.26 shows that because sublimation is not being implemented when examining finite-rate reactions, after 54 seconds, there will be lower recession due to carbon remaining on the surface of the material. The new recession is 0.49 cm, a decrease of 32% from the absence of nitridation and a 55% decrease from the equilibrium case. Despite the sharp decrease seen at 70 seconds in the char rate for the sublimation-absent case, the only observable dissimilarity in recession trends between the three cases is the final recession value is reached slightly faster, about ten seconds earlier, in the sublimation-absent case due the charring has significantly slowed down.

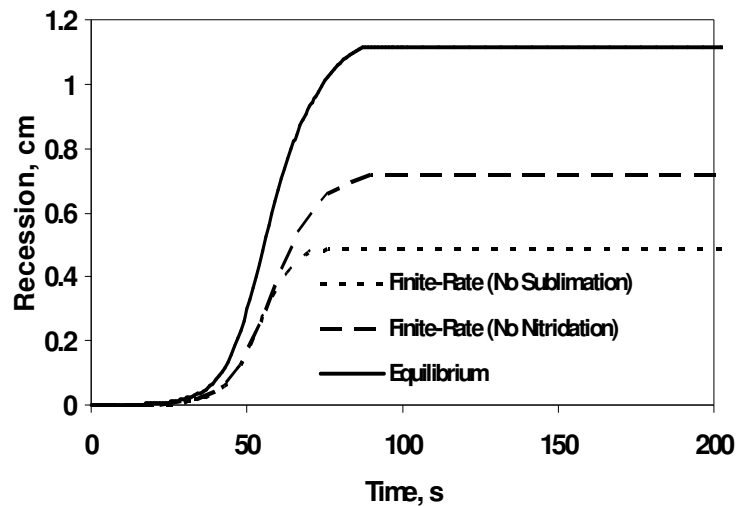


Figure 3.26. The recession profile for three finite-rate assumptions for the preliminary SRC trajectory.

Looking at the convective heat flux for the case where no sublimation occurs reveals another effect caused by the lack of sublimation. As seen in Fig. 3.27, the convective heat flux becomes mostly negative after 60 seconds. This means that the heat flux is convecting out of the material by high wall enthalpy. Additionally, there

are oscillations in the convective heat flux beginning at 76 seconds and ending at 90 seconds. The greatest oscillation is between -310 W/cm^2 and 270 W/cm^2 , which is the first oscillation. Figure 3.28 compares the wall enthalpy for equilibrium, nonequilibrium without nitridation, and nonequilibrium without nitridation and sublimation. Sublimation is not properly accounted for at the surface and it affects the wall enthalpy, causing the wall enthalpy to decrease due to less C_3 being in the mixture. Without finite-rate sublimation, the wall enthalpy remains nearly constant as there is no further depopulation of high enthalpy species. Because the wall enthalpy remains high but the recovery enthalpy decreases in the trajectory, their difference becomes smaller and eventually more negative. The enthalpy due to wall chemistry is high due to more species being present than what actually may be physically apparent while there is decreasing flow enthalpy. This changes the convective heat flux gradient from one that flows into the material to one that has heat flowing out.

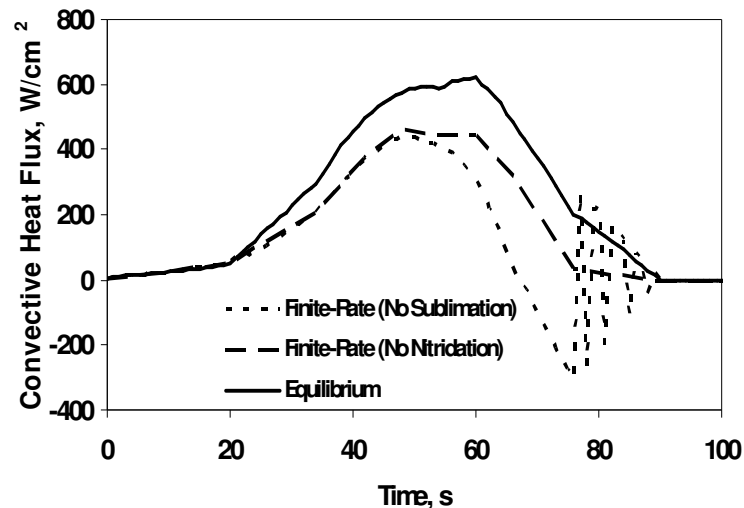


Figure 3.27. The convective heat fluxes for equilibrium, nonequilibrium without nitridation and nonequilibrium without nitridation and sublimation for the preliminary SRC trajectory.

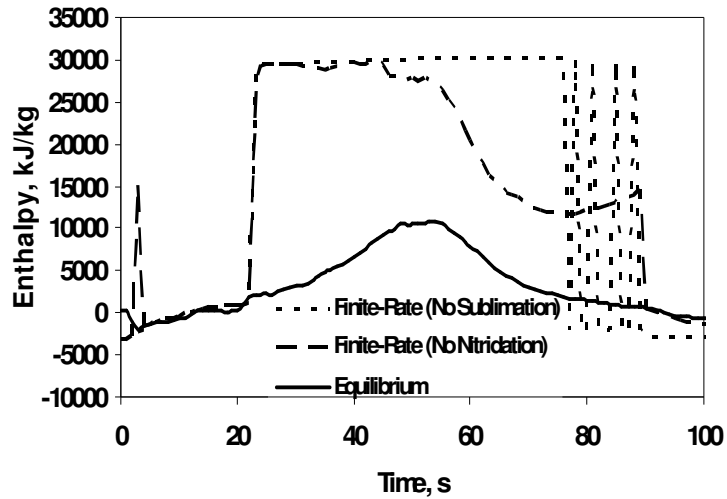


Figure 3.28. The wall enthalpy for the three cases under examination for the preliminary SRC trajectory.

The oscillations are generated due interpolation errors inherent in FIAT. Recall that at 70 seconds both the surface temperature and char rate see a sharp decline. FIAT calculates the char ablation and pyrolysis gas rates internally then goes to the B' tables to interpolate such parameters as wall enthalpy which is used to calculate the next time iteration's char and pyrolysis gas rates. The char rate calculated at 70 s will be much lower than what MAT calculates for the char rate at the pressure, pyrolysis gas, and temperature at that trajectory point. Resulting in interpolation error as FIAT will need to calculate a rate not found between any two points on the table. The oscillations get smaller as FIAT interpolates further to match data in the surface chemistry of the B' table. The oscillations end when the char ablation rate approaches the rates found previously in equilibrium and nonequilibrium, which are contained within the B' table, and do not have to interpolate outside of the table to follow the surface chemistry.

The quick decrease in the char ablation rate at 70 seconds also affects the blown transfer coefficient. Figure 3.29 shows that both nonequilibrium assumptions (without nitridation and without nitridation and sublimation) result in higher blown transfer coefficient than in equilibrium coefficient, with the sublimation-absent case resulting in the highest coefficients. This is due to less mass appearing around the surface as one takes into account nonequilibrium. Further examination of the blown transfer coefficient without sublimation shows that at 70 seconds, where the char ablation and total ablation rates decrease greatly, the coefficient goes from 0.186 to 0.193 $\text{kg/m}^2\text{-s}$, where as beforehand, the coefficient was steadily decreasing. This is due to a sudden decrease in mass that would be surrounding the surface, as char ablation is significantly decreased.

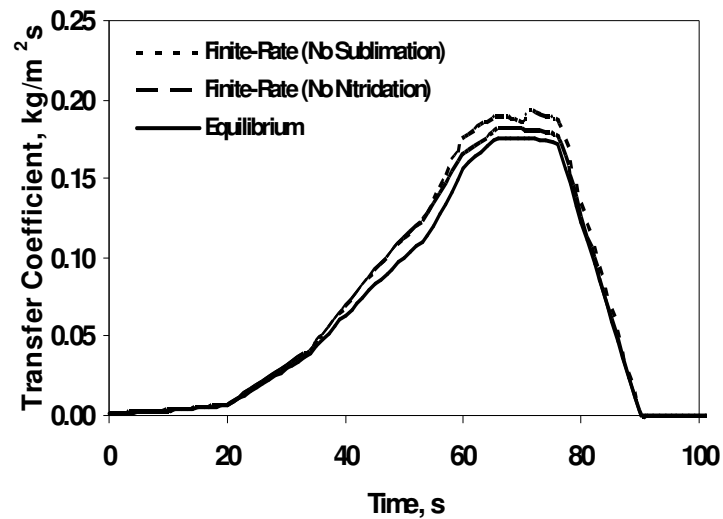


Figure 3.29. The blown transfer coefficient for equilibrium, nonequilibrium without nitridation, and nonequilibrium without nitridation and sublimation for the preliminary SRC trajectory.

The total heat flux at each trajectory point plus the convective and radiative heat fluxes are shown in Fig. 3.30. The peak total heating still occurs at 54 seconds

and is 550 W/cm^2 , which is 6.8% lower than the nonequilibrium case without nitridation and 25% less than the equilibrium case. Because of the presence of negative convective heat flux and near zero surface radiation, there is a negative total heat flux, -300 W/cm^2 , later in the trajectory. At this time, the environment is experiencing a heat flux from the surface. In all three unique cases (equilibrium, nonequilibrium without nitridation, and nonequilibrium without nitridation and sublimation), after 90 seconds, the convective, radiative, and total heat fluxes reach zero. This is due to the heat pulse ending at around the same time.

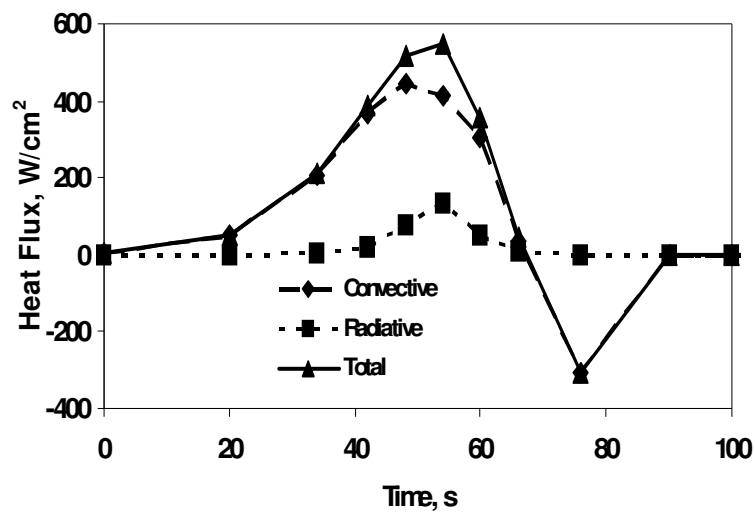


Figure 3.30. The heat fluxes when sublimation is not considered at each preliminary SRC trajectory point.

The large oscillations in the convective heat flux have minimal impact on the convective and total heat loads. Figure 3.31 shows the heat load profile. The convective heat load and total heat load both decrease in the time period of 70 to 82 seconds due to the negative convective heat flux between 60 and 90 seconds. Before the decline, the convective and total heat loads were closely following the previous nonequilibrium predictions. Due to the decrease, there is a maximum reached before

steady-state is achieved. The maximum convective and total heat load, respectively, are 13 kJ/cm^2 and 15 kJ/cm^2 at 66 seconds, each 4 kJ/cm^2 less than what was achieved in nonequilibrium without nitridation. They are around 50% less than what is experienced during equilibrium.

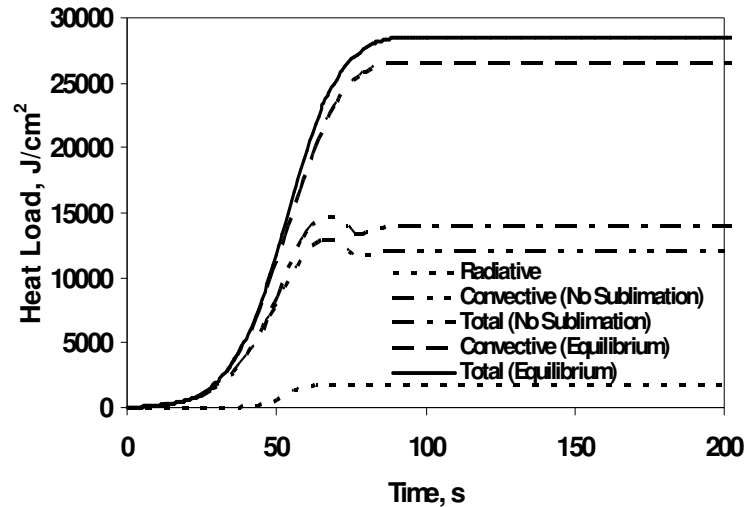


Figure 3.31. The heat loads for equilibrium and nonequilibrium without nitridation and sublimation for the preliminary SRC trajectory.

Due to the discrepancies seen in the absence of sublimation when compared to a full reaction set, it is concluded that sublimation is an important driver of the nonequilibrium reaction set. Its removal makes the development of nonequilibrium surface conditions behave in a nonphysical sense, with sudden drops in charring rates and temperatures not experienced in equilibrium. It was previously shown in the Apollo analysis that nonequilibrium and equilibrium surface conditions show comparable trends between the two cases and such characteristics of a greatly negative convective heat flux and sharp drops in char ablation and temperature do not occur.⁴ For trajectories dealing with the SRC, sublimation should be kept in finite-rate models.

3.2 Final Design Trajectory

A final design trajectory was developed and used in post-flight analysis of the Stardust Return Capsule.⁴³ The final design trajectory for the Stardust Return Capsule is shorter than the preliminary trajectory, only lasting for 133 seconds. However, there are more time points in the final design trajectory than the preliminary one, with enthalpy, pressure, and heat transfer coefficient predictions at every second of the design trajectory. The final trajectory does not include any radiation into the material.

In addition to an updated trajectory, the final design analysis includes an updated material database. The updated material database is an important change as it will dictate how the PICA material reacts to the new trajectory. For example, the preliminary trajectory used in conjunction with the new material database leads to a reduction in the recession prediction, meaning that the previous material database was more conservative in its properties relating to recession than the new database. The new database comes from more arc-jet data being collected for the PICA material. Due to International Traffic in Arms Regulations (ITAR), the differences between the two databases cannot be discussed any further. The preliminary trajectory analysis is run with the older material database due to previous research also using the older material database.^{10,11} Equation 3.2 is the surface energy balance equation used for analysis of the SRC final design trajectory:

$$C_H H_R + \dot{m}_g h_g + \dot{m}_c h_c - (\dot{m}_g + \dot{m}_c) h_w - \sigma \epsilon_w T_w^4 - q_{cond} = 0 \quad (3.2)$$

Figure 3.32 is a physical representation of the heat flux acting upon the surface of a material for this analysis. The heat flux due to charring is $\dot{m}_c h_c$, the heat flux due to

pyrolysis gas formation is $\dot{m}_g h_g$, and the heat of ablation, or the heat flux injected into the flow from the material response, is $(\dot{m}_g + \dot{m}_c)h_w$. Previous analysis ignored the contribution to the heating on the surface due to the chemistry and did not separate that heating flux into its char, pyrolysis, and injected terms. Since char has been shown to greatly affect the material properties and the recession of the PICA material, it cannot be ignored and alongside pyrolysis-driven heating (which has an effect both on the surface and in-depth) and the injected heat (which will effect the flow and possibly the amount of energy absorbed by the injected products), it is analyzed for the final design trajectory.

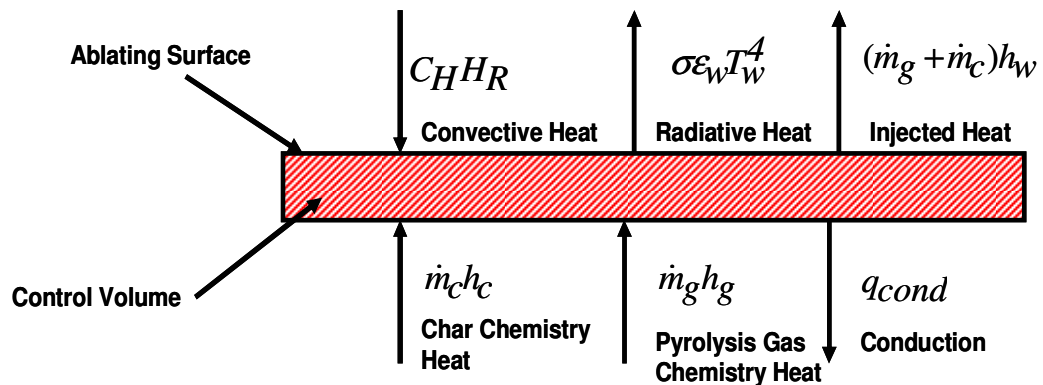


Figure 3.32 The heat flux terms acting upon the surface of a material.

There are no robust analyses of the individual chemistry terms or in-depth heating terms for the SRC in previous pre- or post-flight analysis. The internal energy balance equation, as defined in Section 2.2, is used in the final design trajectory analysis to examine the effects of conduction and pyrolysis gas formation. In addition, the complex process need to find the molecular mass in the molecular velocity equation in the Park Model (Eq. 2.18) is eliminated through the ideal gas law:

$$NkT = \frac{m}{M} R_u T \quad (3.3)$$

M is the molecular weight of the element being considered, m is its mass, R_u is the universal gas constant, and N is the number of element particles. An assumption still needs to be made for N , but it is a more direct assumption than using a volume assumption to find the mass; an assumption of 10^6 (or, the universal gas constant in terms of kJ or thousands of ft-lb and N being 1000) gets the charring rate to match the magnitude found by Ref. 9. Using this new equation for molecular velocity in the preliminary trajectory results in no significant discrepancy between results generated with a volume assumption and those generated with a particle assumption. Isolating the N term in the revised molecular velocity equation shows that it effectively becomes a constant coefficient term:

$$\bar{v} = \sqrt{N} \sqrt{\frac{R_u T_w}{2\pi M}} \quad (3.4)$$

Since N is not calculated within MAT and must be assumed, one can then restate the velocity equation as:

$$\bar{v} = C \sqrt{\frac{R_u T_w}{2\pi M}} \quad (3.5)$$

where C is some constant, that while is related to the number of particles in the system, is found and used as a scaling term to match previously published results (here, as found in Ref. 9). In the previous analysis, the volume assumption adds a level of complexity to the molecular velocity equation, as it needs partial pressures to arrive at the mass and is especially difficult to use when the derivative of the mass loss rate equations with respect to pressure and temperature is used in calculating the

change in error. The assumption of the number of particles in the system is directly involved in the velocity calculation, is not affected by temperature or pressure in this assumption, and does not change as the analysis changes the conditions. By revising the molecular velocity equation to include molecular weight and to eliminate molecular mass, the analysis is less prone to calculation errors due to less steps needed to find all the parameters in the equations.

The PICA heatshield in the final design trajectory is slightly thicker (5.82 cm) than the one used in the preliminary design trajectory (5.08 cm). Figure 3.33 is the layout of the final design heatshield. The final design trajectory predicts temperatures at three user-defined in-depth locations in the PICA material in addition to a surface temperature prediction. The depths of these predictions are 0.64, 1.91, 5.48 cm. There is also a user-defined temperature prediction located in the aluminum honeycomb. The initial surface and in-depth temperature is 253 K.

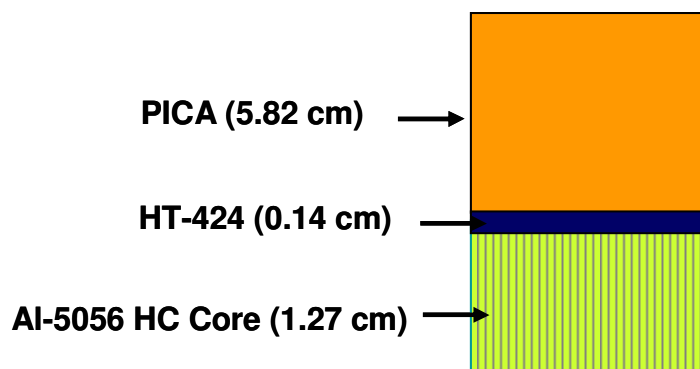


Figure 3.33. The heatshield material layout for the final design SRC trajectory analysis.

3.2.1 Stagnation Point – Entire Trajectory

At the stagnation point, the total heat flux between the two trajectories remain nearly the same (there is about a 6% difference of the total heat flux at 54 seconds, which was identified as the time of peak heating for the preliminary trajectory), but the cold wall convective heat flux for the final design trajectory is higher than that for the preliminary trajectory to compensate for the absence of radiation (Fig. 3.34). The final design trajectory's enthalpy can be up to 17% smaller than the preliminary trajectory's enthalpy, so the increase in cold wall convective heat flux is not due to the change in enthalpy, rather the increase is due to the increase in the heat transfer coefficient term (Fig. 3.35). While these changes will affect how the material responds in terms of recession rate, they should not affect the chemical processes; it is assumed that sublimation is still the driver of the reactions on the surface as the surface temperature will exceed 3000 K for some nontrivial amount of time. The peak pressure at the stagnation point is 0.37 atm (38 kPa), with the average pressure being 0.11 atm (11 kPa). Both of the pressure values are lower in the final design trajectory than in the preliminary design trajectory and with the heating remaining nearly the same there is a slightly increased chance of nonequilibrium based on molecular collisions.

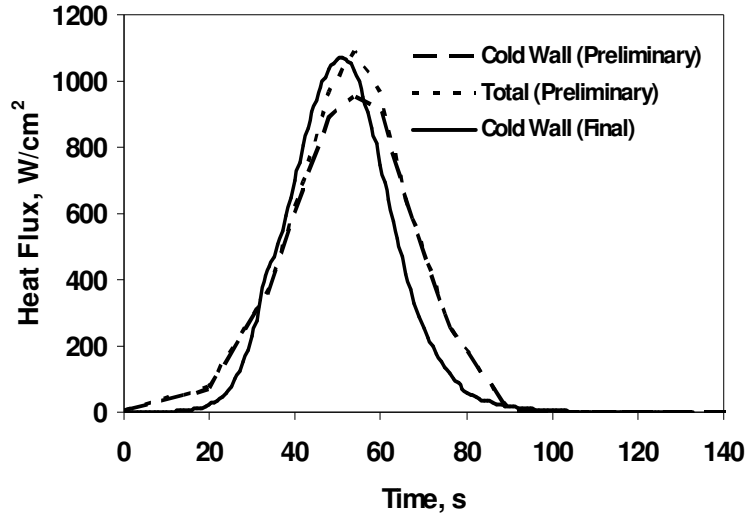


Figure 3.34. The environmental heat fluxes, not including radiation, at the stagnation point for the preliminary and final SRC trajectories and with the convective and total heat flux being the same for the final trajectory.

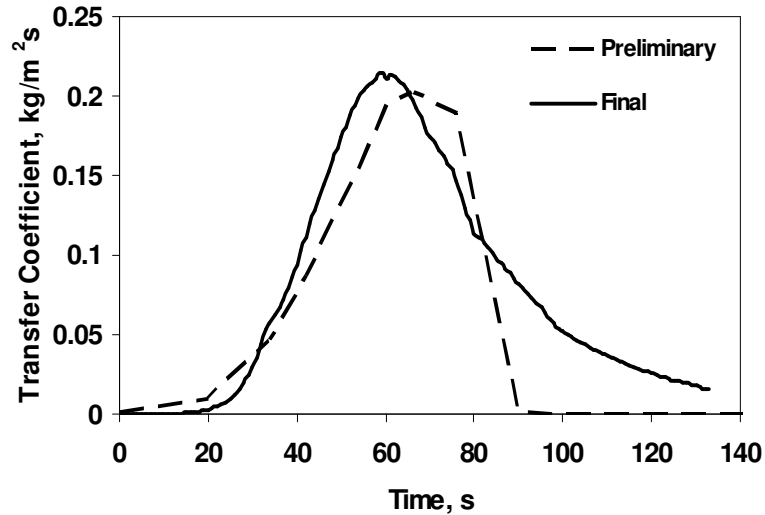


Figure 3.35. The heat transfer coefficient at the stagnation point for the preliminary and final SRC design trajectories.

The initial surface temperature of 253 K is 14% lower than the initial temperature in the preliminary analysis. Figure 3.36 is the predicted temperature

profile for the final trajectory when considering equilibrium. The peak predicted surface temperature remains 3370 K. At the first thermocouple depth (0.64 cm), the peak temperature is 2890 K at 64 seconds. After 64 seconds, there are no more predicted temperatures at that depth because the PICA material has ablated past that point. At the second thermocouple depth (1.91 cm), a peak of 694 K is reached near the end of the trajectory. At 5.48 cm, the peak temperature is 253 K, which is the starting temperature of the material. Likewise, at a depth of 6.80 cm, which is in the aluminum honeycomb, the temperature remains 253 K as well. This indicates that the PICA material insulation properties are such that after a certain depth the heating on the surface has a very small, almost nonexistent effect on temperature at that depth, at least for the heat pulse as defined in the final SRC trajectory.

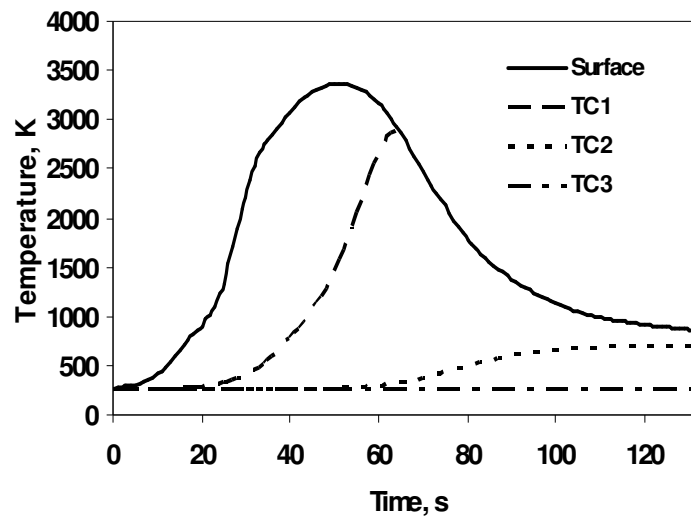


Figure 3.36. The temperature profile for the final design SRC trajectory.

There is a decrease in the amount of char loss from the PICA heatshield due to the changes in the trajectory. Figure 3.37 shows that while the peak char mass flux occurs at around the same time for both trajectories, the final design trajectory has a

peak char mass flux ($0.066 \text{ kg/m}^2\text{s}$) that is 20% lower than the one for the preliminary design trajectory. Conversely, Figure 3.38 shows that the pyrolysis gas fluxes reaches in the final design trajectory as much larger than the ones reach in the preliminary design trajectory, being almost twice as large, due in part to the larger heat transfer coefficient allowing for heat to travel to the surface and into the material. However, there is a bigger decrease in the char rate than the pyrolysis gas rate, and the total ablation for the final trajectory is less than that of the preliminary design trajectory (Fig. 3.39).

The total rate for the final design trajectory includes mechanical failure, which is any recession caused by melting or spallation of the heatshield. It is assumed in the final design trajectory that any mechanical failure is equal to 5% of the charring; there is not a large difference between the total ablation with and without failure added. Even with the additional consideration for failure, the peak total ablation ($0.081 \text{ kg/m}^2\text{s}$) in the final design trajectory is 7% smaller than the peak for the preliminary design trajectory. Since there is a decrease in the total charring rate, even when including fail, the total recession prediction for the final design trajectory will be less than the total recession prediction for the preliminary design trajectory. The recession for the final trajectory is 0.99 cm, a difference of 12% from the previous prediction of 1.12 cm.

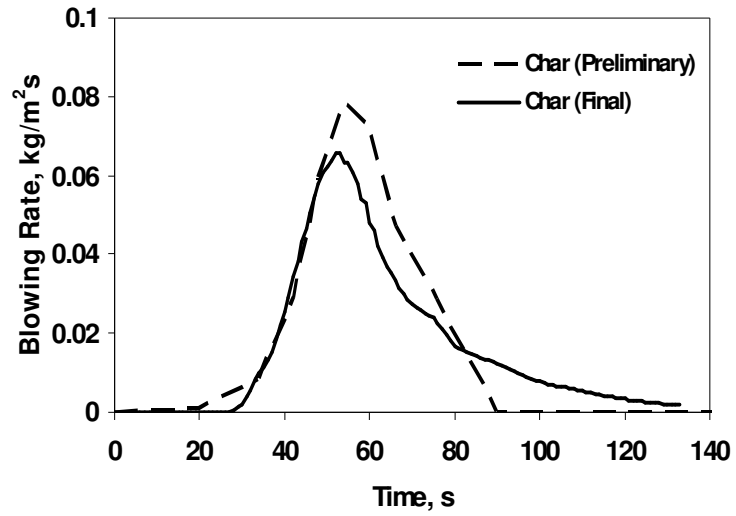


Figure 3.37. The predicted char rate profile for the preliminary and final design SRC trajectory.

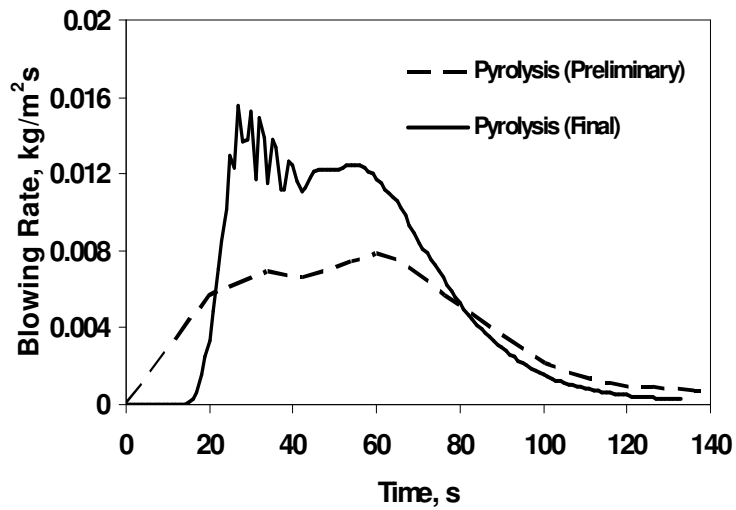


Figure 3.38. The predicted pyrolysis gas rate profile for the preliminary and final design SRC trajectory.

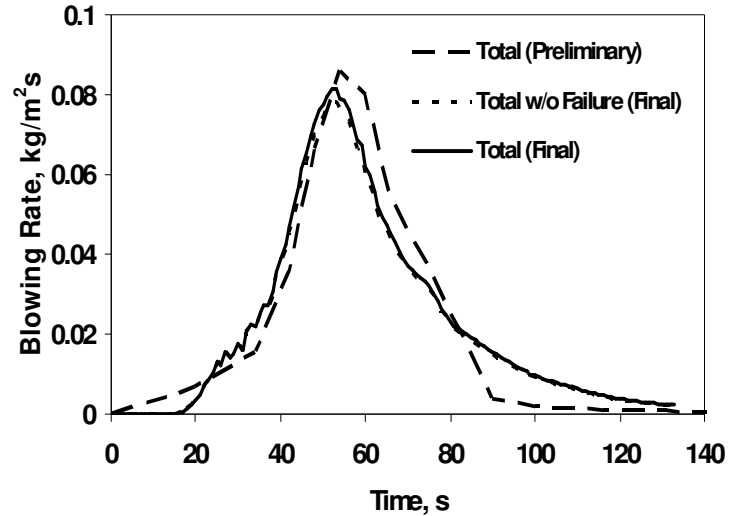


Figure 3.39. The predicted total ablation rate profile for the preliminary and final design SRC trajectory, with and without failure.

The heat fluxes acting upon the surface, and used in the surface energy balance equation, are seen in Figs. 3.40 and 3.41. Note that there is no wall enthalpy included in the calculation of the convective heat flux. While the preliminary trajectory convective heat flux output included the wall enthalpy, that output was created for the purposes of comparison with pre-flight analysis of Stardust¹⁰ using the preliminary trajectory. For the final design trajectory, the wall enthalpy is not used in the convective heat flux term because numerous Stardust Return Capsule post-flight reports^{13,45} leave the wall enthalpy out of their convective heat flux. The wall enthalpy contribution to convective heat flux is largely not used in this dissertation's analysis of the SRC so it could match the methodology of established models.

Due to the individualization of the chemistry heat fluxes in this dissertation, wall enthalpy is not totally ignored on the surface and is used to calculate the injected heat flux. Figure 3.41 isolates the terms that make up the general chemistry term seen

in the preliminary analysis and conduction. The heat fluxes that are negative in value are those that are being transferred away from the surface. For the surface to be considered in equilibrium from a heating standpoint, the amount of heat that enters the surface should also be leaving the surface. The majority of energy enters the surface through net convection and leaves the heatshield through particles radiating off of its surface. Table 3.4 contains the peak values for each terms at the time at which the peak occurs.

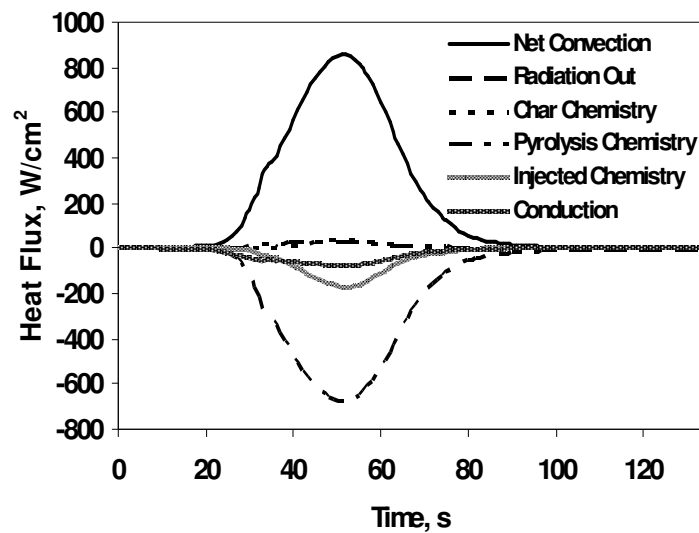


Figure 3.40. The predicted heating profile, including chemistry terms, for the final design SRC trajectory.

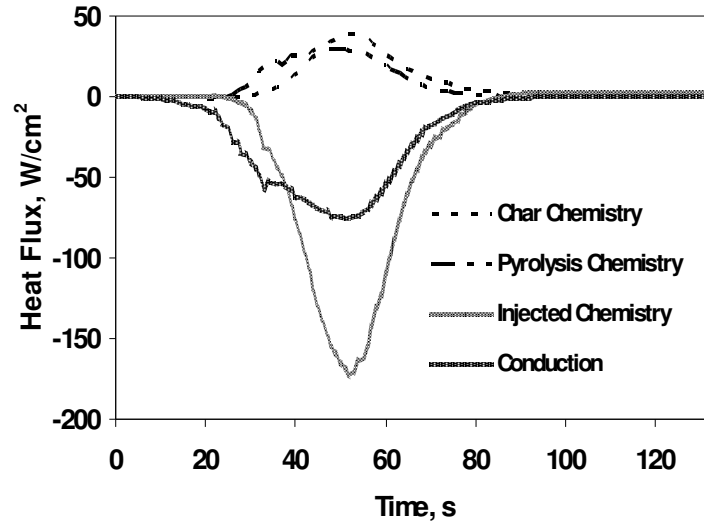


Figure 3.41. The predicted heating profile only considering chemistry terms and conduction for the final design SRC trajectory.

Table 3.4. The peak values of the surface heating terms for the final SRC trajectory.

Heating Type	Flux (W/cm ²) (Relative to Surface)	Time (s)
Net Convection	860 (In)	52
Radiation	680 (Out)	51
Char Chemistry	39 (In)	52
Pyrolysis Gas Chemistry	30 (In)	48
Injected Chemistry	170 (Out)	52
Conduction	75 (Out)	52

The convective heatload on the surface for the final design trajectory is approximately 26000 J/cm², which is only 2000 J/cm² less than the equilibrium convective heat flux (that includes wall enthalpy) found in the preliminary trajectory. The heat loads for radiation out, the chemistry heat fluxes and conduction are seen in Figs. 3.42 and 3.43. The largest heat loads other than the convective heat load is the radiation out as the surface radiation is used to eject the heat from convective heat flux. The maximum total heat load on the surface, not including radiation out, is

about 21000 J/cm². This is less than the convective heat load due to the injected and conduction heat load carrying some of the heat away from the surface. If radiation leaving the surface was included, than the total heat load would be near zero. The magnitudes of the heat loads as compared to one another is the same as a comparison of magnitudes for the heat fluxes due to the heat loads being the heat fluxes integrated over time. The heating due to pyrolysis gas and char formation is about the same, both in the heat flux and heat load calculations. The injected heating is the second biggest process to take heat away from the surface, behind the radiation.

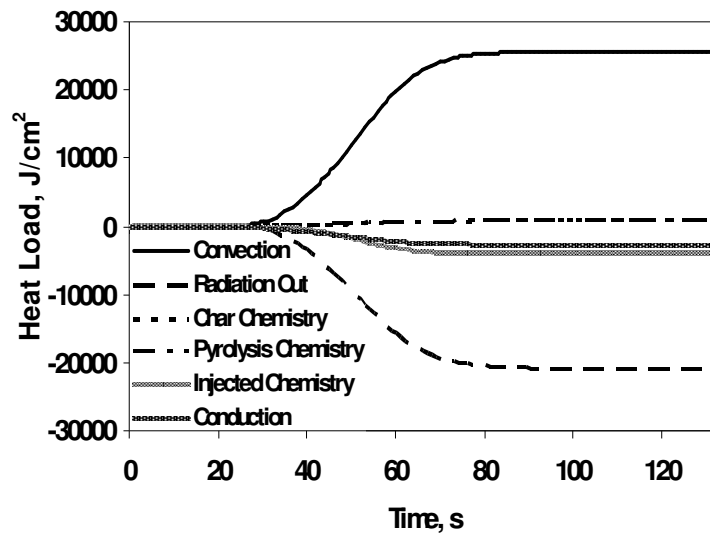


Figure 3.42. The predicted heat loads, including chemistry terms, for the final design SRC trajectory

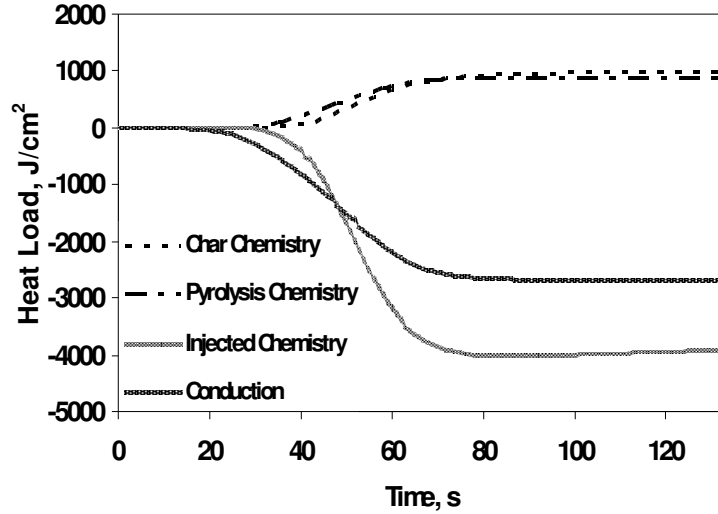


Figure 3.43. The predicted chemistry and conduction heat loads for the final design SRC trajectory

The conduction from the surface affects in-depth energy. To see how much energy is present through the material, Fig. 3.44 represents the PICA material in-depth at the time of peak heating. The material has ablated nearly half a centimeter so the first point of reference in-depth is nonzero when considering distance from the original surface. The in-depth energy becomes nearly zero after a depth of 2 cm from the ablated surface. The entire heatshield is about 6.76 cm thick at peak heating after ablation and having the internal energy reach zero only 2 cm from the surface indicates the PICA material is fairly insulative and the majority of the heatshield experiences no heat flux at all. This is the cause in the temperature predictions at the deeper nodes not getting much hotter than the set initial temperature of the material.

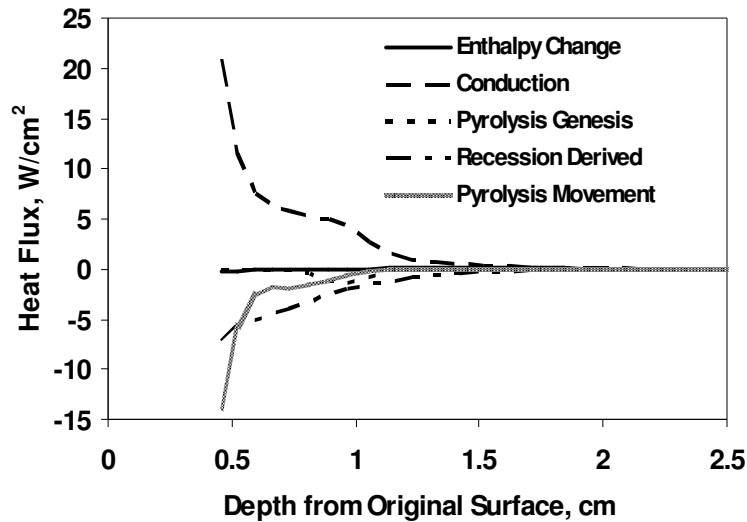


Figure 3.44. The in-depth heating as a function of depth at the stagnation point at peak heating for the final design SRC trajectory.

Figure 3.45 is the sum of the energy found at various points in-depth during the final design trajectory (the area under the curves of Fig. 3.44). This summation will be referred to as the in-depth heat flux in the dissertation. There is little difference between the amount of heat conducted from the surface and the sum of the amount of heat conducted at each node point throughout the entire material (Fig. 3.46); the similarity between the surface conduction and in-depth conduction means the amount of heat conducted from the surface remains conducted throughout the material. This is a property of the PICA material, which has little pyrolysis gas formation and decomposition so the conduction energy is not transferred into another type of energy. While other energy is generated, the internal chemistry is activated through heating from conduction but does not greatly consume conducted energy as it generates the additional energy.

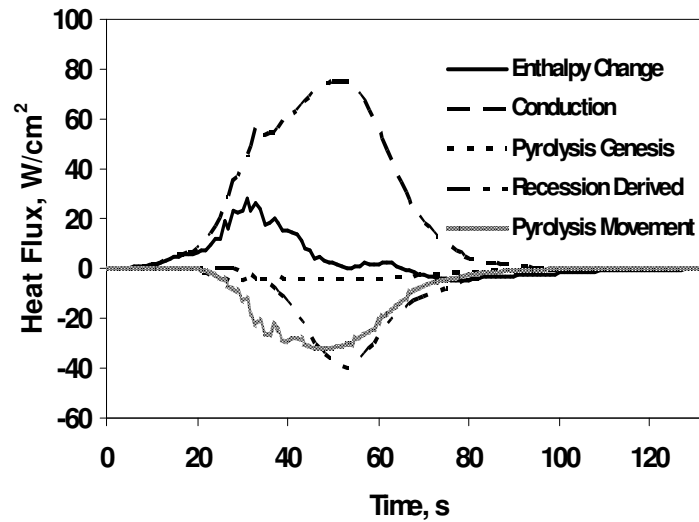


Figure 3.45. Summation of the heat fluxes in-depth during the final design SRC trajectory at the stagnation point.

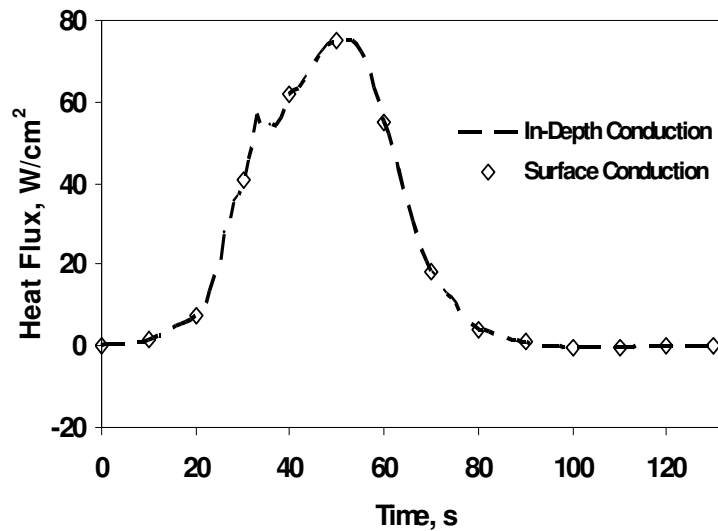


Figure 3.46. A comparison of the conduction leaving the surface and the conduction present in-depth.

In the finite-rate analysis of the final trajectory at the stagnation point, the mass loss rate is nondimensionalized by the heat transfer coefficient at 54 seconds again. At that time, the coefficient is $0.20 \text{ kg/m}^2\text{s}$, which is higher than the coefficient

at the same time in the preliminary trajectory. Since the mass loss rate is being divided by a larger number in the final trajectory, it is expected that the recession should be lower; the finite-rate char rate from MAT will be less than it was in the preliminary trajectory. When the finite-rate Park Model is applied throughout the final trajectory the final recession is 0.54 cm, which is a reduction from the finite-rate recession prediction of 0.72 cm for the preliminary trajectory. Figure 3.47 compares the recession as a function of the trajectory for the four cases: the preliminary trajectory in equilibrium and nonequilibrium and the final trajectory in equilibrium and nonequilibrium. When the final design trajectory is in equilibrium, recession occurs during almost the entire trajectory, while in the other three cases, recession stops around the time the heat pulse ends. This is due to the changes in the heating profile between the trajectories and the chemical reactions that affect the carbon material changing between equilibrium versus nonequilibrium.

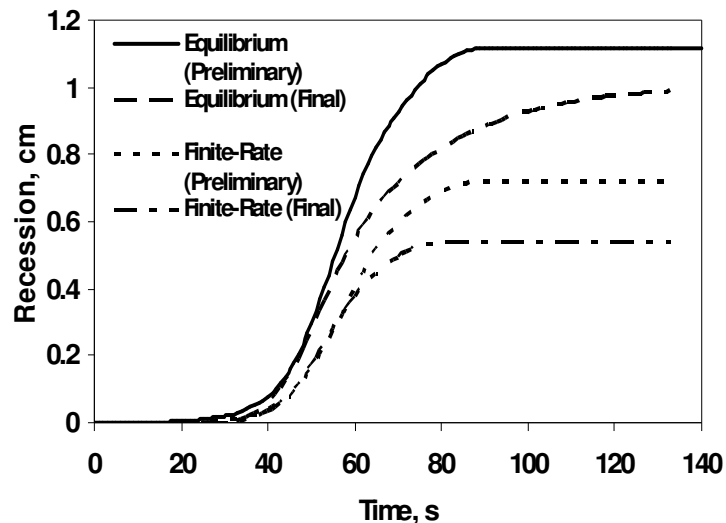


Figure 3.47. The recession for the two SRC trajectories, both in equilibrium and nonequilibrium.

The change in recession is reflected in the changes to the rates of pyrolysis gas and char. Figure 3.48 compares the pyrolysis rate from the two chemical cases in the final design trajectory, Fig. 3.49 compares the char rate and Fig. 3.50 is a comparison of the total ablation. The peak pyrolysis gas rate remains about the same whether the Park Model is applied or the reactions are allowed to occur in equilibrium, however, later in the trajectory there is a more pronounced divergence between pyrolysis predictions. After 70 seconds there is a divergence of 90%, but these pyrolysis values are very small, a magnitude of 10^{-5} .

The peak char drops from $0.066 \text{ kg/m}^2\text{s}$ in equilibrium to $0.051 \text{ kg/m}^2\text{s}$ in the application of the Park Model. This is once again the biggest driver in the decrease of total ablation. The peak ablation rate with finite-rate chemistry is $0.062 \text{ kg/m}^2\text{s}$, which is 23% lower than the equilibrium peak and mirrors the percent decrease of the char rate. This indicates that finite-rate chemistry affects the charring rate the most when applied to the final design trajectory in a similar matter to how finite-rate reactions affected the preliminary trajectory and is another indicator that the PICA material does not form pyrolysis gas that easily and achieves insulation through charring.

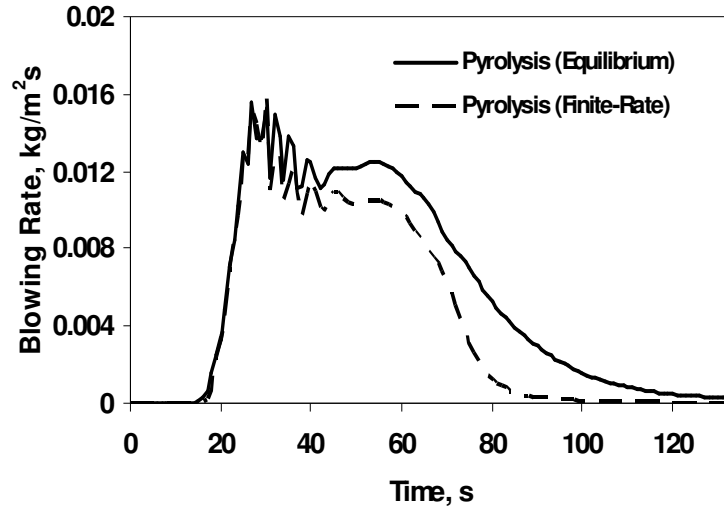


Figure 3.48. The pyrolysis gas rate for the final design SRC trajectory in equilibrium and nonequilibrium.

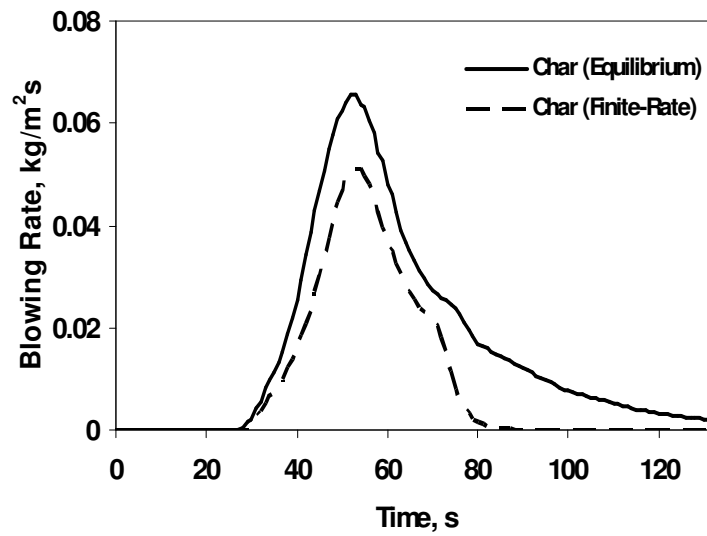


Figure 3.49. The char rate for the final design trajectory in equilibrium and nonequilibrium.

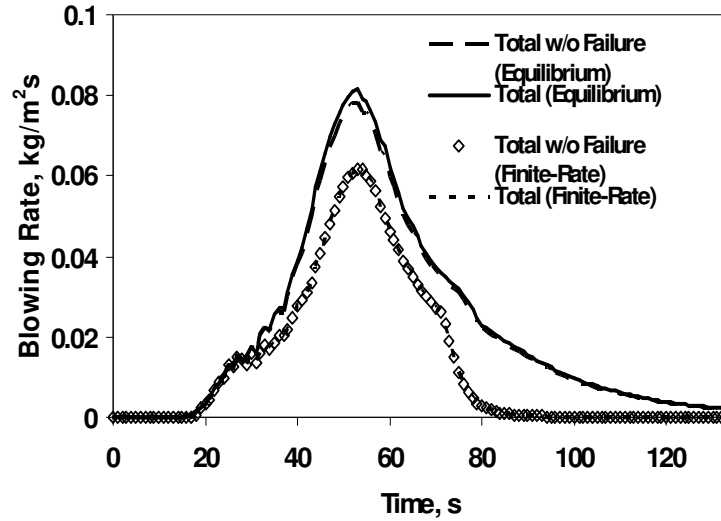


Figure 3.50. The total ablation rate for the final design trajectory in equilibrium and nonequilibrium.

The finite-rate temperature profile as compared to the equilibrium profile is seen in Fig. 3.51. TC 3 is omitted because it remains at the initial temperature throughout the trajectory. TC 2 is omitted because only its steady-state temperature at significantly changes between the equilibrium and finite-rate states, from 690 K to 510 K. The two biggest differences in the temperature profile come at the surface and at the first depth. At the surface, the temperatures in both equilibrium and finite-rate assumptions remain about the same for the first thirty seconds, but after that they diverge and the finite-rate temperature predictions are less than those found in equilibrium. Nonequilibrium over the entire trajectory causes a peak temperature of 3140 K, which is decreased from 3370 K when in equilibrium. In both cases, the peak temperature is reached at roughly peak heating. At the first thermocouple depth, the finite-rate assumption does not cause a stoppage of predictions at 65 seconds. Because of the decrease in recession due finite-rate chemistry, the PICA material

does not ablate past the thermocouple depth, allowing FIAT to continue to make predictions at that thermocouple. The equilibrium TC 1 predictions become much hotter than the nonequilibrium predictions until ablation forces the stoppage of predictions. While the hottest equilibrium temperature at TC 1 is 2890 K, in nonequilibrium, TC 1 only reaches a temperature of 2000 K, which is 31% lower than the last prediction in equilibrium. The finite-rate assumption decreases the recession and temperature predictions.

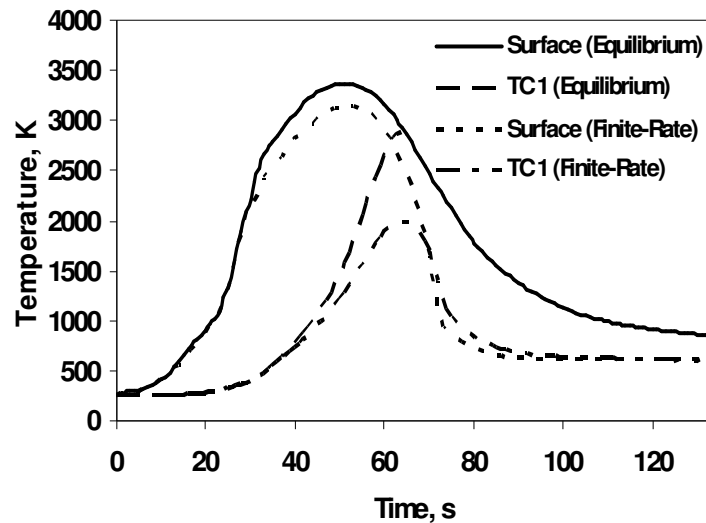


Figure 3.51. The surface and TC 1 temperature predictions for equilibrium and finite-rate chemistry models for the final design SRC trajectory.

The reduction in temperature and char formation is caused by a reduction in the heating upon the surface. The net convective heat flux increases to 900 W/cm^2 in the finite-rate case; this is due to the decrease in B' (less ablative product in the flow) causing an increase in the corrected blown transfer coefficient, noted in the preliminary trajectory. Additionally, the increase in the net convective heat flux in the final trajectory analysis is due to wall enthalpy not being computed the heat flux and

not acting as a counterbalance to the rising heat transfer coefficient. The finite-rate assumption leads to less recession and less product injected into the flow so there are fewer particles available for interaction and absorption of heat. If the wall enthalpy is included, the net convective heat flux does decrease. Figure 3.52 contains all the convective heat fluxes, with and without the wall enthalpy.

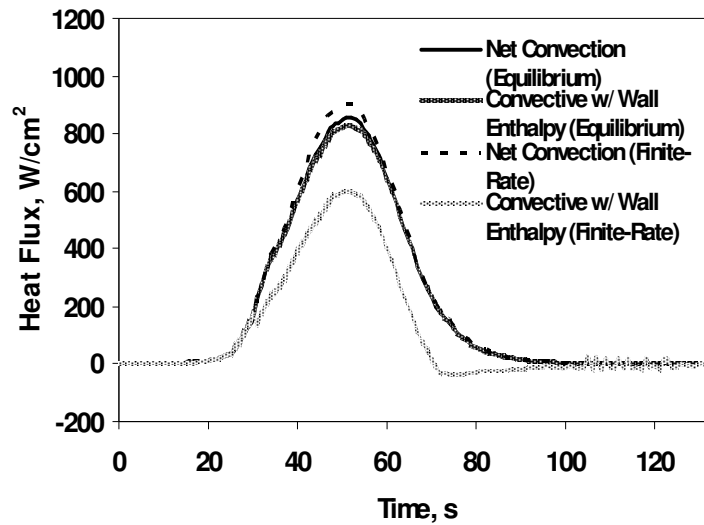


Figure 3.52. The net convective heat flux predictions for equilibrium and finite-rate chemistry models, with and without wall enthalpy, for the final design SRC trajectory.

The peak convective heat flux that includes wall enthalpy is 830 W/cm^2 in equilibrium and 600 W/cm^2 in nonequilibrium. The equilibrium peak including wall enthalpy is only 30 W/cm^2 less than the equilibrium convective heat flux without wall enthalpy which may be the reason why wall enthalpy is ignored in the convective calculations of previous final SRC trajectory analyses. In nonequilibrium, the peak value is 33% lower than the equilibrium value showing that wall enthalpy plays a role in calculating heat fluxes in a finite-rate simulation. The decrease of the net

convective heat flux when enthalpy is included indicates that the wall enthalpy is increasing when considering finite-rate reactions. The increase of enthalpy is partly due to an increase in the mole fractions of high enthalpy species due to fewer moles of the products found in the Park Model.

The lower char and pyrolysis gas mass fluxes give their respective heat fluxes to be lower in the finite-rate model than in the equilibrium model (Figs. 3.53 and 3.54). The finite-rate peak values for the chemistry terms are compared to their equilibrium values in Table 3.5. The char heat flux decreases by 30%, while the pyrolysis gas heat flux decreases by 40%. The injected heat flux becomes much larger in a finite-rate analysis. Though the injected heat flux is the sum of the char and pyrolysis gas rates and should be smaller in a finite-rate approximation based on the decrease of those two parameters, it also is calculated from the wall enthalpy. The large wall enthalpy in the finite-rate model drives the injected heat flux to be higher than what it is found to be in equilibrium.

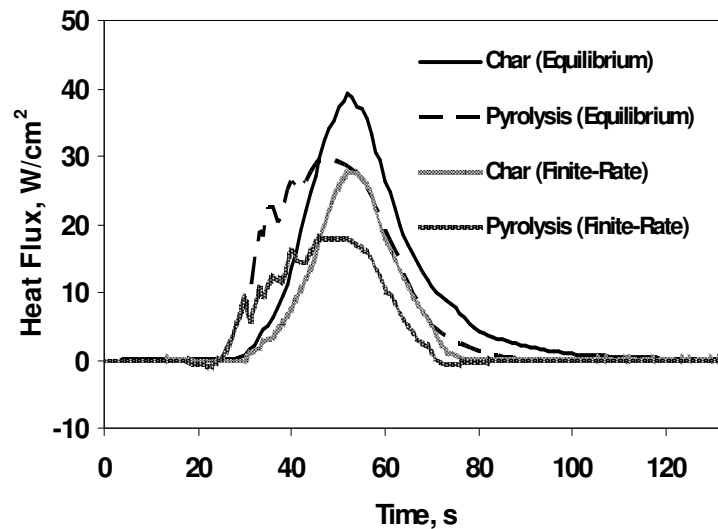


Figure 3.53. The char and pyrolysis gas heat flux predictions for equilibrium and finite-rate chemistry models for the final design SRC trajectory.

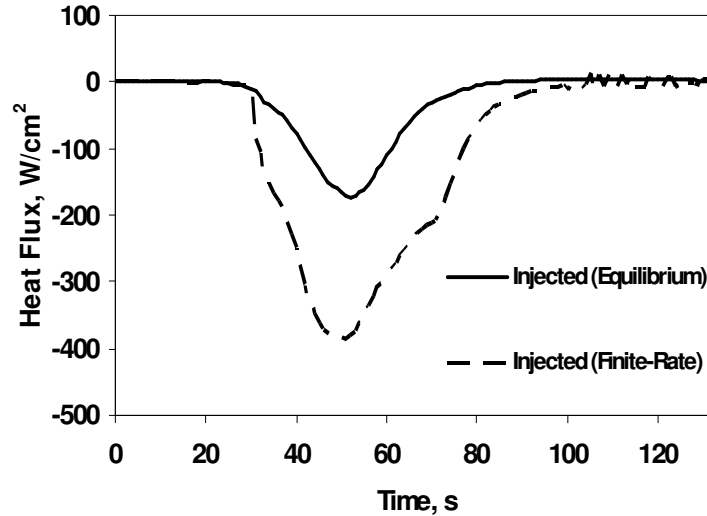


Figure 3.54. The injected heat flux predictions for equilibrium and finite-rate chemistry models for the final design SRC trajectory.

Table 3.5 The peak values of the surface chemistry heating terms in equilibrium and finite-rate models for the final SRC trajectory.

Heating Type	Flux (W/cm ²)	Flux (W/cm ²)
	(Relative to Surface)	(Relative to Surface)
	Equilibrium	Finite-Rate
Char Chemistry	39 (In)	27 (In)
Pyrolysis Gas Chemistry	30 (In)	18 (In)
Injected Chemistry	170 (Out)	390 (Out)

Radiation from the surface is dependent on surface temperature, so with a lower surface temperature in a finite-rate assumption, there will be lower radiation. The conduction that travels in-depth through the material is one process used to take heat away from the surface and keep it in heating equilibrium. The radiation out is 510 W/cm² and conduction is 54 W/cm² (Fig. 3.55), both of which are lower than their values in equilibrium. The heat loads (Fig. 3.56) follow a similar trend to that of their heat flux counterparts, with the maximum convective heat load slightly

increasing and the maximum injected heat load becoming much bigger in finite-rate calculations. Most of the heat is being carried away from the surface by the injected heat flux.

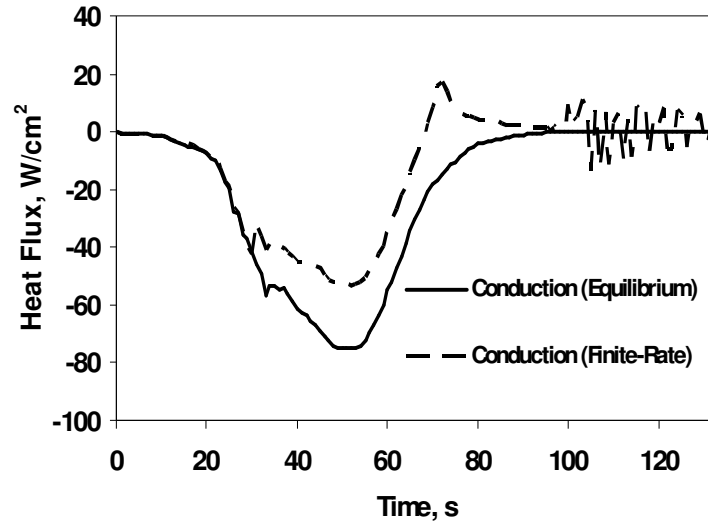


Figure 3.55. The conduction predictions for equilibrium and finite-rate chemistry models for the final design SRC trajectory.

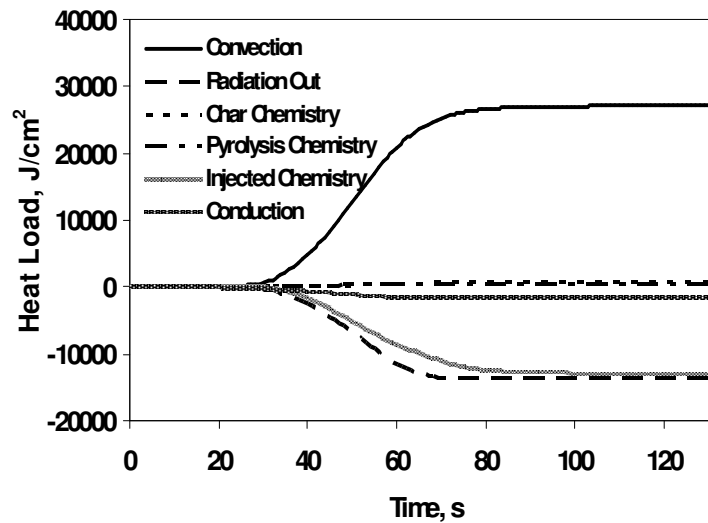


Figure 3.56. The heat load predictions for the finite-rate chemistry model for the final design SRC trajectory.

There is oscillation in the predicted conduction and chemistry heat fluxes starting at around 100 seconds into the final trajectory when applying finite-rate chemistry. These oscillations are the result of a similar oscillation in the wall enthalpy (Fig. 3.57) and are due to the interpolation error seen previously in the preliminary trajectory analysis of the sublimation-absent case. Oscillations start near the end of the heat pulse where charring will slow down or stop; the finite-rate B' tables generated do not consider conditions where there will be no char at all while the material is experiencing a specific pressure and B'_g . If the nonchar sections are included, the wall enthalpy oscillations and heat fluxes change (Figs. 3.58 and 3.59). There are now bigger oscillations that occur starting at around 80 seconds, but are dampened by 100 seconds into the trajectory. The bigger oscillations are due to the Modified Park Model not being as physically accurate during noncharring conditions, as Eq. 2.17 shows that the Park Model is built upon the assumption that some charring will occur from its reactions. There is a slight increase in the finite-rate recession, from 0.54 to 0.57 cm, a less than 10% increase. Similarly, there are small increases in the heat fluxes and temperatures. In equilibrium, the inclusion of the nonchar indexes has an even lesser impact: recession prediction increases from 0.99 to 1.00 cm and there is only about a 1% increase in the peak convective heat flux. Since there are smaller oscillations when the nonchar index is eliminated and no more than a 10% difference between the predictions when nonchar indexes are included or not included, the nonchar index is not present in the B' table in this analysis unless otherwise noted.

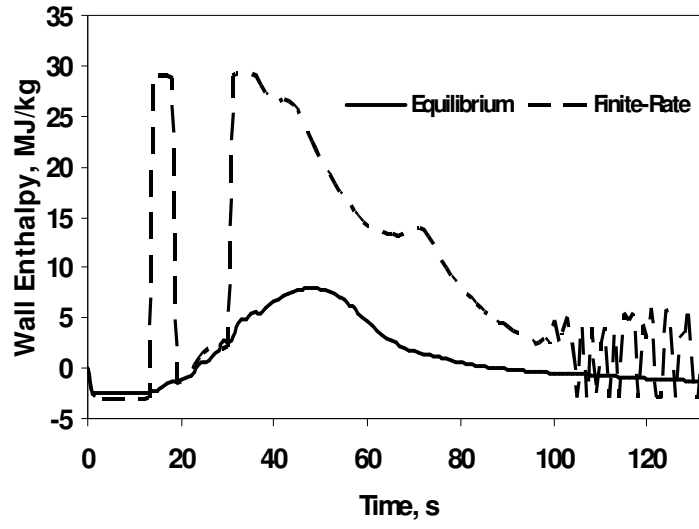


Figure 3.57. The wall enthalpy predictions for equilibrium and finite-rate chemistry models for the final design SRC trajectory.

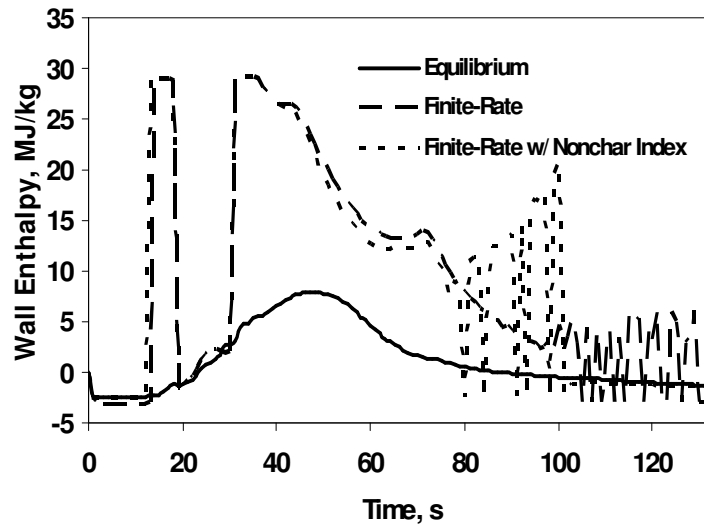


Figure 3.58. The wall enthalpy predictions for equilibrium and finite-rate chemistry models, with and without nonchar indexes, for the final design SRC trajectory.

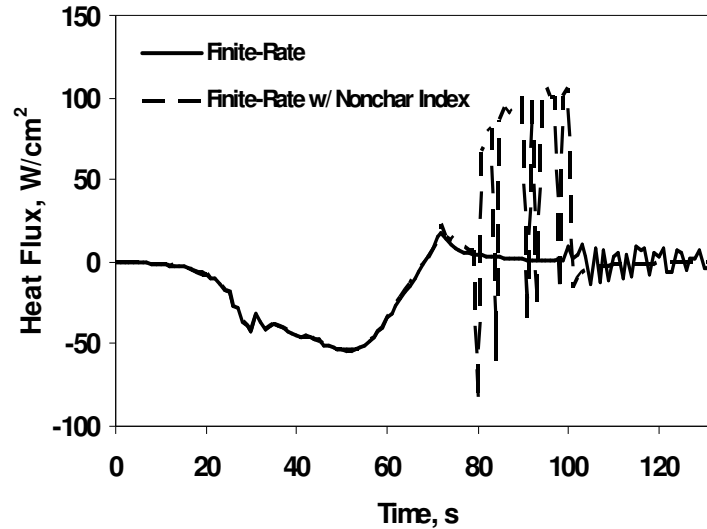


Figure 3.59. The conduction predictions for the finite-rate chemistry model, with and without nonchar indexes, for the final design SRC trajectory.

The in-depth heat fluxes are shown in Fig. 3.60. The finite-rate assumption does not affect the material properties of PICA and the conduction in-depth remains the same as the conduction on the surface, as seen in the equilibrium case; the in-depth conduction decreases causing a decrease in the other in-depth heat fluxes. Additionally, because of the wall enthalpy oscillations during the heating tail affecting the conduction, in-depth, the enthalpy change also oscillates during the heating tail to off-set the largest contributor to in-depth heating. The same conclusions that were reached in equilibrium in regards to the insulative properties of the PICA material can be reached in the finite-rate case as the only significant difference is that there is less conduction through the material.

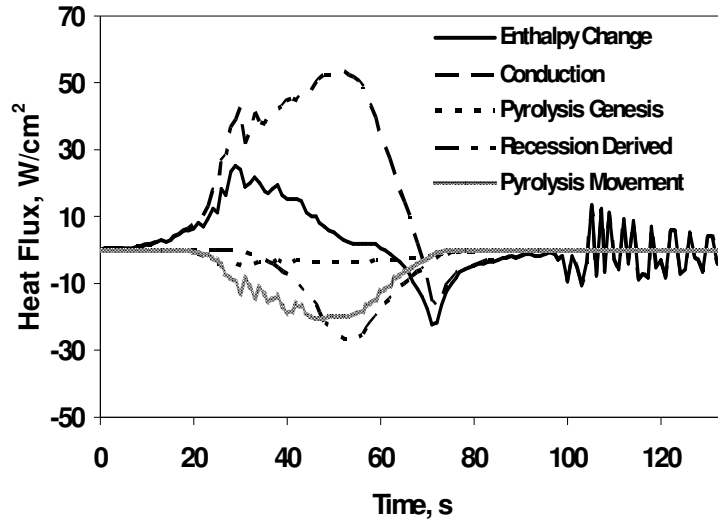


Figure 3.60. The in-depth heat flux predictions for the finite-rate chemistry model for the final design SRC trajectory.

The surface thermochemistry table is generated before any material response model is applied to a material, dictating that the heat transfer coefficient used to nondimensionalize the finite-rate mass flux is one constant value though it is changing in the trajectory. At each trajectory point, the reactions are being modeled as if they were occurring at that peak heating coefficient, though the actual conditions may not match that coefficient. To make the calculations more robust, FIAT and MAT are coupled together in a new program called BFIAT. At each trajectory point the unique pressure and heat transfer coefficient are used in the surface thermochemistry calculations and create a smaller B' table. The new B' table reduces employs the correct nondimensionalized term so the charring rates are reflective of the actual heating on the surface.

The Park Model only deals with forward reactions and has a small set of reactions, so it cannot approximate equilibrium even if the conditions dictate that

equilibrium can be reached on the surface. The Park Model role in constructing a B' table assumes that nonequilibrium occurs at every time point in the trajectory, which may not be true. To correct this in the BFIAT setup, the B' table can be derived in equilibrium and nonequilibrium, with the user determining the proper conditions for each case and telling the surface thermochemistry calculation to include or exclude the Park Model.

Three states are examined in the Stardust Return Capsule trajectory, in terms of when to apply nonequilibrium: during the heating tail (where the oscillations in wall enthalpy are seen), after peaking heating (starting at 54 seconds), and after the surface temperature has reached 3000 K (where sublimation, identified as the major reaction in the Park Model for the preliminary trajectory, will start). Before these conditions are met, the trajectory is considered in equilibrium. The initial heat transfer coefficients that may be so small that when they are used to nondimensionalize the finite-rate mass flux, the magnitude of the resulting finite-rate value makes Eq. 2.93 negative, so there is cautious application of finite-rate reactions during the period. A similar program to BFIAT that combines the mathematical processes of FIAT and MAT, called the Fully Implicit Ablation, Thermal response, and Chemistry (FIATC) program is currently being developed by Milos and Chen⁸⁰ but it does not deal with surface chemistry in the same way (no generation of a B' table) and its significant contribution is modeling how the pyrolysis gas travels through the material.

Reference 79 mentions that a problem with reading from B' tables in FIAT is how the interpolation between pressures can cause errors. BFIAT eliminates that problem by creating only one B' table at the current trajectory point pressure. There is

a small difference in calculations between the use of BFIAT in equilibrium and a complex B' table for the SRC trajectory. The largest changes occur around predictions at peak heating. Peak convective heating, for example, increases by 7%; most predictions from using the single pressure BFIAT table remain within $\pm 10\%$ of the predictions using multiple pressure B' table. The interpolation reduction afforded by BFIAT has only a slight effect on predictions and is not large enough to significantly alter TPS design specifications by itself. The main intent of BFIAT is to allow for equilibrium and nonequilibrium calculations to occur at different times in the trajectory and to study the thermochemistry at the surface. To help illustrate the gas/surface interaction BFIAT also has the ability to calculate the mole fractions and their rate of change for each species defined at the gas/surface interface at each trajectory point. This helps identify how the interface is being populated and depopulated on a molecular level and can be used to identify important products of the reactions.

3.2.2 Stagnation Point – Heating Tail

The heating tail is when the convective heat flux on the surface is lower than 100 W/cm^2 . In the Stardust Return Capsule trajectory, this starts roughly at 80 seconds. FIAT may overpredict recession during the heating tail.^{81,82} When the Stardust Return Capsule analysis reaches 80 seconds, the nonequilibrium calculations begin and surface remains in nonequilibrium for the rest of the trajectory. By switching from equilibrium to finite-rate calculations during the heating tail any suspected recession overprediction should be decreased, since it is demonstrated that finite-rate reactions decrease recession on the PICA surface.

The recession is shown in Fig. 3.61 and the recession rates for equilibrium, finite-rate reactions over the entire trajectory, and finite-rate reaction only during the heating tail is shown in Fig. 3.62. Once finite-rate reactions are turned on, the recession rate begins to approach the rate found when nonequilibrium is applied to the entire trajectory, decreasing the total recession. There is a decrease of 68% in the recession rate between the trajectory point at 80 seconds and the trajectory point at 81 seconds, when finite-rate ablation is turned on. The final predicted total recession when finite-rate reactions are applied only during the heating tail is 0.85 cm, which is less than the 0.99 cm recession found in full trajectory equilibrium but greater than the 0.54 cm found in full trajectory nonequilibrium. Making an assumption of finite-rate reactions during the heating tail decreases any perceived overprediction by FIAT during the low heating while keeping the rest of the trajectory in equilibrium.

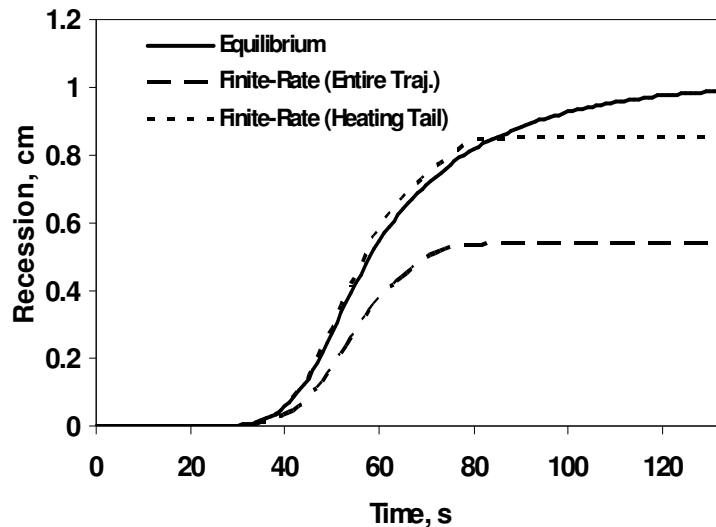


Figure 3.61. Recession predictions for the equilibrium assumption, finite-rate over the entire final design SRC trajectory assumption, and finite-rate only at the heating tail assumption.

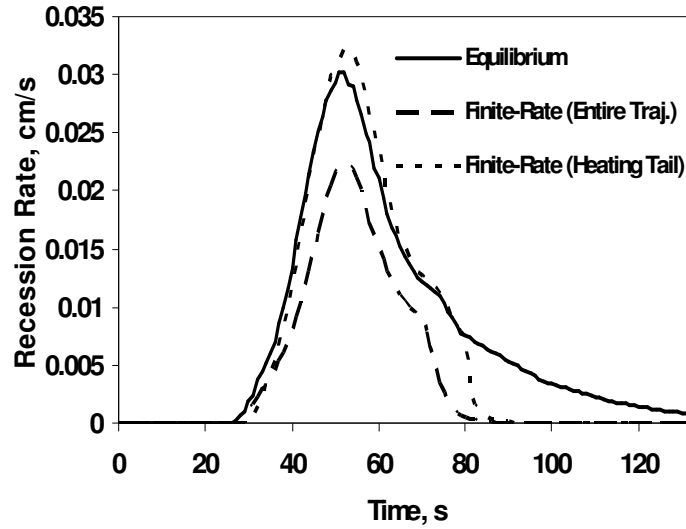


Figure 3.62. Recession rate predictions for equilibrium assumption, finite-rate over the entire final design SRC trajectory assumption, and finite-rate only at the heating tail assumption.

Not only does the implementation of finite-rate reactions during the heating greatly affect the recession rate and final recession, it also affects the other predictions. Since recession is dependent on the char and pyrolysis gas rate, Figs. 3.63 and 3.64 reflect the recession trend in that the char and pyrolysis gas rates respectively follow equilibrium predictions for the first 80 seconds then approach finite-rate predictions once finite-rate reactions are applied to the trajectory. The total ablation rate (Fig. 3.65) follows a similar trend to what was seen in the recession rate in that it slows down when nonequilibrium reactions are applied to the surface starting at 80 seconds.

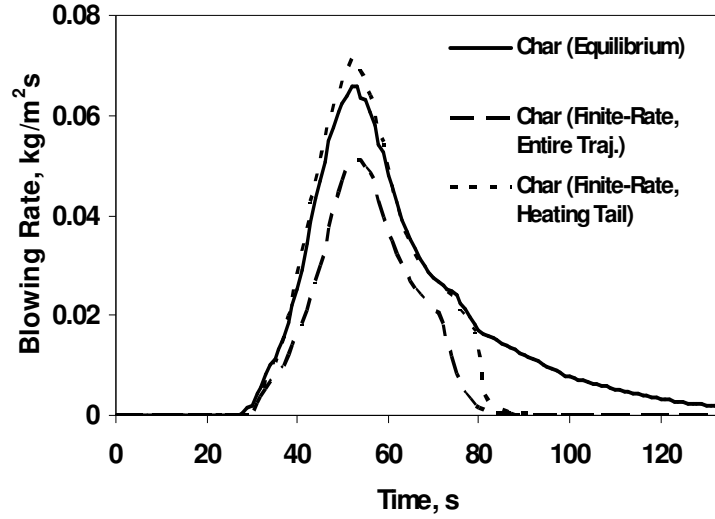


Figure 3.63. The char rate for the final design trajectory in equilibrium during the entire trajectory assumption, finite-rate during the entire trajectory assumption, and finite-rate during the heating tail assumption.

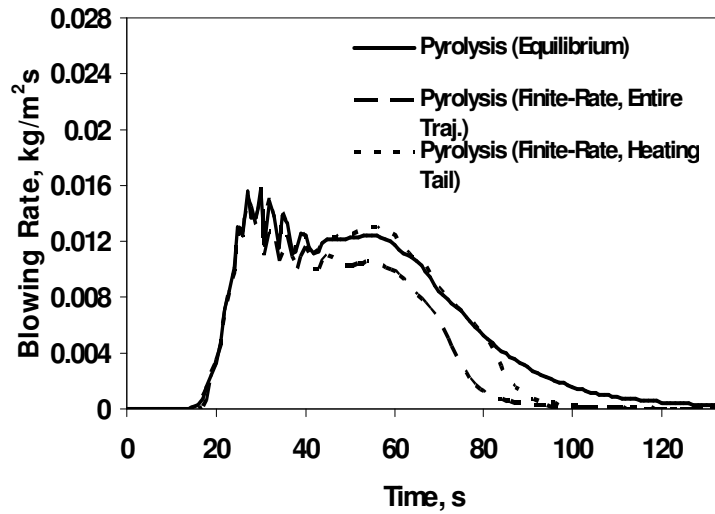


Figure 3.64. The pyrolysis gas rate for the final design trajectory in equilibrium during the entire trajectory assumption, finite-rate during the entire trajectory assumption, and finite-rate during the heating tail assumption.

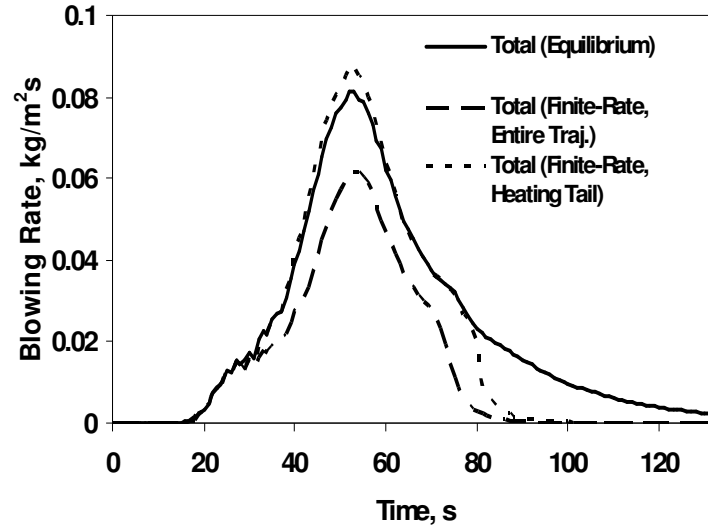


Figure 3.65. The total ablation rate for the final design trajectory in equilibrium during the entire trajectory assumption, finite-rate during the entire trajectory assumption, and finite-rate during the heating tail assumption.

The surface temperature and TC 1 trends for the heating tail case follow both the equilibrium and finite-rate trends when each state is being calculated (Fig. 3.66). TC 1 is ablated past like in equilibrium, but on the surface, once finite-rate reactions are applied, the temperature approaches the same temperature seen in the case where nonequilibrium is applied to the entire trajectory. This trend is also apparent in the surface heat fluxes (Figs. 3.67 and 3.68). Convective and radiative heat fluxes are near zero whether it is an equilibrium or nonequilibrium case and are not shown in the figures. The injected heat flux prediction for the heating tail is larger than the full trajectory nonequilibrium prediction at the instant the finite-rate assumption is activated due to interpolation errors when going from equilibrium to nonequilibrium char predictions during conditions that lead to slow char growth; however, after that time point, the predictions closely match. Some of the oscillations seen in the injected

heat flux are damped out when using BFIAT because one unique B' table reduces interpolation error.

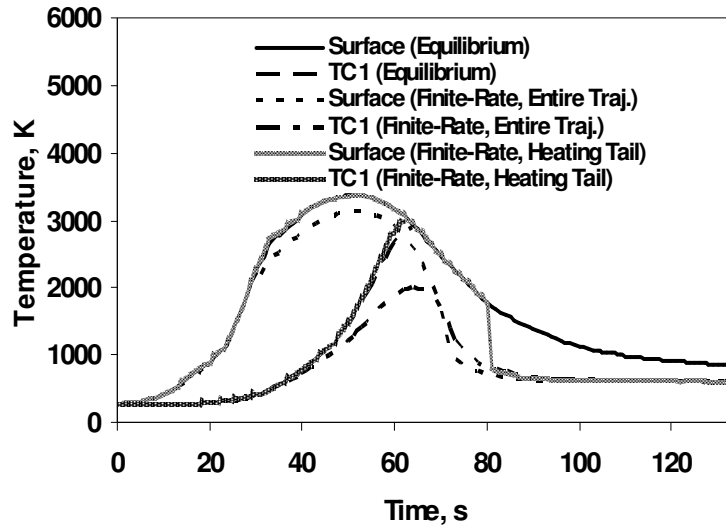


Figure 3.66. The surface temperature and the temperature at the depth of the first thermocouple couple for the final design trajectory in equilibrium during the entire trajectory assumption, finite-rate during the entire trajectory assumption, and finite-rate during the heating tail assumption.

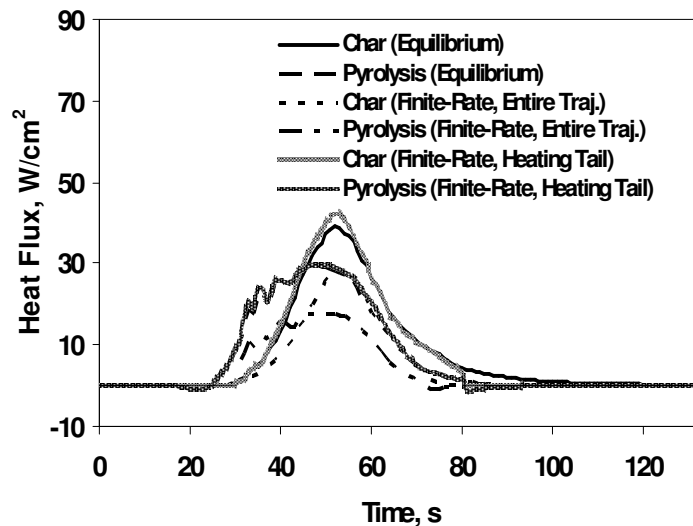


Figure 3.67. The char and pyrolysis gas heat fluxes on the surface for the final design trajectory in equilibrium during the entire trajectory assumption, finite-rate during the entire trajectory assumption, and finite-rate during the heating tail assumption.

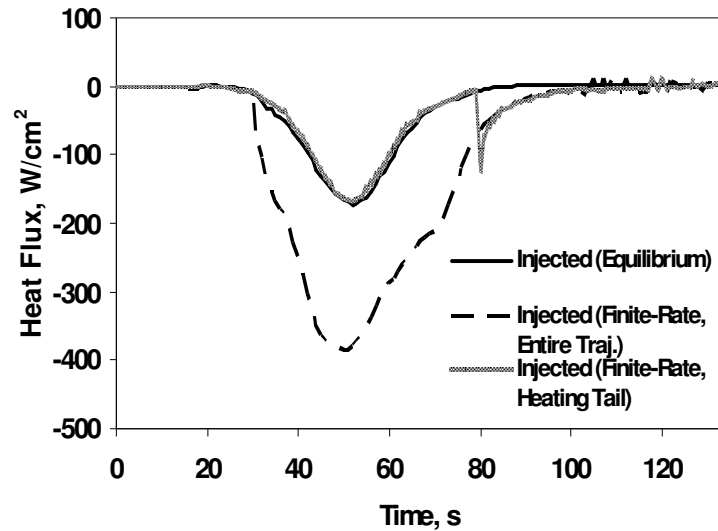


Figure 3.68. The injected heat flux for the final design trajectory in equilibrium during the entire trajectory assumption, finite-rate during the entire trajectory assumption, and finite-rate during the heating tail assumption.

The spike in the injected heat flux causes a large spike in the conduction, whose calculation is dependent on how the heat is entering and leaving the surface from the other heat fluxes (Fig. 3.69). The conduction found in the spike is approximately 30 times larger than what is predicted in the full trajectory finite-rate analysis. The sudden spike in conduction only greatly affects the conduction and enthalpy change in-depth as seen in Fig. 3.70. Other than the sudden and temporarily jump in the enthalpy change and conduction terms in-depth, the trends seen due to a change in the chemistry assumption in-depth follow those seen in the other predictions: after 80 seconds, the equilibrium predictions approach the nonequilibrium predictions previously predicted when finite-rate ablation is assumed over the entire trajectory.

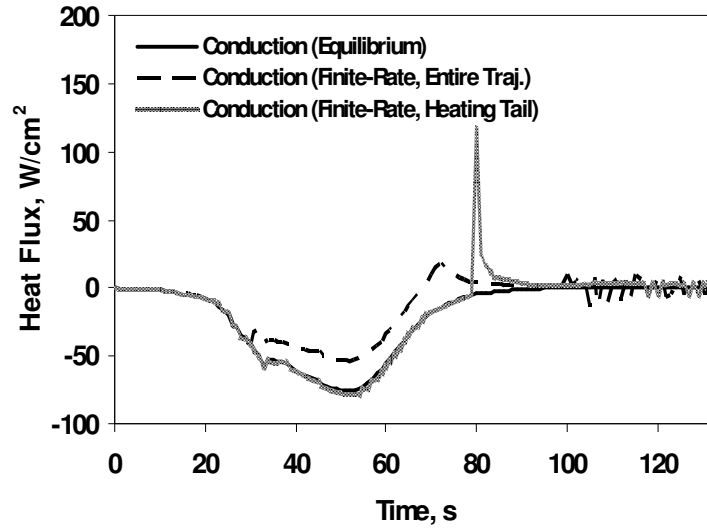


Figure 3.69. The surface conduction heat flux for the final design trajectory in equilibrium during the entire trajectory assumption, finite-rate during the entire trajectory assumption, and finite-rate during the heating tail assumption.

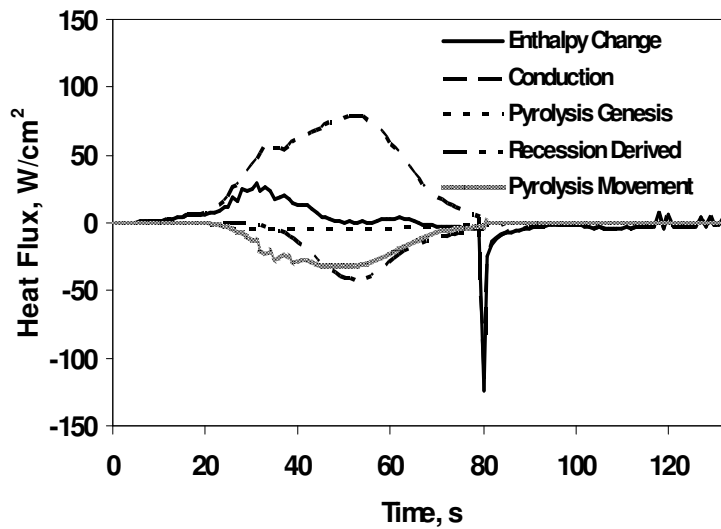


Figure 3.70. The in-depth heat fluxes for the final design trajectory in a finite-rate during the heating tail assumption.

Overall, the application of finite-rate reactions to the heating tail can have varying affects on the predictions in comparison to equilibrium conditions and

depending on what the finite-rate predictions would be if finite-rate was applied during the entire trajectory. Since the heating tail lasts less than half the total trajectory time and occurs, by definition, during low heating, while there are changes in some of the surface and in-depth heat fluxes, they are relatively minor either in terms of magnitude or affect the heat fluxes steady-state predictions. The impact of the heating tail case is most importantly felt in the parameters that affect or relate to ablation where the difference between nonequilibrium and equilibrium are more clearly illustrated: recession and its rate, the blowing rates, and the injected heat flux. While there is a large increase in conduction when finite-rate reactions are taken into account, it lasts for less than a second and may be considered an example of a discontinuity in the calculations when the switch is made and some of the oscillations seen during the heating tail are eliminated.

3.2.3 Stagnation Point – Post Peak Heating

A finite-rate reaction set is assumed post peaking heating (54 seconds) in this case. Earlier implementation of finite-rate reactions than for the heating tail case will further demonstrate how the use of both equilibrium and nonequilibrium over the trajectory affects the final predictions by giving the finite-rate reactions more trajectory time to affect the heatshield. Additionally, heating will only be decreasing after peak heating is reached, simplifying the finite-rate analysis by keeping the finite-rate reactions in the region of the trajectory where the material is “cooling off,” making sublimation less likely to occur as the surface temperature is decreasing from 3000 K.

The recession over the entire trajectory is shown in Fig. 3.71. The final recession is 0.72 cm, less than the recession predicted when finite-rate reactions only take place during the heating tail and less than the recession predicted during equilibrium over the entire trajectory. As the finite-rate assumption occurs earlier in the trajectory, the recession prediction is approaching the recession found when nonequilibrium is implemented over the entire trajectory. The recession rate, as seen in Fig. 3.72, remains near the equilibrium predictions for the first 54 seconds then after finite-rate reactions are turned on, the rate predictions approach the full finite-rate results, similar to what was seen when only the heating tail was being considered in nonequilibrium. There is a 27% difference in the recession rate between the trajectory point at 54 seconds and the recession rate at 55 seconds. This is less of a percent change than what is experienced before and after nonequilibrium was turned on in the heating tail case, but the recession rate during peak heating is larger than the recession rate found during the heat tail, so the difference is larger. So while the recession rate change at the peak heating is not as significant in terms of relative magnitude as the change found when looking at the heating tail only, the decrease in the actual amount of recession change is more significantly and lowering the rate sooner in the trajectory. This is what leads to a lower final recession.

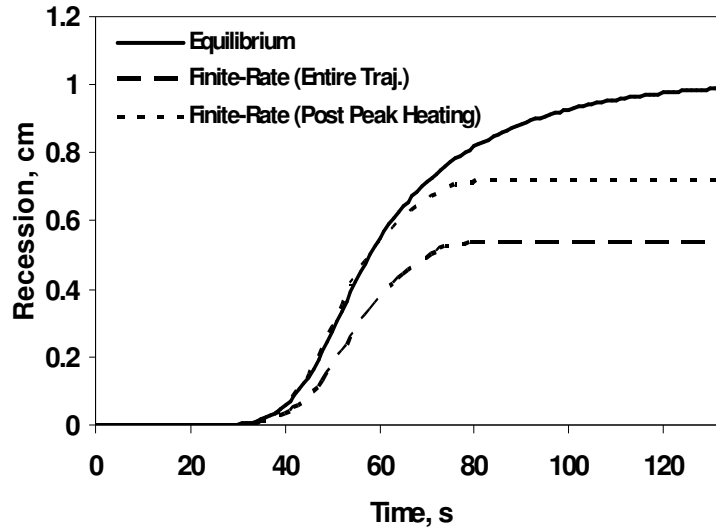


Figure 3.71. Recession predictions for the equilibrium assumption, finite-rate over the entire final design SRC trajectory assumption, and finite-rate beginning at the peak heating assumption.

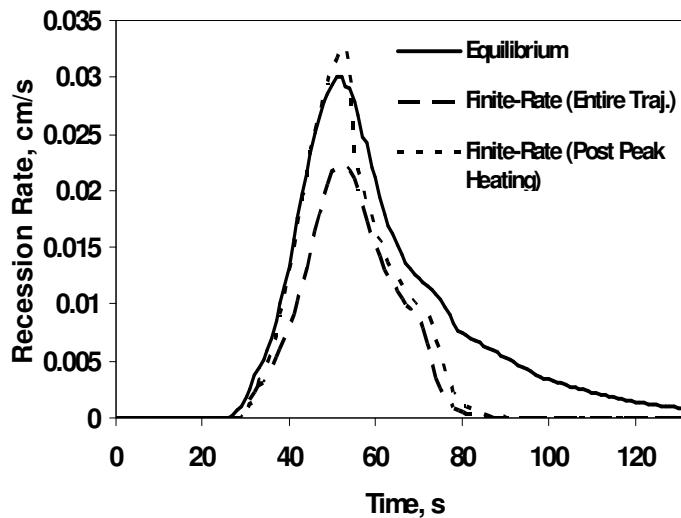


Figure 3.72. Recession rate predictions for the equilibrium assumption, finite-rate over the entire final design SRC trajectory assumption, and finite-rate beginning at the peak heating assumption.

The char ablation rate (Fig. 3.73), pyrolysis gas rate (Fig. 3.74) and total ablation rate (Fig. 3.75) when finite-rate reactions start to occur at peak heating

follow similar trends as what as seen when the heating tail is considered in nonequilibrium. The char rate approaches finite-rate predictions almost immediately after the assumption is turned on while the pyrolysis gas rate more slowly approaches it which shows again how the finite-rate reactions affect the charring rates more than the pyrolysis rates. The total ablation rate once again reflects the trends seen in the char rate.

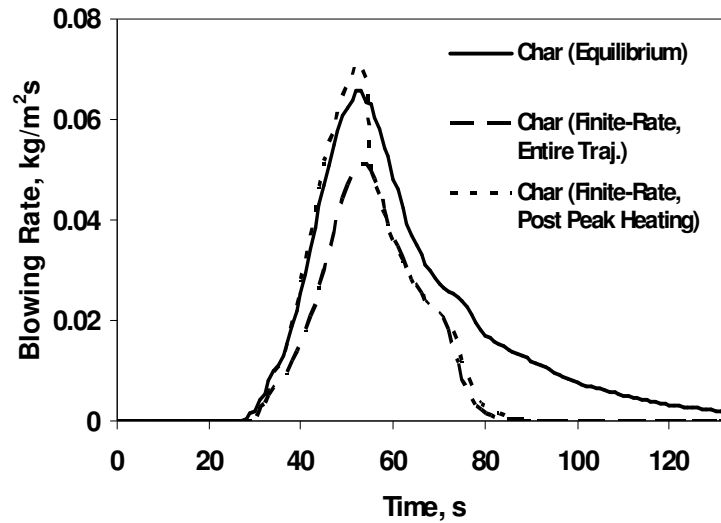


Figure 3.73. The char rate for the final design trajectory in equilibrium during the entire trajectory assumption, finite-rate during the entire trajectory assumption, and finite-rate after peaking heating assumption.

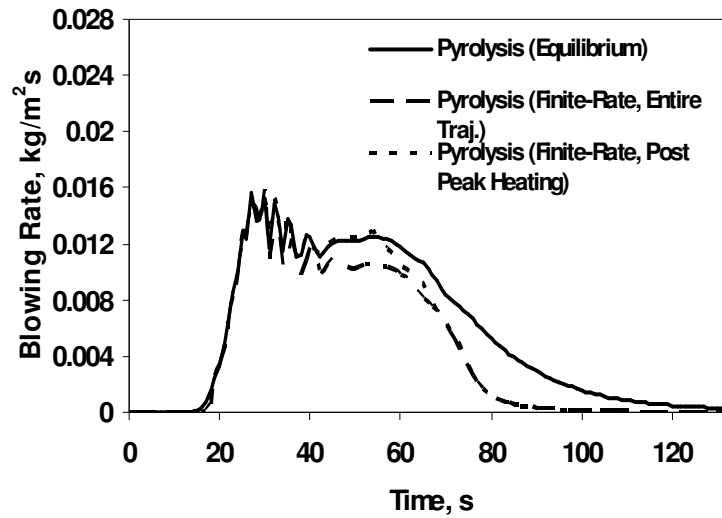


Figure 3.74. The pyrolysis gas rate for the final design trajectory in equilibrium during the entire trajectory assumption, finite-rate during the entire trajectory assumption, and finite-rate after peaking heating assumption.

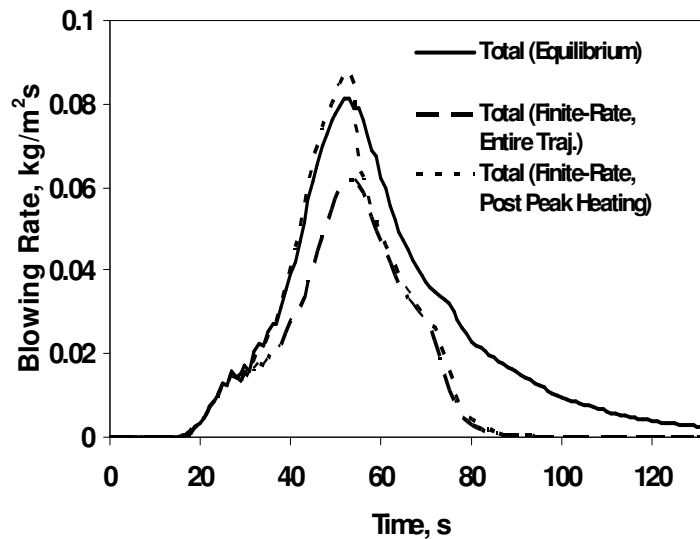


Figure 3.75. The total ablation rate for the final design trajectory in equilibrium during the entire trajectory assumption, finite-rate during the entire trajectory assumption, and finite-rate after peaking heating assumption.

For the surface and in-depth temperatures (Fig. 3.76), while the surface temperature almost immediately trends towards the finite-rate application over the

full trajectory, the temperature at TC 1 does not approach its finite-rate equivalent after 54 seconds. It ends up between the equilibrium and nonequilibrium over the full trajectory predictions. When finite-rate reactions are applied starting at peak heating at 54 seconds it lowers the recession rate and TC 1 remains above the recession line for 68 seconds, 4 seconds longer than in equilibrium. Slowing down the recession rate starting at peak heating will not keep TC 1 viable for the entire trajectory. The last temperature predicted at TC 1 for equilibrium is 2890 K and for finite-rate reactions occurring at peak heating, it is a temperature of 2180 K. TC 1 remains a viable depth for predictions for a few seconds longer than in equilibrium, so it is ablated away at a cooler temperature than it would be in equilibrium.

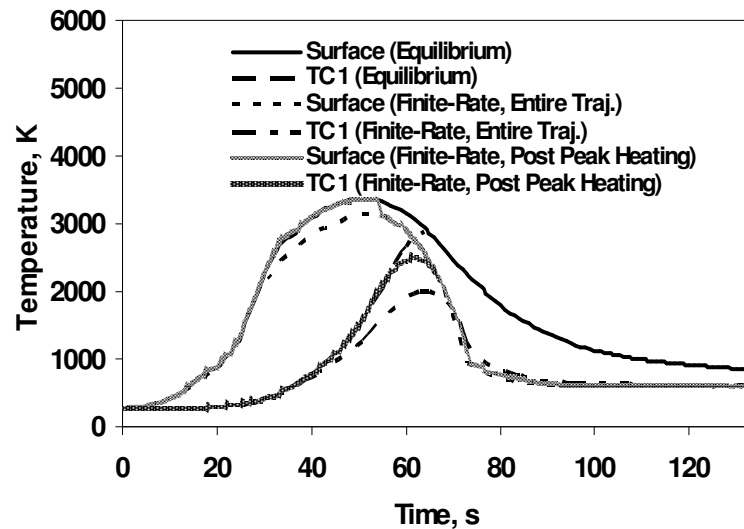


Figure 3.76. The surface temperature and the temperature at the depth of the first thermocouple couple for the final design trajectory in equilibrium during the entire trajectory assumption, finite-rate during the entire trajectory assumption, and finite-rate after peak heating assumption.

There is only a small difference between the net convective heat flux on the surface between the equilibrium over the full trajectory, finite-rate reactions over the

full trajectory, and finite-rate reactions starting at peak heating since there was only a small difference between the convective heat flux in the full equilibrium and full nonequilibrium cases (Figs. 3.77 and 3.78). However, because there is a difference between the radiation out predictions in equilibrium and nonequilibrium due to the difference in surface temperatures, when finite-rate reactions are applied at peak heating, there is a trend towards a less radiation out, similar to what happens when nonequilibrium is applied throughout the trajectory.

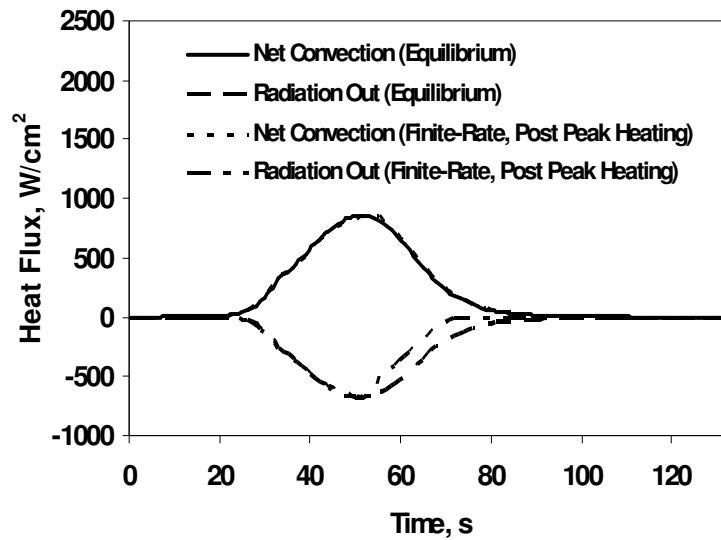


Figure 3.77. The net convection and radiation out heat flux predictions when equilibrium is assumed over the entire final design SRC trajectory and when finite-rate reactions are applied after peak heating.

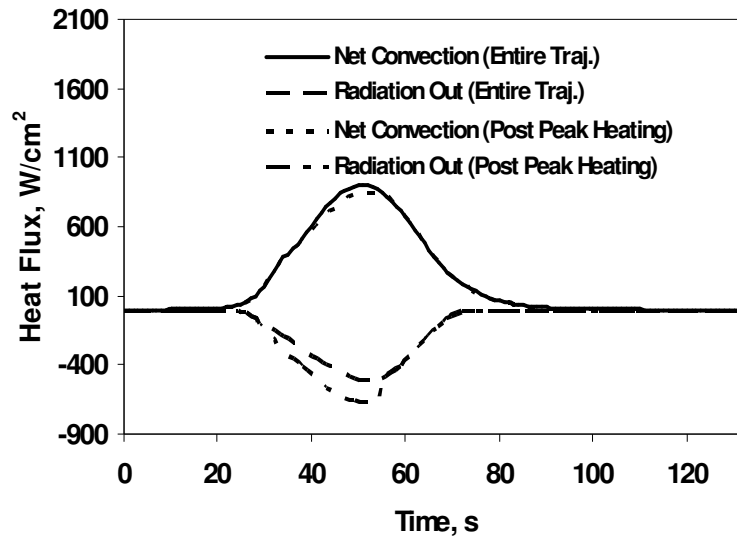


Figure 3.78. The net convection and radiation out heat flux predictions when nonequilibrium is assumed over the entire final design SRC trajectory and when finite-rate reactions are applied after peak heating.

The char, pyrolysis, and injected heat fluxes when finite-rate reactions are applied after peaking heating are predicted as expected: they follow the equilibrium predictions when equilibrium is being applied then trend towards the nonequilibrium predictions after peak heating (Figs. 3.79 and 3.80). The injected heat flux experiences a sharp increase which will affect the conduction into the material. The conduction (Fig. 3.81) does not experience as large of a spike like in the heating tail case and more closely follows the nonequilibrium trends. Implementation of finite-rate reactions at the heating peak results in fewer oscillations during the end of the trajectory, like in the post heating tail case. With finite-rate reactions being turned on at peak heating, the surface heat fluxes fall between the full nonequilibrium and full equilibrium predictions better than the heating tail case.

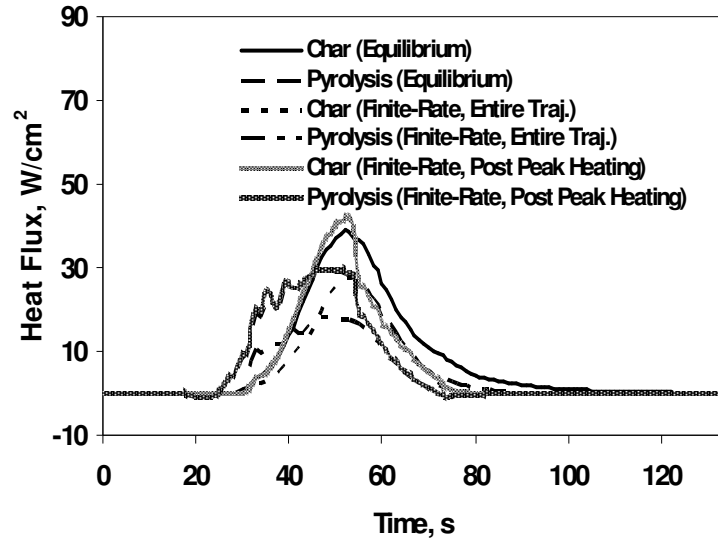


Figure 3.79. The char and pyrolysis gas heat fluxes on the surface for the final design trajectory in equilibrium during the entire trajectory assumption, finite-rate during the entire trajectory assumption, and finite-rate after the peak heating assumption.

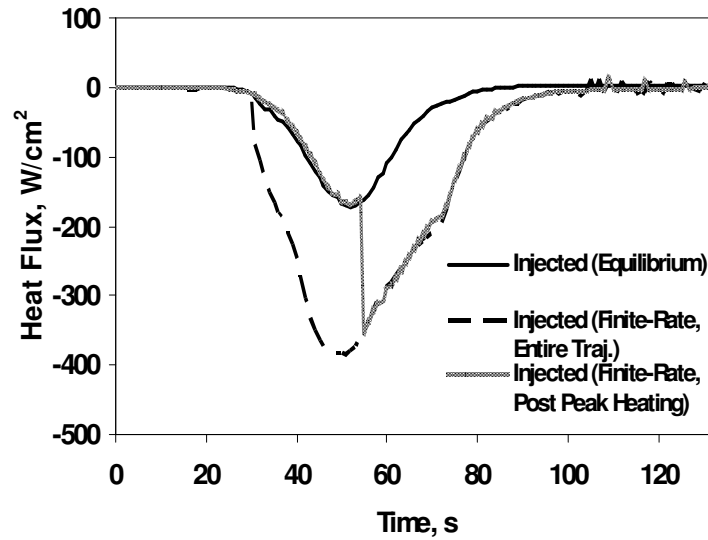


Figure 3.80. The injected heat flux for the final design trajectory in equilibrium during the entire trajectory assumption, finite-rate during the entire trajectory assumption, and finite-rate after the peak heating assumption.

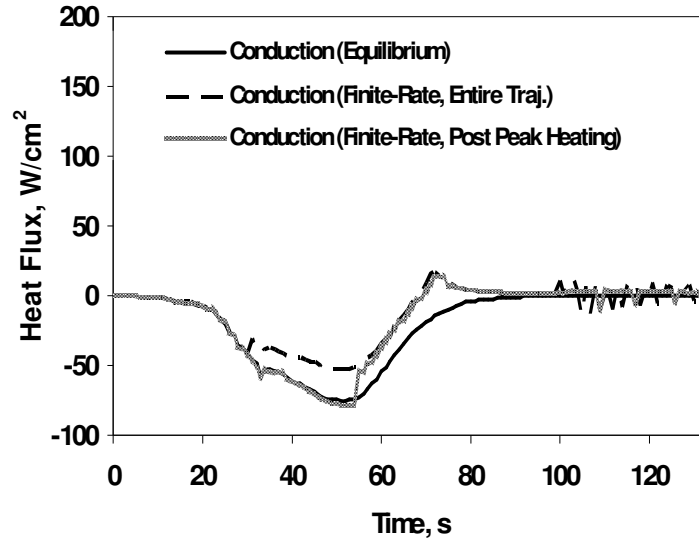


Figure 3.81. The surface conduction heat flux for the final design trajectory in equilibrium during the entire trajectory assumption, finite-rate during the entire trajectory assumption, and finite-rate after the peak heating assumption.

The conduction prediction continues to affect the in-depth heat fluxes. The trends of the in-depth heat flux predictions when nonequilibrium is applied after peak heating follow the same trends seen in that time frame when nonequilibrium is applied to the entire trajectory (Fig. 3.82) because a large conduction spike is not present. Overall, the in-depth predictions perform much more as expected, matching either equilibrium or nonequilibrium depending on the trajectory time, when finite-rate reactions are applied at peak heating than when the reactions were applied only at the heating tail.

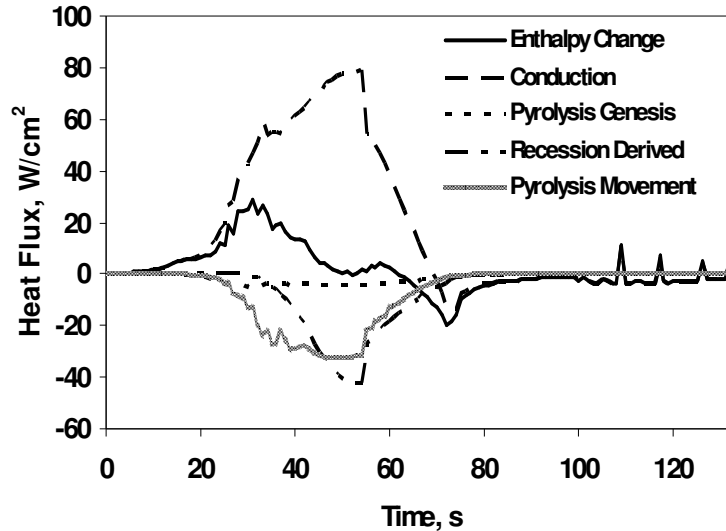


Figure 3.82. The in-depth heat fluxes for the final design trajectory in a finite-rate after the peak heating assumption.

Application of finite-rate reactions at peak heating eliminates the large jump in conduction seen when only the heating tail is considered to be occurring in nonequilibrium. It also allows for a lower recession rate and less overall ablation. This causes the thermocouple at a depth 0.64 cm to remain viable for temperature predictions for four seconds longer in the trajectory. The case also illustrates how the change from an equilibrium prediction to a nonequilibrium predictions affects the surface heating terms, in particular, the radiation leaving the surface due to decrease in surface temperature. These effects are not as clear later in the trajectory due to the heating on the surface approaching zero.

3.2.4 Stagnation Point – Post Sublimation

The previous two cases are based on heating concerns and not any concerns about the reactions on the surface. When the preliminary Stardust Return Capsule

trajectory was examined, sublimation drove the finite-rate predictions signifying its importance in the Park Model's application to the SRC trajectory. In the final design trajectory, finite-rate reactions are implemented when the surface temperature is over 3000 K, the activation temperature of sublimation.

In equilibrium, the surface temperature reaches over 3000 K at 39 seconds. Once the finite-rate assumption is turned on after crossing the temperature threshold, the surface temperature decreases to below 3000 K to 2940 K. However, the finite-rate assumption remains though the Park Model does not calculate the mass loss due to sublimation until the surface temperature is above 3000 K again. It does reach that plateau again at 43 seconds into the trajectory, so it is only a temporarily that sublimation is not taken into account. Figure 3.83 shows the surface temperature and TC 1 predictions for the sublimation case versus full trajectory equilibrium and nonequilibrium. TC 1 is not ablated past due to the recession rate being slowed down early in the trajectory. TC 1 does predict slightly higher temperatures when finite-rate sublimation is driving activation (a peak temperature of 2150 K) versus when nonequilibrium is applied throughout the trajectory (a peak temperature of 2000 K). The differing peak temperatures at TC 1 are due to the properties of the PICA and how heat travels through the material. Because the formation of char is quicker in the time region where equilibrium is assumed than during that same period in nonequilibrium, the higher thermal conductivity will drive in-depth temperatures slightly higher even if the nonequilibrium assumption is made at a later point.

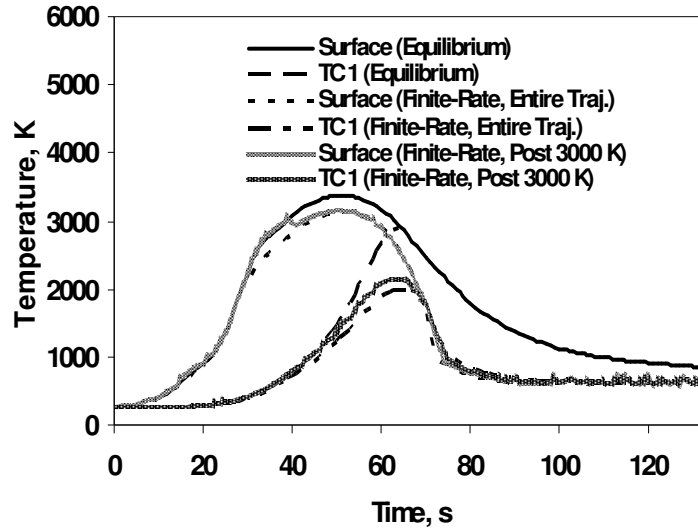


Figure 3.83. The surface temperature and the temperature at the depth of the first thermocouple couple for the final design trajectory in equilibrium during the entire trajectory assumption, finite-rate during the entire trajectory assumption, and finite-rate after 3000 K assumption.

The recession rate over the trajectory in the sublimation case follows the equilibrium rate when it is in equilibrium and the nonequilibrium rate when it is in nonequilibrium (Fig. 3.84), as expected. Since the majority of the trajectory is spent in nonequilibrium, the finite-rate assumption when sublimation is theorized to occur leads to a final recession close to what is predicted when finite-rate reactions occur over the entire trajectory (Fig. 3.85). The final recession prediction in this case is 0.62 cm, which is 15% more recession than the recession predicted with the full trajectory finite-rate assumption and 38% less than the final recession predicted in equilibrium. The char, pyrolysis gas, and total ablation rates (Figs. 3.86-3.88) when the finite-rate assumption is made beginning with sublimation follow the similar trend as previously seen in mirroring the equilibrium development while in equilibrium and the nonequilibrium development while in nonequilibrium.

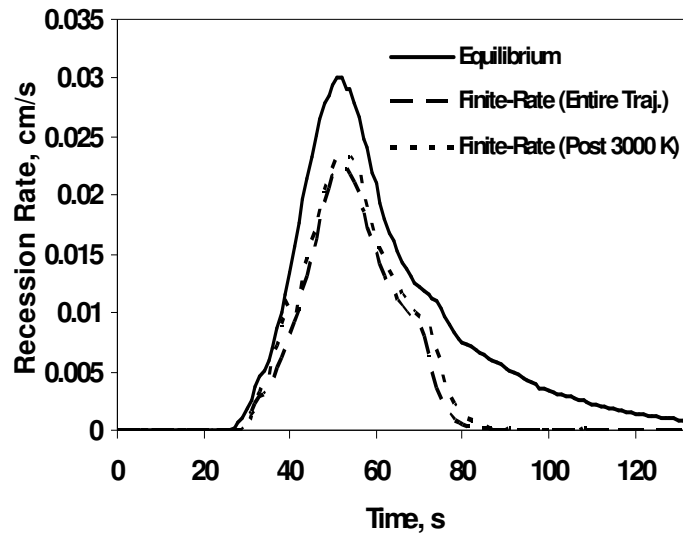


Figure 3.84. Recession rate predictions for the equilibrium assumption, finite-rate over the entire final design SRC trajectory assumption, and finite-rate after 3000 K assumption.

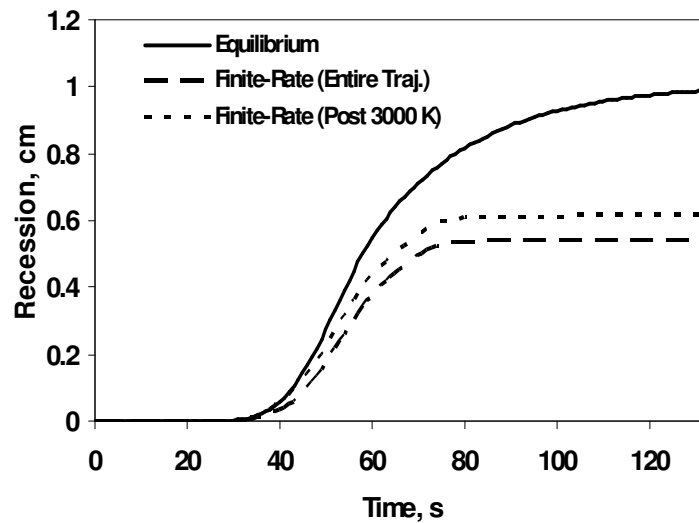


Figure 3.85. Recession predictions for the equilibrium assumption, finite-rate over the entire final design SRC trajectory assumption, and finite-rate after 3000 K assumption.

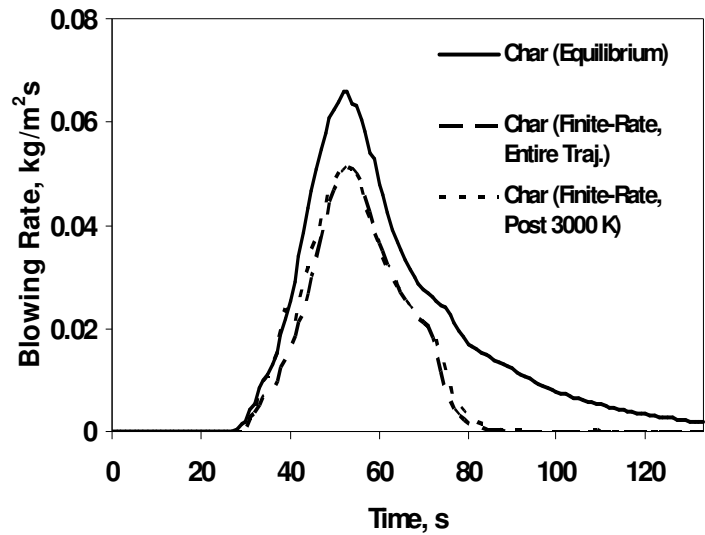


Figure 3.86. The char rate for the final design trajectory in equilibrium during the entire trajectory assumption, finite-rate during the entire trajectory assumption, and finite-rate after 3000 K assumption.

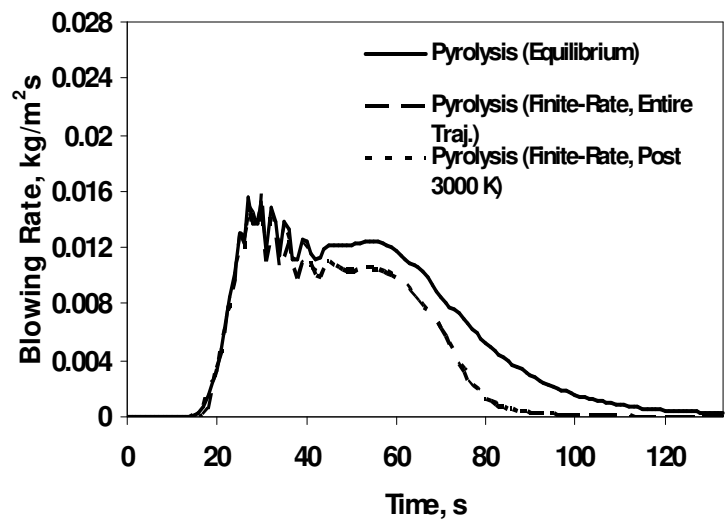


Figure 3.87. The pyrolysis gas rate for the final design trajectory in equilibrium during the entire trajectory assumption, finite-rate during the entire trajectory assumption, and finite-rate after 3000 K assumption.

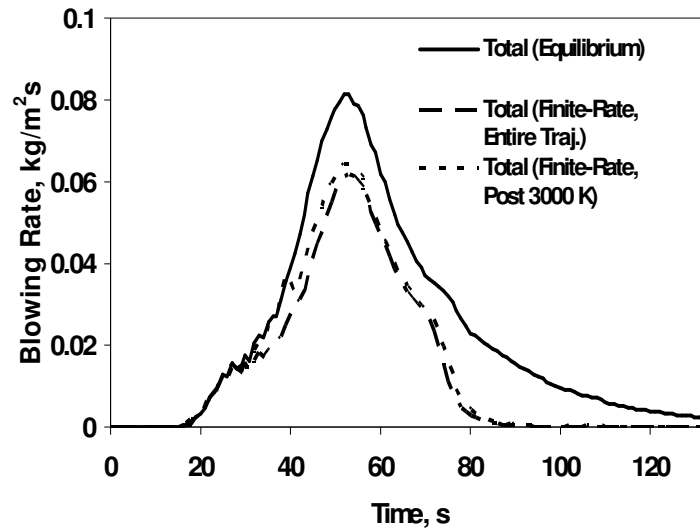


Figure 3.88. The total ablation rate for the final design trajectory in equilibrium during the entire trajectory assumption, finite-rate during the entire trajectory assumption, and finite-rate after 3000 K assumption.

For the surface heat fluxes, the radiation that leaves the surface follows the previous trends in being dependent on how the chemical assumption affects the surface temperature (Figs. 3.89 and 3.90). The char and pyrolysis gas heat fluxes also follow the equilibrium and nonequilibrium predictions in those activated phases (Fig. 3.91). The injected heat flux predictions experience a jump in the prediction at the point of finite-rate implementation to match full nonequilibrium predictions right at activation, but then becomes less than the full nonequilibrium predictions until it is within 10% of those full trajectory finite-rate predictions at roughly 60 seconds (Fig. 3.92). Because of the temporary decrease in surface temperature driving it below 3000 K previously noted, sublimation will appear to disappear briefly, like a discontinuity, driving the wall enthalpy calculations downward which will impact the injected heat flux. Though sublimation is only absent based on surface temperatures

for four seconds, the effects on the chemistry is longer lasting, as shown by the injected heat flux not matching the nonequilibrium case that keeps the application of sublimation in a more continuous manner. The effects of the application of finite-rate reactions once sublimation occurs on the conduction and in-depth heat flux terms follow the same trends as seen before: less conduction in the nonequilibrium phase because of the increase of injected heat flux leading to less internal heating. Implementation of the Park Model based on when of its reactions, sublimation, will take place leaves the predictions more closely trending towards nonequilibrium over the entire trajectory but still leaves roughly $\frac{1}{4}$ of the trajectory in equilibrium.

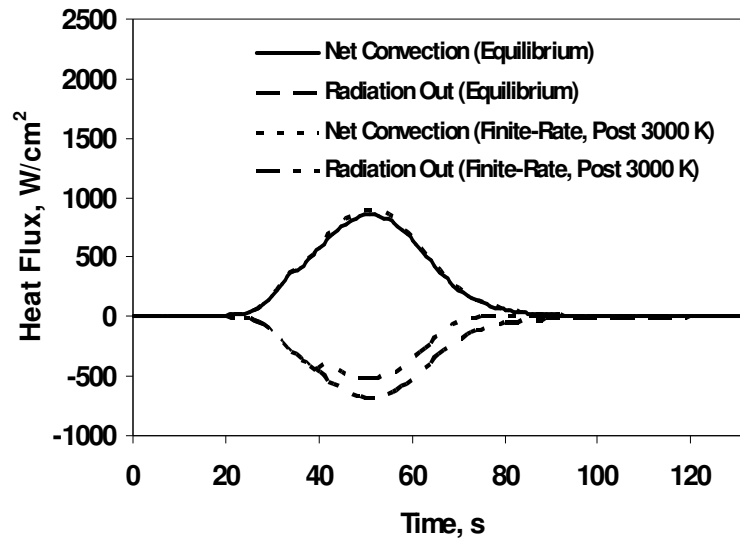


Figure 3.89. The net convection and radiation out heat flux predictions when equilibrium is assumed over the entire final design SRC trajectory and when finite-rate reactions are applied after 3000 K.

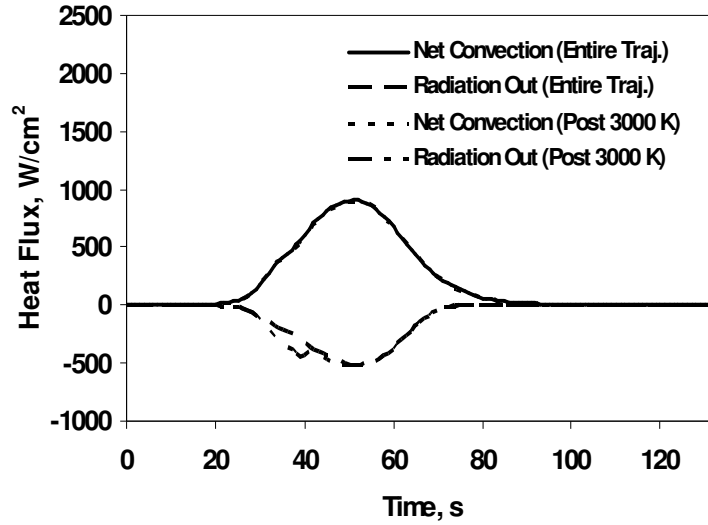


Figure 3.90. The net convection and radiation out heat flux predictions when nonequilibrium is assumed over the entire final design SRC trajectory and when finite-rate reactions are applied after 3000 K.

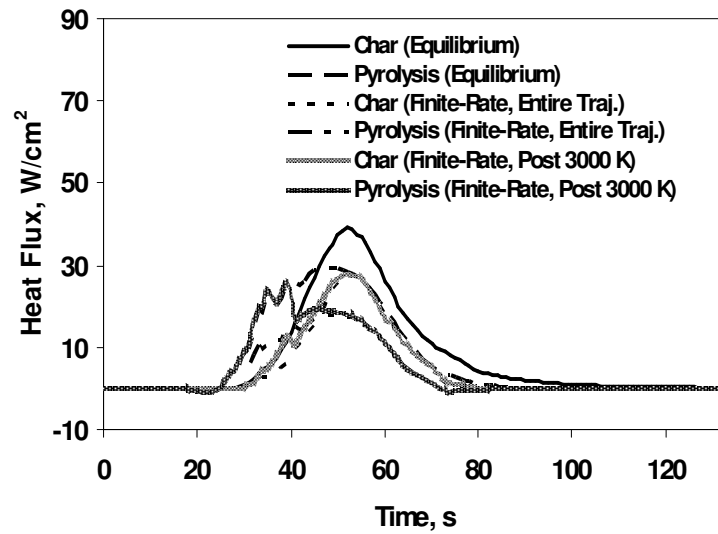


Figure 3.91. The char and pyrolysis gas heat fluxes on the surface for the final design trajectory in equilibrium during the entire trajectory assumption, finite-rate during the entire trajectory assumption, and finite-rate after the 3000 K assumption.

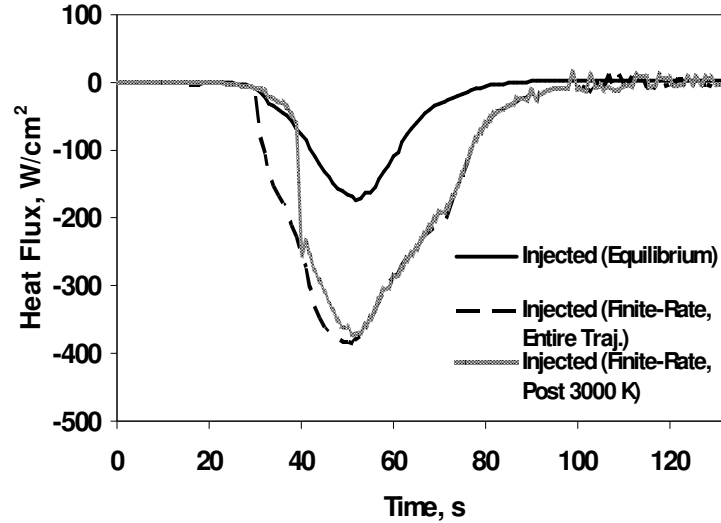


Figure 3.92. The injected heat flux for the final design trajectory in equilibrium during the entire trajectory assumption, finite-rate during the entire trajectory assumption, and finite-rate after 3000 K assumption.

3.2.5 Near Stagnation Point – Equilibrium

Analysis is carried out at the stagnation point due to previous pre-flight studies of the Stardust Return Capsule reentry concentrating on that point.^{8,10} Post-flight analysis also included predictions at the stagnation point for comparison purposes, with two additional points modeled, where at these points there were physical measurements. The material response at stagnation point itself is not physically measured because the capsule crashed and rolled upon its nose, invalidating physical measurements at the stagnation point.^{13,83,84} Figure 3.93 shows the physical locations of the near stagnation and flank core points where measurements of recession and char were taken. Computational and physical analysis of these two points in addition to the stagnation point aids in creating a clearer picture

of the effects of reentry over the entire heatshield. The same thermocouple depths and initial material temperature are used for the different locations.



Figure 3.93. The near stagnation and flank core points, along with a shoulder point, indicated in red on the Stardust Return Capsule.⁸⁴

At the near stagnation point, the computational heating environment is close to that found at the stagnation point (Figs. 3.94 and 3.95). The flow enthalpies at the two locations are the same and while at peak heating the heat transfer coefficient is less than what is found at the stagnation point. This causes less cold wall heating at the near stagnation point at peak heating when compared to the stagnation point (Fig. 3.94). Similarly, around peak heating the pressure profile at the near stagnation point diverges from the profile at the stagnation point (Fig. 3.95). This means that the near stagnation point may have similar predictions to the stagnation point until peak heating, when the decreased heating, from 1100 W/cm^2 to 1000 W/cm^2 , on the surface should cause a difference. Since pressure remains about the same at the

stagnation and near stagnation points, there is an equal chance of nonequilibrium based on the low number of possible molecular collisions.

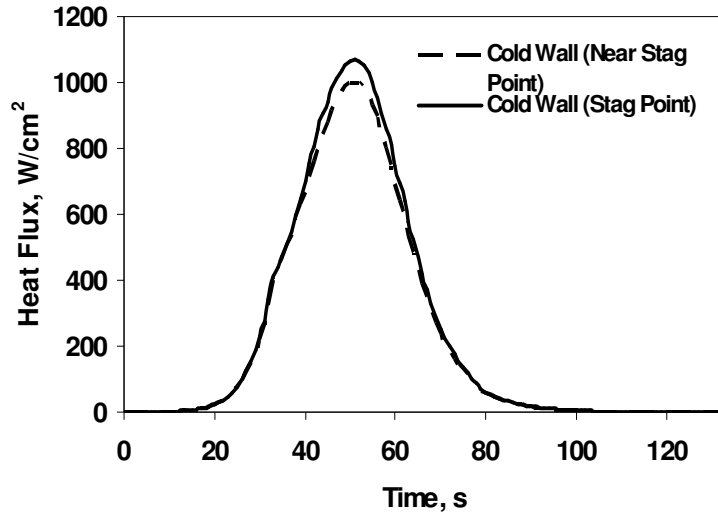


Figure 3.94. The cold wall heat flux for the stagnation point and the near stagnation point location for the final design SRC trajectory.

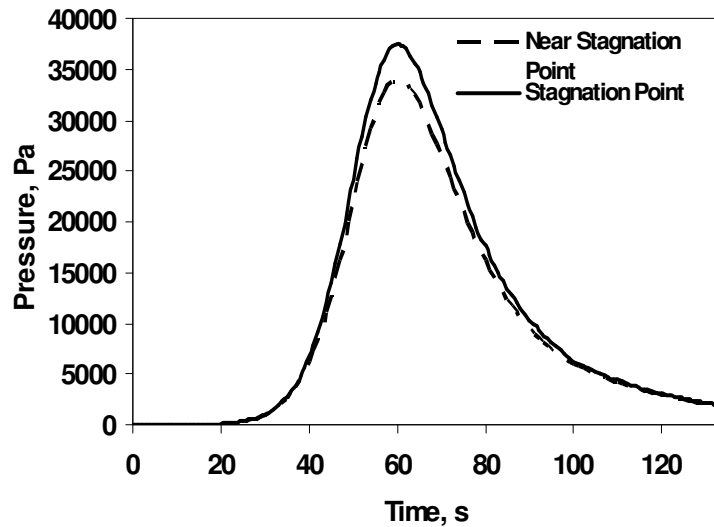


Figure 3.95. The pressure profile for the stagnation point and the near stagnation point location for the final design SRC trajectory.

The different environmental profiles for the two locations around peak heating clearly affects predictions of recession and the material changes that cause of recession. Figure 3.96 shows that the char ablation rate prediction at the near stagnation point follows the char rate at the stagnation point until peak heating; after peak heating, the char rate is less than at the stagnation point. Figure 3.97 shows no significant change in the pyrolysis gas rate. There is an overall decrease in the total ablation between the two locations as seen in Fig. 3.98 due to the decrease in char. Figures 3.99 and 3.100 compare the predicted recession and recession rate at the two points. Until peak heating, the recession rate and recession at the two points are the same. After peak heating, the recession rate decreases more at the near stagnation point than at the stagnation point and slows down recession, similar to what is seen in the char rate. Once the recession rate slows down, the recession predictions between the two locations start to differ. The final recession at the near stagnation point is less than that predicted at the stagnation point, 0.90 cm to 0.99 cm.

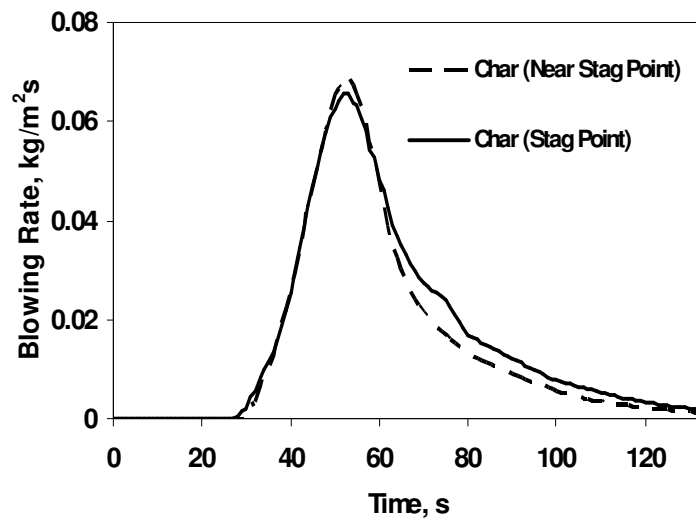


Figure 3.96. The predicted char ablation rate for the stagnation point and near stagnation point locations for the final design SRC trajectory.

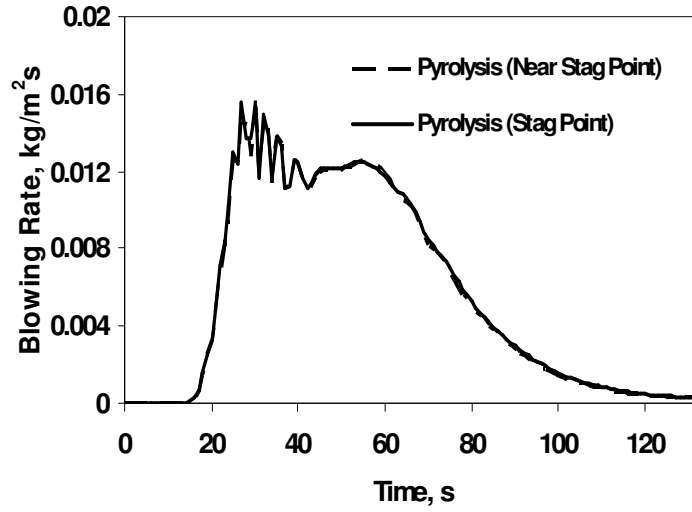


Figure 3.97. The predicted pyrolysis gas rate for the stagnation point and near stagnation point locations for the final design SRC trajectory.

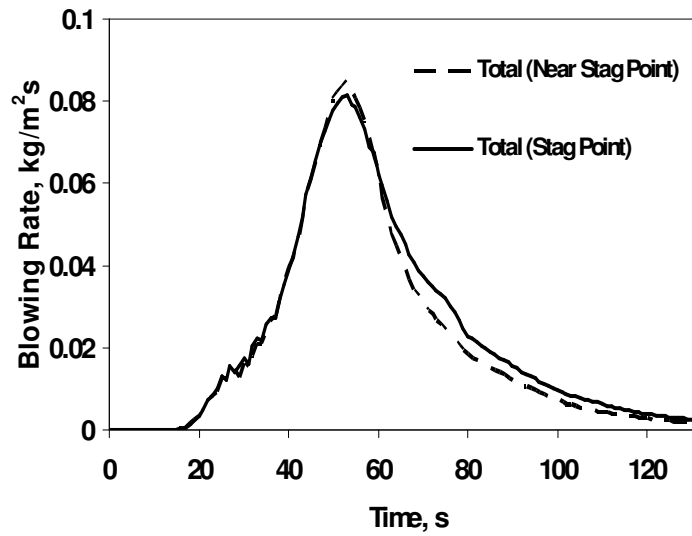


Figure 3.98. The total ablation rate for the stagnation point and near stagnation point locations for the final design SRC trajectory.

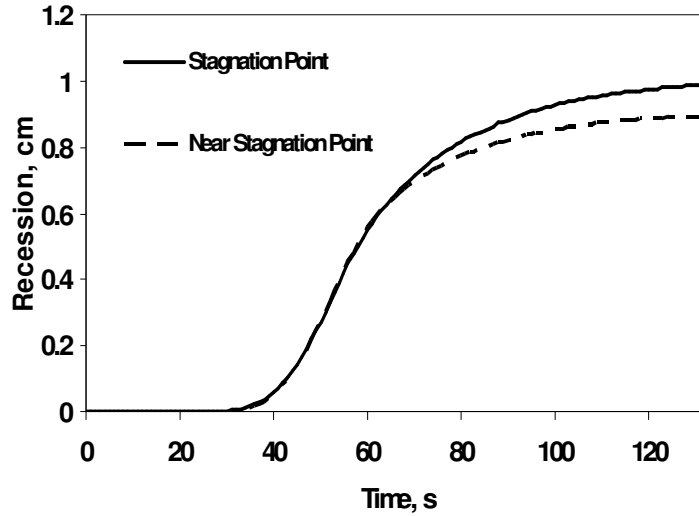


Figure 3.99. The recession profile for the stagnation and near stagnation points for the final design SRC trajectory

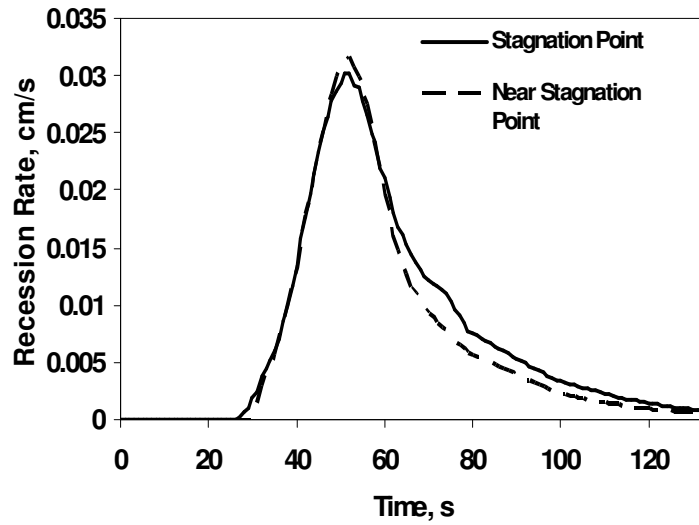


Figure 3.100. The recession rate profile for the stagnation and near stagnation points for the final design SRC trajectory

The peak heating on the surface at the near stagnation point is 3300 K compared to 3370 K predicted at the stagnation point, only a 2% difference. The first thermocouple is ablated past at nearly the same time and temperature at the near

stagnation point as at the stagnation point. Because of the same initial material temperature, similar environmental profiles and constant PICA thickness throughout the heatshield, the more in-depth thermocouples have a less than 2% difference between the near stagnation and stagnation point predictions.

There are larger differences in the surface heat flux predictions. The peak net convective heat flux at the near stagnation point is 780 W/cm² compared to the peak of 860 W/cm² at the stagnation point, a difference of less than 20%. This is similar to the difference in the cold wall heat flux at peak heating. Table 3.6 compares the peak near stagnation point surface heat fluxes to the peak stagnation point heat fluxes. The reason for the difference in the heat fluxes is due to less overall heating reaching the surface from the environment. Only the convective heat flux is entering the material from the environment and independent of what is going on at the surface or within the material. Char and pyrolysis gas heat come from inside the material, generated from heat delivered in-depth from earlier heating effects. The char and pyrolysis heat flux decrease due to less conduction entering the material and with a time delay associated with heat traveling through an insulative material, the peak values of the various fluxes do not change as much as the net convective heat flux at its peak value.

Table 3.6 The peak values of the surface heating terms for two points of the heatshield for the final SRC trajectory.

Heating Type	Flux (W/cm ²)	Flux (W/cm ²)
	(Relative to Surface) Stagnation Point	(Relative to Surface) Near Stagnation Point
Net Convection	860 (In)	780 (In)
Radiation	680 (Out)	630 (Out)
Char Chemistry	39 (In)	40 (In)
Pyrolysis Gas Chemistry	30 (In)	27 (In)
Injected Chemistry	170 (Out)	150 (Out)
Conduction	75 (Out)	73 (Out)

The small difference between the peak conduction on the surface at the two points results in similar in-depth heating profiles, at least up until the peak heating. The difference between the heat fluxes at the two locations is less than 8% for first 50 seconds. After that, some of the heat fluxes start to differ largely between the two locations because of the differences in heating that can reach into the material. Figures 3.101 and 3.102 are the heat fluxes going into and going out of the surface heat flux, respectively, and Fig. 3.103 is the in-depth heat flux percent differences between the two locations as a function of trajectory time. The largest percent differences appear when the prediction is about or less than 1 W/cm^2 , it is due to internal FIAT round off error.

Table 3.7 compares the total heat loads found at the stagnation point and at the near stagnation point. Because the heat fluxes are smaller at the near stagnation point, the total heat load is also smaller at that location. The same trends seen in equilibrium at the stagnation point are present in the heat loads: the convective and radiative heat load mirror each other, with the injected heat load also contributing to keeping the material in heating equilibrium.

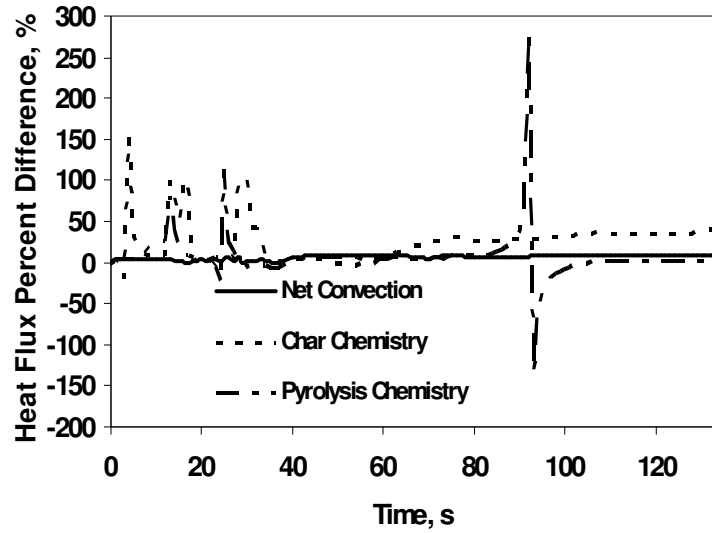


Figure 3.101. The percent difference of the surface heat fluxes that are entering the surface when considering the stagnation point and near stagnation point locations for the final design SRC trajectory.

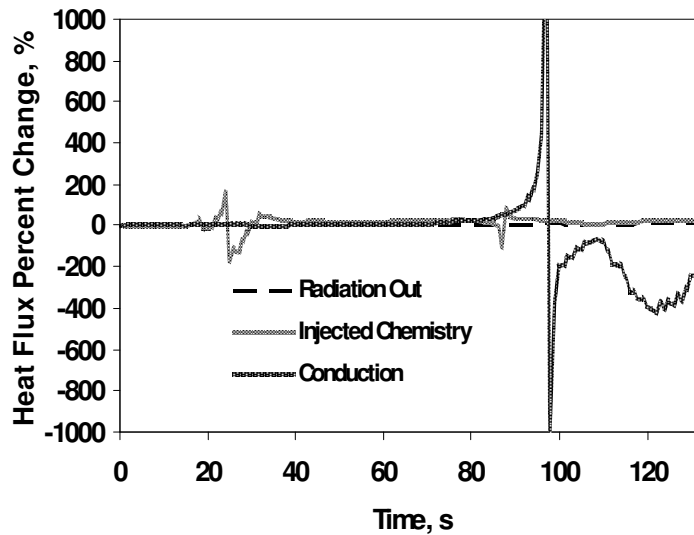


Figure 3.102. The percent difference of the surface heat fluxes that are leaving the surface when considering the stagnation point and near stagnation point locations for the final design SRC trajectory.

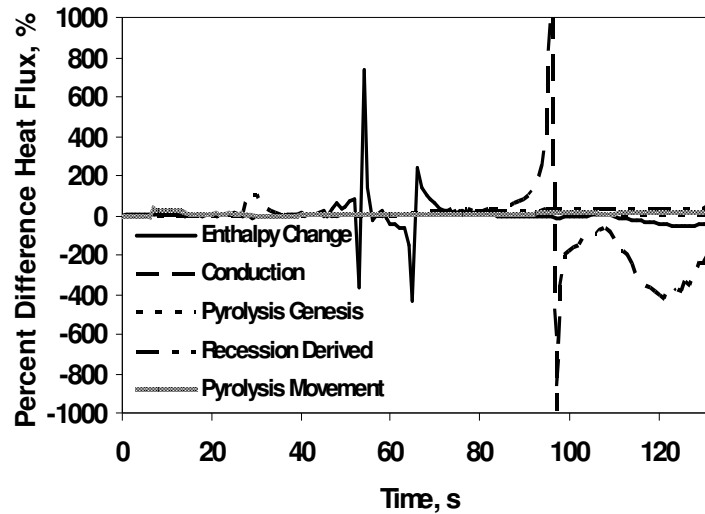


Figure 3.103. The percent difference of the in-depth heat fluxes when considering the stagnation point and near stagnation point locations for the final design SRC trajectory.

Table 3.7 The total heat loads of the surface heating terms at the stagnation and near stagnation point for the final SRC trajectory.

Heating Type	Load	Load
	(J/cm ²) (Relative to Surface) Stagnation Point	(W/cm ²) (Relative to Surface) Near Stagnation Point
Net Convection	26000 (In)	24000 (In)
Radiation	21000 (Out)	20000 (Out)
Char Chemistry	980 (In)	910 (In)
Pyrolysis Gas Chemistry	880 (In)	850 (In)
Injected Chemistry	3900 (Out)	3200 (Out)
Conduction	2700 (Out)	2600 (Out)

At the near stagnation point, the predictions are similar in magnitude and trends to what is predicted at the stagnation point. Any differences are due to the peak heating value at the near stagnation point being less than the peak value at the stagnation point. The similarities will allow for limited extrapolation of the measured

data at the near stagnation point to estimate what may have physically occurred at the stagnation point.

3.2.6 Near Stagnation Point – Nonequilibrium

An analysis of how finite-rate reactions at the near stagnation point affect predictions will show the impact of nonequilibrium. Though the equilibrium predictions at the near stagnation point are similar to those at the stagnation point because nonequilibrium calculations include an additional parameter, the heat transfer coefficient for nondimensionalization, the differences between the stagnation point and near stagnation point predictions are more varied in nonequilibrium. The coefficient at peak heating, which is smaller at the near stagnation point than the stagnation point, is used to nondimensionalize the mass rate for the entire trajectory.

The recession at the near stagnation point while finite-rate reactions are occurring during the entire length of the trajectory is presented in Fig. 3.104. In equilibrium, the final recession is 0.90 cm; in nonequilibrium, the final recession is 0.46 cm. It is a 49% reduction in the recession which is similar to the 45% reduction of recession between equilibrium and nonequilibrium at the stagnation point. Analysis of the charring rates for finite-rate and equilibrium at both points (Fig. 3.105) shows that at peak heating, the finite-rate charring rate at the near stagnation point is 26% lower than at the stagnation point, affecting the recession rate. The difference between the pyrolysis gas rate when finite-rate reactions are taking place and when they are not at the near stagnation point follows the same trend found at the stagnation point (Fig. 3.106), and the same conclusions can be reached about the important role of the charring rate on the surface. The total ablation rate is seen in

Fig. 3.107. Since the char rate is much less in the finite-rate assumption case, the total rate is similarly smaller when considering finite-rate reactions.

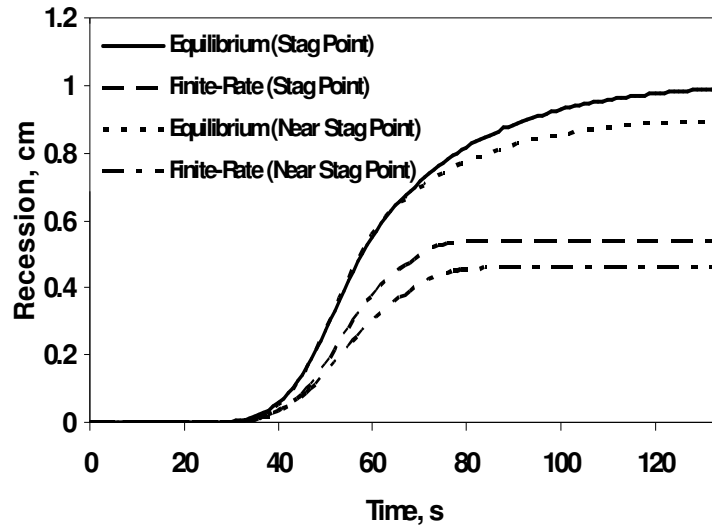


Figure 3.104. The recession profiles for the stagnation point and near stagnation point in equilibrium and with finite-rate reactions for the final design SRC trajectory.

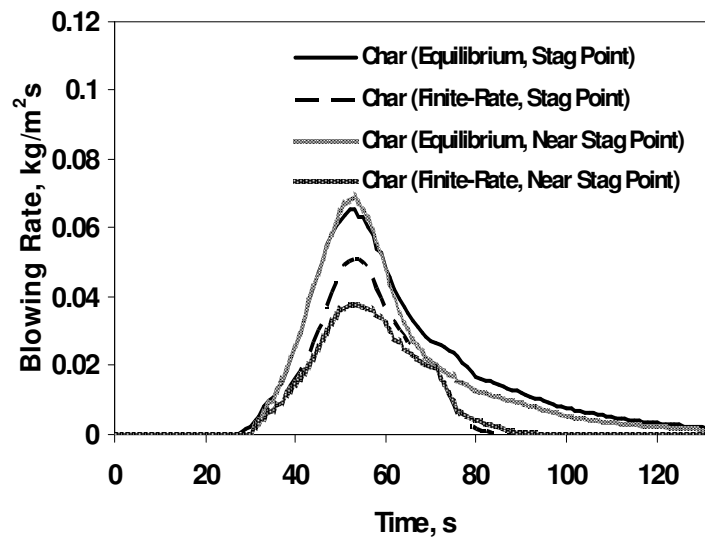


Figure 3.105. The char ablation rates for the stagnation point and near stagnation point in equilibrium and with finite-rate reactions for the final design SRC trajectory.

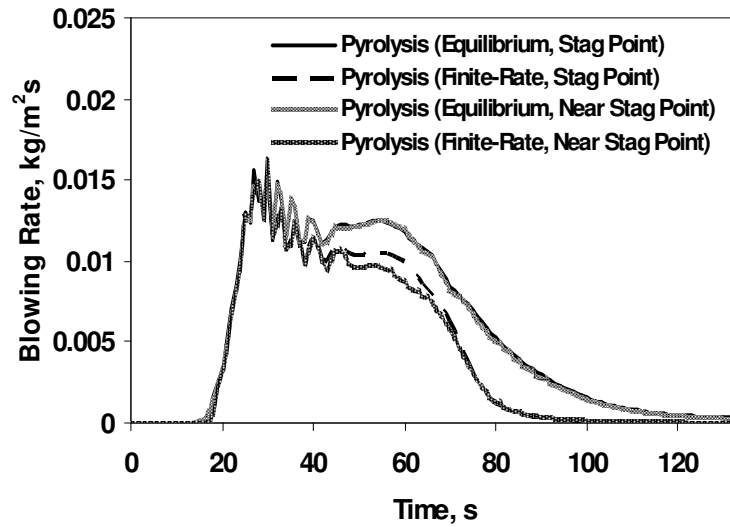


Figure 3.106. The pyrolysis gas rates for the stagnation point and near stagnation point in equilibrium and with finite-rate reactions for the final design SRC trajectory.

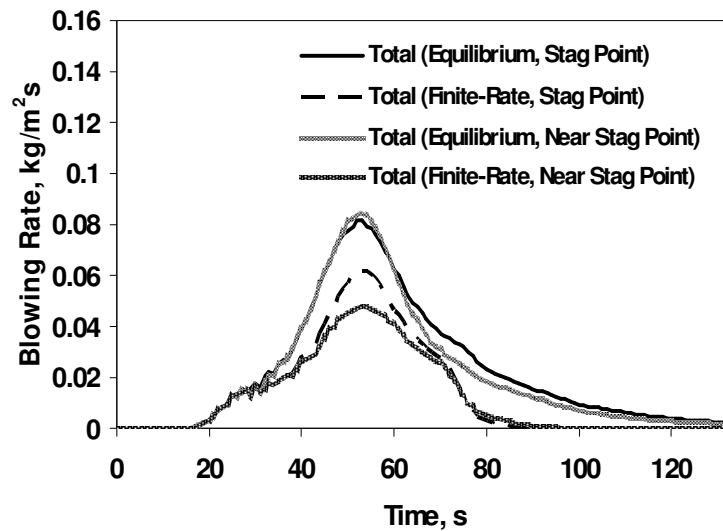


Figure 3.107. The total ablation rates for the stagnation point and near stagnation point in equilibrium and with finite-rate reactions for the final design SRC trajectory.

The temperature trends seen at the near stagnation point in nonequilibrium are similar to those seen at the stagnation point, although the temperatures at the near

stagnation will be lower than those at the stagnation point. Figure 3.108 compares the predicted temperatures at the surface and at TC 1 for the near stagnation point. The peak temperature on the surface during the finite-rate process is 3010 K, which is 8.8% less than the equilibrium peak temperature. The temperature profile at the TC 1 is consistent with both the material properties of the PICA material and the effects of the finite-rate assumption. Because the recession is slower during the finite-rate calculations, TC 1 is not ablated past at the near stagnation point, much like what occurs at the stagnation point.

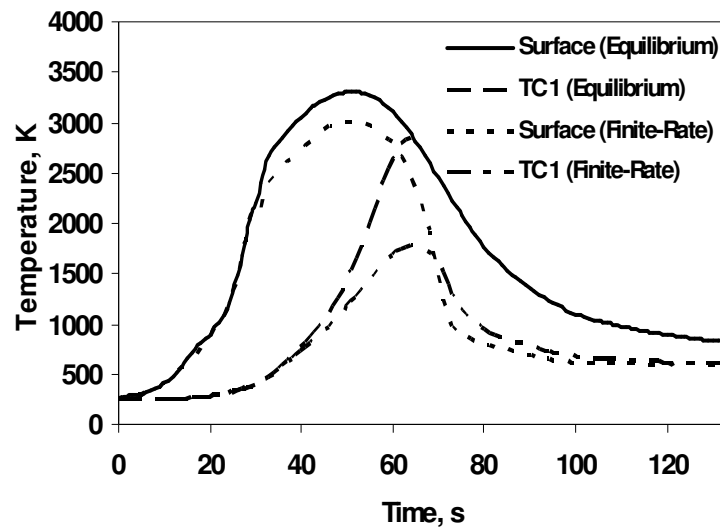


Figure 3.108. The temperature profiles at the surface and at the TC 1 depth location at the near stagnation point in both equilibrium and nonequilibrium for the final design SRC trajectory.

The heating on the surface of the heatshield at the near stagnation point during a nonequilibrium analysis follows the trends seen at the stagnation point, that is, some of the heating terms become less while there are increases to the injected heat flux and net convective heat flux. Table 3.8 compares the heating on the surface between

the equilibrium and nonequilibrium cases at the near stagnation point. Additionally, at near stagnation point there are fewer oscillations in the injected heat flux and conduction profiles (Figs. 3.109 and 3.110). This is due to the difference between the heat transfer coefficient being used to nondimensionalize the finite-rate ablation term during the heating tail at the stagnation and near stagnation points. The lower heat transfer coefficients, which are used for nondimensionalization, help construct a better finite-rate B' table so that there is a minimization of interpolation effects.

The total heat loads in nonequilibrium versus equilibrium at the near stagnation point are presented in Table 3.9 and follow what was previously seen at the stagnation point. The in-depth heat fluxes are less in the finite-rate case at the near stagnation point due to decreased conduction. The general trend in-depth is similar to the trends seen at the stagnation point: the conduction and enthalpy change terms mirror each other and are the largest fluxes (Fig. 3.111). The in-depth heat flux similarities between the two locations both in equilibrium and nonequilibrium are another example of the consistency of the material properties of the PICA material throughout the heatshield layout.

Table 3.8. The peak values of the surface heating terms at the near stagnation point during two chemical assumptions for the final SRC trajectory.

Heating Type	Flux (W/cm ²)	Flux (W/cm ²)
	(Relative to Surface) Equilibrium	(Relative to Surface) Finite-Rate
Net Convection	780 (In)	870 (In)
Radiation	630 (Out)	430 (Out)
Char Chemistry	40 (In)	19 (In)
Pyrolysis Gas Chemistry	27 (In)	15 (In)
Injected Chemistry	150 (Out)	430 (Out)
Conduction	73 (Out)	44 (Out)

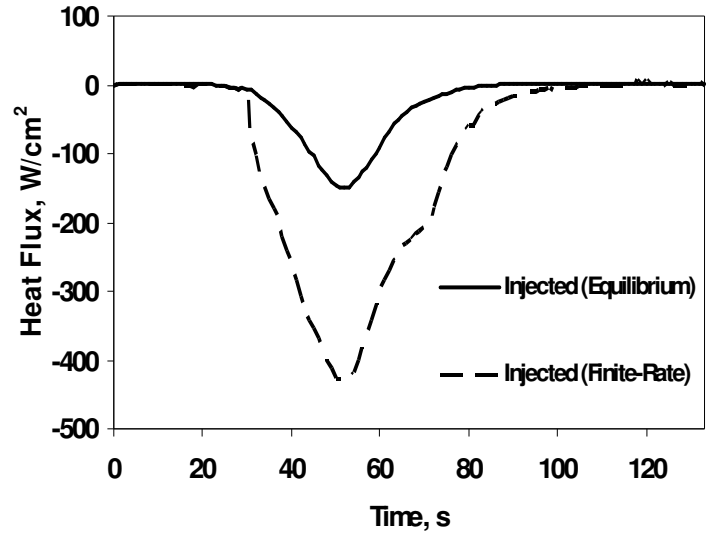


Figure 3.109. The injected heat flux at the near stagnation point when undergoing equilibrium and nonequilibrium reactions for the final design SRC trajectory.

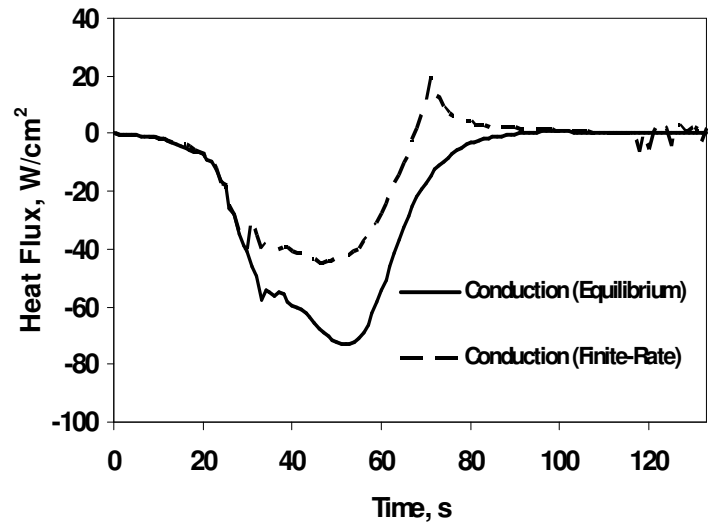


Figure 3.110. The injected heat flux at the near stagnation point when undergoing equilibrium and nonequilibrium reactions for the final design SRC trajectory.

Table 3.9. The total heat loads of the surface heating terms at the near stagnation point in equilibrium and nonequilibrium for the final SRC trajectory.

Heating Type	Load	Load
	(J/cm ²) (Relative to Surface) Equilibrium	(W/cm ²) (Relative to Surface) Finite-Rate
Net Convection	24000 (In)	26000 (In)
Radiation	20000 (Out)	12000 (Out)
Char Chemistry	910 (In)	440 (In)
Pyrolysis Gas Chemistry	850 (In)	400 (In)
Injected Chemistry	3200 (Out)	13000 (Out)
Conduction	2600 (Out)	1400 (Out)

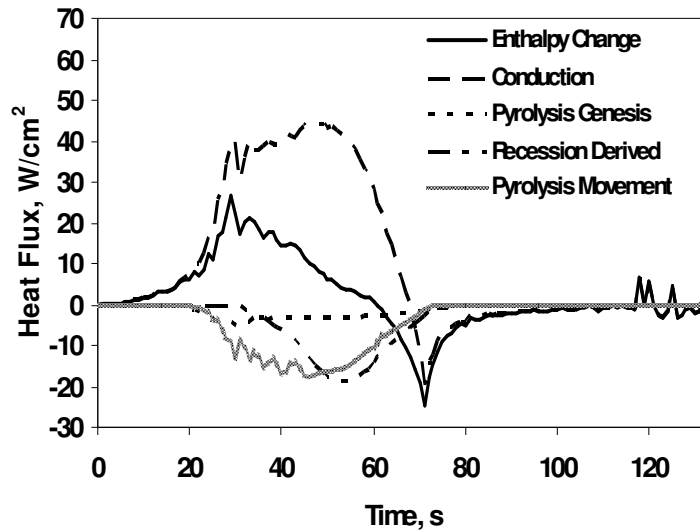


Figure 3.111. The in-depth heat fluxes at the near stagnation point when undergoing nonequilibrium reactions for the final design SRC trajectory.

The impact of finite-rate reactions at the near stagnation point does not greatly differ from the impact seen at the stagnation point. The near stagnation point has a similar environment to the profile seen at stagnation point, though the near stagnation point has a slightly lower heat pulse. This leads to having similar heat fluxes on the surface and in-depth and recession profiles both in equilibrium and nonequilibrium for the two locations.

3.2.7 Core 2 – Point 47 – Equilibrium

The second core point, labeled Core 2 – Point 47 for the analysis of the Stardust Return Capsule analysis, is further away from the stagnation point than the first core point. Because of its distance away from the stagnation point the Core 2 – Point 47 location will have a markedly lower heating and pressure profile when compared to the profiles seen at the stagnation and near stagnation points (Figs. 3.112-3.114). Though Core 2 – Point 47 location experiences a heat pulse during the same time period as the stagnation point, the peak cold wall heat flux is 570 W/cm², which is 47% lower than the peak cold wall heat flux at the stagnation point. The lesser heating at the point should lead to lower recession when compared to the stagnation point regardless of whether the analysis is being done in equilibrium or with finite-rate reactions. Based on pressure alone, there should be less molecular collisions at the Core 2 point than at the other two points, but with lower heating, surface temperature will be lower than at the stagnation point, counteracting the lowered pressure.

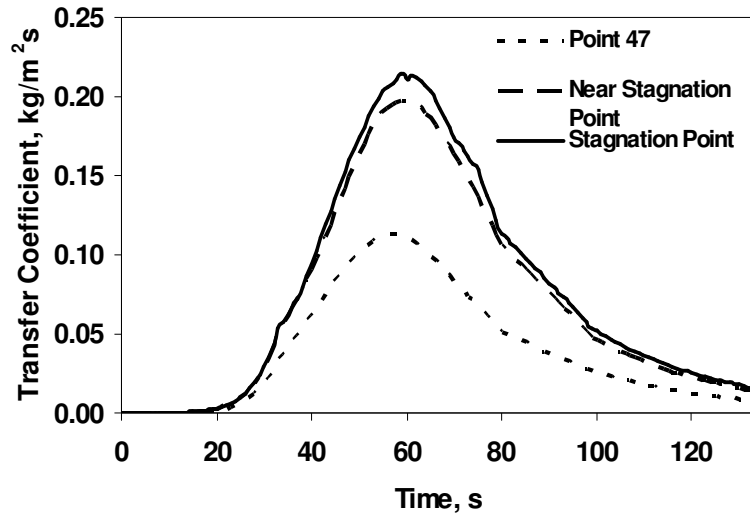


Figure 3.112. The heat transfer coefficient for the three locations on the SRC heatshield for the final design trajectory.

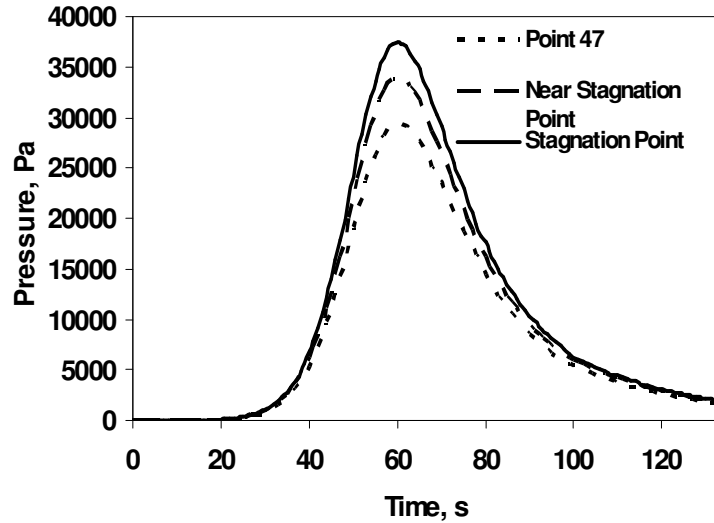


Figure 3.113. The surface pressure for the three locations on the SRC heatshield for the final design trajectory.

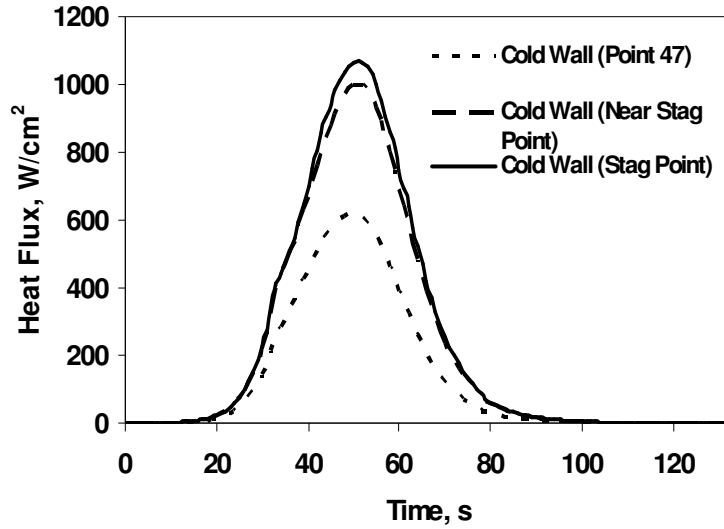


Figure 3.114. The cold wall heat flux for the three locations on the SRC heatshield for the final design trajectory.

As seen in Fig. 3.115, the recession rate is slower at the Core 2 – Point 47 location than the previous two points and causes a final recession of 0.37 cm, 63% lower than the recession predicted at the stagnation point (Fig. 3.116). The recession and its rate is driven by the total ablation rate, which at the Core 2 – Point 47 location, has a peak value of 0.033 kg/m^2s , with the char rate contributing 0.022 kg/m^2s to the mass loss rate at its peak. The char ablation rate is 67% lower than the ablation rate at the stagnation point, while the total rate is 60% lower than the total rate found at that location. The pyrolysis gas rate peak at the Core 2 – Point 47 location is similar to what is predicted at the stagnation point (Fig. 3.117). At Core 2 – Point 47 though, there is more of a decline after the peak than what was seen at the stagnation point, starting at when the SRC is 40 seconds into its entry. This may be due to the decrease in heat flux acting upon the surface which causes less heat to be delivered internally to the heatshield and results in less pyrolysis gas formation.

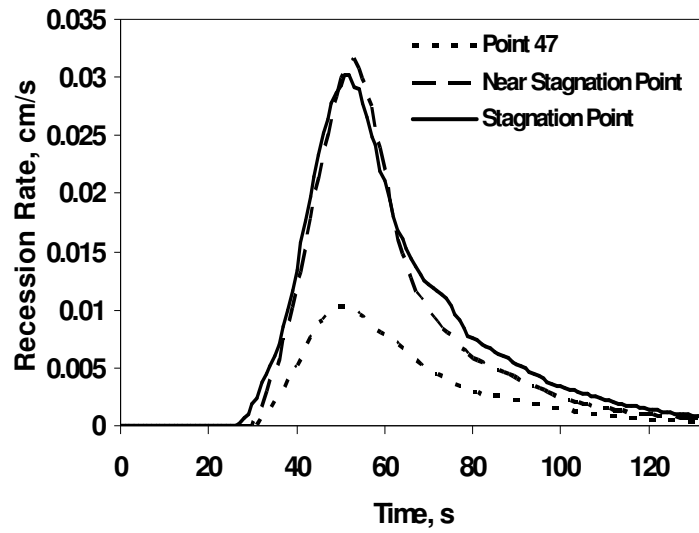


Figure 3.115. The recession rate at the three locations on the SRC heatshield for the final design trajectory.

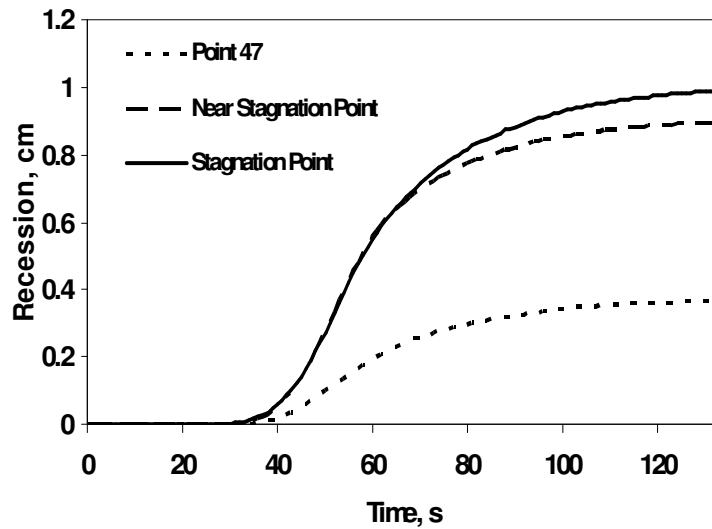


Figure 3.116. The recession profile at the three locations on the SRC heatshield for the final design trajectory.

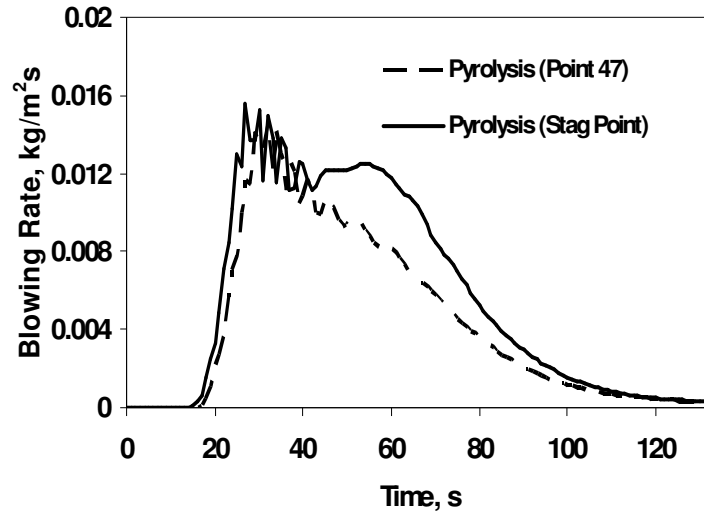


Figure 3.117. The pyrolysis gas rate at the Point 47 and stagnation point locations for the final design SRC trajectory.

Another result of the decrease in the environmental heating at the Core 2 – Point 47 location is the decrease in surface temperature. The peak surface temperature at the Core 2 location is 3060 K, which is cooler than the temperature found on the surface at the stagnation point. Though the temperature found at the interface of the PICA material and the epoxy remain the same at all locations due to the material properties of PICA, at the first thermocouple depth, 0.64 cm, the decrease in overall heating at the Core 2 point is reflected again. At TC 1, the peak predicted temperature is 1610 K at Core 2 – Point 47 and 2890 K at the stagnation point. Also, as illustrated in Fig. 3.118, TC 1 is not ablated past at Core 2 – Point 47 because of the small recession rate at that location and the thermocouple is able to predict in-depth temperatures for the entire trajectory.

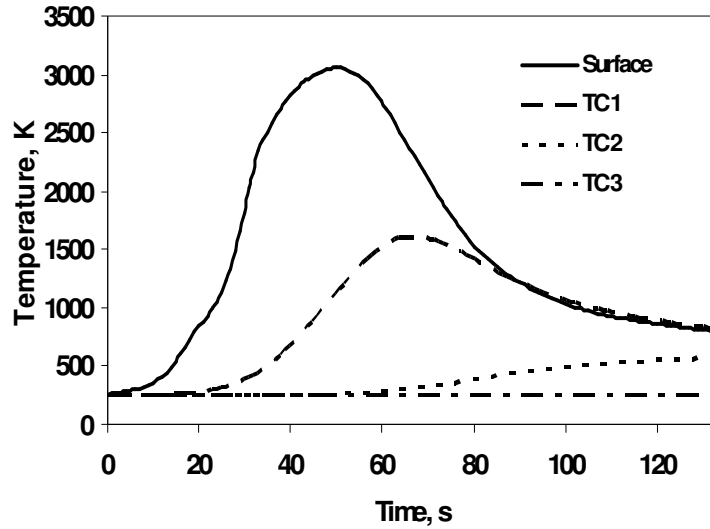


Figure 3.118. The predicted surface temperature and in-depth temperatures at the Core 2 – Point 47 location for the final design SRC trajectory.

Table 3.10 compares the peak surface heat fluxes at the stagnation point and Core 2 location. The chemistry heat fluxes are decreasing the as there is movement away from the stagnation point, with reductions over 50%. This is due to less heat entering the material from the surface, leaving less energy to use in chemical reactions that form char and pyrolysis gas. Table 3.11 is a comparison of the total heat fluxes at the stagnation point and Core 2 – Point 47 locations and Table 3.12 compares the in-depth heat fluxes. The heat loads are less overall than at the stagnation point due to less heating on the surface, but follow the same trends as seen at the stagnation point. The insulative properties of PICA coupled with the thickness of the heatshield means that the temperature in-depth remains constant the deeper one analyzes into the material, regardless of heating on the surface and will likely remain the same virgin material and properties. So the change in time of the temperature in-

depth, integrated over the entire thickness, will be very similar at different locations meaning that the enthalpy change will also be very similar at the points.

Table 3.10. The peak values of the surface heating terms for two points of the heatshield for the final SRC trajectory.

Heating Type	Flux (W/cm ²)	Flux (W/cm ²)
	(Relative to Surface) Stagnation Point	(Relative to Surface) Point 47
Net Convection	860 (In)	520 (In)
Radiation	680 (Out)	460 (Out)
Char Chemistry	39 (In)	12 (In)
Pyrolysis Gas Chemistry	30 (In)	17 (In)
Injected Chemistry	170 (Out)	49 (Out)
Conduction	75 (Out)	45 (Out)

Table 3.11 The total heat loads of the surface heating terms at the stagnation and Core 2 – Point 47 location for the final SRC trajectory.

Heating Type	Load (J/cm ²)	Load (W/cm ²)
	(Relative to Surface) Stagnation Point	(Relative to Surface) Point 47
Net Convection	26000 (In)	15000 (In)
Radiation	21000 (Out)	13000 (Out)
Char Chemistry	980 (In)	310 (In)
Pyrolysis Gas Chemistry	880 (In)	440 (In)
Injected Chemistry	3900 (Out)	1000 (Out)
Conduction	2700 (Out)	1500 (Out)

Table 3.12 The absolute value of the peak in-depth heat flux terms at the stagnation and Core 2 – Point 47 location for the final SRC trajectory.

Heating Type	Flux (W/cm ²)	Flux (W/cm ²)
	Stagnation Point	Point 47
Enthalpy Change	28	28
Conduction	75	46
Pyrolysis Genesis	4.8	4.6
Recession Derived	40	12
Pyrolysis Movement	32	20

There is less recession and less heat entering the material at the Core 2 – Point location due to less heating from the environment. This means there is less heat leaving both the surface and in-depth. Despite significantly less heating, the peak enthalpy change in-depth remained the same as it is at other locations, signifying its reliance more on the material properties of the PICA material than solely on the amount of heat present within the heatshield.

3.2.8 Core 2 – Point 47 – Nonequilibrium

In equilibrium at the Core 2 – Point 47 location, the surface does not heat past the 3000 K threshold for sublimation to take place by more than a few tens of Kelvin. Thus, the impact of sublimation is not as greatly felt because the surface does not get as hot as the other two locations and the changes between an equilibrium and nonequilibrium case are reduced though the general trends do follow what was previously seen at the stagnation point and near stagnation point. Recession rate and final recession is reduced (Fig. 3.119 and 3.120), with the final recession being 0.24 cm. This is the smallest change in recession in terms of magnitude between the equilibrium and nonequilibrium cases of the three points, but it is still comparable to the relative magnitude of the reduction, or percent change, which at the Core 2 location, is a 34% reduction. The stagnation point recession experienced a change of 45%, while the near stagnation point experienced a reduction of 49%, so the percent change at Core 2 – Point 47, while smaller due to the heat threshold for sublimation being limited, is no more than 15% smaller than those other points. This means that the other three reactions in the Park Model are being relied on more the further away one goes from the stagnation point and they have some effect on the final prediction.

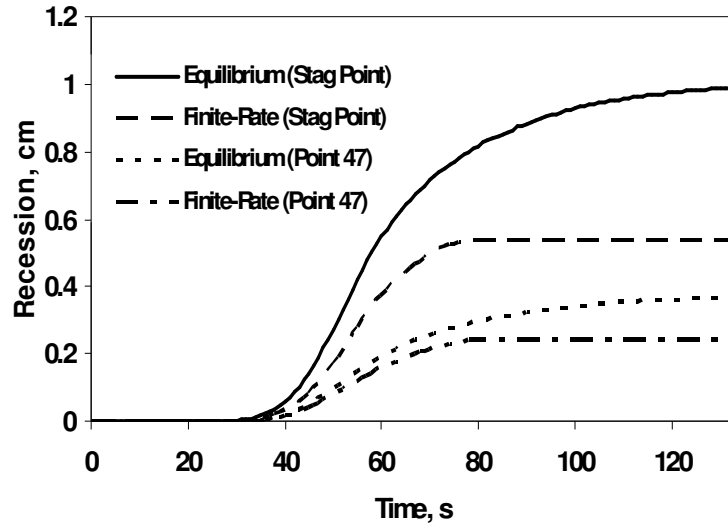


Figure 3.119. The recession profile comparing the Core 2 - Point 47 location to the stagnation point for the final design SRC trajectory.

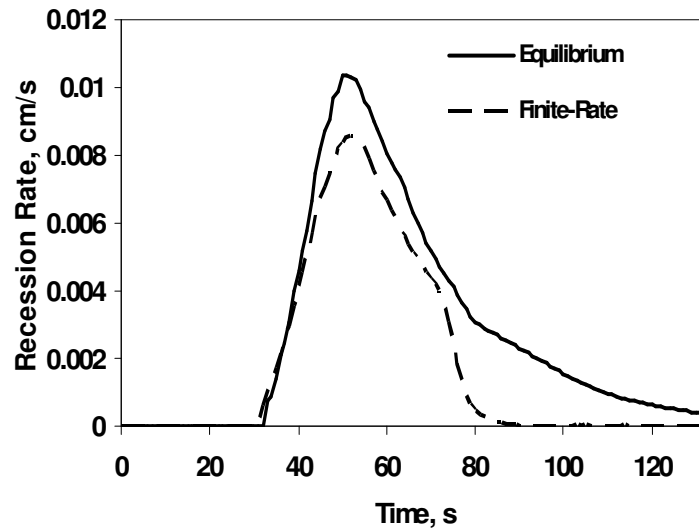


Figure 3.120. The recession rate profile comparing the equilibrium to nonequilibrium implementation at the Core 2 – Point 47 location for the final design SRC trajectory.

The peak surface temperature at Point 47 in nonequilibrium is 2910 K and is only 5% lower than the peak temperature during equilibrium (Fig. 3.121), with the temperature profiles in the two chemical cases being similar until peak heating. After

peak heating there is a divergence between the predictions and may be due to sublimation being activated post 3000 K. Since in equilibrium TC 1 remains a viable location for temperature predictions, the difference between equilibrium and nonequilibrium for TC 1 is not as important since TC 1 predicts temperature for the entire trajectory in both chemical cases. The peak temperature at the TC 1 depth in nonequilibrium is 1470 K, which is only 140 K less than the peak temperature at that depth in equilibrium.

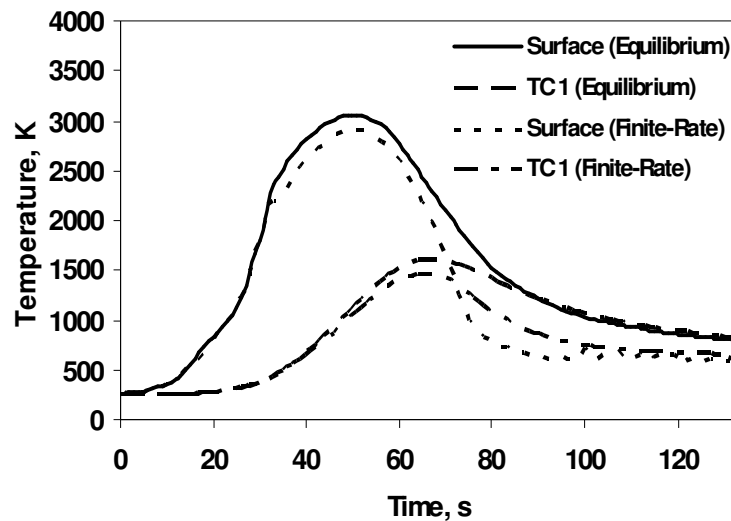


Figure 3.121. The surface and TC 1 temperature profile comparing the equilibrium to nonequilibrium implementation at the Core 2 – Point 47 location for the final design SRC trajectory.

Like at the other points, the char and total ablation rate predictions are significantly reduced when finite-rate reactions are applied to the entire trajectory at the Core 2 – Point 47 location, while the pyrolysis gas rate prediction in nonequilibrium remains close to the equilibrium predictions (Figs. 3.122-3.124). For the char and total rates, the reductions are like the reductions in recession and temperature: smaller in magnitude and percent change than is predicted at the

previous two locations. In analyzing the predictions in equilibrium and nonequilibrium, Table 3.13 compares the peak surface heat fluxes on the surface, Table 3.14 compares the heat loads, and Table 3.15 compares the in-depth heat fluxes. The heat flux and load predictions follow the trends seen before at the other points on the heatshield, with reductions in most of the terms except the net convection (due to decrease in the B' term) and the injected heat flux. Despite surface temperatures being lower at the Core 2 location and nearing the threshold of sublimation activation, the nonequilibrium predictions are only affected in terms of the magnitude of change and not in the general development. The three locations analyzed in equilibrium and nonequilibrium can serve as a basis of comparison when looking at previous post-flight analysis and the measured values at those locations to gauge the impact of finite-rate reactions on the predictions.

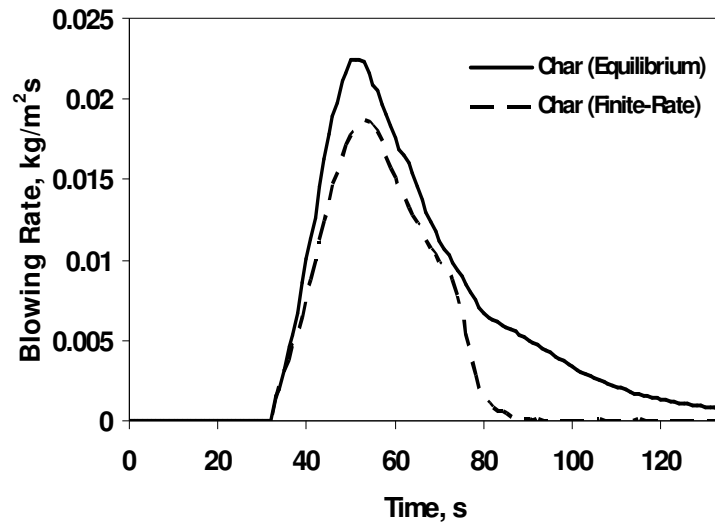


Figure 3.122. The char ablation rate comparing the equilibrium to nonequilibrium implementation at the Core 2 – Point 47 location for the final design SRC trajectory.

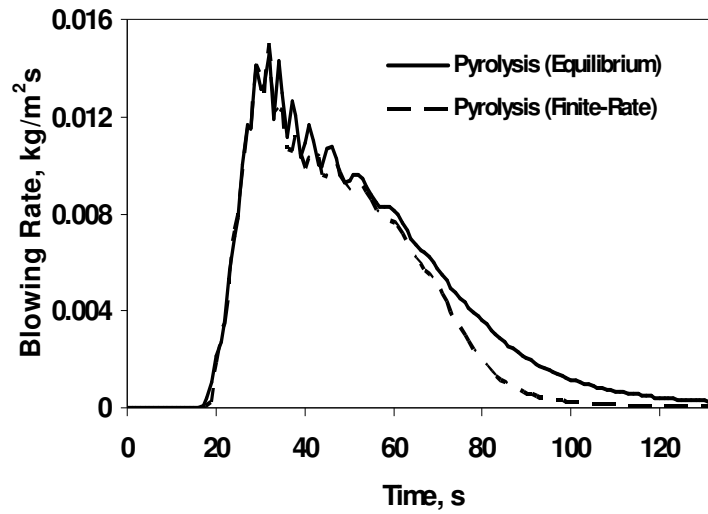


Figure 3.123. The pyrolysis gas rate comparing the equilibrium to nonequilibrium implementation at the Core 2 – Point 47 location for the final design SRC trajectory.

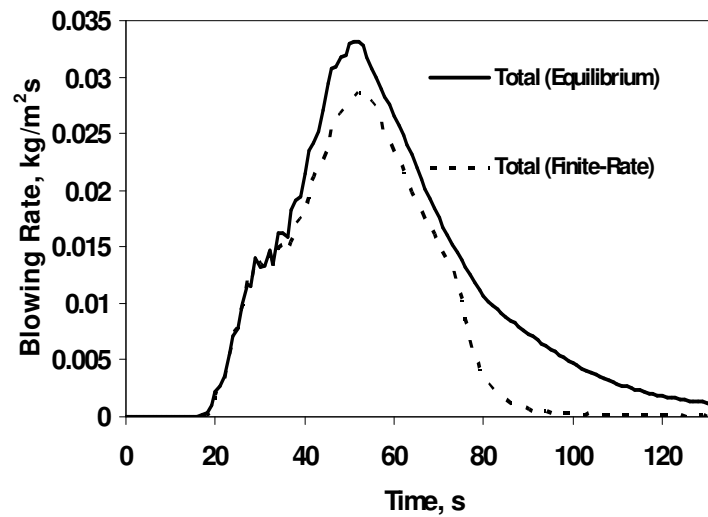


Figure 3.124. The total ablation rate comparing the equilibrium to nonequilibrium implementation at the Core 2 – Point 47 location for the final design SRC trajectory.

Table 3.13. The peak values of the surface heating terms for equilibrium and nonequilibrium at Core 2 – Point 47 for the final SRC trajectory.

Heating Type	Flux (W/cm ²)	Flux (W/cm ²)
	(Relative to Surface) Equilibrium	(Relative to Surface) Nonequilibrium
Net Convection	520 (In)	540 (In)
Radiation	460 (Out)	380 (Out)
Char Chemistry	12 (In)	9.1 (In)
Pyrolysis Gas Chemistry	17 (In)	12 (In)
Injected Chemistry	49 (Out)	140 (Out)
Conduction	45 (Out)	39 (Out)

Table 3.14. The total heat loads of the surface heating terms for equilibrium and nonequilibrium at the Core 2 – Point 47 for the final SRC trajectory.

Heating Type	Load (J/cm ²)	Load (W/cm ²)
	(Relative to Surface) Equilibrium	(Relative to Surface) Nonequilibrium
Net Convection	15000 (In)	15000 (In)
Radiation	13000 (Out)	9600 (Out)
Char Chemistry	310 (In)	210 (In)
Pyrolysis Gas Chemistry	440 (In)	290 (In)
Injected Chemistry	1000 (Out)	5200 (Out)
Conduction	1500 (Out)	1100 (Out)

Table 3.15. The absolute value of the peak in-depth heat flux terms for equilibrium and nonequilibrium at the Core 2 – Point 47 for the final SRC trajectory.

Heating Type	Flux (W/cm ²)	Flux (W/cm ²)
	Equilibrium	Nonequilibrium
Enthalpy Change	28	19
Conduction	46	39
Pyrolysis Genesis	4.6	4.7
Recession Derived	12	9.2
Pyrolysis Movement	20	15

Chapter 4

Comparison with Experimental, Numerical, and Flight Test Data Sets

To study the impact of the finite-rate model at the surface of the PICA material, there are many cases that can be used for comparison purposes. For the Stardust Return Capsule analysis, there exist previous studies dealing with the application of a finite-rate model to individual preliminary trajectory points. There are also measured values of recession and surface temperatures from the SRC reentry, alongside an analysis of what some of the possible species were surrounding the capsule during its reentry. Additionally, there is arc-jet test experiments run for the PICA material with data collected for recession and recession rates; these results were less than what PICA predicted, depending on the surface conditions. Finally, there is a program similar to BFIAT developed recently that looks at surface thermochemistry in the same manner that FIAT and MAT models it. These cases are compared against the implementation of the Park Model and conclusions are made about the physics of the Park Model and the surface interactions of the PICA.

4.1 Park Model and the SRC Preliminary Design Trajectory

Analysis of finite-rate implementation for the preliminary trajectory can be compared against similar approaches used in pre-flight analysis. A comparison of the

usage of the Park Model implemented in MAT/FIAT with the results garnered from Milos and Chen's finite rate ablation model⁹ which uses the preliminary trajectory will serve as an initial benchmark. The researchers study only the inclusion and omission of the nitridation reaction and do not examine any other reaction. Milos and Chen use a simple iteration scheme (seen in Eq. 2.19) to solve for surface conditions, which is not as complex as the Newton-Raphson method used in MAT. Milos and Chen directly calculate parameters such as heat flux from their iterative approach, while the MAT/FIAT setup takes into account the original B' rates of pyrolysis and char when constructing a nonequilibrium B' table. Essentially, the MAT/FIAT setup has one more iterative loop than Milos and Chen's approach.

For the Stardust Return Capsule, Milos and Chen examine the conditions at the peak total heating rate, 54 seconds into the trajectory using the equilibrium value, absent any radiation. Table 4.1 compares the convective heating results and total mass blowing (ablation) rates at the stagnation point. In the autonomous implementation of the Park Model in Ref. 9, nitridation causes an increase of 63% of the total ablation rate over a non-nitridation assumption and a 5.6% increase over the chemical equilibrium assumption. Using MAT/FIAT however shows no significant difference between a reaction set with or without nitridation in terms of total ablation rate or convective heat flux. The total mass blowing rate predicted by FIAT for both the nitridation and non-nitridation cases is similar to the result found by Milos and Chen for the case where the reaction set does not include nitridation. The effects of nitridation are unknown based on the ablation rates alone.

The results from Ref. 9 show that the total ablation rate relative to each model differs from one another, but these differences do not greatly affect the net convective heat flux. Ref. 75 explains that the nitridation reaction may significantly increase the ablation rate, but release only a small amount of energy. There is no significant change in the net convective heat flux due to nitridation seen by FIAT. Comparing the FIAT non-nitridation and Milos and Chen's non-nitridation cases shows only a 15% difference between the net convective heat fluxes, with the results from FIAT being the smallest of the pair. When compared to the nitridation results found previously, the FIAT datum is 8% smaller. The differences in the convective heat fluxes between the two implementations may be due in part to the inclusion of radiation in the FIAT procedure. The total heat flux that includes both convective and radiative heat fluxes used in the FIAT analysis is closer to the values of Milos and Chen's convective heat flux in equilibrium and when nitridation is not included in the Model.

Milos and Chen's work with the Park Models indicate that nitridation's main impact is on ablation rate and through that, the recession, while the heat flux is only minimally impacted, corresponding to the conclusions reached in Ref. 75. The results found by FIAT also reinforce the minimal effects of nitridation though they show that nitridation's effects are near zero for all predictions. Work by Goldstein⁷⁷ shows that CN may not form around ablating graphite, such that nitridation does not occur. Instead of nitridation by itself, it is likely that the CN molecules undergo an exchange reaction with nitrogen atoms and produce nitrogen and carbon. Carbon may then be condensed back into the wall. This set of secondary reactions is equivalent to a

nitrogen surface catalytic process which may eliminate the assumption of nitridation as chemically and physically the reaction would have no last impacting.

Table 4.1. The total mass blowing (ablation) rate and convective heat flux at 54 seconds for a direct iterative scheme using Stardust peak heating conditions and for a process using MAT and FIAT.

Approach	Total Mass Blowing Rate (kg/m²s)	Convective Heat Flux (W/cm²)
Milos and Chen⁹ (Approximate)		
Equilibrium	0.090	700
Park (Nitridation)	0.095	500
Park (No Nitridation)	0.058	530
MAT/FIAT		
Equilibrium	0.086	590
Park (Nitridation)	0.054	450
Park (No Nitridation)	0.054	450

Park derived a numerical model⁸ for the Stardust Return Capsule that uses Milos and Chen's finite-rate ablation model⁹ to calculate the species concentrations on the surface and whose reaction set included sublimation, nitridation and one oxidation reaction. However, Park does not calculate the total rate at which these reactions will ablate the char material, using the total ablation rates found from Olynick et al.'s¹⁰ equilibrium analysis as parameters. Park holds the total rate constant between and equilibrium and nonequilibrium and computes the pyrolysis gas rate from the subtraction of char rate as computed in Eq. 2.17 from the total ablation rate. Olynick and Park use the preliminary trajectory for their SRC environments. Figure 4.1 compares the pyrolysis gas rates found from Park, Olynick, and this research.

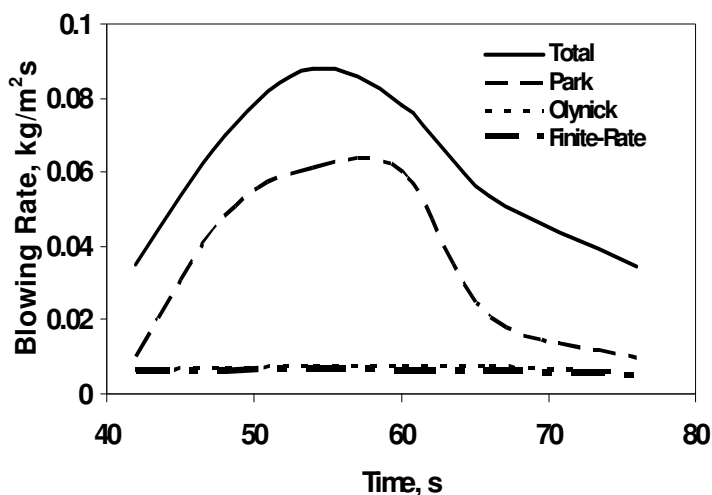


Figure 4.1. The pyrolysis gas and total blowing rate for Park and Olynick's assumptions, with a comparison to the nonequilibrium assumption applied to the preliminary SRC trajectory.

Under Park's assumptions, the pyrolysis gas rate makes up the majority of the total rate. Milos and Chen's finite-rate ablation model, which uses Park's finite-rate model, has the pyrolysis rate making up only 21% of the carbon total mass blowing rate. Park's pyrolysis gas rate is dependent only on calculated mass loss from limited oxidation, sublimation and nitridation and a total rate calculated outside of the analysis, significantly different from the values calculated from FIAT and Olynick, where the assumption is not that the total rate is independent of the pyrolysis and char rate. The nonequilibrium pyrolysis gas rate, using Park's reactions and calculated independently of the total ablation rate, is closer to Olynick's than Park's. Both Olynick's and the nonequilibrium assumption's gas rate are significantly smaller than Park's linear relationship between the total ablation rate and a calculated char rate.

Park assumes that the surface temperature remains at 3000 K for the trajectory, allowing for sublimation, and compares his heat flux results with those from Olynick where Olynick assumed no ablation. The total heating rates for Park

with laminar flow, Olynick (no ablation), equilibrium and the Modified Park Model, with the complete reaction set and without sublimation are shown in Fig. 4.2. Park's results are greater than those found by FIAT for the ablating case and are similar to Olynick's predictions for a nonablating material. Olynick's nonablating heat flux is essential the same as the cold wall flux for the preliminary trajectory because without ablation the unblown heat transfer coefficient is used to calculate convective heat flux and the wall enthalpy is assumed to be near zero. Ablation considerations will include the wall enthalpy and have a corrected transfer coefficient. Sublimation allows for higher heating later in the trajectory as compared to its absence and the Modified Park Model as integrated into a material response model produces lower heating than if the model is used with pre-calculated total ablation rates and surface temperatures. Due to Park validating his ablating heating rates against those of Olynick's without ablation, further validation between the results found by the use of nonequilibrium and those in Ref. 8 cannot be made.

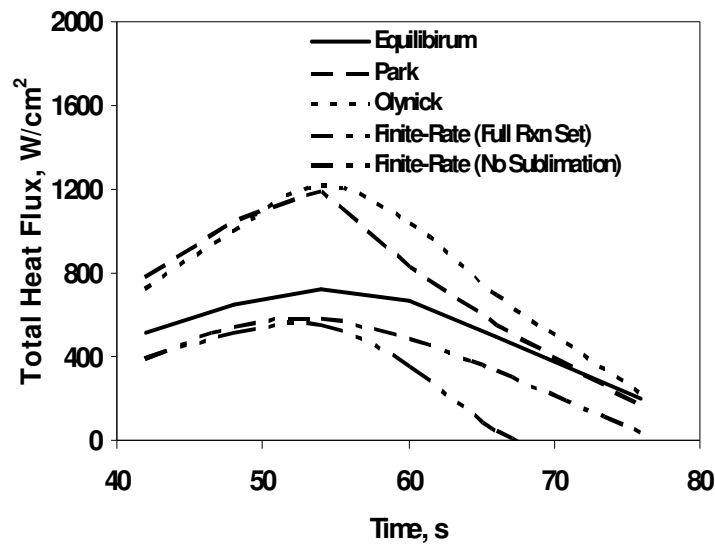


Figure 4.2. The total heat flux for various models for the preliminary SRC trajectory.

4.2 Stardust Return Capsule Measured Data

As previously mentioned, the Stardust Return Capsule was recovered on January 16, 2006. The capsule itself was not instrumented with any devices to measure its reentry conditions. This led to observations from the air tracking the reentry and post-flight analysis being used to determine such parameters as surface temperature and recession. There was an airborne observance of 60 seconds of the reentry. For the generation of the final trajectory and post-flight analysis involving the flow the solver used is Data-Parallel Line Relaxation (DPLR)⁸⁵ Method program.

Table 4.2 is the analysis of the recession of the PICA material. The predicted values come from an assumption of surface equilibrium. The measured recession comes from 3-D mapping of the capsule and the difference in the recovered capsule and the computational design dimensions.⁸³ The pre-flight analysis overpredicts the recession rate at all points of interest. While the actual stagnation point recession is unknown, the general discrepancy found in the near-stagnation Core 1 region is considered to be the same discrepancy at the actual stagnation point based on their like heating environments. As illustrated in the table, the prediction for the near-stagnation core greatly overestimated the recession. There is a $\pm 5\%$ error in the measured recession.⁴⁵ Reference 45 has the final predicted recession at the stagnation point as 0.96 cm which is less than the predicted recession in this dissertation for equilibrium but the two predictions are within 5% of each other and within the allowable error envelope.

Table 4.2. The measured recession and the predicted recession for the SRC.

Location	Measured (cm)	Predicted		
		Kontinos et al. ⁴⁵ (cm)	Equilibrium (cm)	Finite-Rate (cm)
Stagnation Point (Preliminary trajectory)			1.12	0.72
Stagnation Point (Final trajectory)	Extrapolated: (0.66 ± 0.04)	0.96	0.99	0.54
Near Stagnation Point	0.57 ± 0.03	0.86	0.90	0.46
Core 2 – Point 47	0.32 ± 0.02	0.39	0.37	0.24

In the Park Model, the inclusion of four reactions (sublimation, oxidation, and nitridation) to account for nonequilibrium surface conditions leads to a reduction of the predicted recession at the stagnation point in the preliminary trajectory to 0.72 cm. It is seen with the final trajectory that the near stagnation point predictions closely follow the trends seen at the stagnation point and its final recession is within 10% of the recession predicted at the stagnation point. Assuming that the stagnation point is interchangeable with the near stagnation core in terms of the percent difference in predicted and measure recession (51%), the measured recession at the stagnation point would be approximately 0.66 cm. The predicted finite-rate recession during the preliminary trajectory of 0.72 cm still over predicts the recession, but now, only by 11%. If nitridation and sublimation are omitted, the predicted recession in the preliminary trajectory is 0.49 cm, which is now underpredicting the recession by 17%. The omission of sublimation causes underprediction and is not conservative. A model without sublimation that is used to design a heatshield for a Stardust-like reentry would lead to a failure of the heatshield upon entering the Earth’s atmosphere as the recession would be greater than the heatshield. So a nonequilibrium assumption

over the entire preliminary trajectory helps lessen the error in the recession calculation, but only the case where the full reaction set is used remains a viable design point.

The actual reentry of the SRC matched the final design trajectory and the final design trajectory recession predictions for the three points (stagnation, near stagnation, and Core 2 – Point 47) can be used to get a more robust comparison between the measured recession and the predictions. It is seen that with the final trajectory, the assumption of nonequilibrium over the entire trajectory leads to an underprediction of recession when compared to the measurement at all three locations. This may indicate that the capsule experiences equilibrium during some part of its reentry. Recession predictions for the three locations for the three finite-rate analysis that is not nonequilibrium over the entire trajectory (during the heating tail, post peak heating, and post 3000 K) is presented in Table 4.3. Since the finite-rate assumption decreases the recession rate, the earlier it is activated, the smaller the final recession. For the stagnation and near stagnation points, activating the finite-rate reactions when sublimation first occurs decreases the recession such that the final value falls within the error margin of the measured recession. As seen in the analysis of the preliminary trajectory, sublimation is a main driver in the Park Model and the Stardust Return Capsule. The measured recession and the predicted recession using the finite-rate model once sublimation is activated offer physical evidence of the role sublimation.

Table 4.3. The measured recession and the predicted recession for the SRC when nonequilibrium is applied only partially to the trajectory.

Location	Measured (cm)	Predicted			Post 3000 K (cm)
		Heating (cm)	Tail	Post Heating (cm)	
Stagnation Point	Extrapolated: (0.66 ± 0.04)	0.85		0.72	0.62
Near Stagnation Point	0.57 ± 0.03	0.76		0.65	0.55
Core 2 – Point 47	0.32 ± 0.02	0.31		0.28	0.27

At the Core 2 – Point 47 point the equilibrium prediction for recession is not as overpredicted as it is at other locations. It still falls outside the error margin for measuring recession, but activating nonequilibrium during the heating tail reduces the recession such that it is now within the margin. As previously stated,^{81,82} FIAT is theorized to overpredict certain parameters during the heating tail due to the low heat flux. In cases where sublimation is not the main driver of the Park Model due to the limitation of surface temperatures, such as at the Core 2 – Point 47 location, including finite-rate reactions during the periods of low heat flux may help FIAT in its predictions. The equilibrium and limited nonequilibrium recession predictions at the Point 47 location being close to the actual measured recession is further proof of the limited abilities of current equilibrium models Park and Tauber found in Ref. 4 with the Galileo and Pioneer-Venus probes study. As one moves further away from the stagnation point, towards lower heating, equilibrium may start to approach or even underpredict the actual results. If the material response model is only operating in one-dimension, like FIAT, then the underprediction is cause by the lack of corner effects and the ignoring of conduction through the plane of the heatshield. The stagnation point is the most likely point where nonequilibrium will occur due to its

higher heating driving sublimation and, depending on the geometry of the craft, the area around the stagnation point may also experience similar heating such that nonequilibrium may occur at those points.

The measured density profile of the near stagnation (Core 1) and Core 2 - Point 47 locations is analyzed in Ref. 84. A density profile can be used to determine the locations where charring has occurred. From the material properties, the char and virgin densities are known. Each core is sectioned into submillimeter segments and the density of that segment is determined from its mass and volume. There is a 4% error associated with measured density. Comparing the measured density to the density predicted in equilibrium, nonequilibrium and finite-rate sublimations shows that the density profile, as laid out when measuring from the ablated surface, does not change greatly between the three cases (Figs. 4.3 and 4.4). What does change is the depth the profile extends to, which is based off of the amount of recession. Equilibrium cases will not have as deep of a density profile because more of the material is recessed. This is also true when comparing the two locations against each other, since the Core 2 point will have less recession which results in a larger char zone. All three cases have a similar profile close to what is measured, with the cases where finite-rate reactions are assumed are only more robust due to its recession rate reduction causing a profile that matches the measured values in terms of densities and lengths. Based on the measured densities alone, all three reaction assumptions are valid, while the relative length of the densities zones seems to favor the case where sublimation signifies the start of the finite-rate reactions.

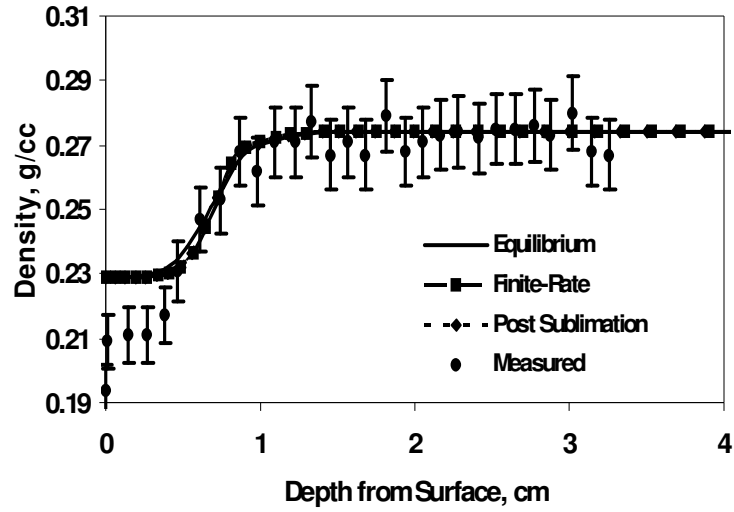


Figure 4.3. The density profile at the near stagnation (Core 1) point.

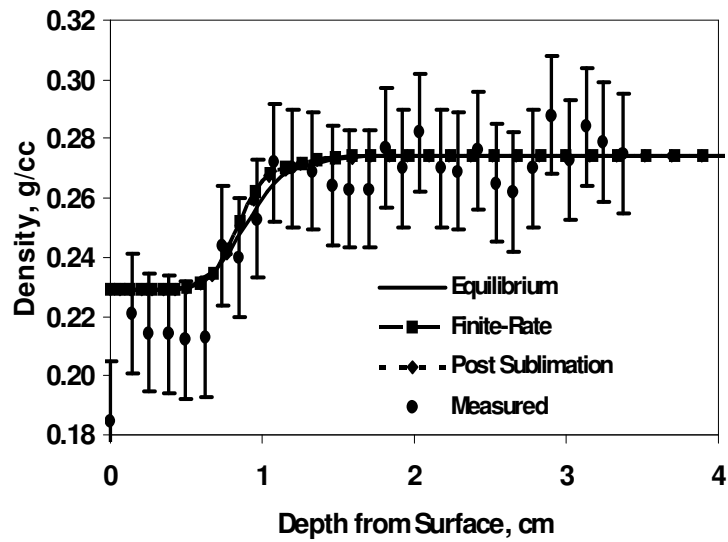


Figure 4.4. The density profile at the Core 2 – Point 47 location.

Spectroscopic observation is used to obtain data such as the temperature profile and presence of species around the return capsule. Two of the main instruments used are an Echelle camera⁴⁴ and a SLIT telescope.⁸⁶ These instruments observe the brightness and wavelength of light emitted from the craft as it streaks

across the sky and from there, temperatures and elemental makeup can be determined. The Echelle camera is used for ten seconds, from the time period of 33 to 44 seconds of the trajectory. The SLIT experiment observed data for roughly twenty seconds from 40 to 60 seconds. The SLIT telescope's time period encompasses the period where the peak heating flux is predicted to occur. Based on the brightness that is recorded, the peak heating flux does occur around the predicted time of 54 seconds.⁴⁴ At the altitude the DC-8 flies at to observe the reentry the use of spectrometry can experience some problems. At that high of an altitude, the absorption of the infrared may be difficult. However, the data that is collected is determined to be accurate and used to make observations.

A study of the species that are observed to be surrounding the capsule can help determine if nonequilibrium is present in a general sense. If there is a lack of the products of the reactions that are accounted for in the finite-rate models that would mean those reactions may be taking place too slowly and be frozen, making the unimportant for this analysis. Conversely, if it is seen that a species is in abundance around the capsule, it can be thought that the reaction quickly reaches completion and equilibrium. The Echelle camera and SLIT telescope cannot determine exactly whether or not the molecules it observes are from the heatshield ablation only or from a combination of the ablation products and the air, however, some level of confidence can be made of the origin based on what elements are theorized to be present in the air and on the surface of the capsule.

An example of determining where a species originates from is the observation of both zinc and sodium being emitted around the craft. The two elements are not

found in Earth's atmosphere naturally. They are also not in the makeup of the PICA heatshield. As such, it is determined that their origins were on the thermal paint on the Stardust capsule.⁸⁷ Cyanide, the product of nitridation, is a strong radiator and can be captured by a spectrograph. CN would not be observable though it would still be present at temperatures below 2500 K according to Ref. 87. In the actual observation⁸⁸ to determine species formed during the Stardust reentry, from 33 seconds into the trajectory to 44 seconds, or from just before peak heating, cyanide is seen to be part of the spectral makeup at an altitude between 81 and 71 km.

Although cyanide is measured during the reentry that does not mean that nitridation as outlined by the Park Model takes place. A spectral simulation of the conditions surrounding the Stardust Return Capsule does not match the results found from observation meaning that some unknown reactions are taking place to populate the air with unexpected species.⁸⁶ Also cyanide may be forming from carbon and nitrogen particles in the surrounding flow and not directly on the surface. Sublimation is identified as an important reaction in the SRC reentry, yet its product C_3 is absent from any measured spectral data. This does not invalidate the claim that sublimation is a key driver because the majority of spectral data is collected before the peak heat flux and surface temperatures consistently above 3000 K.

For simulations of the molecular concentration around the SRC, the instantaneous mole fraction capability in BFIAT has the fractions calculated at the conditions under analysis at that unique trajectory time point. These calculations are not dependent on what the previous fraction in any earlier time. Zinc and sodium are not considered because of the previously mentioned condition that the two elements

do not occur naturally in the atmosphere and are a product of the paint, not the material. The three species of the most interest are the three that are the products in the Park Model: CO, CN, and C₃. Figure 4.5 compares the mole concentration over the trajectory when considering full equilibrium and full nonequilibrium. The analysis shows that CN makes up between 5 and 10% of the instantaneous moles found during the heat pulse, which is why it is visible when performing spectrometry. From the equilibrium concentrations it can be concluded that sublimation is more significant than nitridation due to C₃ having a higher concentration, indicating that the reaction is occurring either more often than nitridation or producing a larger quantity of its product per reaction. The large concentration of C₃ reaffirms its importance in the Park Model. C₃ may not have been visible in the spectroscopic analysis due to its wavelength and intensity properties not being in the range of observation.

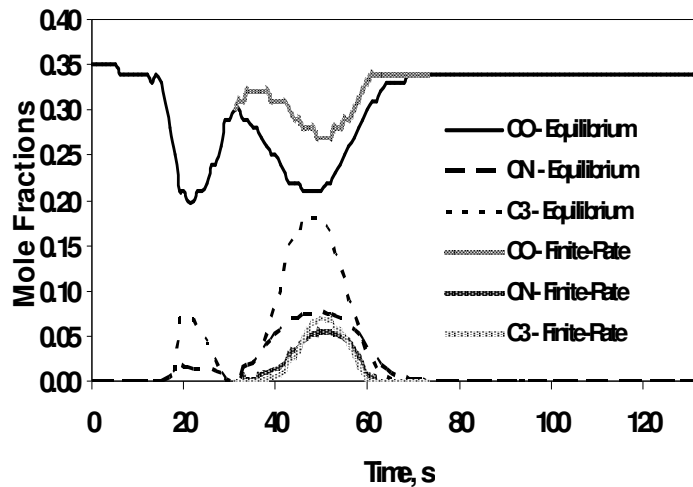


Figure 4.5. The equilibrium and finite-rate mole fractions for the three products of the Park Model during SRC reentry as experienced in the final design trajectory.

Under the conditions of the SRC trajectory, there is a reduction of the CO mole fraction. The production of CO in equilibrium is either not as large as the production of other species (as C_3 mole fraction increases, the CO mole fraction decreases, for example) or CO is being consumed at greater quantities than it is being produced in the trajectory, both of which will reduce the mole fraction. There is a relative increase in CO between the equilibrium and nonequilibrium cases though the Park Model assigns a finite-rate to CO producing reactions. CO starts with a large, nonzero concentration of moles which helps keep its mole fraction high when other reactions are occurring in a finite-rate manner, as any reduction in CO formation may be counteracted by a similar reduction in the formation of C_3 , allowing for the mole fraction in nonequilibrium to not decrease as much as in equilibrium under the conditions. Another reason why the concentration may increase is that the reduced heating and surface conditions at the gas/surface interface causes the reactions that use CO as a reactant to not consume CO at the same rate in time as in equilibrium due to less CO available, causing these reaction to act “finite-rate” way. In nonequilibrium, the larger concentration of CO compared to equilibrium is one reason why there is a larger enthalpy at the wall in the nonequilibrium case; its contribution to the enthalpy at the wall is significantly larger than it is in the equilibrium case.

Looking at the effects of nonequilibrium and the Park Model, the C_3 concentration is greatly reduced, by nearly 60% at peak heating, when the reaction is assumed to be occurring in a finite-rate sense. CN is only reduced by 31% with CO's concentration increasing by 17% at peak heating. Figure 4.5 also shows that C_3 reaches high levels of concentration outside of the spectroscopic observed time frame.

If the observed time frame was larger sublimation may have been seen and follow the instantaneous mole fractions.

Due to the lack of instrumentation on the Stardust Return Capsule, only surface temperatures can be calculated with no in-depth temperature information being available. This is due to the method of determining the surface temperature is relating the wavelengths recorded by the Echelle camera and SLIT telescope to the temperature through Planck's formula for a gray body. The wavelengths observed can be converted into temperatures based on assumptions made such as constant temperature on the surface of the heatshield. The surface temperature on unique points other than the stagnation point on the heatshield during reentry cannot be accurately determined leading to the average surface temperature being the parameter used for comparison to the model.

The wavelength data collected from the Echelle camera compared to the wavelengths from the temperatures calculated from the equilibrium model can be found in Ref. 89. There are two approaches to modeling the temperature data: one is an area-average surface temperature that is the superimposed gray body function of each radiating surface element at its local temperature and the other is the average-temperature approach, using the surface average temperature for the gray body equation.⁸⁹ The area-average method is an assumption that the highest surface temperature will occur at the stagnation point and over the rest of the body, there is a linear distribution such that the average surface temperature observed by the Echelle and SLIT cameras is reached. This approach sets an upper bound for the surface temperatures. The average-temperature method sets the lower bound by stating that

the surface temperature is constant on the entire surface such that it is equal to the average observed temperature.

The models overpredict the observed temperatures to some degree. The actual SRC body is white which contradicts the gray body assumption. Additionally, the temperature methods do not account for the presence of any paint on the material. As the material ablates and zinc and sodium, products from the thermal paint, are seen in the spectroscopic analysis the later time periods, the overprediction decreases because actual heatshield is becoming similar to the heatshield considered in the material response model, that is, without paint. To better account for the paint, Trumble et al.⁸⁹ adds an error margin of ± 50 K to the predicted surface temperatures and within these bounds the previous equilibrium predictions better match the Echelle camera data.

The observed temperature profile of Winter et al.⁸⁶ using the SLIT telescope is used to compare as the “actual” temperatures to those predicted by the Park Model nonequilibrium. The equilibrium and finite-rate surface temperatures calculating the surface temperature at 142 points on the heatshield and then taking the average of those temperatures. Figure 4.6 contains the data collected by Winter with both a constant temperature assumption and a linear distribution serving as upper and lower bounds. The predicted surface temperature is from the three chemical assumptions: equilibrium, full nonequilibrium, and nonequilibrium only after the activation of sublimation. Winter finds that the equilibrium material response temperatures fall within the bounds of the SLIT telescope, except early in the trajectory (corresponding to an altitude of 73 km), where it starts to overpredict the upper bound of the SLIT data. Since the nonequilibrium case with a full reaction set predicts lower

temperatures and leads to a lower average surface temperature, its use would lessen or eliminate this overprediction while still falling within the bounds later in the trajectory.

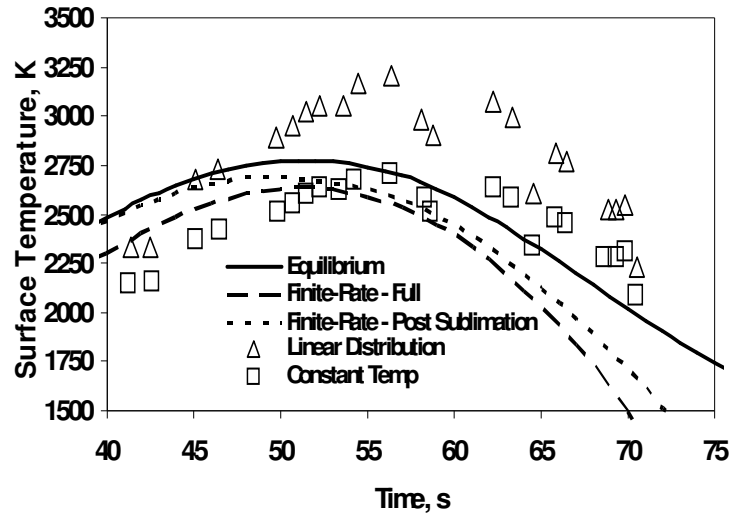


Figure 4.6. The FIAT surface temperature predictions for the three chemical assumptions versus the SLIT data processed with the two methods to get upper and lower bounds.

All three chemical assumptions underpredict surface temperatures between approximately 60 and 70 seconds according to the SLIT telescope. It is around peak heating, at 54 seconds, where both equilibrium and nonequilibrium surface predictions approach and then become less than the lower bound of the observed surface temperature. The paint castoff may be affecting the surface temperatures in a greater quantity than the 50 K theorized by Ref. 89 since it is being ablated away the fastest during peak heating. A time-dependent adjustment of the error due to the paint should be taken into consideration in processing the SLIT data or in the error margin for the predicted temperatures. For the current theorized error, the equilibrium assumption is better than the two finite-rate assumptions during the later trajectory

time period because while it is still underpredicting the temperatures, it is the closest to observed data between 60 and 70 seconds.

The finite-rate assumption, either occurring throughout the entire trajectory or only after sublimation is activated, leads to predicted surface temperatures that match the SLIT observed temperatures taken earlier in the trajectory, from 40 seconds to approximately 60 seconds than the equilibrium predicted surface temperatures. During this trajectory period is when conditions where sublimation occur, explaining why a sublimation-based finite-rate model may improve the temperature prediction. Even when considering the paint during this time period and allowing for a ± 50 K envelope, the same conclusions for the later trajectory predictions can be made since the difference in the observed and predicted temperatures is often more than 50 K. The comparison with observed surface temperature does not indicate one model is better than another, as each model performed well depending on the heating conditions during the observational time period. However, of the three chemical cases, none performed worse than 26% less than what was observed. This means that any adjustment to better match the equilibrium predictions to the observed data, either through a different processing method for the observed data to take into account a white body or through a bigger error envelope to account for the ablating of the paint, can improve the fidelity of the predictions in relation to the observed data.

A comparison with the measured recession from the Stardust capsules shows that the finite-rate application after sublimation is activated leads to the best match to the data at the stagnation and near stagnation point. At the Core 2 point, equilibrium and nonequilibrium recession starts to approach, then underpredict, the measured

recession, similar to what is seen in the heat flux at the frustum region when analyzing the Galileo and Pioneer-Venus probes⁴, signifying the likely need to consider some shoulder effects at the Core 2 point. Looking at the predicted instantaneous mole fractions and the observed species based on flux shows some similarities in terms of what species should be present, but the observed data is during the time frame before C₃ would be present to account for any sublimation. The predicted instantaneous mole fractions highlight the importance of the sublimation reaction for the SRC trajectory as it is seen that C₃ increase substantially during the conditions where sublimation make take place. The surface temperatures calculated from SLIT observations and predicted from FIAT for the three chemistry assumptions have some resemblance, but a conclusion as to which of the three chemistry models works best based off of surface temperature cannot be made due to paint-driven error and the observed surface temperatures only serving as upper or lower bounds, based on the processing method.

4.3 Arc-Jet Test Data

In an effort to build a material database for the PICA material and spurred on by the choice of PICA to be one of two possible heatshield materials in the spacecraft that would go to the Moon and return under the Constellation project, arc-jet experiments have been conducted on PICA to examine the effects of different heating regimes on the material in the Earth atmosphere.^{46,49,90} The arc-jet testing and analysis carried out by Covington et al.^{49,90} examine four heating regimes and compare the measured results to those predicted by FIAT. The heating rates run in the NASA Ames 60 MW Interaction Heating Facility⁹¹ by Refs. 49 and 90 are 400, 580, 1150

(close to the predicted heating environment of the Stardust Return Capsule, which is 1200 W/cm^2), and 1630 W/cm^2 , with sample thicknesses ranging between 2.74 cm and 5.72 cm. For the two highest heating rates, the pressure is 0.65 atm (66 kPa), while for the two lowest heating rates, the pressure is 0.45 atm (46 kPa) for the 580 W/cm^2 test and 0.20 atm (20 kPa) for the 400 W/cm^2 test. A constant total enthalpy of 29.5 MJ/kg is measured for all four heating regimes. Because both enthalpy and cold wall heat flux is known, the heat transfer coefficient can be calculated and used as an environmental input for FIAT. Radiation heating from the shock layer is found to be negligible for the arc-jet conditions. Covington examines two cases where he makes an assumption for the blowing rate. The first case is no or low surface blowing. With no surface blowing (pyrolysis gas is escaping through the sides of the material, not the surface), the material's ablation is driven by purely diffusion-controlled oxidation. The other case Covington examined is a similar to the SRC analysis in that the surface blowing is caused by pyrolysis gas escaping up through the material and is some nonzero term. For comparison purposes, since the exact blowing rate used by Covington is not stated, when the results are recreated in pursuit of validating the nonequilibrium model, the blowing rate remains 0.5 as it has been used in the Stardust analysis.

Post-test, the recession is measured and Covington calculates the recession rate from the final recession and the run time of the test. This means that there is an assumption of a constant recession rate (due to the heating environment being constant). Thermocouples are placed within each sample to measure in-depth temperatures and surface temperature is measured via optical pyrometers. Covington

found that FIAT overpredicted the recession rate when compared to the measured rate even with a reduced surface blowing rate. Covington lists physical limitations of the actual samples such as the small diameters of the billets causing small pressure drops and the rounding of the billets as recession occurs which causes different recession rates as time progresses as possible reasons as to the discrepancies between FIAT in its assumptions of surface blowing.

The use of nonequilibrium for the two highest heating rates helps decrease the recession rate overprediction without the need to change the surface blowing rate. Figures 4.7 and 4.8 show the nonequilibrium results, the surface blowing equilibrium results, and the measured results for the recession rates. The error bars of the model predictions come from a possible error in the cold wall heat flux measured of $\pm 10\%$, since the arc-jet facility in which the samples were tested in has previously been stated to have a minimum amount of uncertainty at that value.⁹² Additionally, the error in the environment is passed along to the finite-rate calculation by the effects on any adjustments on the heat transfer coefficient if the assumption is that the cold wall heat flux is changing but not the enthalpy. If coefficient changes, the nondimensionalized finite-rate reaction term used in Eq. 2.96 will change. So variations in the heating environment do not only physically affect the amount of heat on the surface, but also mathematically in terms of the mass loss due to the finite-rate assumption.

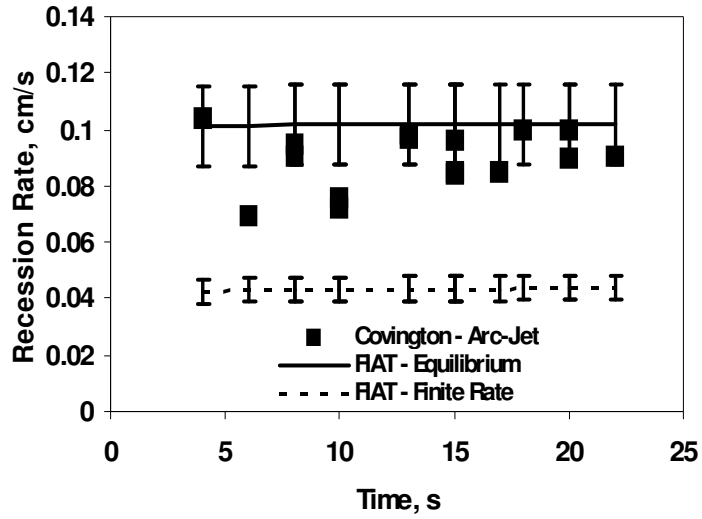


Figure 4.7. The recession rate measurements and FIAT predictions for a heating environment of 1630 W/cm^2 .

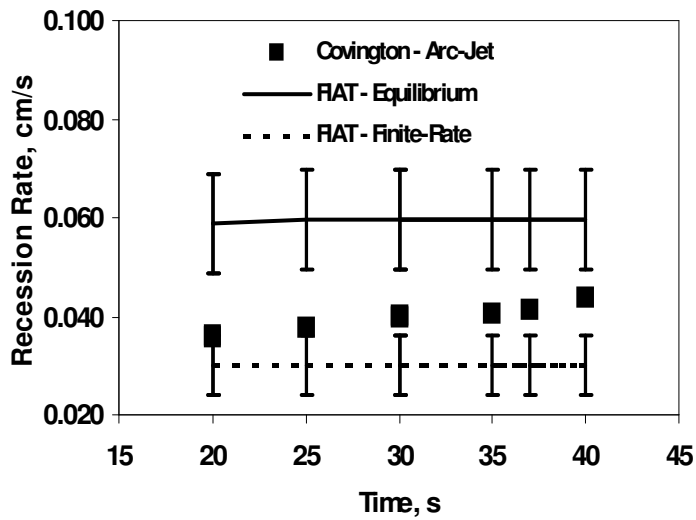


Figure 4.8. The recession rate measurements and FIAT predictions for a heating environment of 1150 W/cm^2 .

Table 4.4 lists the average recession rate, measured and predicted, for two chemistry assumptions, for the two high heating cases. It also lists the root mean square error,⁹³ which comes from analysis between each run of the arc-jet experiment

and the analogous FIAT study. In both heating cases, recession rate goes from overpredicting the measured data to underpredicting it. Applying nonequilibrium to the highest heating case, the 1630 W/cm² case, causes the recession rate to decrease so that there is a larger error between what is measured and what is predicted than seen in equilibrium. In the slightly lower heating environment, the 1150 W/cm² case while the recession rate in nonequilibrium is now being underpredicted in terms of overall average, it is only approximately 15% less and the root mean square error decreases from 0.020 cm/s to 0.010 cm/s. Recall that sublimation is an important reaction in the Park Model that it will not reach a steady state to approximate equilibrium in the model. At heating where sublimation is likely to occur (Stardust-like conditions and higher), if the heating is significantly high, then the sublimation reaction should occur quickly in time and appear to be steady and in equilibrium. The Park Model cannot account for steady-state reactions and keeps the sublimation reactions “finite.” Hence at high heating like 1630 W/cm², where sublimation is most likely to be in equilibrium, application of the Park Model leads to significant underprediction as the reaction is not trending towards equilibrium in the model. At heating rates where sublimation is more likely to be occurring in a finite way, like at 1150 W/cm², the application of the Park Model leads to a more robust prediction.

Table 4.4. The average measured recession rate and the average predicted recession rate for the two highest Covington heating environments.

Heating Environment	Measured (cm/s)	Predicted		Root Mean Square	
		Equilibrium (cm/s)	Finite-Rate (cm/s)	Equilibrium (cm/s)	Finite-Rate (cm/s)
1630 W/cm ²	0.098	0.102	0.043	0.016	0.047
1150 W/cm ²	0.039	0.059	0.030	0.020	0.010

In Ref. 49, Covington states that the surface temperature data was obtained using two different single-optical pyrometers and dual-wavelength optical pyrometer. The estimated error of the use of the dual-wavelength pyrometer, which provided the most consistent data, is ± 527 K (± 254 °C) for a 1% difference in ratio of emissivity. This is a large error envelope and as seen in Figs. 4.9 and 4.10, both the equilibrium and nonequilibrium temperature prediction for the 1630 W/cm² and 1150 W/cm² heating regimes typically fall within the temperature error envelope, even without the added environmental error. Table 4.5 is the average surface temperature for the two high heating regimes and the root mean square error. While the root mean square error decreases in the 1630 W/cm² regime when finite-rate reactions are applied, the error is still large, outside of the 527 K envelope, and is only a 7% decrease from the equilibrium root mean square error. The root mean square error increases in nonequilibrium in the 1150 W/cm² regime, but still remains within the error envelope. The surface temperature behavior reinforces that the 1150 W/cm² heating environment is likely to have sublimation occurring as finite-rate reaction while the higher heating regime is closer to equilibrium.

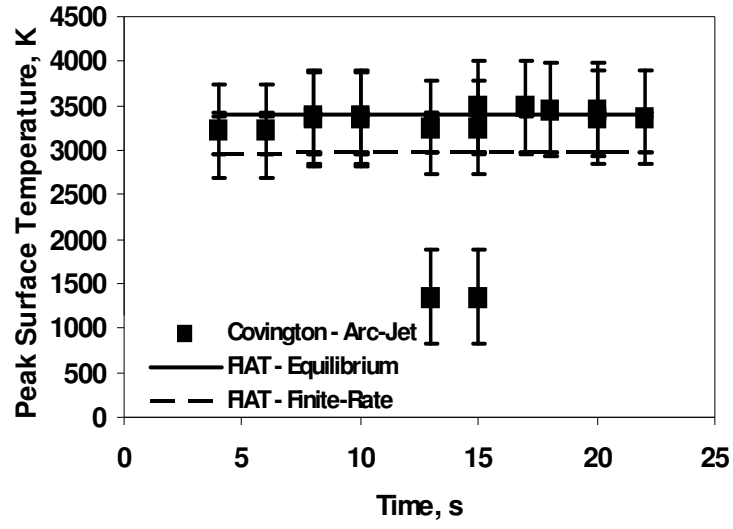


Figure 4.9. The surface temperature measurements and FIAT predictions for a heating environment of 1630 W/cm^2 .

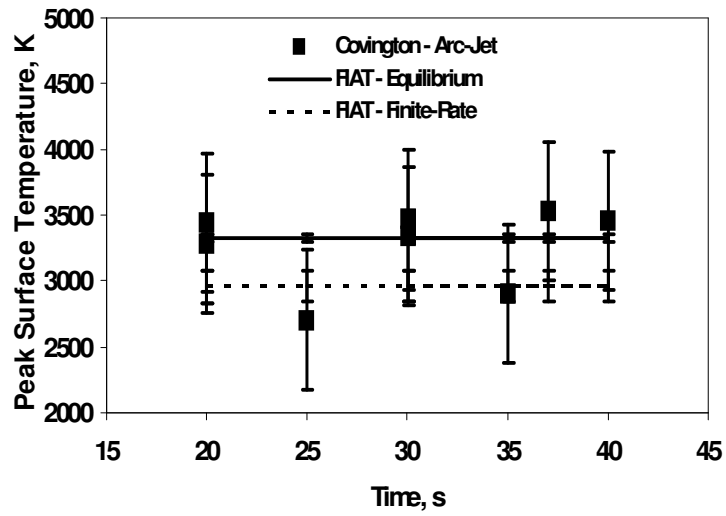


Figure 4.10. The surface temperature measurements and FIAT predictions for a heating environment of 1150 W/cm^2 .

Table 4.5. The average measured surface temperature and the average predicted surface temperature for the two highest Covington heating environments.

Heating Environment	Measured (K)	Predicted		Root Mean Square	
		Equilibrium (K)	Finite-Rate (K)	Equilibrium (K)	Finite-Rate (K)
1630 W/cm ²	3100	3410	2970	734	683
1150 W/cm ²	3260	3320	2960	287	415

For the two lowest heating regimes that Covington studies, the 580 W/cm² and 400 W/cm² environments, the average recession rate using the equilibrium assumption in FIAT is results in a slight underprediction when compared to measured recession rate predictions. Though it is underpredicting the recession rate, the allowable environmental of envelope of $\pm 10\%$ means that the equilibrium predictions can be considered to match the measurements. Table 4.6 lists the average recession rate for the lower regimes and the root mean square analysis, while Figs. 4.11 and 4.12 show the rate measured and predicted at various time points.

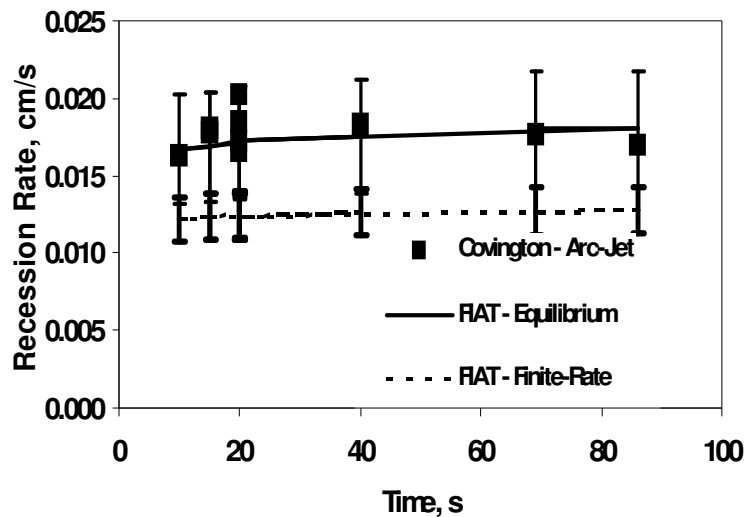


Figure 4.11. The recession rate measurements and FIAT predictions for a heating environment of 580 W/cm².

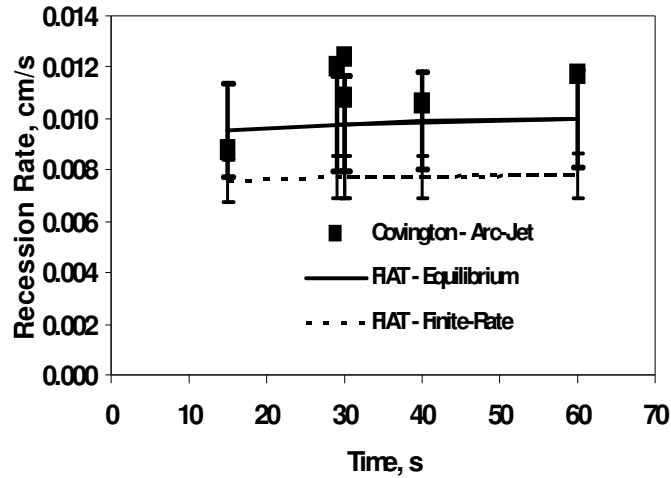


Figure 4.12. The recession rate measurements and FIAT predictions for a heating environment of 400 W/cm^2 .

Since a finite-rate reaction assumption lowers the recession rate due to reactions not fully taking place, the finite-rate recession predictions will be lower than the equilibrium predictions and moving away from the measure values. They end up underpredicting the recession rate outside of the $\pm 10\%$ envelope. For the surface temperature, as shown in Table 4.7, equilibrium and nonequilibrium predictions remain within the 527 K envelope for the 580 W/cm^2 environment despite there being an increase in the root mean square error in finite-rate calculations, and both chemistry cases remain outside that envelope in its root means square error analysis for the 400 W/cm^2 case. However, in terms of average surface temperature, the nonequilibrium assumption results in more robust predictions.

Table 4.6. The average measured recession rate and the average predicted recession rate for the two lowest Covington heating environments.

Heating Environment	Measured (cm/s)	Predicted		Root Mean Square	
		Equilibrium (cm/s)	Finite-Rate (cm/s)	Equilibrium (cm/s)	Finite-Rate (cm/s)
580 W/cm ²	0.018	0.017	0.013	0.001	0.005
400 W/cm ²	0.011	0.010	0.008	0.002	0.004

Table 4.7. The average measured surface temperature and the average predicted surface temperature for the two lowest Covington heating environments.

Heating Environment	Measured (K)	Predicted		Root Mean Square	
		Equilibrium (K)	Finite-Rate (K)	Equilibrium (K)	Finite-Rate (K)
580 W/cm ²	2890	3010	2700	178	223
400 W/cm ²	2440	2780	2430	670	575

The predictions of the finite-rate assumption at the lower heating regimes make it appear that the Park Model approaches equilibrium at these conditions as some of its predictions do not differ as greatly between what is found in nonequilibrium and what is found in equilibrium than what is seen in the 1150 W/cm² and 1630 W/cm² cases. This is similar to what is seen at the Core 2 – Point 47 location on the SRC, where there was also low heating. The nonequilibrium charring rate at the Core 2 location is only 20% lower than its equilibrium counterpart, a much smaller reduction than what is found at the other locations. At these lower heating regimes, the actual reverse reaction rates may be small enough to be considered approximately zero; the physical reactions are then similar to those built on the negligibly reverse rate assumptions of the Park Model, making the model appear to approach equilibrium. This does not mean the Park Model can predict equilibrium as it remains rigidly defined as never including a reverse rate so it will still lack the

ability to approach equilibrium at high heating regimes; the low heating predictions show that during conditions where equilibrium may be occurring but the reverse reaction rate is small enough to be reasonably approximated as zero the Park Model can “approach” equilibrium because it does not consider the reverse reaction rate during any heating regime. The conditions presented by Covington are a specialized case. Once the reverse reaction rate cannot be approximated as zero, the Modified Park Model cannot appear to calculate both equilibrium and nonequilibrium.

The Park Model and equilibrium predictions diverge more as the heating environment increases above 1000 W/cm^2 due to the likelihood that sublimation has reached equilibrium, which is unable to be compensated for in the Park Model. A comparison between the 400 W/cm^2 and 580 W/cm^2 regimes, where the nonequilibrium assumption applied to 400 W/cm^2 resulted in a smaller temperature error than at the 580 W/cm^2 regime, also shows that lower relative heating environments are likely to result in finite-rate reactions dissimilar to those found in regions where equilibrium is likely to occur. The comparison on the Park Model to Covington’s arc-jet experiments shows that at the higher heating regimes, the Park Model results in predictions that more closely match the measured parameters while at the lower heating regimes, the equilibrium and nonequilibrium predictions are similar to each other, like what is seen at the Core 2 point on the SRC, due to the slowing down of char formation.

PICA testing in argon-rich (which is applicable to MSL TPS design⁹⁴ though not to Stardust TPS design¹⁰) and nitrogen-oxygen flows are carried out by Milos and Chen in Ref. 92. Within each environment, the arc-jet tests are run at different mixing

conditions, with different mass fractions of oxygen or argon in the flow. This makes a comparison with FIAT difficult because while the standard elemental environment makeup of MAT for an oxygen-nitrogen flow has only two elements in the gas flow, nitrogen and oxygen, and it is easy to adjust one based on the knowledge of the other, in an argon-rich environment, there are three elements, argon, nitrogen, and oxygen, so knowing the mass fraction of argon in an arc-jet flow is not enough to recreate the environment in MAT. As such, the standard argon-rich arc-jet environment is used in MAT, where there is 7.4% argon added to the flow. The thickness of each test sample is the same as its diameter, 10.16 cm. Since the thickness is the same as its diameter, the analysis can be one-dimensional. Milos and Chen do runs both FIAT and TITAN for the test cases, with little difference between the two models.

There were 22 cases examined, four of them in a nitrogen-oxygen flow, with multiple runs for some cases. The test samples had thermocouples placed in-depth and recession was measured as the difference between the initial dimensions and the final dimensions. Surface temperatures were determined from the same single- or dual-wavelength pyrometer process as Covington^{49,90} employed, though Milos and Chen assign a 5% error to the temperatures and not a constant Kelvin error. There is a ± 0.05 cm error in the measured recession.

For the facility in which the nitrogen-oxygen flow experiments were conducted, it was observed that the physical models tend to flatten in the center as they ablate and that the stagnation conditions vary along the centerline more than experiments in other facilities. This means that the stagnation heat flux decreases as a function of time in the facility, such that the measured enthalpy is not considered as

constant enthalpy. Milos and Chen used DPLR flowfield calculations to arrive at a more suitable enthalpy that can account for the decrease in heat flux. The arc-jet runs lasted 120 seconds and the concentration of oxygen was allowed to vary in the flow. Tables 4.8 and 4.9 show how the change in enthalpy affects FIAT predictions, along with how changing the oxygen concentration affects predictions. There are no measured surface temperatures for the cases run in a variable oxygen environment.

Table 4.8. The results from the four arc-jet cases where a nitrogen-oxygen flow is used and FIAT's predictions using the measured enthalpy.

Heating Environment	Measured		Equilibrium		Finite-Rate	
	Recession (cm)	Enthalpy (MJ/kg)	Recession (cm)	Surface (K)	Recession (cm)	Surface (K)
416 W/cm²						
(0% Oxygen)						
+10%			0.13	2910	0.08	2840
As Is	0.17	26.6	0.08	2850	0.05	2800
-10%			0.04	2780	0.02	2740
408 W/cm²						
(10% Oxygen)						
+10%			0.84	2880	0.54	2590
As Is	1.20	25.5	0.69	2820	0.48	2560
-10%			0.56	2750	0.41	2480
407 W/cm²						
(23% Oxygen)						
+10%			1.64	2860	1.17	2290
As Is	2.05	25.2	1.41	2800	1.06	2280
-10%			1.19	2740	0.95	2270
415 W/cm²						
(30% Oxygen)						
+10%			2.00	2860	1.47	2190
As Is	2.39	26.3	1.71	2810	1.33	2200
-10%			1.45	2750	1.20	2190

Table 4.9. The results from the four arc-jet cases where a nitrogen-oxygen flow is used and FIAT's predictions using the DPLR enthalpy to account for shape change.

Heating Environment	Measured		Equilibrium		Finite-Rate	
	Recession (cm)	DPLR Enthalpy (MJ/kg)	Recession (cm)	Surface (K)	Recession (cm)	Surface (K)
416 W/cm² (0% Oxygen)						
+10%			0.14	2870	0.07	2770
As Is	0.17	18.4	0.08	2810	0.04	2730
-10%			0.04	2740	0.02	2680
408 W/cm² (10% Oxygen)						
+10%			1.15	2840	0.65	2270
As Is	1.20	17.8	0.96	2790	0.59	2270
-10%			0.78	2730	0.53	2260
407 W/cm² (23% Oxygen)						
+10%			2.24	2830	1.47	1120
As Is	2.05	17.8	1.94	2780	1.41	1220
-10%			1.66	2720	1.27	1470
415 W/cm² (30% Oxygen)						
+10%			2.82	2840	1.60	1010
As Is	2.39	18.3	2.43	2790	1.57	1040
-10%			2.09	2730	1.52	1080

The changes from the higher measured enthalpy to the lower DPLR enthalpy, keeping the cold wall heat flux constant, shows the physical repercussion of increasing the heat transfer coefficient in that it increases the predicted recession. Because increasing the heat transfer coefficient to the surface will increase the amount of heat arriving on the surface, the material will experience an increase in ablation. The change in the surface temperatures due to environmental uncertainties at the heating regimes near 400 W/cm² shows the sensitivities of material to changes in the environment and the finite-rate reactions. As seen in Ref. 94, increasing the heat transfer coefficient or the enthalpy will increase the recession, char, and temperatures

due to an increase in the heating on the surface. If the heat transfer coefficient increases, the environmental sensitivity would dictate an increase the temperatures, char rate, and recession. However, an increase in the heat transfer coefficient would decrease the dimensionless char ablation rate found by the Park Model, which would lead to a decrease in the recession and temperatures. Conversely, a smaller heat transfer coefficient will increase the B'_c used in interpolation and increase char rates, recession and wall temperatures. When there is less charring, there will be a lower total ablation rate which means the corrected blown transfer coefficient will be larger. This results in more net convective heat flux, which increases the surface temperature if wall enthalpy is not under consideration. The heat transfer coefficient has a direct physical effect on the material through how much heat it transfers to the surface and also a chemical effect in how it used to determine the char rate from the Park Model.

The magnitude of the recovery enthalpy plays a role too. Recall that Ref. 94 found that the heat transfer coefficient affects surface predictions in only a slightly larger quantity than the enthalpy. Physically, if the recovery enthalpy is near zero, any convective heat flux is being driven away from the surface by the wall enthalpy (H_R is zero in Eq. 2.7). From the environmental standpoint, this places an increased emphasis in the corrected blown transfer coefficient (the heat transfer coefficient) since it is being used with the wall enthalpy to generate convective heat flux.

The injected heat flux is also affected by changes in the charring rate and wall enthalpy as it is heat ejected to the flow from the wall by the pyrolysis gas and char. Unlike radiation leaving the surface, the injected heat flux is not directly dependent on surface temperatures and unlike conduction, it is not explicitly dependent on

material properties. Like convective heat flux, it is dependent on what is occurring away from the surface, the pyrolysis gas and char formation with the material. So the convective heat flux and the injected flux do not directly rely on surface temperatures and be thought of as affecting the surface temperatures by dictating how much heating remains on the surface to be carried away by radiation or conduction.

The relative effects on the surface temperature through changes on the convective and the injected heat flux via the heat transfer coefficient vary depending on the conditions. The surface temperature prediction when a low enthalpy is coupled with an increasing heat transfer coefficient seems to indicate that under those conditions, the increase in convective heat flux is counteracted and overcome by the increase the injected heat flux. There is more heat being ejected into the flow than entering the surface from the environment and the surface temperature will be lower. When the heat transfer coefficient is decreased, the convective heat flux is decreased, but not as much as the injected heat flux so more heat is going into the surface, increasing the surface temperature. The cold wall heat flux determines what is a low enough enthalpy such that the heat transfer coefficient is the biggest driver of heating and hence its importance in both the corrected blown transfer coefficient equation. Enthalpies lower than 20 MJ/kg typically start to exhibit behavior such that increasing the heat transfer coefficient in nonequilibrium can result in a lower surface temperature as opposed to a decrease in the coefficient.

Another important takeaway from Tables 4.8 and 4.9 is the impact on the concentration of oxygen in the flow. The nitrogen-oxygen tests were run at 4 concentrations: 0%, 10%, 23%, and 30%. Since all four tests are run at nearly

identical cold wall heat fluxes and enthalpies and for the same amount of time, changes in the recession and temperatures will be due in part to the amount of oxygen available in the flow. No oxygen means there are no oxidation reactions taking place at the surface. This means there will be less mass loss on the surface. The arc-jet test results show that when there is no oxygen in the flow, the recession is very low almost 100% lower than if there was only 10% oxygen in the flow. It is important to properly account for oxygen in the surrounding flow of a PICA material. Increasing the percentage of oxygen in the flow increases the amount of recession on the surface, as more oxygen particles are available to form CO or CO₂ with the carbon material. Also, increasing the oxygen concentration makes the differences between an equilibrium assumption and nonequilibrium assumption larger, because more reactions are being assumed to be unsteady in time, reducing the predictions. The impact of increasing the oxygen concentration is counteracted when the finite-rate reactions are curbing the impact of more oxygen reactions.

For the argon environment, Milos and Chen's predictions matched the measure values of surface temperature and recession. The work carried out in this dissertation keeps the argon mass fraction constant at 0.086 while the actual test argon fraction gets as high as 0.277. The predictions in Table 4.10 are representative of the effects of assuming a smaller fraction of the species than what may actually be present. The measured values are the averages from the multiple tests run at that condition.

Table 4.10. The results from the argon arc-jet cases where there is a significant amount of argon in the flow but only a mass fraction 0.086 in MAT.

Heating Environment	Measured		Equilibrium		Finite-Rate	
	Recession (cm)	Surface (K)	Recession (cm)	Surface (K)	Recession (cm)	Surface (K)
107 W/cm²						
(0.276 Argon)						
+10%			0.23	2050	0.09	750
As Is	0.23	2040	0.21	2010	0.08	763
-10%			0.19	1950	0.08	771
169 W/cm²						
(0.142 Argon)						
+10%			0.38	2290	0.12	836
As Is	0.45	2260	0.34	2230	0.12	846
-10%			0.30	2180	0.12	870
246 W/cm²						
(0.108 Argon)						
+10%			0.52	2520	0.44	1140
As Is	0.52	2420	0.46	2470	0.41	1260
-10%			0.41	2410	0.36	1380
395 W/cm²						
(0.080 Argon)						
+10%			0.48	2790	0.36	1970
As Is	0.45	2730	0.42	2740	0.33	2000
-10%			0.36	2680	0.28	2020
552 W/cm²						
(0.076 Argon)						
+10%			0.63	2990	0.43	2410
As Is	0.52	2960	0.54	2940	0.39	2400
-10%			0.46	2880	0.34	2380
744 W/cm²						
(0.080 Argon)						
+10%			0.80	3150	0.48	2780
As Is	0.51	3030	0.67	3110	0.43	2760
-10%			0.55	3060	0.37	2720
1102 W/cm²						
(0.146 Argon)						
+10%			0.58	3320	0.33	2970
As Is	0.48	3230	0.49	3290	0.29	2950
-10%			0.41	3250	0.25	2920

Despite the mass fraction of argon differing between the facility arc-jet runs and the predictions, the equilibrium predictions from FIAT match the measured values in a similar manner to that of Milos and Chen's use of argon-adjusted B' tables. All predictions are within the measurement and environmental errors for the parameters. Because argon is being used to protect the facility and not as a driver of reaction and being present in less quantities than oxygen and nitrogen, it is not a major species in the flow and the difference between the amount actually present in the flow and the amount accounted for in the surface chemistry calculations does not drive the predictions to fall outside the error envelope.

One trend seen with the differing argon mass fractions is that as the facility fraction approaches the fraction in MAT, the FIAT predictions go from underpredicting the measured results to overpredicting them. Though having incorrect argon fractions at the surface did not result in predictions outside the allowable error envelope, it does lead to different relations to the measured data in that the predictions may be either over or under the measured data. It is an important distinction when it comes to design a TPS material because designing around an underprediction can lead to mission failure. Though argon is not the main driver of reactions on the surface, the larger mass fraction in the facility flow does mean there is more argon present for its associated reactions in the flow and less of the other species. More argon may mean less oxygen available for reactions on the surface, leading to lowered recession. The constant argon mass fraction allows for the same amount of reactions to occur in each case. So when the two fractions, the actual argon and the constant argon, are approximately the same, the amount of reactants relative

to the other elements in the flow is approximately the same. The actual argon fraction being higher means less of the other species, making the lower constant fraction predictions higher due to the availability of the key species.

As the cold wall heat flux approaches and surpasses 1000 W/cm^2 , it is again seen that equilibrium overpredicts recession and surface temperature while the finite-rate assumption results in predictions that may be slightly underpredicting the measurements but are closer to the measured values and within the error envelope. At the higher cold wall heat fluxes, the surface temperature is surpassing 3000 K , activating sublimation. A comparison with Covington^{49,90} results shows that in argon and oxygen-rich flows, if the surface temperature reaches 3000 K or approaches 1000 W/cm^2 , then the Park Model's addition helps compensate for the overprediction due to the sublimation reaction occurring in a finite-rate sense. Since sublimation is concerned with only one element, carbon, and there will always be carbon presence if the heatshield material is carbon-based, the amount of argon or oxygen in the air does not affect the sublimation reaction. The driver of the reaction is the surface temperature which is driven by the cold wall heat flux.

The arc-jet data from Milos and Chen does not show that nonequilibrium is a more robust assumption than equilibrium for the conditions run for the experiments, but illustrates the physics behind the chemical reactions that models such as the Park Model are trying to recreate. The amount of oxygen in the flow around the PICA material affects the amount of recession on the surface for similar heating regimes by allowing for more or less surface reactions to take place. High levels of oxygen and low heating in an argon flow causes large reductions in surface temperatures with the

assumption of finite-rate reactions due to a decrease in energy being released by the reactions. For the oxygen-rich flows, the finite-rate reduction is multiplied by the higher amount of oxygen reactions taking place while at low heating for argon flows, since the finite-rate model of Park is missing an argon consideration, the full set of reactions are not properly being accounted for and energy is missing for that model.

4.4 State of the Art Park-Based Material Response Model

Milos, Chen, and Gokcen study low heat fluxes and low pressure environments for nonequilibrium analysis of the PICA material in Ref. 95. The thermochemical flow model included in their analysis contains argon. They found that the recession rate is closely related to the atomic oxygen, as carbon and oxygen join to form carbon dioxide. The diffusion-limited oxidation causes a near constant B'_c for a range of surface temperatures. As B'_g becomes larger, the plateau becomes more of a curve because oxygen is reacting with the pyrolysis gas that comes from the material change. At low pressures, pyrolysis gas does not react quickly with the boundary layer gas which is why there would be a plateau at low values B'_g whose low value indicates a relative low rate of formation of pyrolysis gas. In order to better capture the effects of the pyrolysis gas and to improve recession predictions, Ref. 95 models the gas as its own set of equilibrating species in addition to the set modeled for the flow. Figures 4.13 and 4.14 are a normally generated B' table considering one flow, the environmental flow and one generated with pyrolysis gas being its own separate species set and flow. The separated pyrolysis gas flow will result in more constant char rates presents for a wide range of B'_g because the two are being considered separate. The ablation rate will be constant until conditions are such that

carbon will begin to sublimate. While Ref. 95 found that separating the pyrolysis gas species resulted in higher recession, they conclude that since their data sets are too sparse they could not say whether that assumption is accurate. Additionally, temperatures between the two cases did not differ significantly. Milos, Chen, and Gokcen recommend a merging of the two tables which in their work results in a 9% error in recession predictions versus the measured values. However, the merged tables need more pressure values around 0.10 atm (10 kPa) to compensate for the transition from low heat flux to high heat fluxes (above and below 100 W/cm^2).

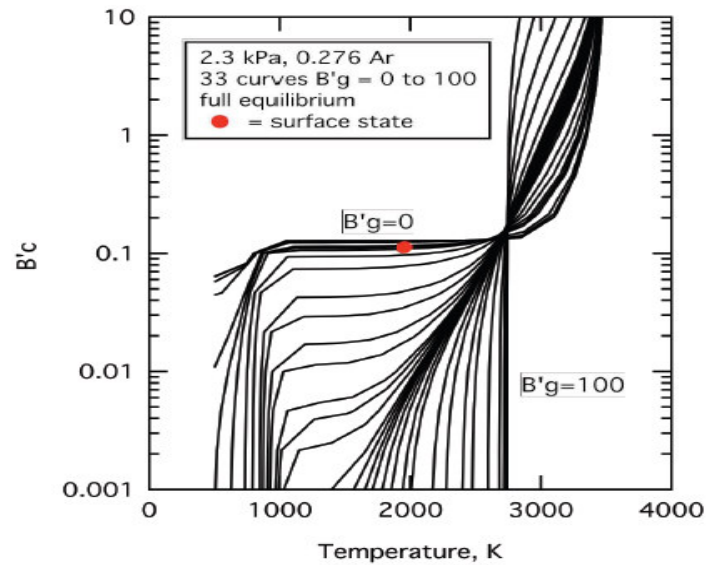


Figure 4.13. A typical B' table where the effects of the pyrolysis gas are not separated from the flow.⁸⁰

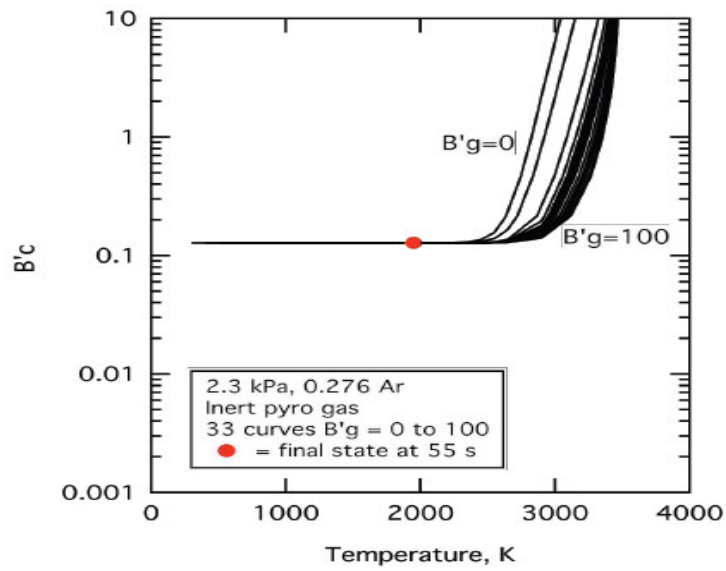


Figure 4.14. A B' table that considers the pyrolysis gas as a separate entity than from the flow, which results in more plateaus.⁸⁰

The two separate models, with and without consideration for pyrolysis gas, overpredict recession at four test conditions carried out by Ref. 95. Also commented upon is that at test conditions where there is high enthalpy and very low pressure in the shock layer, the low pressure allows the high dissociation of oxygen to reach the surface and oxidize at a nonequilibrium rate. To capture this dissociation and to better predict recession at the conditions, Milos, Park, and Gokcen use three of the reactions found in the Park Model: the diffusion-limited oxidation, nitridation, and sublimation. However, they found the rates for nitridation and sublimation to be negligible at the conditions when compared to oxidation. This is similar to previous comparison to arc-jet data where the low heating regimes meant that sublimation would not be activated and the results were driven by the other three reactions in the Park Model leading to predictions that were less robust as when sublimation is activated.

FIATC does not involve B' tables and its surface thermochemistry methodology is outlined in Ref. 80. Milos and Chen essentially eliminate FIAT's need to interpolate a B' table by integrating MAT's surface thermochemistry model directly in the material response. They also allow for standard, predefined mole and mass fractions for eight different atmospheres (Venus, Earth, Mars, Jupiter, Saturn, Uranus, Neptune, and Titan). This process is similar to the one implemented in BFIAT, but is simpler in one regard (only one line of a B' table is needed), more complex in another (more species data is needed to be known to run the material response program), and unknown in others (there is no mention of how the Park Model does not trend towards equilibrium and how to compensate for that when a flow may be occurring in both equilibrium and nonequilibrium. Since FIATC is essentially MAT added within FIAT the problems with the use of the Park Model remain).

In addition to the use of pyrolysis gas as its own separate species set, Ref. 80 specifies an edge fraction of atomic oxygen in the mass fraction of each element equation such that Eq. 2.96 becomes:

$$Y_{kw} = \frac{Y_{ke} + B'_g Y_{kg} + B'_c Y_{kc} - B'_{kr} + Y_{oe}}{1 + B'_g + B'_c} \quad (4.1)$$

The reasoning as to its inclusion is due to the flowfield and not the reactions on the surface as Ref. 95 states that atomic oxygen is added because the flowfield is not in chemical equilibrium and the primary source of the atomic species of O and N is the boundary layer edge. As seen in Ref. 92 with the arc-jet tests that vary oxygen makeup and how FIAT's predictions change due to differing makeups, the compositions of the elements in the edge gas affects recession. Eq. 2.96 already

counts edge element concentration in its Y_{ke} term, so the addition of atomic oxygen concentration leads to double counting it when the element oxygen is being considered. Additionally, atomic oxygen may be playing a large role in nonequilibrium calculations at the heating regimes studied due to the high level of oxidation and would not hold up as a valid element to add to the calculations at heating regimes where nitridation and sublimation are not occurring in negligible rates.

Implementation of the additional edge atomic oxygen consideration into a BFIAT-like setup results in the B' table not converging due to large elemental mass fractions. This casts doubt upon its use in Ref. 80 since the nonequilibrium setup is essentially MAT rewritten within FIAT and it should encounter the same nonconvergence. They choose to ignore the second oxidation reaction in the Modified Park Model for the counting of edge oxygen, which does have a physical reason that should be applicable to both equilibrium and nonequilibrium as long as the flowfield remains in nonequilibrium. Milos and Chen in Ref. 80, however, do not include the atomic oxygen consideration in their FIATC equilibrium calculations. The use of atomic oxygen to help nonequilibrium predictions as outlined in Ref. 80 is a mathematical improvement only for nonequilibrium. However, mathematically speaking, there would have to be more changes to the surface thermochemistry calculations to integrate that physical reasoning and even then, it may only be applicable at certain conditions. The only consideration made in the FIATC setup that is robust no matter the environmental conditions and is based solely on a physical reasoning is analyzing the pyrolysis gas as its own separate flow.

Figure 4.15 compares the percent difference in the FIATC and BFIAT recession predictions and the BFIAT recession predictions and measured recession from 15 arc-jet test cases that use argon. Figure 4.16 compares the actual measured and predicted recession for the two models and the arc-jet cases. Again, while the actual argon mass fraction is changing in each run and FIATC accounts for that, the current finite-rate model does not and keeps it at 0.086. The differences between the BFIAT predictions and the measured predictions decrease as enthalpy increases, further proof that the current model is more robust at SRC-like enthalpies. For nonequilibrium, the FIATC predictions are more accurate than the BFIAT predictions for recession. While this would seem to indicate that the FIATC nonequilibrium predictions are more accurate than the BFIAT predictions, FIATC includes the inert pyrolysis gas assumption, which is independent of whether or not the reactions are occurring in a finite-way and keeps the char rate at some constant value, leading to increased recession even when it is applied to equilibrium. The char rate in FIATC is more likely to remain constant and not change though temperature may be changing due to the pyrolysis gas influence. FIATC also includes the problematic atomic oxygen consideration. The robustness of FIATC's recession predictions cannot be said to be solely due to its surface kinetic model but is more likely due to the separation of pyrolysis gas from the species set causing more constant charring and the mathematical assumptions in the inclusion of atomic oxygen.

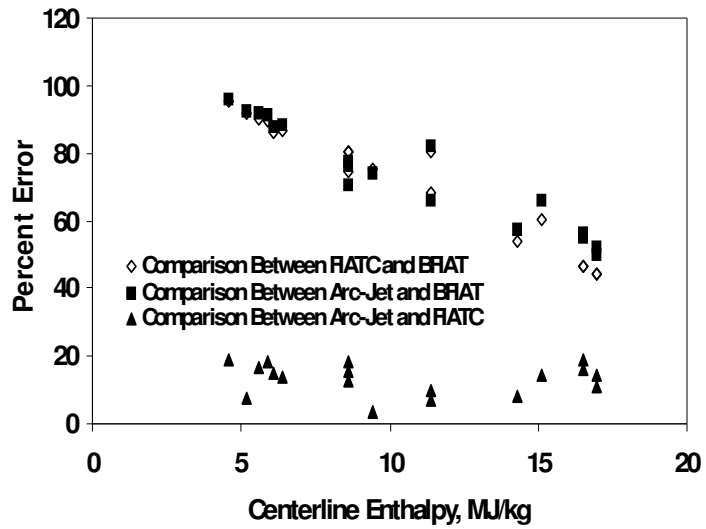


Figure 4.15. The percent error between the various finite-rate implementations and the actual measured values.

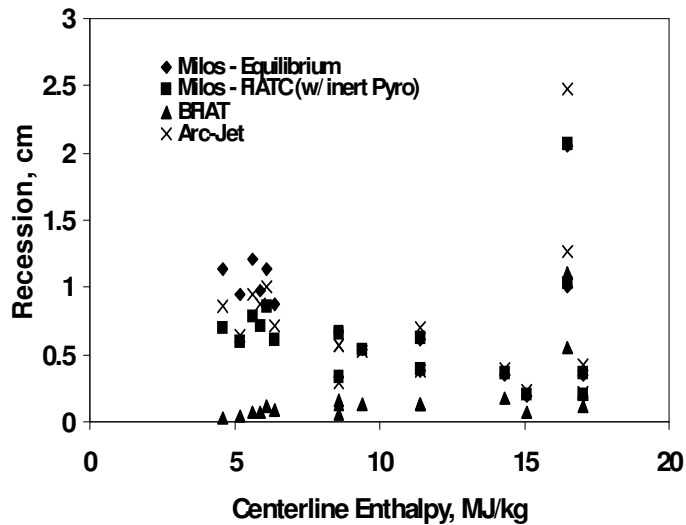


Figure 4.16. The recession predicted for various finite-rate implementations and the actual measured values.

Table 4.11 is a comparison to Milos and Chen's simple surface kinetic model, one that does not use atomic oxygen and pyrolysis gas separation, and the BFIAT model as outlined in this dissertation, which uses the full Modified Park Model, for

various cold wall test cases. Note that not all the cases are run for the same length of time, the data presented is for the longest test run for each case, and the argon mass fraction is not changing with the full Modified Park Model. The full Modified Park Model has two oxidation reactions, diffusion-controlled and rate-controlled, while the simple kinetic model only uses one oxidation reaction, the diffusion-controlled reaction. This results in the recession predictions using the full Modified Park Model at certain heating regimes being larger than the simple kinetic model's recession predictions because the rate-controlled oxidation is being ignored in the simple model. When the two predictions are similar, it is during heating regimes where rate-controlled oxidation may be negligible. The discrepancy shows the importance of the set of reactions being used to capture finite-rate effects. The rate-controlled oxidation reaction is briefly considered in Refs. 80 and 95 but is discarded for atomic oxygen due to the agreement between the atomic oxygen driven results and the measured data.

In cases with higher enthalpy, such as the 165 W/cm^2 with an enthalpy of 14.3 MJ/kg , the full Modified Park Model as implemented in this dissertation predicts higher recession than in FIATC. Though both programs predict recession much smaller than found in the arc-jet tests, BFIAT outperforms a simple kinetic model as implemented in FIATC Ref. 95 states that the simple surface kinetics model was thrown out due to a large reduction in B'_c . To combat that reduction, FIATC includes atomic oxygen, but that alone is not the driver of improved recession predictions. The pyrolysis gas, which keeps char constant and hence is the reason why the char rate is

not reduced, is the driver and it is not involved in the surface kinetics. BFIAT works better from a surface kinetics standpoint, without the considering pyrolysis gas.

Table 4.11. The results from the argon arc-jet cases where there is a significant amount of argon in the flow but only a mass fraction 0.086 in MAT for comparison between finite-rate and simple kinetics predictions.

Heating Environment	Measured		Simple Kinetics ⁸⁰ (Approximate)		Finite-Rate	
	Recession (cm)	Surface (K)	Recession (cm)	Surface (K)	Recession (cm)	Surface (K)
73 W/cm² (0.086 Argon)						
+10%			0.10	N/A	0.08	668
As Is	0.74	1760	0.07	N/A	0.08	678
-10%			0.04	N/A	0.08	686
107 W/cm² (0.276 Argon)						
+10%			0.08	N/A	0.08	740
As Is	0.23	2030	0.06	N/A	0.08	748
-10%			0.04	N/A	0.08	759
143 W/cm² (0.173 Argon)						
+10%			1.03	N/A	1.13	804
As Is	2.47	2190	1.01	N/A	1.11	815
-10%			0.91	N/A	1.10	826
165 W/cm² (0.117 Argon)						
+10%			0.13	N/A	0.17	814
As Is	0.40	2120	0.12	N/A	0.17	824
-10%			0.11	N/A	0.16	836
183 W/cm² (0.117 Argon)						
+10%			0.40	N/A	0.17	789
As Is	0.68	2140	0.35	N/A	0.17	799
-10%			0.30	N/A	0.17	810

Chapter 5

Summary and Conclusions

To protect the spacecraft from high heating, computational material response models are applied in TPS design for crafts experiencing atmospheric entry in order to design a heatshield. The heatshield can make up a significant amount of the total mass of a spacecraft⁵. A TPS material may char or produce pyrolysis gas, affecting its material properties, complicating the model. Equilibrium surface interactions are often assumed because it is a conservative approach as the reactions have no consideration for time and are allowed to fully react. Under this assumption, the predictions for such parameters as recession and surface heat flux have been much larger than what actually was experienced by the craft.^{4,13} Overprediction leads to heatshields that are more massive than what could actually have been safely used on the spacecraft. The heatshield mass, as seen in the Pioneer-Venus probes.⁵ One possible solution to lessen the overpredictions is to include a finite-rate surface interaction reaction set while calculating surface thermochemistry. The equilibrium condition is a subset of the nonequilibrium condition, which allows for consideration as to how long the reactions will take to complete. This consideration may mean that a reaction will not fully react in a given time frame and cause a reduce reaction rate. While an equilibrium assumption is a conservative approach as it assumes all the reactions are steady in time and less conservative approach can reduce the problem with the overprediction of needed heatshield mass.

The Stardust Return Capsule is a case where the heatshield was designed around a recession prediction that was 50% more than necessary, with high heating on the surface between 1000 and 1200 W/cm². The material response program used for analysis is FIAT¹¹ and the surface thermochemistry program used to simulate the surface reactions is MAT.¹² The Modified Park Model^{7-9,61,63} and the Zhlukov Model^{9,64} are chosen to approximate carbon-reactant, finite-rate reactions on the surface of the SRC heatshield, which is made of PICA, a carbon-based low density material. Only the Modified Park Model is able to be implemented in MAT and can produce a range of char and pyrolysis gas rates for the SRC trajectory. The Modified Park Model has 4 reactions of 3 types: oxidation, nitridation, and sublimation.

Applying the Modified Park Model to the stagnation point and near stagnation point on the SRC heatshield showed:

- The limitation of the Modified Park Model as it does not approach equilibrium.
- Finite-rate reactions greatly impact the char formation and drives down recession.
- Sublimation is the main reaction taking place during the SRC, congruent with findings by Graham and Candler^{19,20} on the altitude-reaction relationship.
- Nitridation has little effect over the entire trajectory despite prior analysis⁹ at peak heating indicating its importance.
- For the preliminary design trajectory, the finite-rate model lessens recession predictions while keeping the prediction conservative (from 1.1 cm to 0.72 cm).

- The basic theory that the convective heat flux is dependent on the total ablation rate and will decrease in there is high pyrolysis gas and char formation.
- For the final design trajectory, it is likely that both equilibrium and nonequilibrium reactions are occurring over the reentry.
- For the final design trajectory, application of finite-rate reactions when sublimation is active brings the recession prediction with the measured recession error envelope (at near stagnation point: prediction: 0.55 cm, measured: 0.57 cm).
- The finite-rate approximation for the SRC (and SRC-like) trajectory can reduced the recession prediction while keeping other parameters close their measured values such that a TPS designed for those conditions can be less massive.

Applying the Modified Park Model to the Core 2-Point 47 location on the SRC heatshield showed:

- Decreased heating leads to slower char formation which will make equilibrium char rates be nearly as slow as finite-rate char rates
- Frustum effects may start to appear due to the geometry of the heatshield and may have impacted the equilibrium predictions.

Analysis at all three locations showed:

- The insulative properties of the PICA material. There was no heat flux across its backface and the initial starting temperature of the spacecraft remained constant during the final design trajectory.

Arc-jet testing allows for analysis of the finite-rate model at different heating regimes and allows for further study of how the type of reactions experienced by the PICA material. These arc-jet tests contributed the understanding of the finite-rate model by showing:

- At very low heating, less than 200 W/cm^2 , the Modified Park Model does not perform better than a fully equilibrium model and greatly underpredicts recession and surface temperatures due to char formation being significantly slowed down at those heating regimes.
- At higher heating regimes, but those less than 1000 W/cm^2 , where sublimation may first be activated, the Modified Park Model and equilibrium predictions are somewhat similar due to similar charring rates caused by reverse reaction rates that may be approximated as zero, bringing the assumptions of the Park Model aligned with the actual physical conditions.
- At heating regimes above 1000 W/cm^2 , similar to SRC heating, the Modified Park Model better matches arc-jet measurements of recession than an equilibrium assumption due to sublimation. If the heating is much larger than 1000 W/cm^2 , the model cannot properly calculate the sublimation reaction approaching equilibrium and the nonequilibrium prediction performs poorly.

Three heating regimes are identified as areas of study for the Modified Park Model applied to PICA. The Modified Park Model will be the best approximation of what is occurring on the surface during the heating regime where there is an existence of finite-rate sublimation. Previous arc-jet tests^{80,92,95} identified only oxidation as a key reaction.

To better approximate the change from equilibrium to nonequilibrium in the Modified Park Model and for any potential model that does not trend towards equilibrium as robustly as needed, a new program, BFIAT is developed. The advantages of this new tool are that:

- It integrates the surface thermochemistry calculations as used in MAT with the material response model of FIAT and allows for the user to define when the surface thermochemistry portion should consider nonequilibrium over equilibrium.
- It allows for surface thermochemistry to be calculated at each point of analysis instead of having to interpolate between predetermined environment conditions.
- It is a more robust surface kinetic model than a similar program FIATC,^{80,95} which improves upon the pyrolysis gas contribution to the surface thermochemistry.

The importance of a finite-rate model in a material response model has been demonstrated, as the Modified Park Model can decrease the conservative approach to predicting recession, leading to a better match with physical results. This means a reduction in mass when designing a thermal protection system that uses ablation to disperse the high heating encountered by a spacecraft. The use of the simple Modified Park Model allows for predictions to match measured data under certain reactions and serves as a first step to understanding the chemistry that can occur at the surface of an ablative material. Taking into account surface effects makes the design process more robust and can lead to an elimination of any unneeded mass.

Chapter 6

Future Work

The research presented in this dissertation is a first step towards a development of a robust surface thermochemistry model that takes into account all chemistry effects on a heatshield. Overly conservative predictions of the chemistry lead to a design process that may overestimate the needed mass for a heatshield. The following recommendations for future work are made: the surface thermochemistry model should be able to account for all reactions and be able to calculate the affects of the reactions; the finite-rate model itself should include any reactions identified as occurring in a non-negligible manner; the pyrolysis gas should be considered its own separate flow to take into the reactions that occur between the gas and the material. analysis should be expanded from one dimension to two dimensions; other trajectory should be analyzed, especially if there is measured data associated with those trajectories; the physical aspect of how a species is interacting with the material should be included in any model.

6.1 Improving the Finite-Rate Model

The level of complexity of a finite-rate model affects the predictions. The Modified Park Model is a simple model consisting of only four reactions and does not follow the typical Arrhenius equation in its calculation of mass loss. That coupled with the absence of any backward reactions and not directly being affected by the

reaction temperatures leaves the Modified Park Model without the capability to approach equilibrium in its calculations. Conversely, the Zhluktov Model is a more traditional finite-rate model, with equilibrium constants and reaction rates. However, the large number of reactions in the model (12) and number of unknowns (13) makes it difficult to implement.

Currently, the Park Model is being widely used in analyzing carbon-phenolic materials despite its limitations.^{8,9,24,80,95} In constructing the next generation model, the foundation should be built upon what makes the Park Model so widely and easily used, the small number of reactions and unknowns, with some added level of complexity, like what is seen in the Zhluktov Model. The four simplified reaction equations in the Park Model should be replaced by their Arrhenius counterparts and include consideration for reverse reactions such that equilibrium may be able to be predicted in the model. The more complex reaction equations for two of the reactions in the Park Model, oxidation and sublimation, can be found in the reaction set for the Zhluktov Model. The more complex equations will make the Modified Park Model better equipped to calculate equilibrium while still remaining relatively noncomplex with only a few reactions.

For Stardust trajectory-like conditions or those with a heating condition above 1000 W/cm^2 , it was seen that sublimation is a large contributor to the finite-rate reaction set. However, the kind of sublimation used in the Modified Park Model, the generation of C_3 , is not the only form of sublimation. Sublimation occurs any time solid carbon is vaporized into gaseous carbon, in any amount. A previously developed graphite surface kinetics program, GASKET⁹⁶, included up to five sublimation

reactions, ranging from the formation of just C to C₅. The approach to modeling sublimation in GASKET is similar to the approach in the Modified Park Model. When expanding the Modified Park Model to include more reactions, more sublimation reactions should be added, especially if the environmental conditions will lead to high temperatures on the surface. This will help properly capture all sublimation effects.

6.2 Inclusion of Pyrolysis Gas Effects

Research by Venkatachari et al.^{97,98} accounts for the properties of char and pyrolysis gas and the equilibrium and finite-rate chemistry of the pyrolysis products. Additionally, thermal nonequilibrium between the char and pyrolysis is also under consideration. Venkatachari et al.⁹⁸ states that high-fidelity models need three submodels: an in-depth heat and mass transfer submodel, a surface recession submodel, and a pyrolysis submodel that governs the rate of pyrolysis in the char. Ref. 98 found that most material response models lack a pyrolysis submodel. FIAT, in particular, does not account for any interaction between the char and the pyrolysis. As seen by the efforts of the researchers in Refs. 80 and 95, assumptions of the chemical effect the pyrolysis gas has on the ablating material can influence the recession rate and the final recession. The inclusion of pyrolysis gas as a set of elements to be reacted with at the surface of a material helped increase the recession predicted by a finite-rate approximation.

A sensitivity analysis performed by Ref. 98 using an independently developed one-dimensional model showed that varying the pyrolysis gas flow rate had a substantial impact on the material response. It is important to consider the pyrolysis

gas within the material because depending on its speed it can add to the heat convection or the heat conduction. Additionally, while working with a nylon-phenolic material, Venkatachari et al.⁹⁸ saw an increase in hydrogen at the gas/surface interface due to the escaping pyrolysis gas. If hydrogen is present in the pyrolysis gas formed from graphite or other carbon-based material, then its addition to the gas/surface interaction reaction model adds another element to be considered in a finite-rate reaction model. In a nylon-phenolic, the presence of hydrogen led to 9 new reactions that had to be considered. Pyrolysis gas cannot be ignored and should be considered an additional flow source not only at the surface of the material but also in-depth in future models.

6.3 Expansion to Two Dimensions

Current material response models that include two-dimensional effects do not include any finite-rate calculations for surface chemistry.^{25,53,99} Finite-rate analysis expanded into two dimensions will allow for a wider range of geometries to be considered. While a one-dimensional analysis is robust when considering a blunt body such that the ablating surface can be considered “flat,” if the material’s geometry is sharper, like that which may be of a hypersonic missile, two-dimensional effects will arise and need to be included in models for accuracy. TITAN is a two-dimensional extension of FIAT and has recently been used alongside FIAT in validating computational models to experimental data.⁹² Since TITAN has the same basic setup as FIAT and uses B' tables, implementation of finite-rate chemistry will not be complicated as the B' tables are not dependent on geometry. If the effects of pyrolysis gas are to be considered as previously suggested, then a two-dimensional

analysis may become complicated as the pyrolysis gas will be interacting with the char in two directions.

6.3 Additional Comparisons Against Varied Atmospheric Entry Data

The only flight test data readily available for this dissertation was that for the Stardust Return Capsule. It was not instrumented and the data came from airborne observation and post-flight measurements of the heatshield. More robust flight data would be that which is collected during the entry into an atmosphere, recorded on the actual surface of the heatshield. Data from the entry into the atmosphere is unlike arc-jet test data in that a wide range of conditions will be experienced over the same section of material. The Mars Science Laboratory (MSL) heatshield will be instrumented and be able to measure in-depth temperatures and char depth.¹⁰⁰⁻¹⁰³ This provides a unique opportunity to both apply a finite-rate model to an atmosphere unlike that of Earth's and to have flight test data available to compare the predictions. Already there is an effort to develop a tool that can recreate the environment experienced by the MSL heatshield by analyzing the measurements from the instruments.⁹⁴ If a fully equilibrium model is implemented in the environment recreation and results in predictions that do not match the measured data, such as predicted recession causing a thermocouple to fail when it continues to measure temperature on the heatshield, then a finite-rate model can be used to better understand the chemistry upon the surface. The MSL data will provide a new data set for comparison between equilibrium and nonequilibrium predictions or some combination of both for a reentry trajectory.

Additionally, there are past benchmark cases where validation of a finite-rate model, whether it is the current Modified Park Model or some other model, can build upon the knowledge base. Using the trajectory environmental data and comparison with measured data from the Apollo, Galileo, and Pioneer-Venus cases similar to what is carried out in Ref. 4 by Park and Tauber is one such example. Though Park and Tauber showed that finite-rate reactions are likely to be occurring at the stagnation point, their reactions set was small and using other models in its place can show one of two things: either the current model is applicable to those conditions faced by the Apollo, Galileo and Pioneer-Venus heatshield or that for those conditions, the current finite-rate model does not hold and must be applied carefully in cases outside where it does work. The comparison against multiple sets of data collected for different trajectory helps make a particular finite-rate model more applicable over a wider range of situations and help identify possibly problem areas.

6.4 Increase Knowledge of the Reactions Physics and Model Building

Currently, material response programs such as FIAT and computational fluid dynamics (CFD) models like DPLR are only loosely coupled, so the flow particles and the material particles never directly interact with each other in a straightforward manner in the model. Assumptions are made to approximate their interactions. Finite-rate models are built upon catalytic behavior of the prescribed set of reactions. These reactions involve both the particles found in the flow and on surface. This means an analysis of the interactions at the molecular level needs should be carried out to better understand the physics behind the model when the two sets of particles have contact with each other.

Work carried out by Refs. 104 and 105 are endeavors to better understand the physical interactions between the gas and the surface. Ref. 104 studies recombination, where a gas species joins the solid material on the surface of material. Neglecting surface recombinations leads to low predicted heat fluxes, but an assumption of a supercatalytic material leads to an overestimate of heat flux. Adsorption as seen in surface recombinations means that the gas and solid molecule are temporarily joined on the surface before being released into the gas phase. This means, theoretically, that for some small fraction of time, there are more particles on the surface of a material than the initially starting value. Arc-jet test data showed the importance of the concentration of oxidation and argon in the flow and similarly, the concentration on the surface of the material will affect the surface reactions. Recession could hypothetically slow down even when the heat is increasing on the surface. In the Modified Park and Zhlukov Models, there are no recombination reactions under consideration. Though the ultimate effect on recession is unknown, recombination effects can determine the heat flux that acts upon the surface, which is an important environmental parameter.

The approach in Refs. 104 and 105 of a catalytic wall from follows the flow species is interacting with a wall species and is concentrated on the effects on the flow. A pursuit of this knowledge from a material response perspective, like that which is concerned with what happens to the material once recombination occurs, will explain the physical molecular causes of the recession and surface temperature predictions. As such, it is important to identify any potential recombination reactions when constructing a new finite-rate model. Any new model should be able to

demonstrate the physics behind each reaction and what the impact of each reaction is upon the surface. Knowing these things will help with knowing the material's chemical composition, its structure, and the crystallographic orientation.^{104,105} The chemical composition is especially important when considering not only what elements will be present on the material's surface but what elements will be present when considering the effects of the pyrolysis gas. A simplified set of computational methods as presented in Refs. 104 and 105 should be adapted to the computational methods used to create surface thermochemistry tables, like those found in MAT, such that both the physical aspect of the gas/surface interaction (if molecules are recombining) and the impact of that aspect (wall temperature, enthalpy, char and pyrolysis gas rates) can be coupled together.

In addition to better understand the physical reasoning behind the finite-rate reactions one wishes to implement, an understanding of how to simplify complex calculations, especially when the analysis is small in both timescale (between one picosecond and one nanosecond) and in physical length (less than one nanometer), can better frame the setup of the model. Deshmukh et al.¹⁰⁶ use microkinetic modeling which is a model developed without considering partial equilibrium or a rate determining step. Corrections are done post computation. This reduces the chemical model such that only one reaction rate expression is used by Ref. 106 to get accurate results. The cases under analysis have disparate timescales, where the reactions on the surface are happening much quicker than those that occur away from the surface. For example, in examining CO, diffusion is seen to occur before desorption, leading to different time scales to consider both events fully.^{107,108} Refs.

106-108 show the underlining principles that can be made when considering a time-dependent, reaction-complex model. Continuing research into identifying the intrinsic kinetic parameters needed for analysis, how best to build a model when considering microkinetics, and the macroscale effects of the reactions as demonstrated by Refs. 104-105 makes future finite-rate models more complete and extends the physical reasoning and timespace which is previously reserved for analysis on how the flow interacts with the material and to the material side. The goal is to develop a complex model that combines the physical aspects of a particle interacting with a surface, the products from ablation like pyrolysis gas, and heating factors from all directions so that robust predictions can be made and help eliminate any overly conservative assumptions that lead to designing a TPS that is more massive than actually needed.

Bibliography

- [1] Koo, Joseph H., Ho, Dave W.H., and Ezekoye, Ofodike A., "A Review of Numerical and Experimental Characterization of Thermal Protection Materials – Part I. Numerical Modeling," AIAA Paper 2006-4936, July 2006.
- [2] Wilmoth, R.G., Dogra, V.K., and Moss, J.N., "Energetics of Gas-Surface Interactions in Transitional Flows at Entry Velocities," *Journal of Spacecraft and Rockets*, Vol. 29, No. 6, November – December 1992, pp. 786 – 793.
- [3] Caledonia, G. E., "Laboratory Simulations of Energetic Atom Interactions Occuring in Low Earth Orbit," *Rarefied Gas Dynamics*, edited by E.P. Muntz, D.P. Weaver, and D.H. Campbell, Vol. 116, Progress in Astronautics and Aeronautics, AIAA, New York, 1989, pp. 129 -142.
- [4] Park, Chul and Tauber, Michael E., "Heatshielding Problems of Planetary Entry, A Review," AIAA Paper 99-3415, June 1999.
- [5] Nolte, L.J., Stephenson, D.S. et al., "Final Report System Design of the Pioneer Venus Spacecraft: Volume 5 Probe Vehicle Studies," NASA-CR-137492, 1973.
- [6] Park, Chul, and Yoon, Seokkwan, "A Fully-Coupled Implicit Method for Thermo-Chemical Nonequilibrium Air at Sub-Orbital Flight Speeds," AIAA Paper, 89-1974, June 1989.
- [7] Park, Chul, and Hyo-Keun Ahn, "Stagnation-Point Heat Transfer Rates for Pioneer-Venus Probes," *Journal of Thermophysics and Heat Transfers*, Vol. 13, No. 1, January – March 1999. pp. 33-41.
- [8] Park, Chul, "Calculation of Stagnation-Point Heating Rates Associated with Stardust Vehicle," *Journal of Spacecraft and Rockets*, Vol 44., No. 1, January – February 2007. pp. 24 – 32.
- [9] Chen, Yih-Kang and Milos, Frank S., "Finite-Rate Ablation Boundary Conditions for a Carbon-Phenolic Heat-shield," AIAA Paper 2004-2270, June 2004.
- [10] Olynick, David, Chen, Y.K., and Tauber, Michael E., "Aerothermodynamics of the Stardust Sample Return Capsule," *Journal of Spacecraft and Rockets*, Vol. 36, No. 3, May-June 1999. pp. 442-462.
- [11] Chen, Y.K. and Milos, Frank S., "Ablation and Thermal Response Program for Spacecraft Heatshield Analysis," *Journal of Spacecraft and Rockets*, Vol. 36, No. 3, May-June 1999, pp. 475-483.

- [12] Milos, F.S., and Chen, Y.K., "Comprehensive model for multicomponent ablation thermochemistry," AIAA Paper 97-0141, January 1997.
- [13] Kontinos, Dean A., and Stackpoole, Mairead, "Overview of Post-Flight Analysis of the Stardust Sample Return Capsule Earth Entry," *IPPW-5*, Bordeaux, France, June 2007.
- [14] Kendall, Robert M., Rindal, R. A., and Bartlett, Eugene P., "A Multicomponent Boundary Layer Chemically Coupled to an Ablating Surface," AIAA Paper 65-642, June 1967.
- [15] Bartlett, E.P., Nicolet, W.E., and Howe, J.T., "Heat-Shield Ablation at Supersonic Reentry Velocities," AIAA Paper 70-202, January 1970.
- [16] Putz, Kurt E., and Bartlett, Eugene P., "Heat-Transfer and Ablation-Rate Correlations for Reentry Heat-Shield and Nostip Applications," AIAA Paper 72-91, March 1972.
- [17] Peterson, David L., and Nicolet, William E., "Heatshielding for Venus Entry Probes," AIAA Paper 73-212, August 1973
- [18] Yang, B.C. and Cheung, F.B., "Numerical Investigation of Thermo-Chemical and Mechanical Erosion of Ablative Materials," AIAA Paper 93-2045, June 1993.
- [19] Keenan, J.A. and Candler, G.V., "Simulation of Ablation in Earth Atmospheric Entry," AIAA Paper 93-2789, July 1993.
- [20] Keenan, J.A. and Candler, G.V., "Simulation of Graphite Sublimation under Reentry Conditions," AIAA Paper 94-2083, June 1994.
- [21] Bouslog, Stanley A., Caram, J.M., and Pham, V.T., "Catalytic characteristics of Shuttle high-temperature TPS materials," AIAA Paper 96-0610, January 1996.
- [22] Milos, F.S. and Marshall, J., "Thermochemical Ablation Model for TPS Materials with Multiple Surface Constituents," AIAA Paper 94-2042, June 1994.
- [23] Milos, F.S., and Chen, Y.K., "Three-Dimensional Ablation and Thermal Response Simulation System." AIAA Paper 2005-5064, June 2005.
- [24] Chen, Yih-Kang, and Milos, Frank S., "Navier-Stokes Solutions with Finite Rate Ablation for Planetary Mission Earth Reentries," *Journal of Spacecraft and Rockets*, Vol. 42, No. 6, November-December 2005, pp. 961- 970.
- [25] Katte, Subrahmanya S., Das, K.S., and Venkateshan, S.P., "Two-Dimensional Ablation in Cylindrical Geometry," *Journal of Thermophysics and Heat Transfer*, Vol. 14, No. 4, October-December 2000. pp. 548 – 556.

- [26] Congdon, William M. and Curry, Donald M., "Thermal Performance of Advanced Charring Ablator Systems for Future Robotic and Manned Missions to Mars," AIAA Paper 2001-2829, June 2001.
- [27] Congdon, William M., Curry, Donald M., and Collins, Timothy J., "Response Modeling of Lightweight Charring Ablators and Thermal Radiation Testing Results," AIAA Paper 2003-4657, July 2003.
- [28] Fujita, Kazuhisa, Yamada, Tesuya, and Ishii, Nobuyuki, "Impacts of Ablation Gas Kinetics on Hyperbolic Entry Radiative Heating," AIAA Paper 2006-1185, January 2006.
- [29] Cybyk, B.Z., Hunter, L.W., Drewry, D.G., and Van Wie, D.M., "A Unified Methodology for Simulation of Aerothermochemistry at Gas/Solid Interfaces," AIAA Paper 02-1086, January 2002.
- [30] Cybyk, B.Z., Drewry, D.G., and Leary, B.A., "High Fidelity Simulation Strategy for Aerothermochemistry at Ablating Gas/Solid Interfaces," AIAA Paper 03-668, January 2003.
- [31] Palaninathan, R., and Bindu, S., "Modeling of Mechanical Ablation in Thermal Protection Systems," *Journal of Spacecraft and Rockets*, Vol. 42, No. 6, November-December 2005. pp. 971-979.
- [32] Suzuki, Toshiyuki, Yamamoto, Yukimitsu, Yamada, Tetsuya, and Sakai, Takeharu, "Coupled Analysis of Flowfield and Thermal Response of Ablative Test piece Under Arc-Heated Flow Conditions," AIAA Paper 2006-778, January 2006.
- [33] Dec, John A., and Braun, Robert D., "An Approximate Ablative Thermal Protection System Sizing Tool for Entry System Design," AIAA Paper 2006-780, January 2006.
- [34] Anderson Jr., John D., *Hypersonic and High Temperature Gas Dynamics*, AIAA, Virginia, 1989.
- [35] Cheng, H.K. and Emanuel, G., "Perspective on Hypersonic Nonequilibrium Flow," *AIAA Journal*, Vol. 33, No. 3, March 1995, pp. 385-400.
- [36] Cheng, Hsien K., "Recent Advances in Hypersonic Flow Research," *AIAA Journal*, Vol. 1, No. 2, February 1963, pp. 295-310.
- [37] Evans, John S., Schexnayder Jr., and Grose, William L., "Effects of Nonequilibrium Ablation Chemistry on Viking Radio Blackout," AIAA Paper 73-260, January 1973.

- [38] Lincoln, Kenneth A., Howe, John T., and Liu, Tsong-Mou, "Assessment of Chemical Nonequilibrium for Massively Ablating Graphite," *AIAA Journal*, Vol. 11, No 8, 1973, pp. 1198-1200.
- [39] Inger, George R., Higgins, Charlotte, and Morgan, Richard, "Shock Standoff on Hypersonic Blunt Bodies in Nonequilibrium Gas Flows," *Journal of Thermophysics and Heat Transfer*, Vol. 16, No. 2, April-June 2002, pp. 245-250.
- [40] Boyce, R.R., Mundt, Ch., and Houwing, A.F.P., "Computational fluid dynamics validation using surface heat transfer measurements of hypersonic flowfields," AIAA Paper 96-0351, January 1996.
- [41] Gupta, R.N., "Aerothermodynamic Analysis of Stardust Sample Return Capsule with Coupled Radiation and Ablation," AIAA Paper 99-16144, January 1999.
- [42] Desai, P.N, Mitcheltree, R.A., and Cheatwood, F.M., "Entry Trajectory Issues for the Stardust Sample Return Capsule," International Symposium on Atmospheric Reentry Vehicles and Systems, Arcachon, France, March 16-18, 1999.
- [43] *Stardust Hypervelocity Entry Observing Campaign Support*, NASA Engineering and Safety Center Report, RP-06-80, August 31, 2006.
- [44] Jenniskens, Peter, "Observations of the STARDUST Sample Return Capsule Entry with a Slit-less Echelle Spectrograph," AIAA Paper 2008-1210, January 2008.
- [45] Kontinos, Dean, and Stackpoole, Mairead, "Post-Flight Analysis of the Stardust Sample Return Capsule Earth Entry," AIAA Paper 2008-1197, January 2008.
- [46] Tran, Huy K., Johnson, Christine E., Rasky, Daniel J., Hui, Frank C.L., Hsu, Ming-Ta, and Chen, Y.K., "Phenolic Impregnated Carbon Ablators (PICA) for Discovery class missions," AIAA Paper 96-1911, June 1996.
- [47] Tran, Huy K., "Development of Lightweight Ceramic Ablators and Arc-Jet Test Results," NASA TM 108798, January 1994.
- [48] Dolton, T. A., Maurer, R. E., and Goldstein, H.E., "Thermodynamic Performance of Carbon in Hyperthermal Environments," AIAA Paper 68-754, June 1968.
- [49] Covington, M.A., Heinemann, J.M., Goldstein, H.E., Chen, Y.K., Terrazas-Salinas, I., Balboni, J.J., Olejniczak, J., and Martinez, E.R., "Performance of a Low Density Ablative Heatshield Material," *Journal of Spacecraft and Rockets*, Vol. 45, No. 2, March-April 2008, pp. 237-247.
- [50] "User's Manual: Aerotherm Charring Material Thermal Response and Ablation Program," Aerotherm Div., Acurex Corp., Mountain View, CA, Aug. 1987.

- [51] Milos, Frank S. and Chen, Y.K., "User's Manual for FIAT.v1," Thermal Protection Branch, NASA Ames Research Center, June 1998.
- [52] Milos, Frank S., Chen, Y.K., and Squire, Thomas H., "Updated Ablation and Thermal Response Program for Spacecraft Heatshield Analysis," TFAWS 2006, University of Maryland, College Park, MD, August 7-11, 2006.
- [53] Milos, Frank S. and Chen, Y.K. "Two-Dimensional Thermal Response and Ablation Program for Charring Materials," *Journal of Spacecraft and Rockets*, Vol. 38, No. 4, July-August 2001, pp. 473-481.
- [54] Chen, Yih-Kanq, Milos, Frank S., Reda, Daniel C., and Stewart, David A., "Graphite Ablation and Thermal Response Simulation Under Arc-Jet Flow Conditions," AIAA Paper 2003-4042, June 2003.
- [55] Hyo-Keun Ahn, Park, Chul, and Sawada Keisuke "Response of Heatshield Material at Stagnation-Point of Pioneer-Venus Probes," *Journal of Thermophysics and Heat Transfers*, Vol. 16, No. 3, July – September 2002. pp. 432-439.
- [56] Brown, Kevin G., "Chemical and Thermal Nonequilibrium Heat Transfer Analysis for Hypervelocity, Low Reynolds Number Flow," AIAA Paper 85-1033, June 1985.
- [57] Vincenti, Walter G., and Kruger, Jr., Charles H., *Introduction to Physical Gas Dynamics*, Krieger Publishing Company, Florida, 1965.
- [58] Viviani, Antonio, Pezzella, Giuseppe, and Cinquergrana, Davide, "Aerothermodynamic Analysis of an Apollo-like Reentry Vehicle," AIAA Paper 2006 – 8082.
- [59] Viviani, Antonio and Pezzella, Giuseppe, "Catalytic Effects on a Non-Equilibrium Aerothermodynamics of a Reentry Vehicle," AIAA Paper 2007 – 1211.
- [60] Park, Chul, *Nonequilibrium Hypersonic Aerothermodynamics*, Jon Wiley, New York, 1990.
- [61] Park, Chul, Jaffe, Richard L., and Partridge, Harry, "Chemical-Kinetic Parameters of Hyperbolic Earth Entry," *Journal of Thermophysics and Heat Transfer*, Vol. 15, No. 1, January – March 2001, pp. 76 – 90.
- [62] Ahn, H.K., Park, C., and Sawada, K., "Dynamics of Pyrolysis Gas in Charring Materials Ablation," AIAA Paper 98-0165, January, 1998.
- [63] Park, Chul, "Stagnation-Point Ablation of Carbonaceous Flat Disks – Part I: Theory," *AIAA Journal*, Vol. 21, No. 11, November 1983, pp. 1588 – 1594.

- [64] Zhluktov, S.V., and Abe, T., “Viscous Shock-Layer Simulation of Airflow past Ablating Blunt Body with Carbon Surface,” *Journal of Thermophysics and Heat Transfer*, Vol. 13, No. 1, January – March 1999, pp. 50-59.
- [65] Blottner, F.G., “Prediction of Electron Density in the Boundary Layer on Entry Vehicles with Ablation,” NASA SP-252, Oct. 1970, pp. 219-240.
- [66] Scala, Sinclair M., and Gilbert, Leon, M., “Sublimation of Graphite at Hypersonic Speeds,” *AIAA Journal*, Vol. 3, No. 9, September 1965, pp. 1635 – 1644.
- [67] Chase, M.W. “NIST-JANAF Thermochemical Tables, Fourth Edition,” *Journal of Physical and Chemical Reference Data*, Monograph 9, Vols.1, 2, 1998, pp 641-1745.
- [68] Havstad, M.A. and Ferencz, R.M., “Comparison of Surface Chemical Kinetic Models for Ablative Reentry of Graphite,” *Journal of Thermophysics and Heat Transfer*, Vol. 16, No. 4, October-December 2002, pp. 508-515.
- [69] Park, Chul, “Effects of Atomic Oxygen on Graphite Ablation,” *AIAA Journal*, Vol. 14, No. 11, November 1976, pp. 1640 – 1642.
- [70] Scala, S.M, “The Ablation of Graphite in Dissociated Air, I. Theory,” General Electric, Missile and Space Division, R62SD72, Sept. 1962.
- [71] Bartlett, E.P., Kendall, R.M., and Rindal, R.A., “An Analysis of the Chemically Reacting Boundary Layer and Charring Ablator. Part IV: A Unified Approximation for Mixture Transport Properties for Multicomponent Boundary-Layer Applications,” NASA CR-1063, June 1968.
- [72] Bianchi, Daniele, Martelli, E., and Onofri, M., “Practical Navier-Stokes Computation of Flowfields with Ablation Products Injection,” 4th International Planetary Probe Workshop, Pasadena, California, June 27-30, 2006.
- [73] Milos, Frank S., “MAT v3 Training,” Slideshow, Thermal Protection Materials and System Branch, Space Technology Division, NASA Ames Research Center, October 30, 2006.
- [74] Boyd, Iain, and Candler, Graham, “Introduction to Hypersonic Aerothermodynamics: Hypersonic Gas Dynamics,” *Hypersonic Aerothermodynamics Short Courses*, National Institute of Aerospace, Hampton, VA, September 10-14, 2007.
- [75] Suzuki, Toshiyuki, Sakai, Takeharu, and Yamada, Tetsuya, “Calculation of Thermal Response of Ablator Under Arcjet Flow Condition,” *Journal of Thermophysics and Heat Transfer*, Vol. 21, No. 2, April – June 2007, pp. 257 – 266.

- [76] Milos, Frank S., "Galileo Probe Heatshield Ablation Experiment," *Journal of Spacecraft and Rockets*, Vol. 34, No. 6, November-December 1997, pp. 705-713
- [77] Goldstein, H.W., "The Reaction of Active Nitrogen with Graphite," *Journal of Physical Chemistry*, Vol. 68, No. 1, 1964, pp. 39-41
- [78] Laub, B. "Private Communication," 2008.
- [79] Maurer, R.E. Powas, C.A., Hartman, G.J., and Foster, T.F., "Graphite Sublimation Under Low and High Convective Mass Transfer Environments," ASME Paper 76-ENAs-68, March, 1976.
- [80] Milos, F.S., and Chen, Y.K., "Ablation, Thermal Response, and Chemistry Program for Analysis of Thermal Protection Systems." AIAA Paper 2010-4663, June 2010.
- [81] Kontinos, D. "Private Communication," 2008.
- [82] Milos, F.S. "Private Communication," 2008.
- [83] Lavelle, Joseph P., Schuet, Stefan R., Dobell, Chris, Verson, Jeff, Stackpoole, Mairead, and Kontinos, Dean, "The 3-D Mapping of Stardust's Post Flight Heatshield," AIAA Paper 2008-1200, January 2008.
- [84] Stackpoole, Mairead, Sepka, Steve, Cozmuta, Ioana, and Kontinos, Dean, "Post-Flight Evaluation of Stardust Sample Return Capsule Forebody Heatshield Material," AIAA Paper 2008-1202, January 2008.
- [85] Wright, M., Candler, G., and Bose, D., "Data-Parallel Line Relaxation Method for Navier-Stokes Equations," *AIAA Journal*, Vol. 36, No. 9, 1998, pp. 1603 – 1609.
- [86] Winter, Michael, and Herdrich, Georg, "Heatshield Temperatures and Plasma Radiation obtained from Spectroscopic Observation of the STARDUST Reentry in the Near UV," AIAA Paper 2008-1212, January 2008
- [87] McHarg, Matthew G., Stenbaek-Nielsenn, H.C., and Kanmae, T., "Observations of the STARDUST Sample Return Capsule Entry using a High Frame Rate Slit-less Spectrograph," AIAA 2008-1211, January 2008.
- [88] Boyd, Iain D., Zhong, Jiaqiang, Levin, Deborah A., and Jenniskens, Peter, "Flow and Radiation Analyses for Stardust Entry at High Altitude," AIAA Paper 2008-1215, January 2008.

- [89] Trumble, Kerry A., Cozmuta, Ioana, Sepka, Steve, and Jenniskens, Peter, "Post-flight Aerothermal Analysis of the Stardust Sample Return Capsule," AIAA Paper 2008-1201, January 2008.
- [90] Covington, M.A., Heinemann, J.M., Goldstein, H.E., Chen, Y.K., Terrazas-Salinas, I., Balboni, J.J., Olejniczak, J., and Martinez, E.R., "Performance of a Low Density Ablative Heatshield Material," AIAA Paper 2004-2273, June 2004.
- [91] Winovich, W., and Carlson, W., "The 60-MW Shuttle Interaction Heating Facility," *Proceedings of the 25th International Instrumentation Symposium*, Instrument Society of America, Pittsburgh, PA, 1979, pp. 59-75.
- [92] Milos, F.S. and Chen, Y.K., "Ablation and Thermal Response Property Model Validation for Phenolic Impregnated Carbon Ablator," *Journal of Spacecraft and Rockets*, Vol. 47, No. 5, September – October 2010, pp. 786-805.
- [93] Beck, J.V., and Murio, Diego A., "Combined Function Specification-Regularization Procedure for Solution of Inverse Heat Conduction Problem," *AIAA Journal*, Vol. 24, No. 1, 1986, pgs 180-185.
- [94] Beerman, A.F., Lewis, M.J., Santos, J.A. and White, T.R., "Development of a Tool to Recreate the Mars Science Laboratory Entry Aerothermal Environment," AIAA Paper 2010-4313, June 2010.
- [95] Milos, F.S., Chen, Y.K., and Gokcen, T., "Nonequilibrium Ablation of Phenolic Impregnated Carbon Ablator," AIAA Paper 2010-981, January 2010.
- [96] Anonymous, "User's Manual Aerotherm Graphite Surface Kinetics Program (GASKET 81)," Acurex Report UM-81-13/ATD, August 1981.
- [97] Venkatachari, B.S., Cheng, G.C., Koomullil, R.P., and Ayasoufi, A., "Computational Tools for Reentry Aerothermodynamics: Part II. Surface Ablation," AIAA Paper 2008-1218, January 2008.
- [98] Venkatachari, B.S., Cheng, G.C., and Koomullil, R.P., "Uncertainty Analysis of Surface Ablation," AIAA Paper 2009-261, January 2009.
- [99] Milos, F.S., and Chen, Y.K., "Two-Dimensional Ablation, Thermal Response, and Sizing Program for Pyrolyzing Ablators," *Journal of Spacecraft and Rockets*, Vol. 46, No. 9, November – December, 2009, pp. 1089-1099.
- [100] Beck, R.A.S., et al., "Development of the Mars Science Laboratory Heatshield Thermal Protection System," AIAA Paper 2009-4229, June 2009.

- [101] Edquist, K.T., Wright, M.J., and Tang, C.Y., "Aerothermodynamic Design Conditions for the Mars Science Laboratory Heatshield," AIAA Paper 2009-4231, June 2009.
- [102] Gazaric, M., et al., "Overview of the MEDLI Project," IEEE Paper 2008-1510, IEEE Aerospace Conference, Big Sky, Montana, March 2008.
- [103] Oishi, T., Martinez, E.R., and Santos, J.A., "Development and Application of a TPS Ablation Sensor for Flight," AIAA Paper 2008-1219, January 2008.
- [104] Valentini, P., and Schwartzentruber, T.E., "A Mechanism-Based Finite-Rate Surface Catalysis Model for Simulating Reacting Flows," AIAA Paper 2009-3935, June 2009.
- [105] Valentini, P., Schwartzentruber, T.E., and Cozmuta, I., "Simulation of Gas-Surface Interactions using ReaxFF Reactive Molecular Dynamics: Oxygen Absorption on Platinum," AIAA Paper 2010-4319, June 2010.
- [106] Deshmukh, S.R., Mhadeshwar, A.B., Lebedeva, M.I., and Vlachos, D.G., "From Density Functional Theory to Microchemical Device Homogenization: Model Prediction of Hydrogen Production for Portable Fuel Cells," *International Journal on Multiscale Computational Engineering*, Vol 2., No. 2, 2004.
- [107] Raimondeau, S., Aghalayam, P., Mhadeshwar, and Vlachos, D.G., "Parameter Optimization of Molecular Models: Application to Surface Kinetics," *Industrial and Engineering Chemistry Research*, Vol. 42, 2003, pp. 1174-1183.
- [108] Raimondeau, S., and Vlachos, D.G., "Front propagation at low temperatures and multiscale modeling for the catalytic combustion of H₂ on Pt," *Chemical Engineering Science*, Vol. 58, 2003, pp. 657-663.